Characterising gadofosveset for use in quantitative MRI studies

Owen Carl Richardson

Submitted in accordance with the requirements for the degree of
Doctor of Philosophy (PhD)

The University of Leeds
School of Medicine

September 2013

The candidate confirms that the work submitted is his own, except where work which has formed part of jointly-authored publications has been included. The contribution of the candidate and the other authors to this work has been explicitly indicated below. The candidate confirms that appropriate credit has been given within the thesis where reference has been made to the work of others.

Chapter 6 is based on the jointly authored publication:
RICHARDSON, O. C., M. L. J. SCOTT, S. F. TANNER, J. C. WATERTON and D. L. BUCKLEY. 2012. Overcoming the low relaxivity of gadofosveset at high field with spin locking. Magnetic Resonance in Medicine, 68(4), pp.1234-1238.
All authors contributed to the concept; OCR wrote the majority of the text, with some contribution from other authors; OCR acquired all data at 0.47 T and was assisted by MLJS in data acquisition at 4.7 T; OCR carried out all data analysis and generated plots; all authors contributed to conclusions.

Acknowledgements

This project was carried out with the aid of a BBSRC industrial CASE award (BB/G017220/1), in partnership with Astrazeneca. I am grateful to my sponsors for their financial support. For assistance with data acquisition I would also like to acknowledge the support of: Neil Woodhouse, José Ulloa, Hervé Barjat, and co-workers, AstaZeneca (Image acquisition, Chapters 4, 6, 7); Chris Smith, Steve Hill, AstraZeneca (ICP-MS, Chapter 5); Peter Wright (formerly of LMBRU), Arshad Zaman, Leeds Teaching Hospitals NHS Trust (Image acquisition, Chapters 4, 7); Peter Hine, Michael Ries, University of Leeds Department of Physics (NMR measurements, Chapters 4, 6); Octavia Bane, Tim Carroll, Michael Markl, Northwestern University, Chicago, imaging volunteers and staff at Northwestern Memorial Hospital, Chicago (Image acquisition, Chapter 7); Thomas Oerther, Bruker BioSpin GmbH (Spin-locking imaging sequence, Chapter 6). For valuable advice, support and suggestions throughout the project, I would like to thank John Waterton at AstraZeneca. For first introducing me to the wonderful world of MRI, I am grateful to Sasha Radjenovic, John Ridgway, Sarah Bacon and Dan Wilson. For being an inspirational and helpful bunch of people to work with, I'd like to thank the other members of Medical Physics (and support staff) at Leeds, in particular fellow book-clubbers John Biglands and Dave Broadbent.

Above all, I extend unreserved thanks to my fantastic supervision team, David Buckley, Steve Tanner, Marietta Scott and Steven Sourbron. I am particularly indebted to David, for the dedication he has shown to this project and the generosity he has displayed in giving his time and lending his experience.

On a personal note I would like to thank my family for their support. In particular, I would like to thank my partner Sharon for allowing me to turn our lives upside down (temporarily, I promise!), and for everything else – especially for our daughter, Isabel. It is to Isabel I would like to dedicate this thesis; I hope that one day she understands what an inspiration she is to me.

Abstract

Background: Gadofosveset is a clinically approved gadolinium-based MRI contrast agent that displays altered pharmacokinetic properties due to its high albumin-binding affinity (around 90% binds at low concentration), although the improved effectiveness due to binding reduces as field strength increases. With the trend for increasing clinical magnetic field strengths, it is important that gadofosveset is fully characterised at higher fields. It may then be possible to utilise the macromolecular properties of bound gadofosveset in tracer kinetic modelling for assessment of functional parameters.

Aims: This study aimed to characterise gadofosveset, in vitro, at relevant field strengths, develop a method for acquiring blood concentration measurements, and assess several novel techniques utilising the agent's binding affinity. The study was extended to include gadoxetate and gadobenate, gadolinium agents with a lower albumin-binding affinity, to provide a broader view of the influence of albumin binding.

Results: Relaxivities were calculated from in vitro measurements in the presence and absence of albumin, including bound relaxivity values at high field that have not previously been published. Extending the conventional model assumption of a single binding site to include up to three bound molecules improved the model fit for gadofosveset at low fields. A technique for using micro-samples of blood to measure gadolinium levels was successfully demonstrated in vitro, which may enable improved accuracy in dynamic studies. A macromolecule-sensitive technique (spin locking) gave a significant increase in albumin-bound gadofosveset relaxation rates at high field. A method for using gadofosveset as a biomarker for albumin was successfully applied in vitro, and the feasibility of in vivo implementation was assessed.

Conclusions: This in vitro characterisation of gadofosveset across a range of field strengths may inform future in vivo tracer kinetic modelling studies. Several novel applications for exploiting these characteristics have been successfully demonstrated in vitro, and warrant further in vivo investigation.

Table of Contents

List of Tables

List of Figures

CHAPTER 1: INTRODUCTION

1.1 BACKGROUND

The field of medical imaging has expanded considerably since Roentgen's discovery of X-rays at the end of the nineteenth century, with the introduction of alternative modalities and the implementation of improved technologies and methodologies. Yet despite these advances, the latest medical imaging techniques still present an imperfect view of the inner workings of the human body. There is a need to strengthen further the diagnostic and therapeutic potential of medical imaging, and it is this requirement that drives the large research community engaged in the improvement of these imaging techniques.

Magnetic resonance imaging (MRI) is the imaging modality most recently adopted into everyday clinical life. Although MRI utilises properties of the simplest and most abundant atom in the human body, hydrogen, image generation is underpinned by a sophisticated blend of fundamental physics and advanced technology. In the 40 years since the feasibility of MRI was first demonstrated, new applications, techniques and opportunities have been identified and developed, with the latest peer-reviewed research setting the agenda for future advances.

One area of MRI research, active since the early 1980s, is the improvement of tissue contrast through the introduction of exogenous contrast agents. Most clinical applications of MRI contrast agent utilise the paramagnetic properties of the gadolinium ion, which must be chelated to a ligand to reduce its toxicity. Differences in chelate design alter the characteristics of each agent, and lead to a range of practical applications. Amongst the clinically approved gadolinium-based contrast agents, gadofosveset demonstrates a unique affinity for serum albumin which sees it binds reversibly and in high fraction on injection. The bound gadofosveset molecule acquires certain macromolecular

properties which influence the effectiveness and pharmacokinetic behaviour of the contrast agent. Although gadofosveset is primarily used for imaging the vessels in MR angiography, its macromolecular properties may also have value in determining functional parameters such as tissue perfusion and capillary permeability.

Not all gadofosveset binds to albumin and the effectiveness of the contrast agent (termed ‘relaxivity’) comprises contributions from both the bound and the free molecule. Previous studies of gadofosveset have assessed the variation in relaxivity across a range of magnetic field strengths, but generally do not extend to the higher fields now in regular clinical use (up to 3.0 T). With the trend for stronger clinical magnets likely to continue, it is important that gadofosveset is fully characterised at magnetic field strengths that are, or may become, clinically relevant. It is only by having a full assessment of the properties of gadofosveset that further applications, beyond angiography and at higher field strengths, can be successfully implemented.

1.2 AIMS AND OBJECTIVES

The initial aim of the project was to fully characterise gadofosveset and its in vivo kinetics prior to application of the tracer in pre-clinical and clinical quantitative dynamic contrast-enhanced MRI studies. Accurate tracer kinetic modelling requires representative input parameters, therefore there were two main objectives: firstly, to assess through in vitro measurement the influence of binding on the relaxivity of gadofosveset and the variation in this relationship with field strength; and secondly, to utilise this knowledge in vivo by measuring a vascular input function for gadofosveset and developing extended tracer kinetic models to account for the reversible binding of the contrast agent. Pre-clinical in vivo assessment was to be carried out in a murine model, where high heart rates and low blood volumes add complexity to the measurement of a vascular input function.

However, gadofosveset was withdrawn from the European market shortly after this project commenced, and as a result it was not possible to carry out the planned in vivo experiments. The emphasis of this study was shifted towards further in vitro gadofosveset characterisation, along with in vitro assessment of a method developed to measure a vascular input function in small mammals. Through this characterisation work, several novel opportunities to exploit the albumin-binding nature of the agent became apparent.

This study has addressed gaps in the current gadofosveset literature and developed novel methods which may have clinical application. To provide a broader view of the influence of albumin binding on contrast agent behaviour, the study was extended to include two other gadolinium-based contrast agents, gadoxetate and gadobenate. These agents also bind to serum albumin, but have a much lower affinity than gadofosveset. In vitro experiments were designed using clinically relevant input parameters, and experimental work was supported by data simulations to provide a broader assessment of the ability to apply these methods in vivo.

The specific objectives of the study were as follows:

1. Determine the relaxivities of the bound and free molecules for gadofosveset, gadoxetate and gadobenate at a range of magnetic field strengths.

2. Extend the relaxation rate model beyond the common assumption of a single binding site on the albumin molecule, to incorporate up to three bound molecules, and assess the relative merits of each approach.

3. Develop a method for measuring gadolinium concentrations in micro-samples of blood, which may be used to generate a vascular input function in small mammals.

4. Measure the impact on relaxation rates when gadofosveset is used at high field in conjunction with an imaging technique, spin locking, which is sensitive to macromolecular content.

5. Assess the feasibility of using an albumin-binding contrast agent as a biomarker for tissue albumin.

1.3 OVERVIEW OF CHAPTERS

Chapter 2 begins with an introduction to the fundamental principles of MRI, including signal generation and the concept of relaxation. The theory behind paramagnetic contrast agents is discussed, and a general overview of the properties of gadolinium-based and other contrast agents is provided.

In Chapter 3 the primary focus is on gadofosveset, with a description of its albumin-binding properties and the influence of binding on relaxivity. A review of published literature is presented, within the context of gadofosveset characterisation and clinical application, to indicate the current level of knowledge associated with this agent. A similar review is also presented for gadoxetate and gadobenate, along with a brief overview of non-clinically approved albumin-binding agents.

Chapter 4 is the first of four experimental chapters, investigating the variation of gadofosveset, gadoxetate and gadobenate longitudinal relaxivities with field strength and temperature using in vitro samples. An existing model of relaxation rate is extended to include up to three binding sites.

In Chapter 5 a novel methodology is established for validating blood concentration levels of gadofosveset and determining a vascular input function, using a blood sampling technique that is well suited to small-animal studies. The feasibility of the technique is established using in vitro samples.

In Chapter 6 the macromolecule-sensitive technique of spin locking is applied to in vitro samples of gadofosveset to assess the feasibility of enhancing the relaxivity of gadofosveset at high fields. This novel combination of gadofosveset with spin locking forms the basis of a published paper (1).

Chapter 7, the final experimental chapter, explores through computer simulation and in vitro measurement the feasibility of a theoretical approach for using gadofosveset as a biomarker for albumin. The theoretical model is then applied to human volunteer data, using images acquired through collaboration with a research team in the USA.

Chapter 8 contains a summary of experimental results, discusses novel findings and draws final conclusions.

CHAPTER 2: BACKGROUND

2.1 INTRODUCTION TO MRI

Magnetic resonance imaging (MRI) generates clinical images of high quality, providing excellent soft tissue contrast without exposing the patient to ionising radiation. MRI is routinely used for accurate treatment planning and diagnosis; the UK National Health Service carries out approximately 1.2 million MRI scans per year (2).

Although MRI has notable advantages, equipment and scanning costs are higher and examination times may be longer than for other imaging modalities. Also, the strong magnetic field utilised in MRI (commonly, 1.5 T or 3.0 T) limits the interventional procedures that may be carried out during scanning, and precludes its use in patients with certain types of metal implant or pacemaker. In addition, the small bore of a conventional clinical scanner may be challenging for sufferers of claustrophobia.

MRI has limitations in areas such as bone or lung imaging, and image quality is susceptible to the effects of cardiac and respiratory motion. However, MRI has become the preferred modality for brain, soft tissue and joint imaging, and an active international research community is ensuring the clinical utility of MRI continues to grow.

2.2 BASIC PRINCIPLES OF MRI

2.2.1 Spin and magnetic moments

A full mathematical description of the theory behind MRI necessitates the inclusion of quantum mechanics. However, the fundamental principles of MRI may be adequately described through classical mechanics without the need to incorporate quantum theory (3). A classical approach is adopted here, and the reader is directed to other published texts for a quantum mechanical description (4, 5).

Although MRI is a relatively recent clinical imaging tool, its principles are built on the foundation of experimental work published in 1946 by Purcell et al (6) and Bloch (7) relating to nuclear magnetic resonance (NMR). A fundamental aspect of this work is that a spinning charged particle, such as the positively charged proton constituting the hydrogen (^{1}H) nucleus, generates an electromagnetic field and has a magnetic moment, μ, that is proportional to the spin angular momentum (with a proportionality constant, γ, known as the gyromagnetic ratio). This magnetic moment may be described by a vector pointing along the axis of rotation (Fig. 2.1a). In a sample containing many particles, the directions of these individual vectors at equilibrium in the absence of a magnetic field is random and the net magnetic moment is zero (Fig. 2.1b).

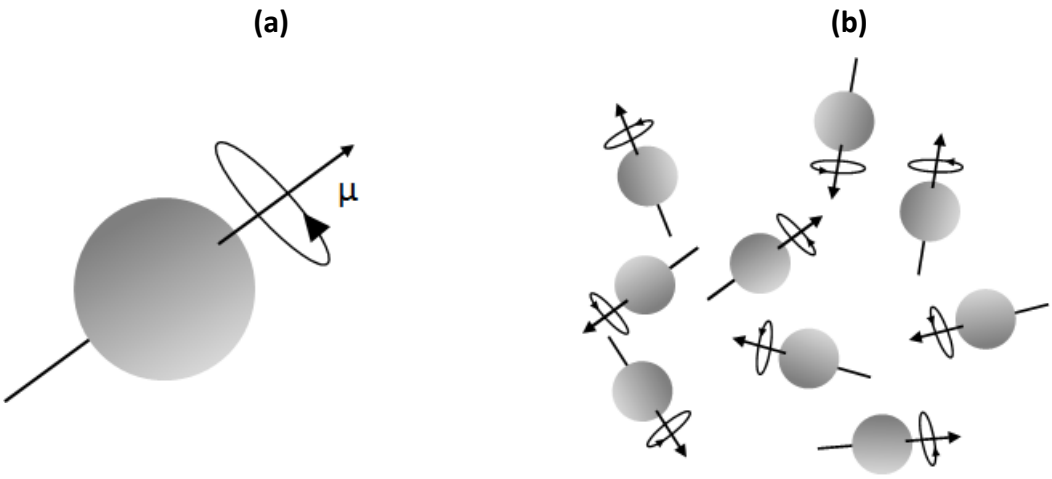

Figure 2.1: (a) A spinning charged particle (such as the proton in the ^{1}H nucleus) has a magnetic moment along the axis of rotation; (b) in a sample of many such particles, magnetic moments are randomly orientated and the net magnetic moment is zero

If this sample is placed within an external magnetic field, B_0, each magnetic moment begins to precess around the field, keeping a constant angle between the spin axis and the field (Fig. 2.2).

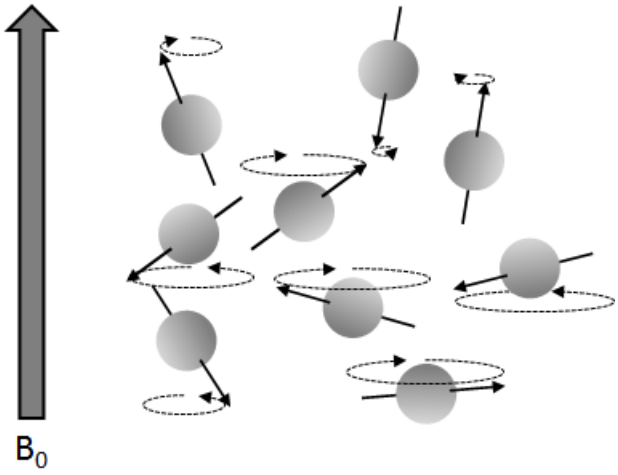

Figure 2.2: An external magnetic field, B_0, is applied, and individual magnetic moments precess around the axis of B_0

The rate at which these spins precess is known as the Larmor frequency, ω_0, and is proportional to the strength of the applied magnetic field, B_0. The Larmor frequency is given by Eq. 2.1.

$$\omega_0 = -\frac{2\mu}{h}.B_0 = -\gamma B_0 \qquad [2.1]$$

where μ = magnetic dipole moment, h = Planck's constant (6.63 x 10^{-34} J s), γ = gyromagnetic ratio.

The sign of the Larmor frequency indicates the direction of spin precession. Most nuclei have a positive γ, so the Larmor frequency is negative and precession is in the clockwise direction (when viewed against the direction of the magnetic field). The ^{1}H nucleus has a gyromagnetic ratio of 42.6 MHz T^{-1}, which is larger than almost any other nucleus; it is the primary target for clinical MRI due to a combination of this high gyromagnetic ratio and its abundance in the body.

The sum of these individual precessing magnetic moments is still very close to zero, as the direction of the vector is not changed by the magnetic field. However, small, rapidly fluctuating magnetic fields are generated on a microscopic scale by electrons and nuclei, and thermally generated interactions with these microscopic fields eventually leads to a breakdown in the isotropic nature of the individual magnetic moments. This leads to a slight tendency for the net magnetic moment to point in the direction of the applied magnetic field, as this is a lower energy state.

The build-up of magnetisation towards its equilibrium value of M_0 in the direction of the applied B_0 field is defined by an exponential time constant, T_1, known as the spin–lattice or longitudinal relaxation time constant. Although the term 'lattice' has its origins in early NMR experiments with the crystal lattice, the name is still employed when measuring liquids and gases. If the applied magnetic field were to be switched off, the individual magnetic moments would eventually revert to their isotropic nature and the longitudinal spin magnetisation would decay to a value approaching zero. In a three-dimensional plot, with orthogonal axes in the x, y and z direction, B_0 and M_0 conventionally

point in the z direction (Fig. 2.3a). The magnetisation M_z at time, t, after the B_0 field is switched on is given by Eq. 2.2 and plotted in Fig. 2.3b.

$$M_z(t) = M_0(1 - e^{-\frac{t}{T1}}) \qquad [2.2]$$

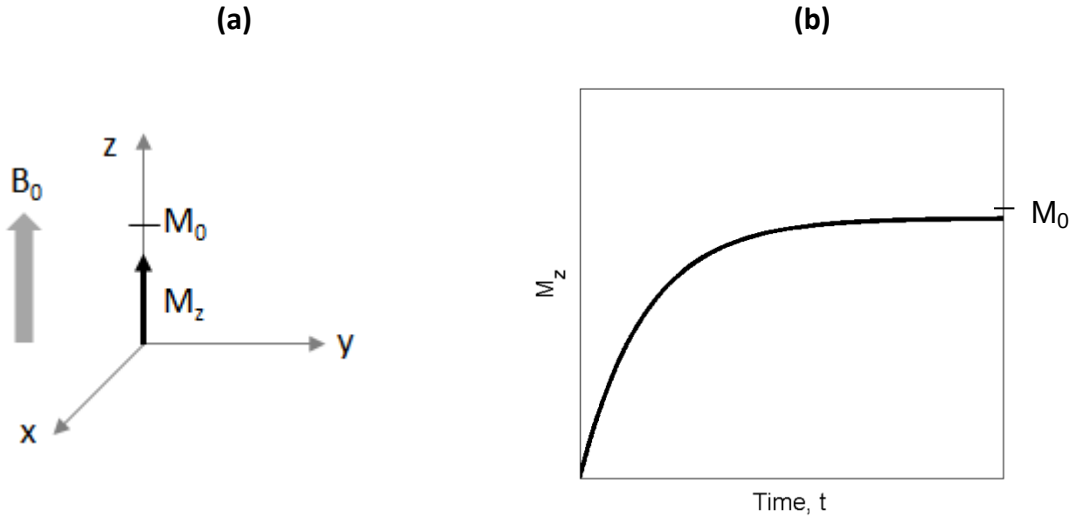

Figure 2.3: When B_0 is applied, magnetisation in the z direction (M_z) grows towards an equilibrium value, M_0; (a) relative axes; (b) increase in M_z with time, according to Eq. 2.2

This magnetisation in the z direction is generally too small to be measured. With the magnetic moments precessing around the B_0 field (z axis) and the net magnetic moment pointing in this direction, there is no net magnetisation perpendicular to the field. However, if every single spin is rotated by 90° around the x axis by an additional radiofrequency (RF) pulse, the net magnetic moment will then point along the –y axis, perpendicular to B_0 (Fig. 2.4a). The RF pulse that flips the net magnetisation into the x–y plane is known as the B_1 field, and will only have an effect when operating at the resonant (Larmor) frequency of the precessing magnetic moments. For the ^{1}H nucleus at a B_0 value of 1.5 T (the most common field strength employed in clinical MRI) the Larmor frequency is 63.9 MHz.

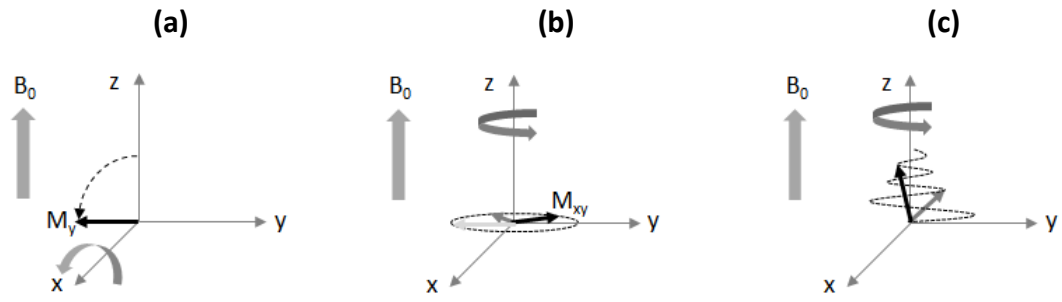

Figure 2.4: (a) An RF pulse rotates the magnetisation around the x axis into the –y direction; (b) the net magnetic moment still precesses around the z axis in the x–y plane; (c) the decay of magnetisation in the x–y plane and recovery in the z direction follows a spiral path

This transverse magnetic moment still precesses around the z axis, at the precession frequency of the individual spins (the Larmor frequency) (Fig. 2.4b). In addition, the transverse component precesses around the axis of the B_1 field at a frequency (γB_1) which is much lower than the precession around the B_0 axis. The combination of both precessional motions would appear to an outside observer as a spiralling down from the longitudinal to the transverse plane. However, when the B_1 field is switched off, the transverse magnetisation decays due to fluctuations in the local magnetic field resulting from random interactions with neighbouring spins, random motion through regions of differing magnetic field strength and variations in tissue magnetic susceptibility. The time constant of this decay, T_2, is known as the spin–spin or transverse relaxation time constant, and is given (within the x–y plane) by Eq. 2.3.

$$M_{xy}(t) = M_0 e^{-\frac{t}{T2}} \qquad [2.3]$$

The decay of magnetisation in the x–y plane occurs at the same time as the recovery of magnetisation in the z axis, and as a result the vector magnetisation describes a spiral from the x–y plane up to the z axis (Fig. 2.4c).

The rates of change of magnetisation with time in the x, y and z directions, M_x, M_y and M_z, respectively, are described by the Bloch equations (7) (Eq. 2.4a – 2.4c).

$$\frac{dM_x}{dt} = \frac{-M_x}{T_2} \quad [2.4a]$$

$$\frac{dM_y}{dt} = \frac{-M_y}{T_2} \quad [2.4b]$$

$$\frac{dM_z}{dt} = \frac{(M_0 - M_z)}{T_1} \quad [2.4c]$$

Any intrinsic inhomogeneity in the main magnetic field will contribute to faster signal loss, acting to shorten T_2. The relaxation measure T_2^* is equivalent to T_2 plus the influence of magnetic field inhomogeneity. Both longitudinal and transverse relaxation occur at the same time, but transverse relaxation is generally quicker ($T_2^* \leq T_2 \leq T_1$). A further measure of relaxation, the spin-lock relaxation time, $T_{1\rho}$, requires an additional locking pulse and will be discussed in Chapter 6. The angle to which the magnetic moment is rotated (90° in the above example) relates to a specific RF pulse amplitude and direction; by varying the properties of this pulse, any angle can be selected. The choice of angle will be discussed further in Section 2.2.3.

The transverse magnetisation generates an oscillating magnetic field perpendicular to the main magnetic field, which may be detected through the electrical current induced in a coil detector. As M_z recovers and transverse magnetisation reduces, the generated signal follows a pattern of free induction decay. It is this detected signal that is used to create images in MRI.

2.2.2 Generating clinical images

The feasibility of generating images using NMR was first demonstrated in 1973 (8), with improved techniques for reduced scan times and clearer images developed over subsequent years (9).

The subject is placed within a strong magnetic field (commonly, a B_0 value of 1.5 T or 3.0 T is used clinically, with higher B_0 values used pre-clinically). By creating a linear magnetic field gradient in the B_0 field, the Larmor frequency varies linearly along the axis of this gradient (according to Eq. 2.1), enabling slices to be selectively excited through the choice of B_1 pulse properties. Additional gradients in orthogonal directions enable signal detection to be pinpointed to a specific location within the patient; repeated measurement with varying gradient parameters enables the generation of spatially encoded datasets in two or three dimensions. For detailed background information on the theory behind spatial encoding with gradients and the mathematical processes involved in converting detected signals to images, the reader is directed to other published texts (10, 11).

The relaxation time associated with an individual voxel (the smallest unit of three-dimensional space within a computer image) of tissue is influenced by, and reflective of, the properties of the tissue within and around that voxel. For example, the compact structure of solids leads to interactions between neighbouring nuclei that are constant with time, resulting in a stronger dephasing effect (and a shorter T_2) than in fluids, where nuclei are constantly experiencing new neighbours. The natural motional frequency of fat is close to the Larmor frequencies used in MRI; as a result, fat is the tissue type with the shortest T_1 value, with solid tissue having an intermediate T_1 and water having a long T_1. As MRI targets the ^{1}H nucleus, proton density also plays a role, with the highest proton density signal coming from relatively free water molecules, such as those found in cerebrospinal fluid. Those tissues with relatively little water content, such as bone or air within the lungs, provide little or no signal.

Example relaxation curves are shown in Fig. 2.5 (based on the magnetisation recovery and decay equations, Eq. 2.2 and 2.3) for a range of arbitrary T_1 and T_2 relaxation times. Note that at time $t = T_1$, 63% of the signal is recovered, with almost the whole signal recovered at five times T_1 (Fig. 2.5a). At $t = T_2$, the signal has decayed to 37% of the original value (Fig. 2.5b).

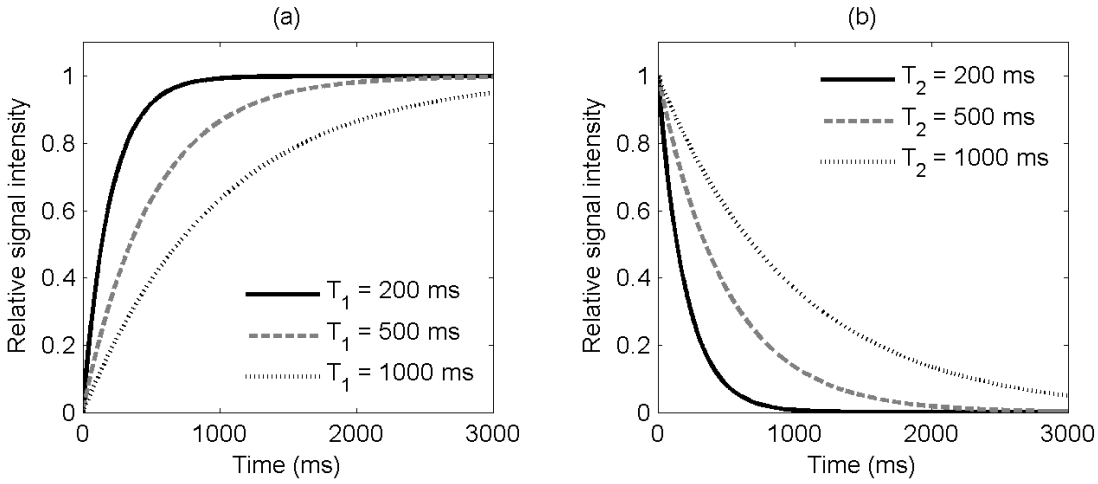

Figure 2.5: (a) Signal recovery curves for three T_1 relaxation times; (b) Signal decay curves for three T_2 relaxation times

2.2.3 Pulse sequences overview

At a basic level, the pulse sequences used for image generation require a combination of RF excitation pulses and spatial encoding gradients, along with read-out echo detection. The strength of the excitation pulse (frequency, amplitude and duration), the repetition time (TR, time between excitation pulses) and the echo time (TE, time between excitation pulse and read-out) may be altered to generate T_1- or T_2-weighted images, according to the tissue of interest. Generally, if a short TR is chosen the variation in signal between tissue types results primarily from differences in T_1, whereas if a long TE is chosen the variation in signal results from differences in T_2.

The two main pulse sequences used are known as spin echo (SE) and gradient echo (GE), although a range of variants have also been developed (12). The standard SE sequence uses a 90° excitation pulse followed at time TE/2 by a 180° refocusing pulse and read-out at time TE (Fig. 2.6a), with free induction decay of the signal occurring between excitation and read-out. The sequence is repeated after time TR, with variations in spatial encoding for each repetition, in order to generate sufficient information for a two- or three-dimensional image. The advantage of the 180° refocusing pulse in the SE sequence is that it eliminates any dephasing caused by magnetic field inhomogeneity. A multi-

echo variation on the SE sequence has a single 90° excitation pulse, followed by multiple 180° refocusing pulses (each producing a read-out echo at a different TE) within a single TR. A third variation, fast spin echo, is similar to the multi-echo approach, in that it employs a single 90° excitation pulse and multiple 180° refocusing pulses, but this time each echo is also phase encoded (and the phase encoding reset after each signal measurement) (Fig. 2.6b). The fast spin echo approach enables images to be acquired more rapidly, and is also known as turbo spin echo or rapid acquisition with relaxation enhancement (RARE).

GE sequences generally use an excitation angle of less than 90°, then generate an echo with a pair of bipolar gradient pulses and repeat the cycle after a short TR (Fig. 2.6c). There is no 180° pulse to refocus the proton spins, resulting in a greater sensitivity to magnetic susceptibility effects, with the rate of decay given by T_2*. Between cycles, any residual steady-state transverse magnetisation may be eliminated by applying spoiling RF pulses or gradients. Acquisition using GE is quicker than conventional SE as TR is generally shorter, but signal-to-noise ratios are often lower than for SE sequences and GE is more prone to susceptibility artefacts.

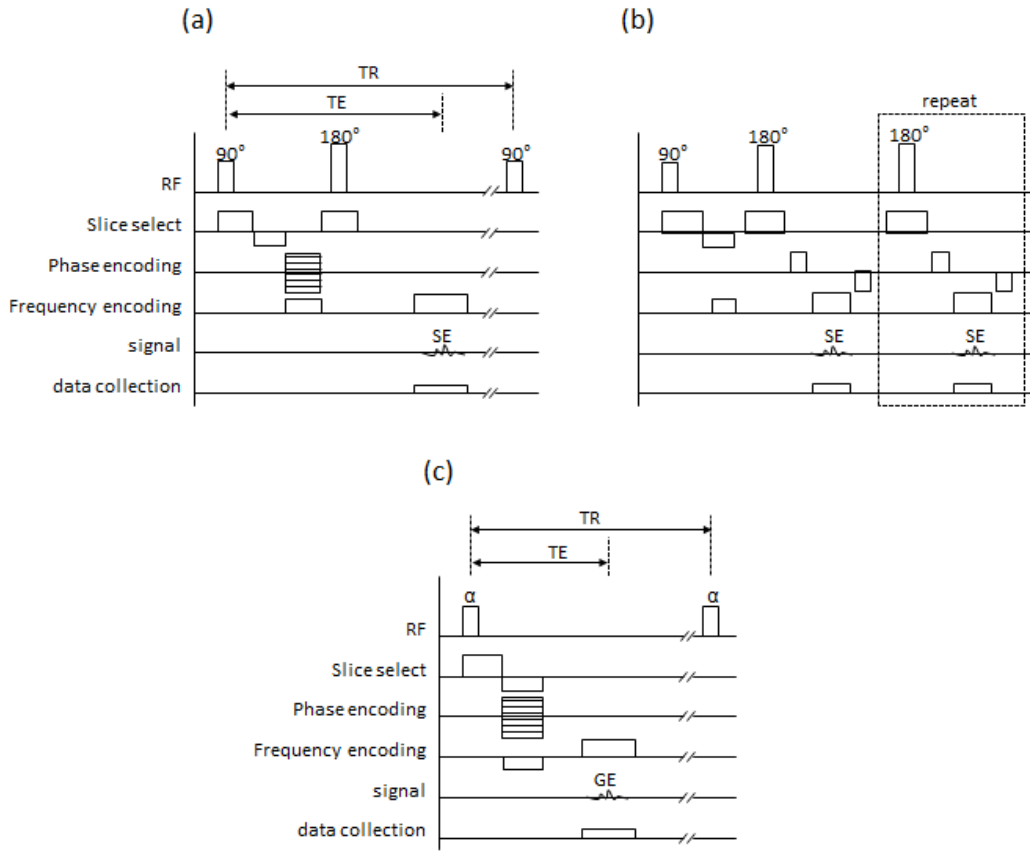

Figure 2.6: (a) Spin echo and (b) fast spin echo (RARE) sequence; horizontal lines in (b) correspond with labels in (a); (c) gradient echo

Many of the pulse sequences applied in the clinic have been adapted for speed of acquisition. Although this may come at the expense of a perceived loss in image quality (for example, through reduced spatial resolution), faster acquisition times have the advantages of reducing image artefacts caused by movement and enabling improved temporal resolution on dynamic acquisitions. In addition, faster acquisition times reduce the time spent by the patient on the MRI scanner, minimising patient discomfort and increasing patient throughput. Although pulse sequences with longer acquisition times may be impractical for clinical purposes, these time constraints are lifted for research involving in vitro solutions and results acquired over longer time periods may give improved accuracy in relaxation time measurement.

Inversion recovery sequences give heavy T_1 weighting. Here, a 180° pulse inverts the magnetisation along the –z axis, and is followed by a 90° pulse to bring the residual magnetisation into the x–y plane where it may be detected. The time between the 180° pulse and the 90° pulse is known as the inversion time (TI). Repeated inversion recovery signal measurements at a range of TIs enable T_1 to be calculated, using Eq. 2.5 (curve shape shown in Fig. 2.7a).

$$SI = S_0.|1 - 2e^{-\frac{TI}{T1}}| \qquad [2.5]$$

where SI is the measured signal intensity and S_0 is the signal intensity at time t = 0. The modulus is taken because images are usually magnitude reconstructions (without negative signal intensity values).

Saturation recovery sequences are able to measure T_1 more rapidly than using inversion recovery. Here, multiple 90° RF pulses are applied at a range of TR values; the first 90° RF pulse is dephased by a spoiling gradient and subsequent magnetisation developing along the z axis is rotated into the x–y plane by another 90° pulse and a gradient echo immediately acquired. Signal intensity is related to T_1 according to Eq. 2.6, and the expected curve shape is shown in Fig. 2.7b.

$$SI = S_0.\left(1 - e^{-\frac{TR}{T1}}\right) \qquad [2.6]$$

T_2 values may be determined by varying the echo time and fitting signal intensity measurements using Eq. 2.7 (curve shape shown in Fig. 2.7c).

$$SI = S_0.e^{-\frac{TE}{T2}} \qquad [2.7]$$

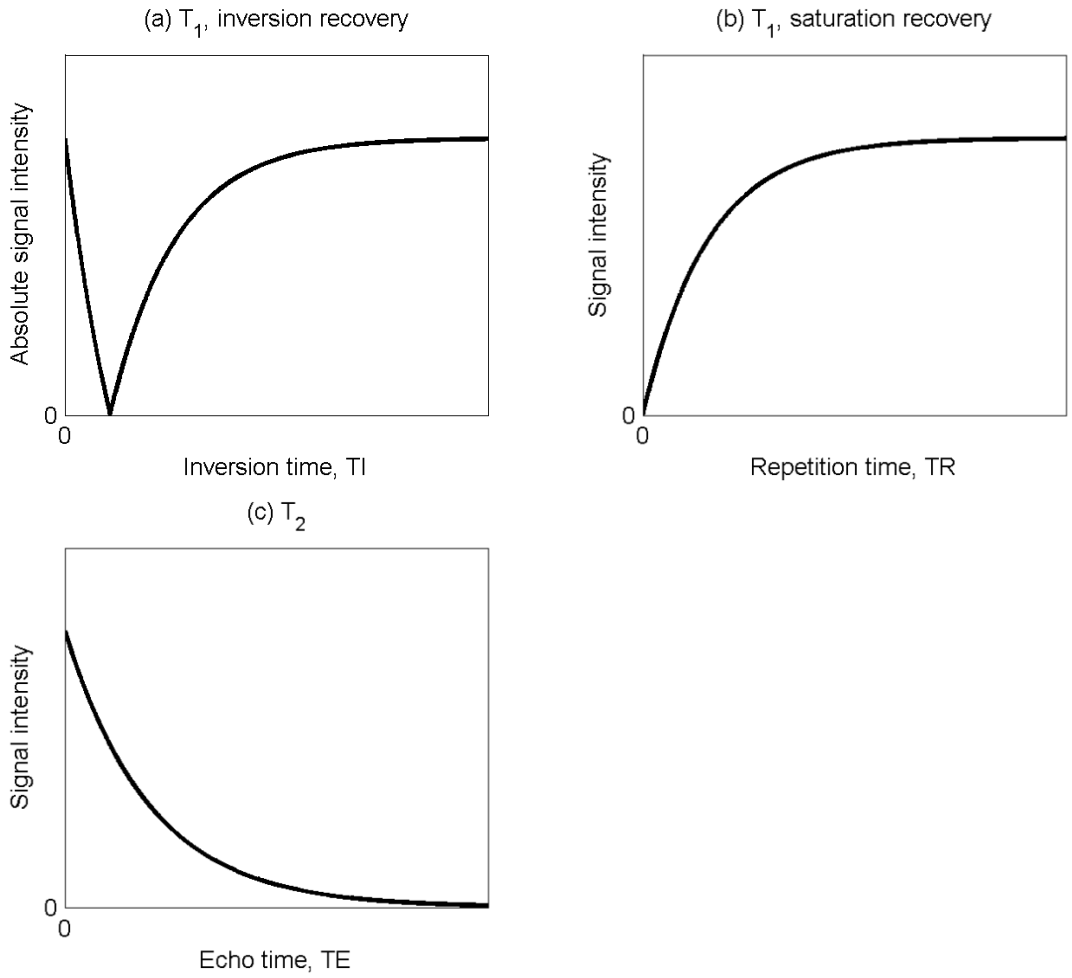

Figure 2.7: Plot of signal intensity versus (a) inversion time (Eq. 2.5), (b) recovery time (Eq. 2.6) and (c) echo time (Eq. 2.7); (a) and (b) represent T_1 recovery curves, and (c) represents T_2 decay

2.3 CONTRAST AGENTS

In MRI, endogenous contrast between tissue types, resulting from differences in longitudinal and transverse relaxation times and proton density, may be selectively emphasised through the variation of pulse sequence parameters. However, the effectiveness of such tissue contrast is limited in scenarios where neighbouring tissue types have similar relaxation times or where pathology, such as a tumour, has comparable relaxation characteristics to its background.

Several techniques have been developed to generate variations in contrast by manipulation of pulse sequences. Magnetisation transfer uses off-resonance

saturation pulses to suppress the signal from protein-bound water molecules, which gives a technique sensitive to macromolecular content (13). A similar concept, known as chemical exchange saturation transfer (CEST), utilises a selective pre-saturation pulse to differentiate bulk water from water bound to an exogenous contrast agent (14). Spin locking is another technique that is sensitive to the presence of macromolecules, using an additional locking pulse to generate relaxation at the (lower) field strength of this pulse rather than the strength of the main magnetic field (15).

Blood oxygenation levels may be utilised to generate endogenous contrast, by assessing differences between signal intensities of diamagnetic oxyhaemoglobin and paramagnetic deoxyhaemoglobin. This technique, known as blood oxygenation level dependent (BOLD) contrast, is primarily used for functional brain imaging (16). A similar technique, arterial spin labelling (ASL), measures perfusion by magnetically ‘tagging’ blood before it flows into the region of interest (17).

2.3.1 Contrast agent definition

Contrast may also be enhanced through the administration of an exogenous contrast agent. The term ‘contrast agent’ in the context of this research refers to a substance that may be administered to a patient with the purpose of adding value to a medical image. Contrast agents are used in all imaging modalities, although the mode of operation for MRI agents differs to that of agents used in other modalities.

An MRI contrast agent has magnetic properties which reduce longitudinal and transverse relaxation times; its influence is observed through an alteration of signal intensity in the vicinity of the agent. An agent that reduces longitudinal relaxation time produces an area of enhanced signal intensity in T_1-weighted images, and may be defined as a positive contrast agent. An agent that reduces transverse relaxation time gives an area of signal loss on T_2-weighted images, and is often described as a negative contrast agent. In reality, contrast

agents reduce both longitudinal and transverse relaxation times, but the extent to which each is affected varies according to the properties of the agent.

2.3.2 Uses of contrast agents

MRI contrast agents have a range of clinical applications, enabling improved assessment of damage, disease and response to treatment. Extending this range of applications, either through the introduction of new contrast agents with novel properties or by finding novel uses for existing contrast agents, represents an important area of ongoing research.

Contrast agents induce changes in image signal intensity that may be used to map the flow of blood, highlighting blood vessels in contrast-enhanced MR angiography (18) or disruption to the blood–brain barrier in brain imaging (19). The spatial distribution of a contrast agent may have clinical value; for example, regions of signal alteration due to contrast agent accumulation (enhancing fraction) may correlate with regions of tumour growth and may be used as a prognostic biomarker in carcinoma (20).

The rate of excretion of the agent may aid assessment of kidney (21) or liver (22) function. Plotting the variation of signal intensity with time provides parameters related to tissue properties, including onset time, mean gradient, maximum signal intensity and wash-out characteristics (23). The shape of such a curve may correlate with tumour malignancy (24), and the area under the curve is related to blood volume and capillary permeability (25), although separation of tissue perfusion and capillary permeability characteristics requires mathematical modelling to account for tracer kinetic behaviour (26). These parameters may be of particular value when assessing tumour physiology (27) or regions of necrosis in myocardial infarction (28)**,** for example. Assessment of microvascular permeability using MRI contrast agents is sensitive to the size of the agent molecule (29, 30), with macromolecular agents potentially being more suitable for selective imaging than small-molecule Gd agents (31).

2.3.3 Mode of operation

MRI contrast agents have magnetic susceptibility properties which alter intrinsic tissue relaxation times by modifying the magnetic field in their immediate vicinity. Unlike other imaging modalities, it is not the contrast agent itself that is observed; instead, MRI detects the influence of the contrast agent on nearby water molecules. Paramagnetic MRI contrast agents have a small, positive susceptibility to magnetic fields, but do not retain their magnetic properties outside the magnetic field. Superparamagnetic contrast agents have higher magnetic susceptibility values, and thus have greater influence over the local magnetic field.

When discussing contrast agents, it is common to use relaxation rates rather than relaxation times (where the relaxation rate is the inverse of the relaxation time). For a dilute paramagnetic solution, the observed solvent relaxation rate (R_{iobs}, $1/T_{iobs}$) is the sum of the relaxation rate of the solvent nuclei in the absence of the paramagnetic solute (R_{i0}, $1/T_{i0}$) and the relaxation rate of the paramagnetic substance (R_i, $1/T_i$) at a given concentration (Eq. 2.8) (32).

$$R_{iobs} = R_{i0} + R_i \qquad [2.8]$$

where *i* = 1,2.

The relaxation rate of a paramagnetic contrast agent is conventionally linearly related to its concentration (C_g), such that Eq. 2.8 can be rewritten as Eq. 2.9.

$$R_{iobs} = R_{i0} + r_i[C_g] \qquad [2.9]$$

where *i* = 1,2.

The relaxation rate (R_i) of a paramagnetic contrast agent consists of two components: inner sphere (IS) and outer sphere (OS) (Eq. 2.10).

$$R_i = R_{iIS} + R_{iOS} \quad [2.10]$$

where *i* = 1,2.

Inner sphere effects result from one or more water molecules binding in the inner coordination sphere of the paramagnetic ion and exchanging rapidly with bulk water molecules. Secondary and outer sphere effects result from water molecules diffusing through the outer-sphere environment. These effects, and the correlation times associated with each, are illustrated graphically in Fig. 2.8.

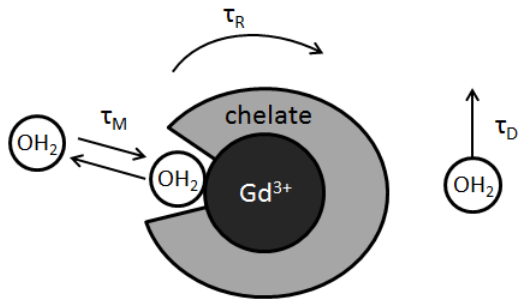

Figure 2.8: Graphical representation of the influence of a chelated Gd ion on nearby water molecules. Inner sphere relaxation is influenced by the correlation time of the coordinated water molecule (τ_M) and the rotational correlation time (τ_R); outer sphere relaxation is influenced by the diffusional correlation time (τ_D)

Inner sphere relaxation

Inner sphere relaxation occurs when a water molecule is associated with the contrast agent for a sufficient amount of time to form an identifiable chemical complex (33). The relaxation rate (R_{iIS}) is influenced by the relaxation rate of the bound water molecule (R_{im}) and the number of water molecules binding in the inner coordination sphere, also known as the hydration number; for most Gd-based agents only one water molecule binds. R_{iIS} is also influenced by the time spent by the water molecule in the inner sphere (τ_M), dictated by the solvent exchange rate ($1/\tau_M$) (Eq. A.1 – A.2 in Appendix A). An increase in this correlation time (i.e. a decrease in the exchange rate of the coordinated water molecule) leads to a reduction in the inner sphere relaxation rate. When this

water molecule exchanges very rapidly (i.e. τ_M << T_{1m}), the relaxation enhancement experienced by the bulk water is dependent on the relaxation rate of this coordinated molecule (R_{1m}). An additional factor which has a small influence on R_{2IS} is the chemical shift difference between the bound water and the bulk water (resulting from differences in resonant frequencies).

Bound water relaxation rates consist of components representing dipole–dipole (DD) and scalar (SC, also known as contact) mechanisms of relaxation (Eq. 2.11).

$$R_{im} = R_{iDD} + R_{iSC} \qquad [2.11]$$

where *i* = 1,2.

These components may be calculated using the Solomon–Bloembergen–Morgan equations (34) (Eq. A.3 – A.6 in Appendix A). Scalar relaxation rates are influenced by the scalar coupling constant between the electron at the paramagnetic centre and the proton of the coordinated water molecule, as well as the electron Larmor frequency and the scalar correlation time (τ_{ei}). Dipole–dipole relaxation rates are strongly influenced by the electron spin–proton spin distance, r (to the inverse sixth power), as well as the nuclear and electron Larmor frequencies, and dipole–dipole correlation times (τ_{ci}). These correlation times may be defined according to Eq. 2.12 and 2.13.

$$\frac{1}{\tau_{ci}} = R_{ie} + \frac{1}{\tau_m} + \frac{1}{\tau_R} \qquad [2.12]$$

$$\frac{1}{\tau_{ei}} = R_{ie} + \frac{1}{\tau_m} \qquad [2.13]$$

where *i* = 1,2, τ_R is the rotational correlation time of the metal–proton vector, R_{1e} and R_{2e} are the longitudinal and transverse electron spin relaxation rates of the metal ion.

R_{ie} varies with magnetic field and is usually interpreted in terms of a zero-field-splitting interaction (a quantum effect associated with spin energy states) (35) (Eq. A.7 – A.9 in Appendix A).

Outer sphere relaxation

As second sphere relaxivity is generally not well characterised (36), the separate contributions of the second and outer sphere are usually combined into a single relaxation rate, R_{iOS} (34). This relaxation rate is influenced by the distance of closest approach of the water molecule and the complex, as well as the diffusion constants of the water and the complex (Eq. A.10 – A.14 in Appendix A).

2.3.4 Contrast agent design

The degree to which a contrast agent influences relaxation time is termed 'relaxivity'; this parameter is generally normalised to contrast agent concentration and expressed in units of L $mmol^{-1}$ s^{-1} (or mM^{-1} s^{-1}). It is clear from contrast agent theory that the effectiveness of a contrast agent is governed by a range of physical and chemical molecular properties. In addition, relaxivity is affected by experimental and environmental factors including temperature, pH and B_0 field. For small, low-molecular-weight paramagnetic contrast agents around 60% of the longitudinal and transverse relaxation results from inner-sphere effects, with the remainder due to outer sphere interaction and bulk water transfer (33). Superparamagnetic agents have no inner coordinating molecule and derive all their relaxivity from outer sphere effects (35).

A linear relationship between contrast agent concentration (C_g) and change in R_1 (ΔR_1) or R_2 (ΔR_2) is often assumed. In this case, for a plot of C_g versus ΔR_1 the slope of a line through measured points and the origin represents

longitudinal relaxivity (r_1); the slope of an equivalent line on a plot of C_g versus ΔR_2 represents transverse relaxivity (r_2) (Eq. 2.14).

$$\Delta R_i = r_i C_g \qquad [2.14]$$

where *i* = 1,2.

However, for contrast agents that bind to albumin, a nonlinear relaxation rate response to contrast agent concentration will be generated due to the variation of relaxivity with binding fraction (37).

The variation in signal intensity with time (inversion time, repetition time or echo time) was shown in Fig. 2.7. A change in relaxation rate, induced by the introduction of a contrast agent, changes the shape of these curves. At low contrast agent concentration and at a given time point, a linear correlation between change in signal intensity and contrast agent concentration is often assumed. However, this assumption of signal linearity is not strictly correct and may lead to miscalculated pharmacokinetic parameters (38). Signal intensity enhancement nonlinearity is increased at high contrast agent concentrations and where T_2 shortening effects are neglected (39). Water exchange rates between cellular and interstitial spaces (40) and solution microviscosity (41) may also contribute to nonlinearity.

Contrast agents are conventionally categorised according to their magnetic susceptibility (paramagnetic or superparamagnetic), biodistribution (extravascular, intravascular, or tissue-specific) and image enhancement properties (positive or negative). Early work (42) showed the promise of utilising paramagnetic contrast agents such as orally administered ferric chloride and inhaled 100% oxygen to enhance natural tissue contrast. Other paramagnetic metal ion chelates, including gadolinium (Gd), were also being considered in the early 1980s (43).

Although much research has been carried out using other agents, most contrast agents currently marketed for clinical use are Gd-based.

2.4 GADOLINIUM-BASED CONTRAST AGENTS

Gadolinium is a lanthanide element with an atomic number of 64 and an atomic mass of 158 in its most common isotope. In its ionic form (Gd^{3+}) it has seven unpaired electrons in its outer shell, making it ideal for use as a contrast agent. However, due to similarities in size Gd can block voltage-gated calcium (Ca^{2+}) channels at very low concentrations, inhibiting processes that require an influx of Ca^{2+} and limiting the activity of certain enzymes (44). To reduce its potential toxicity, Gd may be chelated to a ligand. Early studies of potential Gd chelates (45) suggested the use of ethylenediaminetetraacetic acid (EDTA) or diethylenetriaminepentaacetic acid (DTPA). Relaxation time was significantly reduced with both chelates, but dose experiments with rats found much higher tolerance for DTPA than EDTA. Gd-DTPA (gadopentetate dimeglumine) now forms the basis of several of the most commonly used, clinically approved MRI contrast agents.

2.4.1 Overview of clinically approved agents

Properties of clinically approved agents

All MRI-approved Gd chelates are nine-coordinate complexes, with a ligand occupying eight of the available binding sites at the metal centre and the ninth site occupied by a coordinated water molecule (34). Gd contrast agents may be grouped according to their ligand properties, being either linear or macrocyclic in structure and ionic or non-ionic in charge. Several agents selectively bind to albumin, or may target specific organs. The relaxivity of the agent, its safety profile, pharmacokinetics and excretion pathway are all influenced by the ligand. A summary of clinically approved Gd-based agents is given in Table 2.1.

Table 2.1: Selected properties of marketed Gd-based contrast agents

Generic name	Acronym & Trade name	Structure	Ionic?	Standard clinical dose (mmol kg^{-1})	Excretion pathway	Relaxivity * (mM^{-1} s^{-1})	
						r_1	r_2
Gadopentetate dimeglumine	Gd-DTPA Magnevist	Linear	Yes	0.1	Renal	4.1	4.6
Gadobenate dimeglumine	Gd-BOPTA MultiHance	Linear	Yes	0.1	96% renal 4% hepatic	6.3	8.7
Gadoxetic acid disodium salt	Gd-EOB-DTPA Primovist/Eovist	Linear	Yes	0.025	50% renal 50% hepatic	6.9	8.7
Gadofosveset trisodium	MS-325 Vasovist/Ablavar	Linear	Yes	0.03	95% renal 5% hepatic	27.7	72.6
Gadodiamide	Gd-DTPA-BMA Omniscan	Linear	No	0.1	Renal	4.3	5.2
Gadoversetamide	Gd-DTPA-BMEA OptiMARK	Linear	No	0.1	Renal	4.7	5.2
Gadoterate meglumine	Gd-DOTA Dotarem	Macrocyclic	Yes	0.1	Renal	3.6	4.3
Gadoteridol	Gd-HP-DO3A ProHance	Macrocyclic	No	0.1	Renal	4.1	5.0
Gadobutrol	Gd-BT-DO3A Gadovist/Gadavist	Macrocyclic	No	0.1	Renal	5.2	6.1

** Relaxivity values measured in plasma at 1.5 T and 37 °C (46)*

Safety

The chelated Gd molecule is designed to be well tolerated during its journey through the body. Minor adverse effects, including nausea and hives, occur in a low number of cases following contrast agent administration, at a similar rate for all agents (47). Severe anaphylactoid reactions are rare, with an estimated incidence of 1:100,000 to 1:500,000 (48). In patients with poor renal function, the clearance rate of the contrast agent is compromised and the chelated molecule may degrade into a more toxic form, potentially resulting in increased Gd bone deposition.

The development of nephrogenic systemic fibrosis (NSF), a hardening of fibrotic tissue found in patients with renal failure, was first linked to

administration of Gd contrast agents by Grobner (49). This link was strengthened with detection of Gd in the skin of patients with NSF having been exposed to a Gd-based contrast agent (50). Although the pathophysiology of NSF is still not fully known, the link to Gd has led to classification of all agents into high-, intermediate- and low-risk groups, with associated restrictions on their use (51). Unconfounded cases of NSF have so far been associated with just three of the Gd agents: gadodiamide, gadoversetamide and gadopentetate, with gadodiamide accounting for by far the greater majority (51).

2.4.2 Gadofosveset, gadoxetate and gadobenate

Gadofosveset trisodium (gadofosveset) is unique amongst the clinically approved agents in that it is the only agent which binds in high fraction to albumin. Through binding, gadofosveset acquires two fundamental properties associated with macromolecules: its speed of rotation and its extravasation rate are both reduced. The latter property influences the kinetic behaviour and excretion rate of the agent, ensuring the bound molecule remains mostly intravascular and prolonging the time window for imaging at steady state; the former property has a significant positive effect on its relaxivity, particularly at lower magnetic field strengths. The intravascular nature of bound gadofosveset leads to its indicated use in angiography. However, in a scenario of increased capillary permeability, such as angiogenesis, it is suggested that pathology may correlate with higher leakage rates and elevated levels of bound gadofosveset in the extravascular space.

Gadoxetic acid (gadoxetate) and gadobenate dimeglumine (gadobenate) also bind reversibly to albumin, at a much lower fraction than gadofosveset. Although both agents demonstrate an increased relaxivity attributable to albumin binding, the lower binding affinity of these agents limits the extent to which their behaviour is modified in vivo.

The properties of gadofosveset, gadoxetate and gadobenate will be discussed in more detail in Chapter 3, along with an in-depth review of current research literature.

2.4.3 Other albumin-binding gadolinium-based agents

Gd permanently bound to albumin (albumin-Gd-DTPA) has been used as a macromolecular agent in animal studies (for example,(39, 52)), although the excessive retention time of this agent makes it less suitable for human studies. Other attempts to create a macromolecular Gd-based agent include the conjugation of Gd chelates to synthetic polymers (53) or to a polyethylene glycol core (54). Biodegradable polydisulfide Gd complexes (55) may prove to be a safer alternative to some macromolecular agents. In addition to these synthetic macromolecular agents, a range of Gd-based contrast agents are being developed to target specific organs or respond to changes in pH, temperature or enzyme activity (56).

2.5 NON-GADOLINIUM-BASED CONTRAST AGENTS

Although the main focus of this research is on the Gd-based contrast agent gadofosveset, with a broader assessment of the other clinically approved albumin-binding agents gadoxetate and gadobenate, it should be noted that a range of alternative MRI contrast enhancement options are available. Other lanthanide ions such as dysprosium (Dy^{3+}) and holmium (Ho^{3+}) have larger magnetic moments than Gd^{3+} (57), but, due to the asymmetry of the electronic states of their orbiting electrons, the electronic relaxation rates of these other lanthanides are too high to influence proton relaxation to the same extent as Gd^{3+} (34). At higher magnetic fields, it may be possible to use lanthanide ions such as Dy^{3+} and Ho^{3+} effectively as negative contrast agents (58).

Iron oxide, in the form of superparamagnetic iron oxide particles (SPIO) or ultrasmall superparamagnetic iron oxide particles (USPIO), is very effective in T_2-weighted imaging. Iron oxide agents typically consist of a particle with a core of magnetic crystals embedded in a coating such as dextran. The size of the crystals governs relaxivity properties; the size of the particle influences

pharmacokinetics. As iron oxide has a lower number of unpaired electrons than Gd (1.33 unpaired electrons per iron atom compared to 7 for Gd), the individual magnetic moment of a molecule of magnetite (Fe_3O_4) is lower than that of a molecule of Gd chelate (57). However, in situ, individual magnetite molecules aggregate and the magnetic moments of neighbouring molecules align, effectively creating one large molecule with increased magnetisation (33). The coating of the iron oxide molecule may be chemically manipulated to target specific tissue, such as liver Kupffer cells (59). Biodegradable SPIOs, with a rate of degradation that enables effective imaging, have substantially lower toxicity than conventional paramagnetic contrast agents (60). An iron oxide molecule, ferumoxytol (marketed in Europe as Rienso, Takeda Pharmaceutical Company Ltd), recently gained clinical approval for intravenous treatment of iron deficiency anaemia and has previously been used as an MRI contrast agent. Manganese is part of the iron group of metals; manganese ions (Mn^{2+}) may be taken up by cells via the calcium (Ca^{2+}) channel, suggesting a possible use in functional brain imaging (61).

2.6 SUMMARY

In summary, clinical MRI utilises the spin properties of the hydrogen nucleus to generate signals, which are then converted into an image. The creation of this image requires selection of pulse sequence parameters to enable differentiation of a range of tissue properties. Exogenous contrast agents alter image contrast by influencing the magnetic properties of water molecules in their immediate vicinity, and may provide additional structural and functional information over non-contrast-enhanced images. The majority of contrast agents in the clinical setting are based on the gadolinium ion, which is chelated to a ligand to reduce toxicity. The chemical properties of this ligand vary for each contrast agent, leading to variations in contrast agent relaxivity and pharmacokinetic behaviour. Of the three clinically approved Gd-based contrast agents that bind reversibly to albumin, gadofosveset has the highest binding affinity, leading to higher relaxivity and lower extravasation and excretion rates than other clinically approved Gd agents.

CHAPTER 3: EXISTING LITERATURE ON GADOFOSVESET AND OTHER ALBUMIN-BINDING AGENTS

3.1 CHARACTERISING GADOFOSVESET

3.1.1 Development of gadofosveset

Gadofosveset trisodium is a clinically approved gadolinium (Gd) based contrast agent, which binds reversibly and in high fraction to serum albumin upon injection. The molecule, shown in Fig. 3.1, has a gadopentetate core and a hydrophobic albumin-binding group (two phenyl rings attached to a cyclohexyl moiety) linked through a negatively charged phosphodiester bond (62). It has a molecular weight of 975.88 g mol^{-1} (with an ionic weight of approximately 907 g mol^{-1}), and an empirical formula of $C_{33}H_{40}GdN_3Na_3O_{15}P$. The injectable solution is manufactured by dissolution of gadofosveset trisodium in water, followed by addition of the ligand fosveset, and specific gravity and pH adjustment using sodium hydroxide and hydrochloric acid.

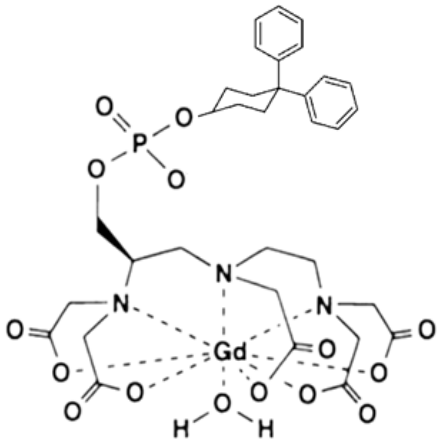

Figure 3.1: Molecular structure of gadofosveset (63)

The use of gadofosveset as a contrast agent was first reported in 1996, under the name MS-325 (64). The agent was developed by Metasyn Inc (later Epix Pharmaceuticals, Cambridge, MA, USA), licensed to Mallinckrodt (St Louis, MI, USA) and developed under the brand name AngioMark from 1998. Development and discovery costs for gadofosveset were estimated at US$85 million over an 8-year period (65). Following phase III clinical trials (66, 67), gadofosveset gained marketing authorisation for human use from the European Medicines Agency in 2005. It was marketed in Europe by Bayer Schering Pharma AG (Berlin, Germany) under the name Vasovist, with contrast-enhanced MR angiography as its labelled indicated use. In 2008, gadofosveset gained approval from the US Food and Drug Administration for use in the USA. Lantheus Medical Imaging (N Billerica, MA, USA) acquired the rights for gadofosveset from Epix in 2009, and the product name was subsequently changed from Vasovist to Ablavar. Although the marketing authorisation in Europe was voluntarily withdrawn by the marketing authorisation holder in 2011, Ablavar continues (at the time of writing) to be available for use in North America. Gadofosveset ceased to be marketed in Europe when Lantheus acquired the marketing rights, although, due to its long shelf-life (approximately three years), gadofosveset in the form of Vasovist may still have been used in Europe up to 2011.

3.1.2 Binding

Gadofosveset is unique amongst the clinically approved Gd contrast agents as it reversibly binds in high fraction to human serum albumin (HSA). HSA is the most abundant protein in blood plasma, constituting around 4.5% of plasma (68). Albumin is essential in regulating the flow of water between blood and tissue, providing around 75% of the colloid oncotic pressure (69), and also transports, via numerous binding sites, endogenous compounds such as long-chain fatty acids (70) and elements including calcium and magnesium (71). Drugs including warfarin and ibuprofen have been designed to bind with HSA so they may be transported easily around the body (72). The heart-shaped HSA molecule consists of three homologous domains (I, II and III), each formed by two smaller subdomains (A and B) (73) (Fig. 3.2).

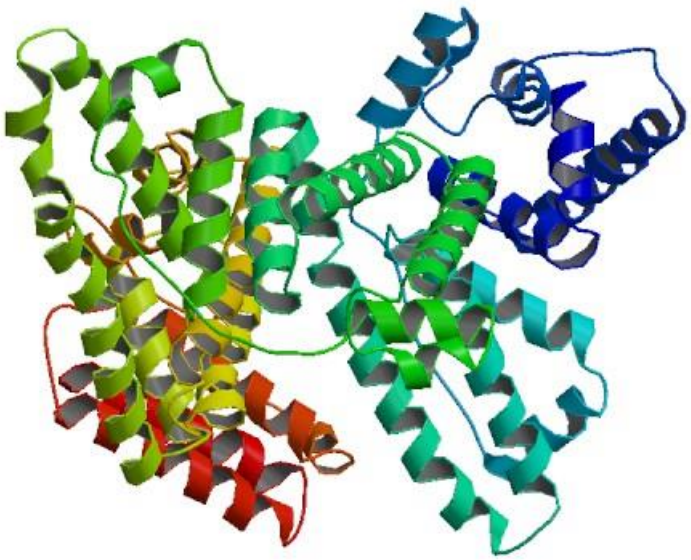

Figure 3.2: Structural diagram of human serum albumin molecule, with colours reflecting different domains (image from the Research Collaboratory for Structural Bioinformatics Protein Data Bank (www.pdb.org) of PDB 1AO6 (74))

Although there are a number of binding locations on the HSA molecule, one binding cavity (subdomain IIIA) is more active and accommodating than the others (73). The binding location for gadofosveset may be identified by analysing the displacement of fluorescent probes which bind at known sites on the HSA molecule. Using this technique it has been demonstrated that, although gadofosveset is able to bind to several sites, site II on subdomain IIIA has the greatest affinity (68).

The number of gadofosveset molecules binding to a single albumin molecule (and therefore the bound fraction) may be assessed by separative techniques such as equilibrium dialysis or ultrafiltration. Here, bound and unbound (free) molecules are separated either by forcing a chemical equilibrium or by physical filtration based on molecular size. Using the ultrafiltration method, it has been demonstrated that, at very high concentrations, up to 20 gadofosveset molecules may bind to a single serum albumin molecule (63). However, at

clinically applicable concentrations (0.1 – 1.0 mM), only one or two molecules of gadofosveset are likely to be bound per HSA molecule (63). Using the ultrafiltration technique it has been shown that, at low concentrations, approximately 90% of gadofosveset binds to albumin in human plasma (68, 75).

An alternative approach for assessment of binding characteristics, known as proton relaxation enhancement (PRE), exploits the differences in relaxation rates between albumin-bound and free paramagnetic molecules. The non-covalent binding equilibrium between a paramagnetic substrate and a protein is defined in Eq. 3.1 (76).

$$[Substrate] + [Protein] \rightleftharpoons [Substrate\text{–}Protein] \quad [3.1]$$

The association constant, or binding affinity (K_a), involving a single equivalent binding site is defined in Eq. 3.2 (76).

$$K_a = \frac{[Substrate\text{–}Protein]}{[Substrate].[Protein]} \quad [3.2]$$

The overall gadofosveset (C_g) and serum albumin (C_{sa}) concentrations may be defined as the sum of their bound and free components (Eq. 3.3 and 3.4).

$$C_g = C_{gbound} + C_{gfree} \quad [3.3]$$

$$C_{sa} = C_{sabound} + C_{safree} \quad [3.4]$$

Assuming a single binding site on the albumin molecule, $C_{sabound} = C_{gbound}$. Binding affinity (Eq. 3.2) may then be expressed in terms of gadofosveset and albumin concentrations (Eq. 3.5).

$$K_a = \frac{C_{gbound}}{C_{gfree}.C_{safree}} \quad [3.5]$$

Removing C_{safree} from Eq. 3.5 using Eq. 3.4 gives Eq. 3.6.

$$K_a = \frac{C_{gbound}}{C_{gfree}.(C_{sa} - C_{gbound})} \quad [3.6]$$

The observed relaxation rate, R_{iobs}, is determined from the sum of the bound and free relaxation rates and the relaxation rate of the blank solution, R_{i0} (Eq. 3.7).

$$R_{iobs} = r_{ibound}.C_{gbound} + r_{ifree}.C_{gfree} + R_{i0} \quad [3.7]$$

where i = 1,2.

Defining the contrast-agent induced change in relaxation rate as ΔR_i, Eq. 3.7 may be restated as Eq. 3.8.

$$\Delta R_i = R_{iobs} - R_{i0} = r_{ibound}.C_{gbound} + r_{ifree}.C_{gfree} \quad [3.8]$$

where i = 1,2.

Combining Eq. 3.3, 3.6 and 3.7 gives Eq. 3.9.

$$R_{iobs} = r_{ifree}.C_g + (r_{ibound} - r_{ifree}).\left\{\frac{(K_a.C_{sa} + C_g.K_a + 1) - \sqrt{\left[(K_a.C_{sa} + C_g.K_a + 1)^2 - 4.{K_a}^2.C_{sa}.C_g\right]}}{2.K_a}\right\} + R_{i0} \quad [3.9]$$

where i = 1,2.

Restating Eq. 3.9 for ΔR_i using Eq. 3.8 gives Eq. 3.10.

$$\Delta R_i = r_{ifree}.C_g + (r_{ibound} - r_{ifree}).\left\{\frac{(K_a.C_{sa} + C_g.K_a + 1) - \sqrt{\left[(K_a.C_{sa} + C_g.K_a + 1)^2 - 4.{K_a}^2.C_{sa}.C_g\right]}}{2.K_a}\right\} \quad [3.10]$$

where i = 1,2.

For *n* binding sites with equivalent binding affinity, Eq. 3.9 may be adapted to Eq. 3.11 (37).

$$R_{iobs} = r_{ifree}.C_g + (r_{ibound} - r_{ifree}).\left\{\frac{(n.C_{sa}.K_a + C_g.K_a + 1) - \sqrt{\left[(n.C_{sa}.K_a + C_g.K_a + 1)^2 - 4.{K_a}^2.n.C_{sa}.C_g\right]}}{2.K_a}\right\} + R_{i0} \quad [3.11]$$

where i = 1,2.

The relationship between C_g and R_{1obs} (Eq. 3.11) is plotted in Fig. 3.3 for two K_a and n values, using arbitrary C_{sa}, r_{1bound} and r_{1free} values. In practice, it may be difficult to independently evaluate n and K_a, particularly at low C_g, therefore binding affinity is sometimes expressed as a composite nK_a term. However, Fig. 3.3 indicates the value of the PRE technique for analysing binding characteristics. The curve is approximately linear up to the point at which the binding sites are filled, and the point of inflection is indicative of saturation of the binding sites. As a result, the ratio C_g/C_{sa} at the point of inflection corresponds approximately to n, assuming all binding sites have an equivalent K_a value.

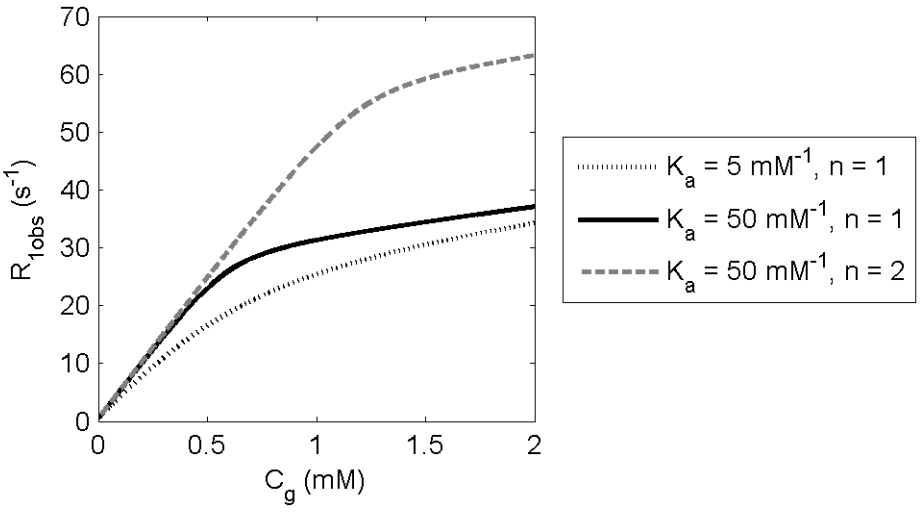

Figure 3.3: Plot of variation of R_{1obs} with contrast agent concentration (C_g) at an albumin concentration (C_{sa}) of 0.6 mM, for two binding affinities (K_a) and up to n = 2 bound molecules (r_{1bound} = 50 mM^{-1} s^{-1}, r_{1free} = 5 mM^{-1} s^{-1}), using Eq. 3.11

Although this approach may be useful in characterising the relaxation rates of certain albumin-binding molecules, a difference of approximately 10^2 in gadofosveset binding affinity between the first and second binding sites (68) precludes the use of the PRE technique in isolation to make assumptions about gadofosveset binding characteristics (34). Combining results from the displacement of fluorescent probes with the shape of the PRE curve, binding at the primary binding site (site II, subdomain IIIA) has been shown to have the greatest influence on gadofosveset relaxivity (68).

A range of gadofosveset binding affinity values at the primary binding site have been reported, influenced by measurement technique and experimental factors such as temperature. Using the PRE technique, K_a values were reported at 25 °C of 30 mM^{-1} (37), and at 37 °C of 6.1 mM^{-1} (77) and 11.0 mM^{-1} (78), although as previously noted the PRE technique should not be used in isolation for gadofosveset. Using ultrafiltration at 37 °C, a K_a value of 11.0 mM^{-1} (68) and values in the range 8.2 – 41.5 mM^{-1} for several lots of HSA (75) were reported. Gadofosveset K_a has been shown to decrease with increasing pH in the range 5.5 to 10, thought to be due to enhanced electrostatic interaction at acidic values and conformational changes in the protein structure at basic values (37).

When gadofosveset concentration exceeds HSA concentration, the number of available albumin molecules with preferential binding sites is reduced, and there is a tendency for the bound fraction to decrease. In addition to varying with gadofosveset concentration, the bound fraction of gadofosveset, and therefore its effectiveness as a contrast agent, varies by species. In humans, serum albumin levels are around 4.5%, but this level may be as low as 2.6% for dogs and 3.2 – 3.3% for rats and mice (79). The bound fraction measured in different species, ranging from around 65% in rats to 91% in humans, is considered to be mostly influenced by these variations in albumin concentration, with some additional variance caused by differences in species' binding characteristics leading to differences in exchange rates of the coordinated water molecule (75). Bound fraction will also vary within species according to individual variations in protein content, which may potentially be symptomatic of disease.

3.1.3 Pharmacokinetics

On binding to albumin, gadofosveset acquires macromolecular properties. As a result, the pharmacokinetic behaviour of the bound gadofosveset molecule differs substantially from that of the free molecule. The free molecule will behave as a conventional, non-binding small molecule Gd agent, readily passing through the vascular wall (although not an intact blood–brain barrier) to the extravascular extracellular space (EES), whereas the bound gadofosveset molecule is often assumed to remain intravascular. However, the assumption that bound gadofosveset remains intravascular may not be entirely valid. Of the four major pathways across the endothelium – tight junctions, breaks in tight junctions, vesicles and leaky junctions – only the tight junctions are small enough to prevent HSA molecules from escaping (80), and albumin is transported across the capillary wall with a natural transcapillary exchange rate of around 5% of intravascular albumin per hour (81). It is suggested through mathematical modelling that around 20% of albumin crossing the endothelium uses the vesicles, 36% may be associated with breaks in tight junctions and 44% through leaky junctions (82), although this will vary in different parts of the body.

It is expected, therefore, that a small proportion of bound gadofosveset will escape to the EES. In addition, free gadofosveset may extravasate and then bind to albumin within the EES. Neither the extent to which unbound molecules cross into the EES before binding nor the binding characteristics within interstitial fluid are fully known. As albumin levels in plasma are around four times those in interstitial fluid (83) the likelihood of binding appears greater in the intravascular space, particularly at low gadofosveset concentrations. Increased levels of albumin in the EES, triggered by disease or damage to the endothelial wall, may lead to increased levels of bound gadofosveset in the EES.

The binding process increases the retention time of gadofosveset by effectively ‘hiding’ the molecule from the kidneys, leading to an excretion half-life in healthy humans of around 16 h (84). The extended half-life of gadofosveset enables signal enhancement for prolonged periods following administration. In a study of gadofosveset in the carotid artery, the signal-to-noise ratio (SNR) was shown to decrease by only 10% between 5 and 50 min post-contrast (85).

Excretion pathway and elimination half-life also vary by species. In humans, the majority of gadofosveset is renally excreted, with less than 10% of the injected dose being excreted via the hepatobiliary pathway (86). In rats, gadofosveset is rapidly taken up by the liver, with around a quarter of the injected dose eventually appearing in faeces (87). The elimination half-life of gadofosveset in rats was measured at 23 min, compared to an elimination half-life of 2 – 3 h for rabbits and monkeys (87).

3.1.4 Relaxivity

As demonstrated in Chapter 2, the effectiveness of a contrast agent is influenced by the rate at which the coordinated water molecule exchanges with the bulk water, the rotational correlation time of the chelated Gd ion and the diffusional correlation time of nearby water molecules.

The binding process increases the molecular weight of gadofosveset to 68 kDa (88) and reduces the rate of rotation of the molecule, resulting in an increase in the rotational correlation time (τ_R) from around 0.1 ns to around 10 ns (89). This slower rotation is closer to the Larmor frequency of the ^1H nucleus at clinical field strengths; as a result, longitudinal relaxivity is increased by a factor of 4 – 10 at low fields (75), peaking at a B_0 value of 20 – 25 MHz (approximately 0.5 T) (77). Gadofosveset relaxivity is additionally enhanced by an increase in outer-sphere relaxivity, possibly due to a long-lived water molecule in the second sphere, and a reduction in the electronic relaxation rate (68). A reduction in the rate at which the coordinated water molecule exchanges with the bulk water ($1/\tau_m$) when gadofosveset binds to albumin, slowed by a factor of 2 – 3, counteracts a proportion of the increase in relaxivity brought about by the increased τ_R (68).

A study of the relationships between relaxation rate, gadofosveset concentration and field strength in whole blood samples (90) found that R_1 increased approximately linearly with gadofosveset concentration (≤ 1.6 mM), and decreased with magnetic field strength (between 1.5 T and 7.0 T). At 0.47 T, a nonlinear increase of R_1 with gadofosveset concentration (≤ 2.0 mM) in human and various animal plasmas was demonstrated (75). Comparison between observed gadofosveset relaxivity values (r_{1obs}, r_{2obs}) at low field (0.47 T) for solutions of water and plasma show an increase in r_{1obs} from 6 mM^{-1} s^{-1} to 28 mM^{-1} s^{-1}, respectively, and in r_{2obs} from 7 mM^{-1} s^{-1} to 40 mM^{-1} s^{-1}, respectively (91). Equivalent values at 3.0 T show a more modest increase in r_{1obs} in plasma (5 mM^{-1} s^{-1} in water, 10 mM^{-1} s^{-1} in plasma) but a large increase in r_{2obs} (6 mM^{-1} s^{-1} in water, 60 mM^{-1} s^{-1} in plasma); at 4.7 T there is little difference between r_{1obs} in water and plasma (6 mM^{-1} s^{-1} and 7 mM^{-1} s^{-1}, respectively), but the difference in r_{2obs} remains large (7 mM^{-1} s^{-1} in water, 60 mM^{-1} s^{-1} in plasma) (91). Although these figures are observed relaxivities, rather than separated bound (r_{1bound}, r_{2bound}) and free (r_{1free}, r_{2free}) values, they support a general pattern of low and approximately field-independent r_{1free} and r_{2free}, high r_{1bound} declining rapidly with field, and high r_{2bound} increasing slightly with field (92).

The addition of energy, in the form of an increase in temperature, reduces correlation times (τ_R and τ_m) and increases exchange rates. For conventional small molecule Gd agents the change in relaxivity with temperature is described by Curie's law, which states that for a paramagnetic material the magnetisation (M_z) is proportional to the applied magnetic field (B_0) and inversely proportional to the temperature (T) (Eq. 3.12) (35).

$$M_z = \frac{N_0 \gamma^2 \hbar^2 I(I+1)}{3k_B T} B_0 \qquad [3.12]$$

where N_0 is the total number of spins, γ is the gyromagnetic ratio, $\hbar$ is the reduced Planck constant (1.05 x 10^{-34} J s), I is the spin quantum number (7/2 for Gd), T is the absolute temperature and k_B is the Boltzmann constant (1.38 x 10^{-23} J K^{-1}).

Applied generally, Curie's law suggests that at a fixed B_0 value paramagnetic materials become more magnetic, and therefore have a higher relaxivity, at lower temperature. This has been demonstrated for the longitudinal relaxivities of gadopentetate (93) and free gadofosveset (37). At low B_0 values, where the macromolecular τ_R is close to the inverse of the Larmor frequency, the longitudinal relaxivity of bound gadofosveset increases with temperature (37). The relaxivities of the bound and free molecules of gadofosveset therefore have opposing relationships with temperature. At higher B_0 values, where τ_R is already beyond its optimal range, an increase in temperature may be expected to have a more limited effect on relaxivity.

For Gd agents at physiological pH, the proton and water exchange rates are equal, but proton exchange is accelerated in acidic or basic solutions due to H^+ or OH^- catalysis (32). The longitudinal relaxivity of bound gadofosveset increases as the solution pH moves from acidic to neutral, and then remains approximately constant at basic pH values (37).

3.1.5 Injection protocol

It has been suggested that, as the bound fraction of gadofosveset varies with time post-bolus, image quality may be affected by injection rate, particularly in examinations using first-pass enhancement. A study (94) found no significant relationship between maximum enhancement and injection rate, suggesting that, within the range of timescales analysed, gadofosveset effectively binds immediately to albumin and results will not be noticeably affected by injection speed.

3.1.6 Safety

Although the binding of gadofosveset to albumin causes it to be retained within the body for longer, the reversible nature of this binding should enable the Gd chelate to be excreted from the body without complication or increased toxicity. A meta-analysis of pooled safety data from eight studies (phase II and phase III clinical trials) (95) found that the rate and severity of adverse events associated with gadofosveset at a dose of 0.03 mmol kg^{-1} were similar to those of a placebo, and concluded that the safety profile of gadofosveset was comparable with other Gd-based contrast agents.

Following the discovery of a potential link between Gd contrast agents and nephrogenic systemic fibrosis (NSF) (49), a scientific advisory group at the European Medicines Agency reviewed the NSF risk for each clinically approved Gd agent. Gadofosveset was classified (with the other albumin-binding agents gadobenate dimeglumine and gadoxetic acid) as being of intermediate risk (96). However, no unconfounded cases of NSF have been reported for gadofosveset; the differentiation between intermediate- and low-risk agents is based on the chemical properties of the agents rather than clinical evidence (51).

3.2 CLINICAL APPLICATIONS AND PREVIOUS RESEARCH

The intravascular nature of the bound gadofosveset molecule leads to increased contrast enhancement within the vessels, and the reduced extravasation and excretion rates provide a longer imaging time window. Utilising these factors, the majority of clinical studies employ gadofosveset in its labelled use of contrast-enhanced MR angiography. At steady state, contrast enhancement in both the venous and arterial systems is observed, which may be advantageous but may also add complexity to image interpretation. As noted in Chapter 2 (Table 2.1), the standard clinical dose for gadofosveset is lower than for most other Gd agents, due to its high relaxivity (0.03 mmol kg^{-1} for gadofosveset versus 0.1 mmol kg^{-1} for the majority of agents).

Phase III clinical studies focused on the use of gadofosveset in MR angiography for assessing peripheral vascular (66), aortoilliac occlusive (67) and renal artery disease (97). Here the intravascular nature of gadofosveset and its relatively high relaxivity at 1.0 – 1.5 T were utilised. Gadofosveset has also been used in cardiac MRI for assessment of structural anomalies (98-100) and function (101, 102). Gadofosveset has been used in first-pass perfusion imaging in the kidneys (103, 104), and to verify vessel closure following treatment for choroidal melanoma (105).

The increased size of the bound gadofosveset molecule limits extravasation from healthy vessels, but macromolecular leakage may increase in damaged or diseased vessels. Gadofosveset has been used to assess vascular permeability in mechanically damaged (106), fibrotic (107), atherosclerotic (108) and angiogenic vessels (109-112). Leakage of gadofosveset across the blood–brain barrier enables improved visualisation of brain tumours (84, 113, 114). The high relaxivity of bound gadofosveset has also been correlated with albumin content in the differentiation of healthy and tumour-invaded lymph nodes (115-117) and in atherosclerotic plaques (118, 119).

Although increased extravascular leakage of bound gadofosveset is expected from damaged or angiogenic vessels, this differential behaviour may be

masked by leakage of the unbound molecule from normal vessels in scenarios where the bound fraction is low (such as at high gadofosveset concentrations or in non-human species). With this in mind, a reduction in administered gadofosveset dose (or injection rate) may be doubly beneficial: ensuring the bound fraction remains high, and reducing the effect of contrast agent signal nonlinearity, discussed in section 2.3.4 (120). In quantitative studies using gadofosveset, the free fraction is often not fully unaccounted for ((121), for example). Low bound fraction may be partly responsible for the outcome of a study of breast tumours in rats, which found no significant correlation between derived MRI parameters (endothelial permeability and fractional plasma volume) using gadofosveset and either microvessel density or histologically assessed tumour grade (122).

While many of the cited studies quantitatively assess changes in contrast based on signal intensity, no published work has attempted to apply pharmacokinetic models to calculate physiological parameters such as perfusion or permeability using gadofosveset in a clinical study of angiogenesis. A search for ‘gadofosveset’ on the ClinicalTrials.gov web site (August 2013) found 22 studies, of which nine were in progress or actively recruiting patients. Three of these nine active studies involve nodal staging; other studies include assessment of vascular or congenital heart disease, liver fibrosis, response to deep vein thrombosis treatment, and a longitudinal study assessing occurrence of nephrogenic systemic fibrosis in patients with kidney disease. One study of prostate cancer is comparing gadofosveset-enhanced images with other MRI techniques and histology, although it is unclear the extent to which pharmacokinetic models will be applied.

3.3 OTHER CLINICALLY APPROVED ALBUMIN-BINDING CONTRAST AGENTS, GADOXETATE AND GADOBENATE

3.3.1 Background

Along with gadofosveset, two other clinically approved gadolinium contrast agents bind reversibly to albumin: gadoxetic acid (gadoxetate, Gd-EOB-DTPA, marketed as Primovist in Europe and Eovist in USA, Bayer Schering Pharma AG, Leverkusen, Germany) and gadobenate dimeglumine (gadobenate, Gd-BOPTA, MultiHance, Bracco Diagnostics Inc, Milan, Italy). Both molecules have a gadopentetate core, a hydrophobic residue which enables non-covalent interaction with serum albumin (123) and a benzyl group that targets hepatocytes (46) (Fig. 3.4). They enter hepatocytes by a specific carrier-mediated mechanism (organic ion transporting polypeptides (124)), then concentrate in the liver and are excreted into bile (43). Unlike gadofosveset, it is noted that the weak albumin binding does not reduce plasma clearance rates (46); indeed, the dual excretion pathway of gadoxetate leads to a faster elimination from the body (125).

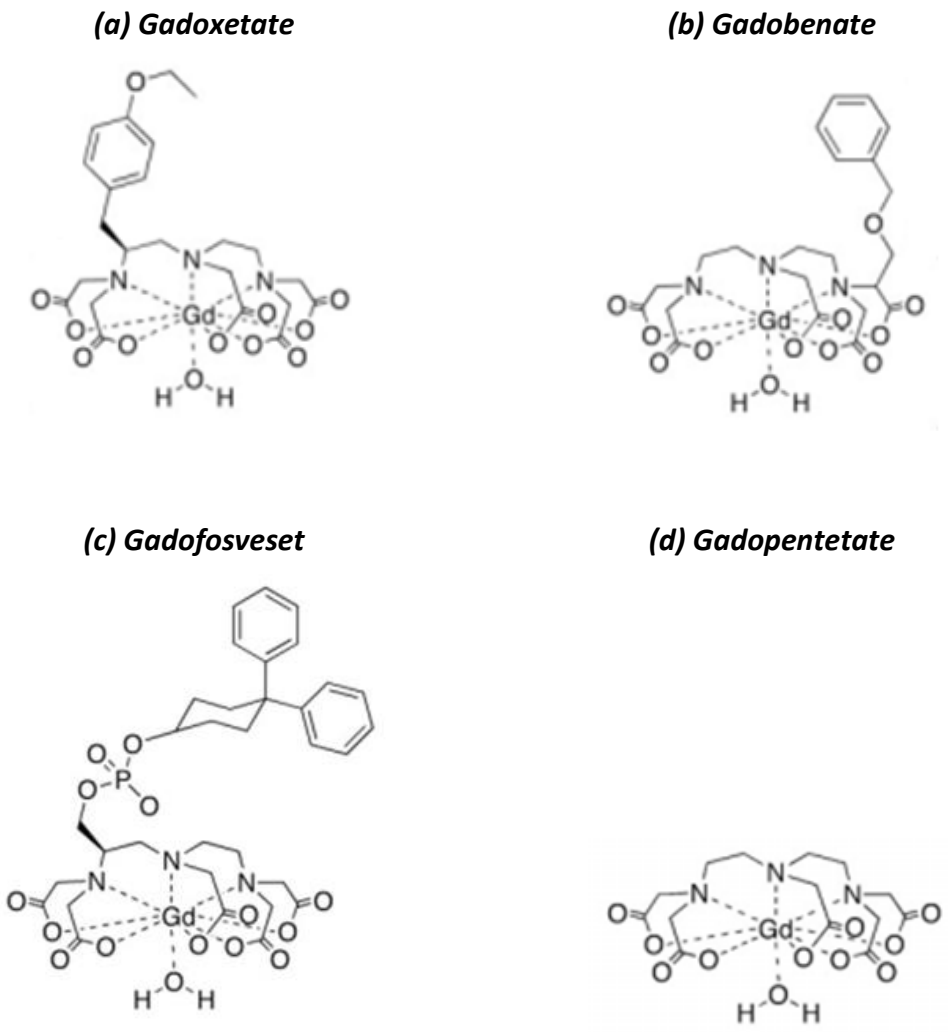

Figure 3.4: Comparison of molecular structures of (a) gadoxetate, (b) gadobenate and (c) gadofosveset; all three molecules have the basic structure of (d) gadopentetate (46)

Gadoxetate and gadobenate have a similar affinity for HSA, with association constants determined by ultrafiltration at the primary binding site of 0.255 mM^{-1} for gadoxetate and 0.226 mM^{-1} for gadobenate (126), compared with 11.0 mM^{-1} for gadofosveset (68). A similar binding affinity for gadoxetate has also been reported elsewhere using equilibrium dialysis (127). Using the proton relaxation enhancement technique a higher binding affinity of 0.490 mM^{-1} was determined for gadobenate (78), although as mentioned in section 3.1.2 this method may be less accurate where a molecule binds at multiple sites with varying affinity (34). The bound fraction has been measured at approximately 10% for gadoxetate (128) and is quoted at 1.6% for gadobenate (129), compared with a much higher value of around 90% for gadofosveset (68, 75).

As with gadofosveset, binding to albumin increases the observed relaxivity of these agents above that of non-binding gadolinium-based agents, primarily by reducing the rotational correlation time (127). At 0.47 T, observed gadoxetate relaxivity increases in the presence of albumin (from 5.3 to 8.7 mM^{-1} s^{-1} for r_1 and from 6.2 to 13 mM^{-1} s^{-1} for r_2), with gadobenate values showing a similar increase (91). At 3.0 T, the presence of albumin leads to a smaller increase in gadoxetate longitudinal relaxivity (from 4.3 to 6.2 mM^{-1} s^{-1} for r_1 and from 5.5 to 11 mM^{-1} s^{-1} for r_2), again with similar gadobenate increases (91). However, calculations used to determine these values were based on just two data points. A study of gadobenate using eight concentrations (≤ 1.0 mM) at 3.0 T gave higher r_1 and r_2 values in plasma of 6.3 and 17.5 mM^{-1} s^{-1}, respectively (130).

Separating the relaxation contributions of the bound and free molecules, it is suggested that the bound and free relaxivities for gadoxetate, gadobenate and gadofosveset are quite similar (78, 126). The difference in observed relaxivity (a composite of bound and free relaxivities) results from differences in bound fraction. This may be expected when the structures of the three molecules are compared (Fig. 3.4): each has a gadopentetate core with a single coordinated water molecule, and a hydrophobic element linking the molecule to serum albumin. The increase in relaxivity on binding (resulting from the reduction in correlation time, discussed in section 3.1.4 for gadofosveset) is applicable for all three agents. As mentioned in Chapter 2, inner sphere relaxivity is also influenced by the distance, r, between the Gd ion and the hydrogen nucleus of the coordinated water molecule (proportional to r^{-6} (34)); this distance is almost identical for gadofosveset and gadobenate (131).

As previously discussed for gadofosveset the effectiveness of an albumin-binding contrast agent depends on the proportion of contrast agent that is bound, which in turn varies according to relative concentrations of albumin and contrast agent. Gadobenate relaxation rates at a fixed contrast agent concentration have been shown to be strongly dependent on albumin concentration, with R_1 and R_2 at 1.5 T both increasing by approximately 40%

when albumin concentration was increased from 3.5 to 5.5 g dL^{-1} (132). Across a wider range of albumin concentrations this increase in relaxation rate was noted to be nonlinear, which is likely to be due to the influence of multiple (up to 10) potential binding sites on the albumin molecule (132). The same study showed a much smaller increase in R_1 and R_2 with albumin concentration for non-binding gadopentetate, thought to be attributable solely to an increase in solution viscosity.

The changing relationship between contrast agent concentration and relaxivity is perhaps most clearly observed during the first pass of the bolus, where contrast agent concentration is initially very high and bound fraction relatively low. As contrast agent concentration decreases over time, an equilibrium level is reached and the bound fraction approaches its maximum value. In a rabbit model, the gadobenate bound fraction was calculated at 7% around the bolus peak and a maximum of 20% at post-bolus phase (78). It is unclear whether gadoxetate and gadobenate bound fractions are species dependent, although gadofosveset bound fraction is known to be strongly species dependent, primarily due to variations in albumin levels between species (75).

3.3.2 Clinical applications

The chemical composition of gadobenate and gadoxetate ensures they are partially excreted through the hepatobiliary pathway and enables their use as targeted liver imaging agents. However, the rates of liver uptake for the two agents are quite different. In humans, 2 – 4% of gadobenate is taken up hepatically compared to 50% for gadoxetate, with the remainder being renally excreted (46). In animals, biliary excretion is generally higher: for example, in rats the biliary excretion rates for gadobenate and gadoxetate are 55% (133) and 73% (125), respectively.

These agents facilitate two distinct phases of liver imaging: an initial perfusion phase, leading to immediate enhancement similar to gadopentetate; and a subsequent hepatobiliary phase (hepatocyte uptake and biliary excretion), which produces a slower increase and leads to a fivefold increase in relaxivity

in the liver for gadoxetate over gadopentetate (22). The high uptake rate for gadoxetate in the liver enables it to be administered in a smaller clinical dose (typically a quarter of that used for most other Gd agents). Evidence suggests that, despite the higher liver uptake level of gadoxetate, the relaxivity of gadobenate within liver tissue is actually greater, possibly due to transient interactions with hepatocyte proteins or membranes (22).

Reduced hepatic uptake of gadoxetate correlates with disruption in liver function due to cirrhosis (134, 135), and enables improved detection of focal liver lesions (136). Delayed-phase imaging may exploit differential uptake rates in benign and malignant liver tissue (137, 138). A dual-input model has been used with gadoxetate to determine both liver perfusion and hepatic uptake for identification of tumours and assessment of response to treatment (139).

Beyond hepatobiliary imaging, the increased gadobenate relaxivity has been utilised in angiography (140-142) and in evaluation of disruption to the blood–brain barrier (143). Gadobenate has been used to identify increased extravascular leakage in infarcted myocardium (133, 144), and in brain (145-147) and breast tumours (148).

It has been suggested that the high hepatobiliary excretion rate for gadoxetate makes this agent only useful for liver imaging (133). However, gadoxetate has been shown to be as effective as gadopentetate in whole-body MRI (149), and has also been used in urography, where the lower renal excretion rate (leading to a lower concentration of contrast agent) reduces the effect of T2* susceptibility (150).

Although the observed relaxivities of gadobenate and gadoxetate are influenced by the proportion of molecules binding to albumin, this bound fraction is not easily measurable in vivo. The dual kinetic profiles of the bound and free molecule may confound standard tracer kinetic models, and under certain conditions quantitative MRI parameters may be more accurately determined using a non-binding agent such as gadopentetate (151). In the kidneys, albumin-binding effects may be accommodated in the calculation of

physiological parameters such as plasma volume but binding may lead to inaccuracy when determining glomerular filtration rate (152).

Despite having relatively low albumin binding affinities (compared to gadofosveset), both gadoxetate and gadobenate demonstrate increased relaxivity in the presence of serum albumin. These favourable relaxivity properties have been utilised for a range of clinical applications. However, the variation in bound fraction with relative contrast agent concentration, resulting in an associated change in observed relaxivity, may reduce the accuracy of quantitative analysis using a single fixed relaxivity value. This may be particularly relevant during the first pass of the bolus, or in disease states where albumin levels are altered or vascular albumin leakage rates are increased.

3.4 NON-CLINICALLY APPROVED ALBUMIN-BINDING AGENTS

A Gd-based contrast agent in development, gadocoletic acid trisodium salt (BB22956/1, Bracco Imaging SpA, Milan, Italy), has a higher bound fraction in HSA than gadofosveset and less variability for binding to the serum albumin of other species (153). The extended retention time and increased relaxivity resulting from binding suggest, as with gadofosveset, a primary use for BB22956/1 in angiography (154). Beyond angiography, a study in rats showed this agent to be effective at monitoring response to anti-vascular endothelial growth factor treatment (155). BB22956/1 also performed well in assessment of changes in vascular permeability in response to treatment of subcutaneous breast tumours in a rat model (156).

The pre-clinical agent albumin-Gd-DTPA is a permanently bound intravascular Gd chelate, consisting of a large number (typically 30 – 35) of gadopentetate dimeglumine molecules attached to a single albumin molecule. Whereas gadofosveset has a free fraction of approximately 10%, albumin-Gd-DTPA is 100% bound. Its prolonged retention time and potential immunologic response currently preclude its use in humans (52), although it has been used

extensively in animal studies. Derived quantitative parameters using albumin-Gd-DTPA have correlated with histology in the assessment of microvascular permeability in reperfused myocardial infarction (157) and tumour angiogenesis (158, 159). A study comparing gadofosveset with albumin-Gd-DTPA (122) found correlation between microvascular permeability and histologically assessed tumour grade in rats for albumin-Gd-DTPA but not for gadofosveset. In a mouse tumour model, quantitative parameters derived using albumin-Gd-DTPA correlated with histology (160). Albumin-Gd-DTPA has also been used to explore the relationship between VEGF and endothelial permeability in rat xenografts (161).

Although macromolecular contrast agents such as BB22956/1 and albumin-Gd-DTPA are not approved for clinical use, there is clear evidence to suggest that macromolecular contrast agents enable measurement of parameters not possible with small-molecule agents. As the only clinically-approved Gd-based contrast agent with a high macromolecular fraction, it may be possible to replicate the pre-clinical successes of these macromolecular agents in humans using gadofosveset.

3.5 SUMMARY

A search of existing literature has established that the chemical behaviour of gadofosveset has been comprehensively assessed in vitro and the safety and efficacy of gadofosveset as an MR angiography agent have been rigorously established in vivo. However, the vast majority of gadofosveset research to date has focused on its use as a high-relaxivity intravascular agent. Aspects such as the influence of the free fraction and the decline in longitudinal relaxivity with B_0 are often neglected, while properties such as multiple binding sites and variations in bound fraction between species may be underplayed. In addition, factors such as the level of binding occurring after the free molecule has extravasated are simply not known.

As the only clinically approved Gd-based MRI contrast agent that binds in high fraction to albumin, gadofosveset is uniquely positioned to facilitate alternative calculation of in vivo perfusion and permeability characteristics. The complex nature of gadofosveset pharmacokinetics, resulting from the large physical differences between its bound and free form and the time-varying ratio of bound-to-free concentrations, has not been adequately modelled. Recent studies suggest that the potential of gadofosveset in areas such as atherosclerosis and angiogenesis is beginning to be realised, although for DCE-MRI models to work successfully, gadofosveset must first be fully characterised.

Alternative clinically approved albumin-binding agents are available, in the form of gadoxetate and gadobenate. Although the albumin binding affinity is much lower for these agents, the level of binding is sufficiently high to modify observed relaxivity and tracer kinetics, and may necessitate adaptation of conventional DCE-MRI models to accommodate this binding behaviour. Only a limited assessment of the influence of contrast agent and albumin concentration on the observed relaxivity has previously been carried out for these agents; a more thorough investigation may be of benefit for improving the accuracy of pharmacokinetic modelling with gadoxetate and gadobenate.

CHAPTER 4: EXPLORING THE LONGITUDINAL RELAXIVITY OF GADOFOSVESET AND OTHER ALBUMIN-BINDING AGENTS AT VARIOUS MAGNETIC FIELD STRENGTHS

4.1 BACKGROUND

As discussed in Chapter 3, gadofosveset binds reversibly with albumin in the blood, leading to a significantly higher longitudinal relaxivity that peaks at around 0.5 T and decreases substantially at higher magnetic fields. Bound fraction is at a maximum at very low gadofosveset concentrations, and varies according to relative gadofosveset and serum albumin concentrations. In dynamic gadofosveset-enhanced studies, the complexity of tracer kinetic modelling is increased due to the variation of bound fraction with time and the direct influence of binding on relaxivity. Rather than employing a simple linear relationship between relaxation rate and contrast agent concentration, with a single, fixed relaxivity to convert signal intensity to concentration at a given field strength, the concept of a ‘dynamic’ or observed relaxivity, varying as gadofosveset binding changes over time, has previously been suggested (78). In addition, the individual relaxivities of the bound and free gadofosveset molecule vary in response to changes in field strength, temperature and pH (37).

Many of these factors are often not accounted for in studies using gadofosveset, with assumptions made to reduce model complexity. Previous gadofosveset relaxivity studies have generally assumed gadofosveset binding at a single site on the albumin molecule (77, 78), which is likely to lead to an underestimation of relaxivity at higher gadofosveset concentrations. It may be necessary to consider additional binding sites when analysing peak concentration levels, such as during the first pass of a bolus. Although the process of binding will not change with field strength, the influence on observed

relaxivity will be modified due to the manner in which bound and free relaxivities vary with field.

It would be beneficial to fully characterise the in vitro properties of gadofosveset prior to modelling its tracer kinetics in vivo, although translation of in vitro gadofosveset relaxivity measurement may not be straightforward. For example, species differences in albumin levels and binding characteristics may create differences in bound fraction (75), and the response of the bound and free molecule to changes in temperature results in opposing variations in relaxivity (37). Another important factor to account for is the influence of field strength on bound and free relaxivity. Much of the initial gadofosveset characterisation work prior to clinical trials was carried out at low fields (63, 77). Although measurement of the relaxivity of free gadofosveset (and observed relaxivity in plasma) has been carried out at field strengths up to 4.7 T (91), it is difficult to find published values of bound gadofosveset relaxivity at field strengths of 3.0 T and above. As the strength of clinical magnets continues to increase, it is important to assess the properties of gadofosveset at field strengths that are, or may become, clinically relevant.

Gadoxetate and gadobenate are clinically approved Gd-based MRI contrast agents with much lower albumin-binding affinities than gadofosveset, leading to a lower bound fraction and a smaller, but measurable, effect on observed relaxivity (see section 3.3.1). Comparing the longitudinal relaxivities of these low-affinity agents with those of gadofosveset, at a range of magnetic field strengths, may provide further evidence regarding the benefits and limitations of gadofosveset, and may support the successful application of these commonly used agents. As with gadofosveset, published values of bound relaxivity could not be found for gadoxetate or gadobenate at 3.0 T and above.

4.2 AIMS AND OBJECTIVES

The primary aim of this study was to gain a greater understanding of the influence of albumin binding on the longitudinal relaxivity of gadofosveset at a

range of field strengths and temperatures. In addition, the study aimed to acquire supplementary information on the influence of albumin binding on the relaxivities of gadoxetate and gadobenate. The following key objectives were set:

1. Measure the longitudinal relaxation rates of in vitro gadofosveset solutions at a range of concentrations, in the presence and absence of serum albumin, at magnetic field strengths between 0.47 T and 9.4 T, at room and body temperature.

2. Use these measured relaxation rates to determine the longitudinal relaxivities of bound and free gadofosveset (assuming a single binding site), and identify variances in relaxivity with field strength and temperature.

3. Repeat the relaxation rate measurements for gadofosveset in mouse plasma, to assess the influence of species differences in albumin levels.

4. Compare the single-binding-site relaxation rate model fits for gadofosveset in serum albumin with equivalent fits incorporating two and three binding sites.

5. Repeat the measurements of relaxation rates and calculations of bound and free relaxivity for gadoxetate and gadobenate in the presence and absence of serum albumin.

Existing literature provides an incomplete picture of the variation of bound relaxivity with field strength for these three agents, particularly at 3.0 T and above. By calculating bound and free relaxivities across a range of fields, an informed choice of dynamic relaxivity may be made for in vivo calculations. Comparing model fits with one, two or three binding sites allows an assessment of the adequacy of the common assumption of a single binding site. Measuring the relaxation rate of gadofosveset in mouse plasma gives further information regarding the binding of this agent, and may aid in the translation of pre-clinical studies. Extending relaxivity calculations to gadoxetate and gadobenate, which

have a much lower binding fraction than gadofosveset, should indicate the extent to which binding and dynamic relaxivity must be considered.

By characterising the in vitro relaxation properties of these albumin-binding agents, across a range of field strengths and at clinically relevant concentrations, it is hoped that future studies may be better informed as to the advantages and limitations of these agents, particularly in relation to tracer kinetic modelling.

4.3 THEORY

4.3.1 Determining relaxivity

The equation to determine the change in longitudinal relaxation rate, ΔR_1, for an albumin-binding contrast agent is taken from Chapter 3 (Eq. 3.10).

$$\Delta R_1 = r_{1free}.C_g + \left(r_{1bound} - r_{1free}\right).\left\{\frac{\left(K_a.C_g + K_a.C_{sa} + 1\right) - \sqrt{\left[\left(K_a.C_g + K_a.C_{sa} + 1\right)^2 - 4.{K_a}^2.C_g.C_{sa}\right]}}{2.K_a}\right\} \quad [3.10]$$

where r_{1bound} and r_{1free} are the relaxivities of the bound and free molecules, respectively, C_g is the total contrast agent concentration, K_a is the binding affinity and C_{sa} is the albumin concentration.

In the absence of albumin, $C_{sa} = 0$ and the second term in Eq. 3.10 vanishes (Eq. 4.1).

$$\Delta R_1 = r_{1free}.C_g \quad [4.1]$$

Eq. 4.1 is of the form of Eq. 2.14 (Chapter 2); linearity is assumed, but may only be valid at relatively low contrast agent concentrations (see section 2.3.4).

Bound and free relaxivities are expected to vary with field strength and temperature, and may be determined by measuring R_1 of in vitro solutions containing known quantities of C_g and C_{sa}. r_{1free} may then be derived using a one-parameter linear fit (Eq. 4.1) to R_1 measurements of in vitro solutions without albumin, and r_{1bound} may be derived using a one-parameter nonlinear fit (Eq. 3.10) to R_1 measurements of solutions containing albumin at a fixed C_{sa} concentration (with a literature K_a value). This process can be repeated at a range of relevant field strengths and temperatures.

4.3.2 Assessing binding sites

Although it is often assumed that only one gadofosveset molecule binds per albumin molecule (77, 78), several molecules are expected to bind at high C_g values (63). Eq. 3.11 (Chapter 3) provides an approach for accommodating additional binding sites where binding affinities at these additional sites are equal, which is not the case for gadofosveset. To allow for the influence of binding at second and third sites with different binding affinities and relaxivities, an adaptation of Eq. 3.10 is suggested.

The observed change in relaxation rate (ΔR_1) may be considered as the sum of changes in relaxation rate induced by the free gadofosveset molecule (ΔR_{1free}) and changes in relaxation rate induced by the first, second and third bound molecules ($\Delta R_{1bound1}$, $\Delta R_{1bound2}$ and $\Delta R_{1bound3}$, respectively) (Eq. 4.2).

$$\Delta R_1 = \Delta R_{1free} + \Delta R_{1bound1} \quad [4.2]$$
$$[+ \Delta R_{1bound2}]$$
$$[+\Delta R_{1bound3}]$$

If the assumption is made that binding sites are filled sequentially, such that binding will not occur at the second site until all primary binding sites are filled and binding will not occur at the third site until all secondary binding sites are filled, the bracketed $\Delta R_{1bound2}$ and $\Delta R_{1bound3}$ terms can be removed from Eq. 4.2

according to relative albumin–gadofosveset concentrations. Assuming the first binding sites are all filled at $C_g = C_{sa}$, the $\Delta R_{1bound2}$ term should be included where $C_{sa} < C_g \leq 2C_{sa}$ and the $\Delta R_{1bound3}$ term included where $C_g > 2C_{sa}$.

Eq. 3.10 includes contributions from the free gadofosveset molecule ($r_{1free}.C_g$) and the first bound molecule (the remainder of the equation). Adding concentration-dependent terms for the second and third bound molecules gives three variations of Eq. 3.10, allowing for binding affinities K_{a1}, K_{a2}, K_{a3} and bound relaxivities $r_{1bound1}$, $r_{1bound2}$, $r_{1bound3}$ at the first, second and third binding sites, respectively. (Eq. 4.3a–c).

For $C_g \leq C_{sa}$: [4.3a]

$$\Delta R_1 = r_{1free}.C_g$$

$$+\left(r_{1bound1} - r_{1free}\right).\left\{\frac{\left(K_{a1}.C_g + K_{a1}.C_{sa} + 1\right) - \sqrt{\left[\left(K_{a1}.C_g + K_{a1}.C_{sa} + 1\right)^2 - 4.{K_{a1}}^2.C_g.C_{sa}\right]}}{2.K_{a1}}\right\}$$

For $C_{sa} < C_g \leq 2C_{sa}$: [4.3b]

$$\Delta R_1 = r_{1free}.C_g$$

$$+\left(r_{1bound1} - r_{1free}\right).\left\{\frac{\left(K_{a1}.C_g + K_{a1}.C_{sa} + 1\right) - \sqrt{\left[\left(K_{a1}.C_g + K_{a1}.C_{sa} + 1\right)^2 - 4.{K_{a1}}^2.C_g.C_{sa}\right]}}{2.K_{a1}}\right\}$$

$$+\left(r_{1bound2} - r_{1free}\right).$$

$$\left\{\frac{\left(K_{a2}.(C_g - C_{sa}) + K_{a2}.C_{sa} + 1\right) - \sqrt{\left[\left(K_{a2}.(C_g - C_{sa}) + K_{a2}.C_{sa} + 1\right)^2 - 4.{K_{a2}}^2.(C_g - C_{sa}).C_{sa}\right]}}{2.K_{a2}}\right\}$$

For $C_g > 2C_{sa}$: [4.3c]

$$\Delta R_1 = r_{1free}.C_g + \left(r_{1bound1} - r_{1free}\right).\left\{\frac{\left(K_{a1}.C_g + K_{a1}.C_{sa} + 1\right) - \sqrt{\left[\left(K_{a1}.C_g + K_{a1}.C_{sa} + 1\right)^2 - 4.{K_{a1}}^2.C_g.C_{sa}\right]}}{2.K_{a1}}\right\}$$

$$+ \left(r_{1bound2} - r_{1free}\right).\left\{\frac{\left(K_{a2}.(C_g - C_{sa}) + K_{a2}.C_{sa} + 1\right) - \sqrt{\left[\left(K_{a2}.(C_g - C_{sa}) + K_{a2}.C_{sa} + 1\right)^2 - 4.{K_{a2}}^2.(C_g - C_{sa}).C_{sa}\right]}}{2.K_{a2}}\right\}$$

$$+ \left(r_{1bound3} - r_{1free}\right).\left\{\frac{\left(K_{a3}.(C_g - 2C_{sa}) + K_{a3}.2C_{sa} + 1\right) - \sqrt{\left[\left(K_{a3}.(C_g - 2C_{sa}) + K_{a3}.2C_{sa} + 1\right)^2 - 4.{K_{a3}}^2.(C_g - 2C_{sa}).2C_{sa}\right]}}{2.K_{a3}}\right\}$$

4.4 METHOD

4.4.1 In vitro solutions

In vitro solutions were prepared using phosphate-buffered saline (PBS, dry powder reconstituted with deionized water, pH 7.4, Sigma Aldrich, St Louis, MO) and bovine serum albumin (BSA, Cohn fraction V lyophilized powder, Sigma Aldrich, in PBS). Gadofosveset (Vasovist) solutions were created at the following concentrations: C_g = 0, 0.25, 0.5, 0.75, 1.0, 1.5, 2.0, 3.0, 5.0 mM (C_{sa} = 0 mM and C_{sa} = 0.67 mM (4.5% w/v BSA)). Solutions of gadofosveset in mouse plasma were created at C_g = 0, 0.25, 0.5, 1.0, 2.0 mM. In vitro solutions of gadoxetate (Primovist) and gadobenate (MultiHance) were created at C_g = 0, 0.2, 0.5, 0.7, 1.0 mM (C_{sa} = 0 mM and C_{sa} =0.7 mM BSA). Approximately 8.0 mL of each solution was decanted to borosilicate NMR tubes of external diameter 10.0 mm, internal diameter 8.0 mm and length 150.0 mm (supplied by

YORLAB, York) for use at 0.47 T. Smaller plastic tubes (external diameter 12.0 mm, length 40.0 mm) containing approximately 1.5 mL of solution were used at higher fields to allow for the small bore size of the pre-clinical scanners.

4.4.2 Measurements at 0.47 T

Measurements were made on a Maran NMR spectrometer (Oxford Instruments, Abingdon) utilising a 0.47 T (20 MHz) permanent magnet attached to a thermocouple heating mechanism and a PC running standard system software. T_1 was measured using an inversion recovery (IR) sequence, with 20 log incremental inversion time (TI) recovery steps and 16 scans. The recovery time (TR) was set to at least five times the expected final T_1 value. Receiver gain, frequency offset and pulse length were automatically set by the system. For the two solutions without contrast agent, 10 linear TI steps and four scans were used (to maintain practical overall scanning times), and the TR was set to 10 s. The bore temperature was allowed to stabilise for at least five minutes before samples were inserted, followed by a further five minutes for solution temperature stabilisation. All solutions were manually agitated to ensure full mixing of the contrast agent. Measurements were taken at 21 – 22 ˚C and 37 ˚C to represent room and body temperature, respectively.

4.4.3 Measurements at 3.0 T

For gadofosveset, tubes were placed vertically in a plastic container filled with PBS at room temperature (20 – 22 ˚C). This container was placed in a Siemens head matrix coil in a 3.0 T Siemens Magnetom Verio scanner. Images were acquired using a spin echo (SE) IR sequence, with two coronal (horizontal) slices through the short axis of the tubes. Sequence parameters: 10 inversion times (TI = 22, 40, 75, 110, 150, 300, 600, 1000, 2000, 4000 ms); TR = 10000 ms; echo time (TE) = 18 ms; field of view (FOV) = 261 x 100 mm; matrix size = 512 x 216 pixels; slice thickness = 5 mm.

For gadoxetate and gadobenate, tubes were placed vertically within a head coil (SENSE-Head 8) in a 3.0 T Philips Achieva TX system at room temperature (18 °C). Images were acquired using an SE IR sequence with a single coronal (horizontal) slice. Sequence parameters: 10 inversion times (TI = 50, 83, 136, 225, 371, 611, 1009, 1665, 2747, 4925 ms); TR = 5000 ms; TE = 6.2 ms; FOV = 230 x 230 mm; matrix size = 240 x 240 pixels; slice thickness = 10 mm.

No heating mechanism was available on either clinical 3.0 T scanner to heat the samples to body temperature.

4.4.4 Measurements at 4.7 T

For gadofosveset, tubes were placed horizontally in a cylindrical cradle of diameter 6.0 cm. An additional tube containing water and a fibre optic temperature probe was also placed into the cradle to monitor solution temperature. The cradle was inserted into a 63 mm quad coil in a horizontal bore 4.7 T magnet with Bruker console running ParaVision 5.1 software (Bruker BioSpin MRI GmbH, Ettlingen, Germany). Images were acquired using a fast spin echo saturation recovery sequence (rapid acquisition with relaxation enhancement, RARE), with two sets of TRs to provide additional detail for those solutions with very short relaxation times. Slice direction was axial (vertical), through the short axis of the tubes. Measurements were made at approximately 19˚C and 37˚C for room and body temperature, respectively. Sequence parameters: Recovery time (long series) = 57.2, 103.5, 183.5, 283.5, 583.5, 1483.5, 2983.5, 7983.5 ms; recovery time (short series) = 57.2, 68.5, 78.5, 88.5, 103.5, 183.5, 283.5, 383.5 ms; TE = 11 ms; slice thickness = 1 mm; FOV = 45 x 45 mm; matrix size = 256 x 256 pixels.

The experimental set-up for the gadoxetate and gadobenate samples was identical to that for gadofosveset, with the exception of a larger FOV (60 x 60 mm) and a single set of recovery times (57.2, 68.5, 78.5, 88.5, 103.5, 183.5, 483.5, 983.5, 2983.5 ms). Measurements were made at approximately body temperature (36 °C) only, due to time constraints.

4.4.5 Measurements at 9.4 T

Gadofosveset samples were inserted into a cylindrical cradle of diameter 4.0 cm, and placed inside a 63 mm quad coil in a horizontal bore 9.4 T Varian scanner. Images were acquired using a FLASH (fast low-angle shot) gradient echo (GE) IR sequence, with 20 TIs, a centre-out phase encoding ordering and one line of k-space acquired per excitation. Slice direction was axial (vertical), through the short axis of the tubes. Measurements were made at approximately 22˚C and 32 – 34˚C for room and body temperature, respectively (temperatures could not be increased to 37 °C due to a fault with the heating mechanism). Delay time prior to application of inversion = 10000 ms; TI = 6.5, 7, 8, 9, 10, 30, 50, 100, 150, 200, 250, 500, 750, 1000, 2000, 5000, 7000, 9000, 12000, 15000 ms; slice thickness = 1 mm; FOV = 50 x 50 mm; matrix size = 128 x 128 pixels. Gadoxetate and gadobenate samples were not measured at this field strength.

4.4.6 Calculating relaxation rate, R_1

The models used for calculating R_1 are summarised in Table 4.1. All model fitting was carried out using a nonlinear regression function in MATLAB (v7.9, MathWorks, USA; ‘nlinfit’ function). Confidence intervals (CI) were calculated at the 95% level using a nonlinear regression parameter CI function in MATLAB (with the exception of gadofosveset at 0.47 T, where CIs were calculated from the standard deviation of three measured R_1 values).

Table 4.1: Summary of sequences used for R_1 measurement

Gadofosveset	0.47 T	3.0 T	4.7 T	9.4 T
R_1 sequence	SE IR	SE IR	RARE SR	FLASH GE IR
Model fit	System calculated	$SI = S_0.\|1 - b.e^{-TI.R1}\|$	$SI = S_0.(1 - e^{-TR.R1})$	$SI = S_0.\|1 - b.e^{-TI.R1}\|$
Temp (°C)	21 & 37	21	19 & 37	22 & 33
Gadoxetate & Gadobenate	0.47 T	3.0 T	4.7 T	9.4 T
R_1 sequence	SE IR	SE IR	RARE SR	Not measured
Model fit	$SI = S_0.\|1 - b.e^{-TI.R1}\|$	$SI = S_0.\|1 - b.e^{-TI.R1} + e^{-TR.R1}\|$	$SI = S_0.(1 - e^{-TR.R1})$	
Temp (°C)	21 & 37	18	36	

where SI is measured signal intensity; S_0 represents the fully recovered signal intensity; b accounts for any deviation in angle from the ideal 180° inversion pulse; SE is spin echo; GE is gradient echo; IR is inversion recovery; SR is saturation recovery

For gadofosveset at 0.47 T, the system software automatically calculated T_1 ($1/R_1$) values by fitting an exponential curve to the plotted signal intensities at the full range of TI values; measurements were repeated three times for each solution, and the mean of these three measurements used in the analysis. For gadoxetate and gadobenate at 0.47 T, an equivalent model was applied offline using the downloaded signal intensity (SI) values at each inversion time. Acquisitions at higher fields were based on imaging sequences, with circular regions of interest (ROI) drawn within each tube image and the average SI of each ROI measured using ImageJ software (v1.42q, Wayne Rasband, National Institutes of Health, USA). For the 9.4 T images, an in-house (AstraZeneca) model was used to reconstruct data to take account of phase and to reduce image noise by k-space filtering. Circular ROIs were then drawn on these reconstructed SI maps as described previously. For gadofosveset at 4.7 T, both

sets of TR were analysed separately for each tube and the R_1 with the smallest fractional CI was used.

4.4.7 Relaxivity

Relaxivity of the free molecule was calculated by applying a linear fit to the PBS (C_{sa} = 0 mM) data (Eq. 4.1). Bound relaxivity was calculated by applying a nonlinear one-parameter fit (Eq. 3.10) to the BSA (C_{sa} = 0.67 mM for gadofosveset; C_{sa} = 0.7 mM for gadoxetate and gadobenate) data at points where $C_g \leq 0.75$ mM. Higher concentrations were excluded to reduce the potential influence of multiple binding sites on the calculation of bound relaxivity. K_a values of 11.0, 0.255 and 0.226 mM^{-1} were used for gadofosveset, gadoxetate and gadobenate, respectively. Overall observed relaxivity (r_{1obs}), a composite of r_{1bound} and r_{1free}, was also calculated by applying a linear fit to low concentration ($C_g \leq 0.75$ mM) solutions of gadofosveset, gadoxetate and gadobenate in BSA.

4.4.8 Additional binding sites

An attempt was made to incorporate up to two additional binding sites for gadofosveset, using Eq. 4.3a–c, with the same (calculated) bound relaxivity at all sites and a binding affinity at the second and third binding sites (K_{a2} and K_{a3}) of 0.86 mM^{-1} and 0.26 mM^{-1}, respectively (68).

4.5 RESULTS

Fig. 4.1 shows relaxation rates at room temperature (approximately 21 °C) at all field strengths. Body temperature values (not shown here, but included in Appendix B (Fig. B.1)) display a similar pattern.

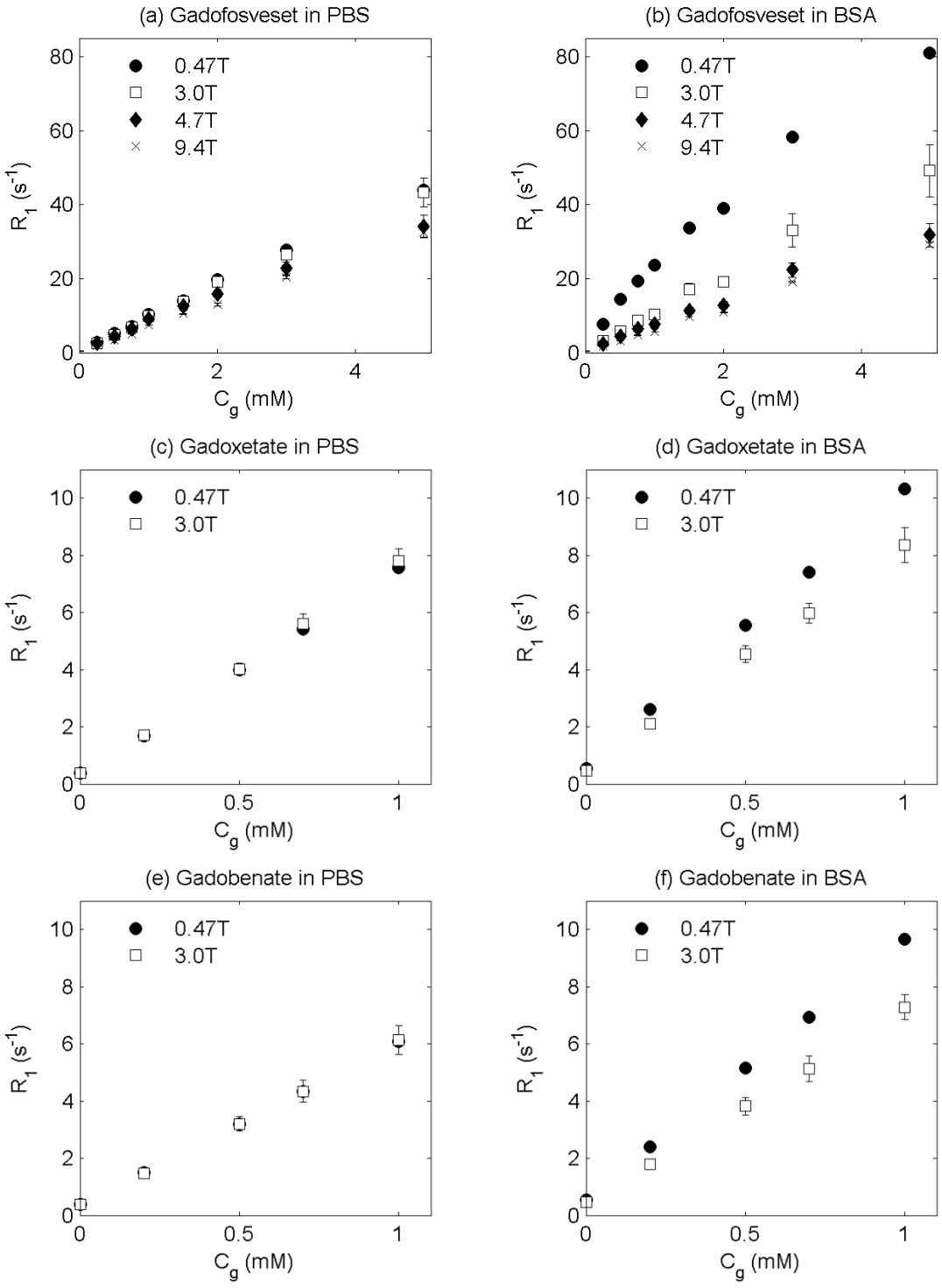

Figure 4.1: Measured relaxation rates (R_1) for gadofosveset, gadoxetate and gadobenate in PBS (left column) and BSA (right column) at room temperature (approximately 21 °C) at 0.47 T and 3.0 T (all agents), and at 4.7 T and 9.4 T (gadofosveset only); error bars represent 95% CI (omitted where smaller than data point)

Following calculation of r_{1free} using the PBS solutions (Eq. 4.1), the nonlinear model (Eq. 3.10) was applied to determine r_{1bound} for the BSA solutions. Fig. 4.2 (gadofosveset) and Fig. 4.3 (gadoxetate and gadobenate) show this model fit, along with the measured ΔR_1 values for each set of BSA solutions.

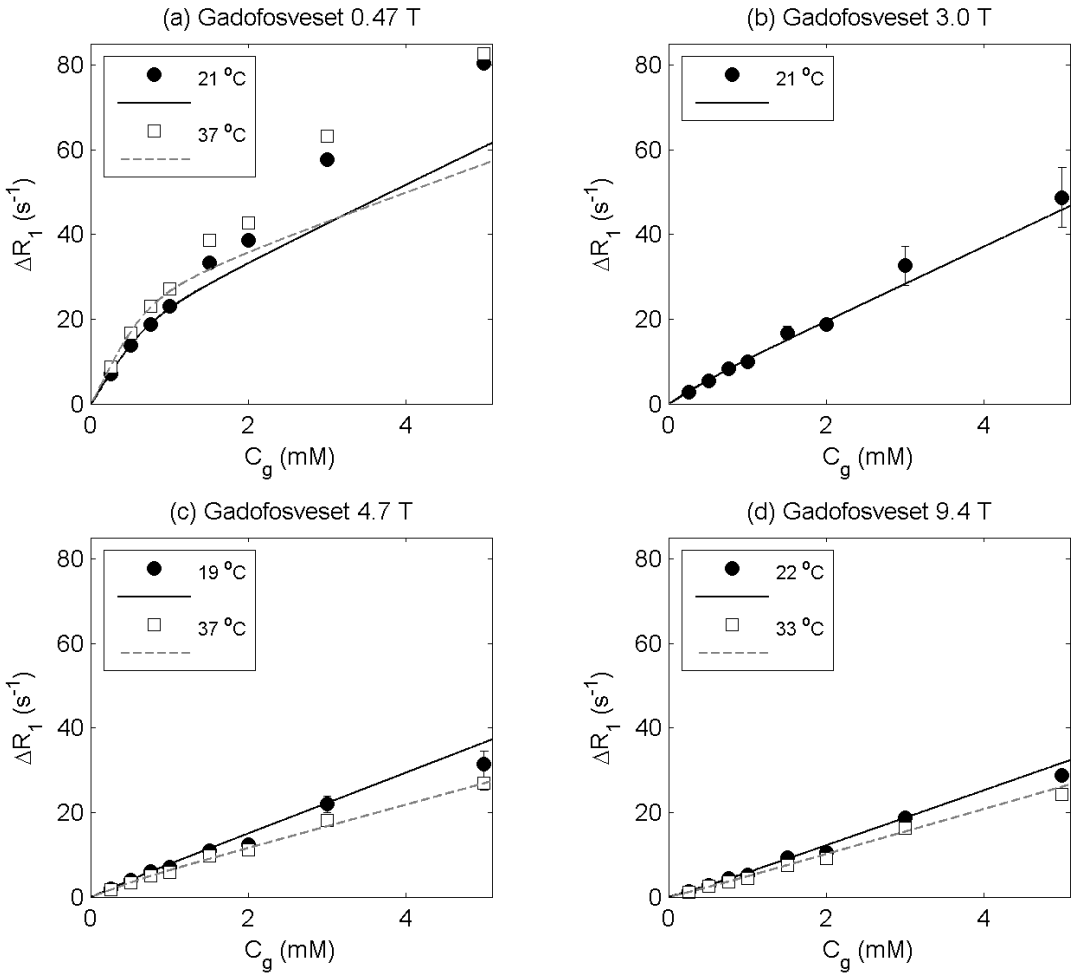

Figure 4.2: Measured ΔR_1 values for gadofosveset in BSA; lines represent nonlinear fit to $C_g \leq 0.75$ mM data points (Eq. 3.10; K_a = 11.0 mM^{-1}); error bars represent 95% CI (omitted where smaller than data point)

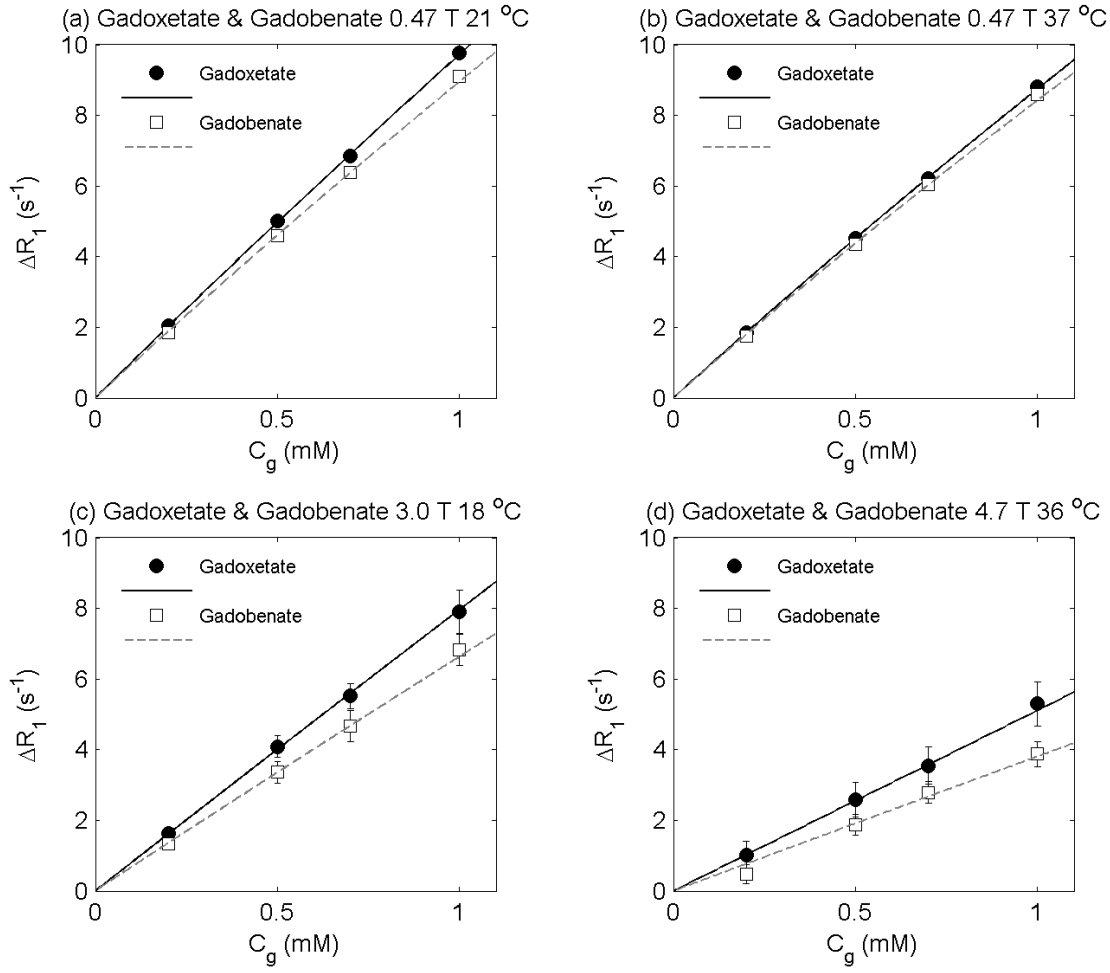

Figure 4.3: Measured ΔR_1 values for gadoxetate (circles) and gadobenate (squares) in BSA; solid (gadoxetate) and dotted (gadobenate) lines represent nonlinear fit to $C_g \leq 0.75$ mM data points (Eq. 3.10; K_a = 0.255mM^{-1} and 0.226 mM^{-1} for gadoxetate and gadobenate, respectively); error bars represent 95% CI (omitted where smaller than data point)

Bound and free relaxivity values are shown in Fig. 4.4 and summarised in Table 4.2. The relaxivity of the bound gadofosveset molecule peaks at low field, showing a sharp decrease between 0.47 T and 3.0 T and a moderate decrease at higher field strengths (Fig. 4.4a). The relaxivity of the free gadofosveset molecule has a much lower peak, and decreases slightly with field strength (Fig. 4.4b). A similar pattern is displayed for gadoxetate and gadobenate. Above 4.7 T, the binding of gadofosveset to albumin does not benefit the observed relaxivity, with bound relaxivity slightly lower than free relaxivity (Table 4.2).

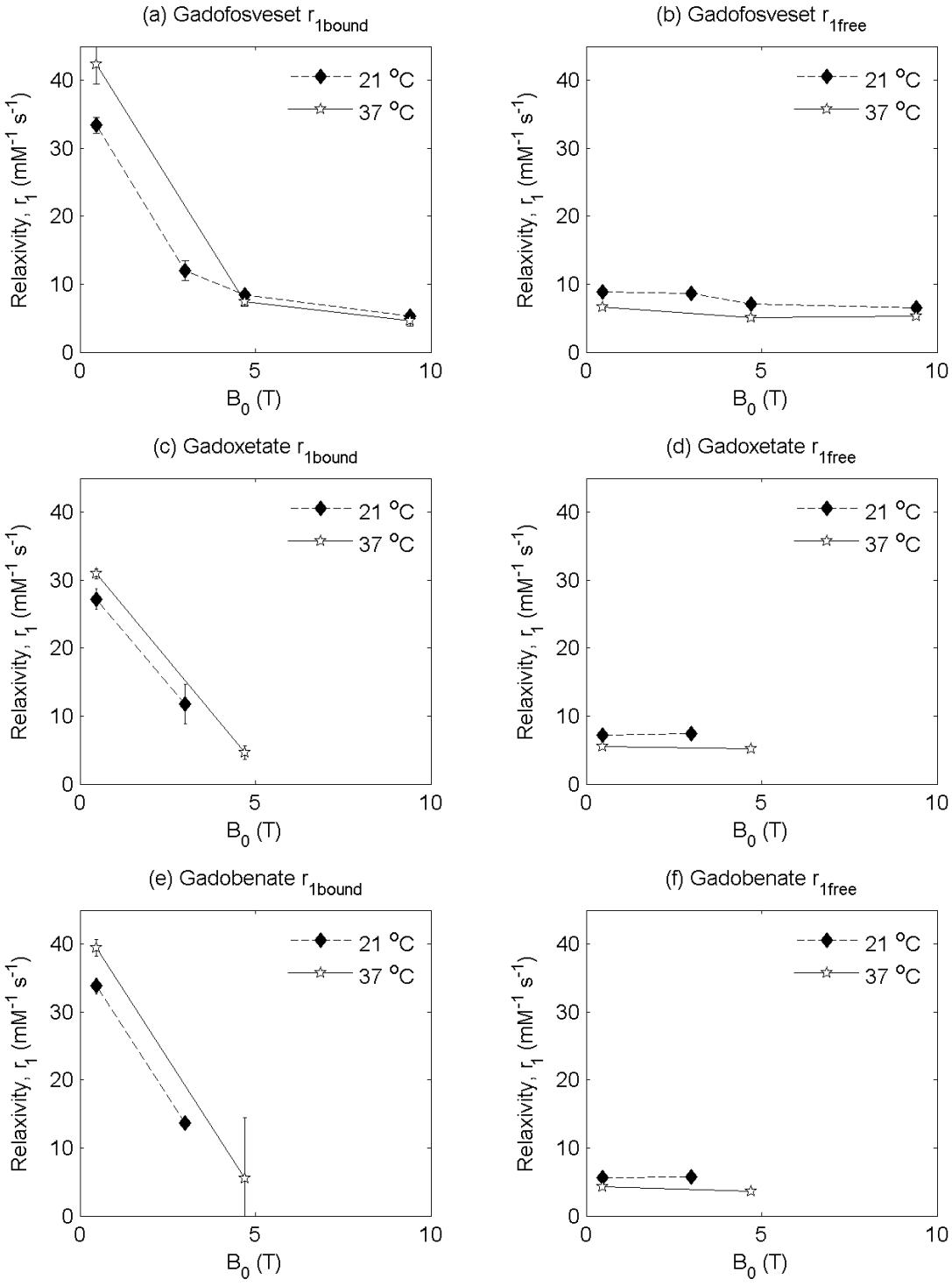

Figure 4.4: Calculated bound (left column) and free (right column) relaxivity values for all three agents, split by temperature (labelled 21 °C and 37 °C, but actual temperatures may differ slightly – see Table 4.1); error bars represent 95% CI (omitted where smaller than data point)

Table 4.2: Summary of calculated relaxivity values and 95% confidence intervals ($mM^{-1} s^{-1}$)

	0.47 T		3.0 T		4.7 T		9.4 T	
Gadofosveset	21 °C	37 °C	21 °C	37 °C	19 °C	37 °C	22 °C	33 °C
r_{1bound}	33.4 (1.2)	42.4 (2.9)	12.0 (1.4)		8.4 (0.5)	7.4 (0.6)	5.3 (0.4)	4.6 (0.8)
r_{1free}	8.9 (0.3)	6.6 (0.2)	8.7 (0.2)		7.1 (0.5)	5.1 (0.3)	6.5 (0.2)	5.3 (0.1)
r_{1obs}	26.1 (4.2)	31.8 (4.6)	11.0 (0.4)		8.0 (0.2)	6.7 (0.1)	5.7 (0.5)	4.8 (0.5)
Gadoxetate	21 °C	37 °C	18 °C			36 °C		
r_{1bound}	27.2 (1.5)	30.9 (0.7)	11.8 (2.9)			4.6 (1.0)		
r_{1free}	7.2 (0.2)	5.5 (0.1)	7.4 (0.2)			5.2 (0.3)		
r_{1obs}	9.9 (0.4)	9.0 (0.3)	8.0 (0.4)			5.1 (0.1)		
Gadobenate	21 °C	37 °C	18 °C			36 °C		
r_{1bound}	33.9 (1.2)	39.5 (1.2)	13.7 (0.4)			5.6 (9.0)		
r_{1free}	5.7 (0.1)	4.3 (0.1)	5.7 (0.1)			3.6 (0.1)		
r_{1obs}	9.2 (0.1)	8.7 (0.1)	6.7 (0.1)			3.8 (1.1)		

The influence of additional binding sites is illustrated for gadofosveset in Fig. 4.5, where the original model is adapted to include second and third binding sites (Eq. 4.3a–c). Model fitting results are shown at room temperature only; body temperature model fits (Appendix B (Fig. B.2)) display a very similar pattern.

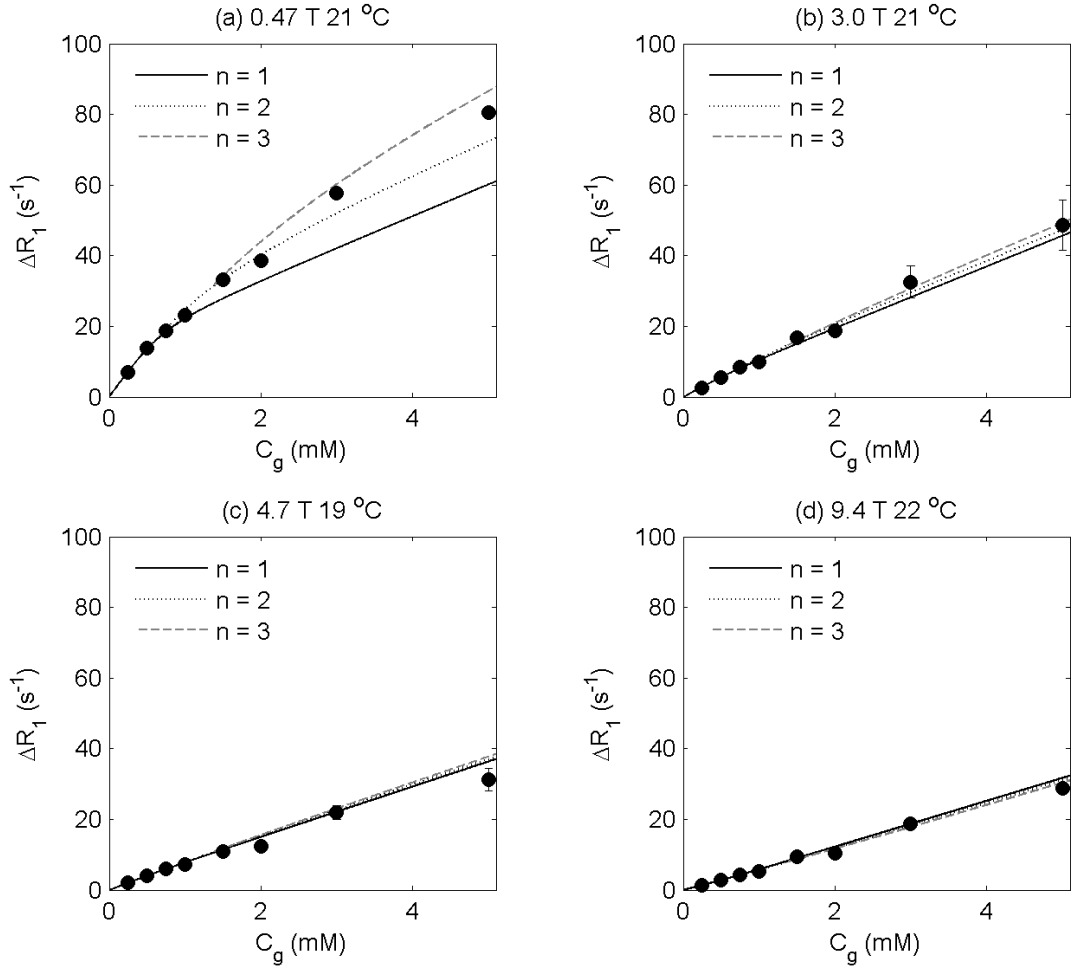

Figure 4.5: Modelling n = 1 – 3 binding sites at all field strengths at room temperature, using Eq. 4.3a–c. Circles represent measured gadofosveset data points; solid line is original model (single binding site, Eq. 4.3a, K_{a1} = 11.0 mM^{-1}); dotted line also includes a second binding site (Eq. 4.3b, K_{a2} = 0.86 mM^{-1}); dashed line also includes a third binding site (Eq. 4.3c, K_{a3} = 0.26 mM^{-1}); the same relaxivity values (from Table 4.2) were used at all three binding sites

A comparison of measured R_1 values for gadofosveset in BSA (at C_{sa} = 0.67 mM) and in mouse plasma at body temperature is shown in Fig. 4.6.

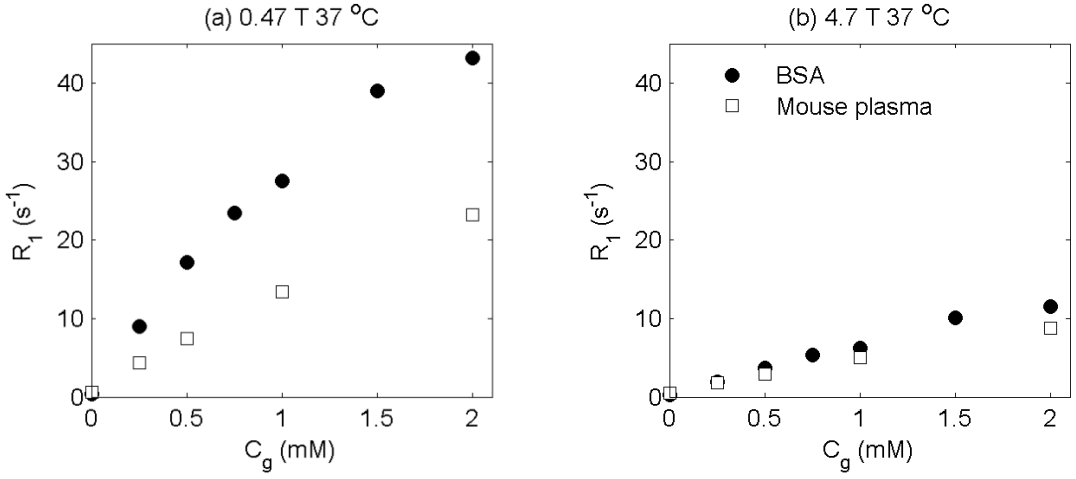

Figure 4.6: Comparison of R_1 values at 37 °C for gadofosveset in BSA (circles, C_{sa} = 0.67 mM) and in mouse plasma (squares) at (a) 0.47 T and (b) 4.7 T

4.6 DISCUSSION

4.6.1 Relaxation rates

Gadofosveset

The relationship between R_1 and C_g for gadofosveset in the absence of albumin is approximately linear, with any differences caused by field strength only being observed at very high C_g (Fig. 4.1a). For gadofosveset in the presence of albumin, a nonlinear relationship between R_1 and C_g is observed (Fig. 4.1b).

Applying the nonlinear ΔR_1 model (Eq. 3.10) to the BSA measurements at low C_g (≤ 0.75 mM), it is clear that the model underestimates ΔR_1 at high C_g at 0.47 T (Fig. 4.2a). This underestimation at high C_g is likely to be due to the assumption of a single binding site. Once this binding site is filled for all albumin molecules (at $C_g = C_{sa}$), additional gadofosveset is assumed to remain free. However, if gadofosveset also binds to other sites on the albumin molecule, this may lead to a greater contribution to observed ΔR_1. The underestimation is not observed at higher fields (Fig. 4.2b to 4.2d), where the

differences between relaxivities of the bound and free molecule are expected to be small. As can be seen from Eq. 3.10, when r_{1bound} approaches r_{1free} the ΔR_1 calculation is dominated by the product of r_{1free} and C_g and the model becomes approximately linear.

Gadoxetate and gadobenate

For both gadoxetate and gadobenate in PBS, there is no difference between R_1 at 0.47 T and 3.0 T (Fig. 4.1c and 4.1e). In the presence of albumin, gadoxetate ΔR_1 values are slightly higher than equivalent gadobenate values (Fig. 4.3); there is some evidence of nonlinearity in these plots at 0.47 T, but the plots at higher fields are approximately linear.

4.6.2 Relaxivity

Gadofosveset

At 0.47 T, the r_{1free}, r_{1bound} and r_{1obs} values at 37 °C in this study (6.6, 42.4 and 31.8 mM^{-1} s^{-1}, respectively) are close to those found in the literature (r_{1free} = 6.8 mM^{-1} s^{-1} (162), r_{1bound} = 42 mM^{-1} s^{-1} (approximately, below C_g = 1 mM) (68) and r_{1obs} = 28.0 mM^{-1} s^{-1} (91)). r_{1free} and r_{1obs} values at 4.7 T at 37 °C are also close to literature values (5.1 and 6.7 mM^{-1} s^{-1}, respectively, in this study versus 5.5 and 6.9 mM^{-1} s^{-1}, respectively, in the literature (91)). Due to variations in experimental set-up, it is difficult to find directly equivalent r_{1bound} literature values for comparison at field strengths of 3.0 T and above.

Bound (and observed) gadofosveset relaxivity at 0.47 T has previously been shown to increase with temperature, with free relaxivity decreasing with temperature (37). This pattern is also demonstrated at 0.47 T in this study (Fig. 4.4). At high field, r_{1free} remains consistently lower at 37 °C than at 21° C (Fig. 4.4b), but r_{1bound} values at high field are very similar for both temperatures (Fig. 4.4a). Although the heating mechanism used at 9.4 T was unable to heat

the samples above 34 °C, it is likely the results would have been very similar at 37 °C.

Gadoxetate and gadobenate

Calculated free relaxivity values at 0.47 T and 4.7 T for gadoxetate and gadobenate (Fig. 4.4d and 4.4f; Table 4.2) closely match those published elsewhere (91), although comparative bound relaxivity values are more difficult to find in the literature. Studies of gadobenate at 0.47 T and 37 °C have calculated r_{1bound} at 36 mM^{-1} s^{-1} in rabbit plasma (78), and 32 mM^{-1} s^{-1} (163) and 42.9 mM^{-1} s^{-1} (126) in human serum albumin. These values are close to the equivalent gadobenate r_{1bound} value of 39.5 mM^{-1} s^{-1} in this study. Also at 0.47 T and 37 °C, r_{1bound} for gadoxetate in human serum albumin has been calculated at 37.3 mM^{-1} s^{-1} (126), compared with a value of 30.9 mM^{-1} s^{-1} in this study.

Calculated r_{1bound} values are lower, and r_{1free} and r_{1obs} values are slightly higher, for gadoxetate than gadobenate across all fields and temperatures. This is generally consistent with values reported elsewhere (91).

4.6.3 Multiple binding sites

As illustrated in Fig. 4.2a, at low field the nonlinear model underestimates gadofosveset ΔR_1 at high C_g. This is likely to be due to the influence of additional binding sites on the albumin molecule not accounted for by the model. Eq. 3.10 is derived based on the assumption of a single bound gadofosveset molecule per serum albumin molecule, with a saturation point at $C_g = C_{sa}$. If gadofosveset were to bind at multiple sites on the albumin molecule, saturation would occur at a higher C_g ($> C_{sa}$). A modified version of Eq. 3.10 accommodating *n* binding sites of equivalent affinity (Eq. 3.11 in Chapter 3) has previously been presented in the context of gadofosveset relaxation rates (37, 77). However, the primary binding site has been shown to have a substantially higher binding affinity than other sites (11.0 mM^{-1} at the

primary site, compared to 0.84 and 0.26 mM^{-1} at the second and third binding sites, respectively (68)), therefore this approach may not be applicable. It is unclear to what extent these additional bound molecules influence the overall relaxivity. A similar relaxivity at all binding sites has previously been assumed (164), although it is suggested that the primary binding site is one of higher relaxivity (68).

An alternative model to accommodate up to three binding sites is suggested (Eq. 4.3). Three versions of the model are plotted in Fig. 4.5 to assess differences between inclusion of one, two and three binding sites, along with measured gadofosveset data points at all field strengths and temperatures. All models use the appropriate r_{1free} value from Table 4.2. As bound relaxivities at the second and third sites are not known, all bound relaxivities were set to the same value ($r_{1bound1} = r_{1bound2} = r_{1bound3} = r_{1bound}$ from Table 4.2).

At 0.47 T, the underestimation of ΔR_1 at high C_g noted in the original model (solid line, Fig. 4.5a) is improved by the inclusion of a second binding site (dotted line), but values at high C_g are overestimated by the inclusion of a third binding site (dashed line). This overestimation for n = 3 is likely to be due to the same r_{1bound} value being used for all three sites; in reality, it may be that $r_{1bound1} > r_{1bound2} > r_{1bound3}$. Additional binding sites provide minimal improvement to the model fit at 3.0 T; at higher fields the difference is negligible and the consideration of additional binding sites may be unnecessary. In vivo, the consideration of additional binding sites is unlikely to be a factor during the post-bolus equilibrium phase (where C_g values are lower). The requirement to consider multiple binding sites may be eliminated altogether if the peak C_g value is sufficiently low, which may be achieved by reducing the dose or injection rate, for example.

A previous study using ultrafiltration showed that gadoxetate and gadobenate interacted with albumin at a single site (126), and no published binding affinity values can be found for a second binding site. The model fits well with a single site (Fig. 4.3); adding a second binding site (with an equal affinity to the first site) does not improve the model fit (see Appendix B (Fig. B.3)).

4.6.4 Species differences: gadofosveset

All measurements of bound relaxivity for gadofosveset were made using bovine serum albumin at a concentration of 0.67 mM (4.5% w/v). As mentioned in section 3.1.2, the variation in the bound fraction of gadofosveset between species is thought to be mostly attributable to differences in albumin level, therefore assessing in vitro gadofosveset samples containing albumin at a level corresponding with that found in humans should ensure the results are relevant for potential clinical translation.

Confirmation of the dominant influence of bound fraction is found not only in the comparison of observed relaxivity between gadofosveset and gadoxetate or gadobenate, but also in the measurements of gadofosveset in mouse plasma. Here, relaxation rates for gadofosveset in mouse plasma at $C_g \leq 2$ mM were compared with values using BSA at $C_{sa} = 0.67$ mM at low (0.47 T) and high (4.7 T) field (Fig. 4.6). The difference in R_1 between BSA and mouse plasma is significant at 0.47 T (Fig. 4.6a), where bound fraction has a much greater influence over the observed relaxivity due to the large difference between r_{1bound} and r_{1free} (Table 4.2). At 4.7 T, there is little difference between BSA and mouse plasma R_1 measurements (Fig. 4.6b), reflective of the small difference between r_{1bound} and r_{1free} at high field, resulting in a lower influence of bound fraction on observed relaxivity.

4.6.5 Limitations

The one-parameter model used to determine r_{1bound} by fitting to experimental ΔR_1 values (Eq. 3.10) assumes a fixed literature value for K_a. An attempt was made to derive K_a rather than take a literature value, by fitting Eq. 3.10 for two unknown parameters. However, this revised model could not be satisfactorily resolved (returning K_a and r_{1bound} values beyond the range that might reasonably be expected). The influence of K_a may be explored by comparing the model fit at additional K_a values; doubling or halving the assumed K_a value

of 11.0 mM^{-1} does not significantly alter the model fit at 0.47 T in this study (Fig. 4.7), and would have even less effect at higher fields. Although some difference in binding affinity may be expected between room and body temperature, a constant K_a value was used at both temperatures as only relevant literature K_a values at 37 °C could be found.

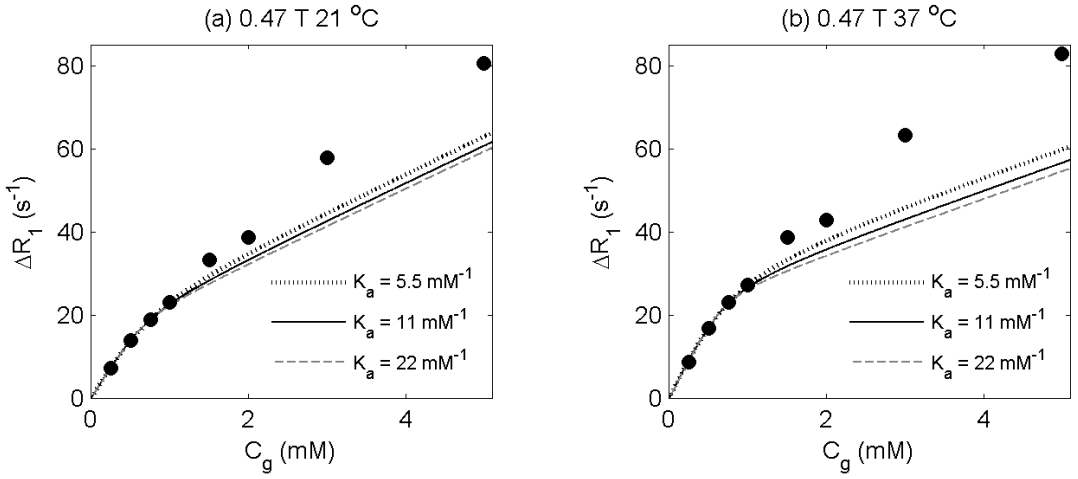

Figure 4.7: Effect of K_a on gadofosveset model fit at 0.47 T at (a) 21 °C and (b) 37 °C; data points and solid lines match those in Fig. 4.2a and 4.2b

A second potential limitation of this study is that bovine serum albumin was used as a surrogate for human serum albumin. Although the binding characteristics of BSA may differ slightly from those of HSA, albumin solutions were created at a typical concentration expected in healthy humans, therefore bound fractions and the proportional influence of the bound and free gadofosveset molecule on observed relaxivity would still be expected to be applicable. Bovine plasma has previously been used as the solvent for assessing the relaxivities of a range of contrast agents (91). BSA has been shown to be similar in structure to HSA, with some differences in binding pockets (165).

As noted in Chapter 2 (Table 2.1) the standard clinical dose for gadobenate is 0.1 mmol kg^{-1}, which is higher than gadoxetate (0.025 mmol kg^{-1}) or gadofosveset (0.03 mmol kg^{-1}). In this study like-for-like concentration comparisons were made (up to 1 mM), and no account was taken of the variation in clinical dose between agents. The physiologically applicable

concentration range could have been extended for gadobenate, although the results as presented remain valid.

For various reasons (time constraints, faulty or unavailable heating mechanisms) it was not possible to acquire data for all contrast agents at all fields at room and body temperature. As gadofosveset is the main focus of this research, priority was given to acquiring data for this agent. Although the dataset is incomplete, the influence of temperature on the relaxivity of the bound and free molecule is clearly observed. Any small variation in ‘room’ or ‘body’ temperature between agents is unlikely to have a significant impact on the conclusions drawn from the results as presented.

4.6.6 Summary

In summary, this study provides information regarding gadofosveset longitudinal relaxivity not currently available elsewhere, particularly in relation to bound relaxivity values at field strengths of 3.0 T and above. Differences between the longitudinal relaxivities of the bound and free gadofosveset molecule are large at low field but small at high field. Factors influencing the bound fraction, such as relative concentrations of gadofosveset and serum albumin, will therefore have a significant impact on the observed relaxivity at low field but will have limited impact at high field. Consideration should be given to incorporating a dynamic relaxivity, which changes with bound fraction, when applying tracer kinetic models at low field. The influence of species differences in albumin levels and binding properties is demonstrated to have a much greater effect at low field, and may markedly alter the outcome of pre-clinical studies using gadofosveset. The common assumption that a single gadofosveset molecule binds per albumin molecule may lead to an underestimation of relaxation rate at low field at high gadofosveset concentration, although this model simplification has little influence at high fields.

As expected from the literature, bound and free longitudinal relaxivities for gadoxetate and gadobenate are generally similar to those for gadofosveset.

However, due to a much lower binding affinity, the observed relaxivity is significantly lower for these agents than for gadofosveset at low field. As with gadofosveset, bound relaxivity values calculated here for gadoxetate and gadobenate at field strengths of 3.0 T and above have not previously been published. As field strength increases, r_{1bound} approaches r_{1free} at high field and the influence of binding on observed relaxivity reduces, although even at low fields the change in relaxation rate with contrast agent concentration is approximately linear. The use of any contrast agent in quantitative MRI studies requires an accurate relaxivity value to precisely monitor contrast agent kinetics. The in vivo relaxivity of an albumin-binding contrast agent is dynamic rather than fixed, varying particularly during the first bolus pass when the bound fraction is changing rapidly. The data presented here for gadoxetate and gadobenate suggests that, unlike gadofosveset, a single relaxivity value may still adequately represent this situation due to the relatively low binding affinity of these agents.

It should be noted that only the longitudinal relaxivity properties of these albumin-binding agents have been explored in this chapter. Transverse relaxivity measurements are discussed in Chapter 7, and may provide an alternative approach to utilising these agents in dynamic contrast-enhanced studies.

CHAPTER 5: A THEORETICAL APPPROACH TO IN VIVO GADOFOSVESET BLOOD CONCENTRATION MEASUREMENT

5.1 BACKGROUND

5.1.1 Contrast agent blood concentration

Establishing the blood concentration of a contrast agent is a fundamental step in calculating many quantitative parameters in dynamic contrast-enhanced (DCE) MRI. DCE-MRI enables functional tissue parameters to be assessed by monitoring the transit of a contrast agent over time. Amongst its many areas of application, DCE-MRI has been used in the quantitative assessment of myocardial (166) and pulmonary (167) perfusion. DCE-MRI may also be used to assess angiogenesis, a process that is fundamental to the progress and metastasis of tumours, along with other biomarkers in oncology (168). Quantification may be based on a simple, non-model-based approach such as measuring enhancing fraction (20). Charting signal intensity against time provides tissue-related parameters including onset time, maximum signal intensity and wash-out characteristics (23).

Alternatively, parameters such as tissue perfusion and micro-vessel permeability may be determined through the application of tracer kinetic models. Commonly, these models consist of two compartments representing intravascular and extravascular extracellular spaces, with the rate of transfer between the compartments determined through mathematical modelling (169). The conventional starting point for such models is the intravascular contrast agent concentration prior to extravasation, known as the vascular input function (VIF), which can be measured in a nearby vessel (170). In such models, quantitative parameters are derived by separating changes in contrast agent

concentration within the tissue of interest from those in a feeding artery using deconvolution (171).

The VIF following bolus injection of a gadolinium (Gd) contrast agent is characterised by a high initial peak in contrast agent concentration during the wash-in phase, of very short duration, followed by a decrease in concentration during the wash-out and clearance phases. Often, the VIF is modelled as either an instantaneous peak or a sharp linear rise to peak concentration, followed by a bi-exponential decay representing extravasation and excretion rates (Fig. 5.1). This simplified approach neglects potential recirculation effects; more complex models attempt to correct for this (172).

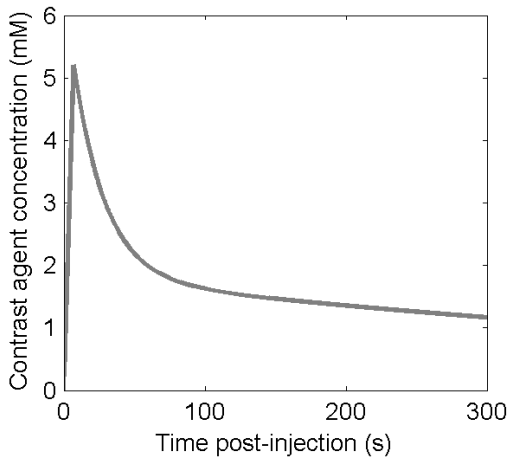

Figure 5.1: Example of a VIF, showing linear rise to peak and bi-exponential decay (not accounting for recirculation effects) ((173), using parameters from (172))

The robustness of tracer kinetic models may be compromised by practical difficulties associated with accurate VIF measurement. Potential errors in converting measured signal intensity to contrast agent concentration may be further complicated when using gadofosveset, due to its binding to albumin, and may be exacerbated by acquisition limitations including temporal resolution, signal saturation, partial volume effects and flow artefacts (174), and by delay and dispersion of the bolus in the tissue of interest (26). In small animals, the requirement for improved spatial resolution due to smaller vessel size must compete with an increased temporal resolution requirement due to a

higher heart rate (175-177). Using a population average VIF, rather than one acquired from an individual subject, may improve model robustness (178), particularly in small animals (179). An alternative approach to measuring vascular signal intensity changes may be to take measurements in a reference tissue within the field of view (180).

Laboratory analysis of ex vivo blood samples eliminates the requirement for signal intensity conversion, and may be considered the gold standard measure of contrast agent concentration in the blood. In humans, good agreement has been shown between VIF curves plotted from blood sample measurements and those using MRI signal intensities following injection of gadopentetate (181). However, using blood sampling techniques to capture the first pass of a bolus injection of contrast agent can be challenging due to the requirement for multiple blood samples in a short time-frame. Limitations regarding permissible sampling volumes add further difficulty in studies using small animals, although a recent study in rats found a good correlation between VIF descriptors calculated from measurement of Gd concentration in blood samples with those determined using imaging techniques (182).

5.1.2 Blood sampling

Blood sampling is one of the most commonly performed procedures in animal studies (183), and is fundamental to the success of pharmacokinetic and toxicology studies. Blood should always be collected in the manner that gives least pain and stress (184), and the amount of blood taken on a single occasion should not exceed 10% of circulating blood volume to prevent hypovolaemic shock (185). In a small mammal such as a mouse, this blood sampling volume limit may be less than 200 µL (79).

Micro-sampling, the removal of less than 100 µL, causes less subject interference than conventional sampling (186). Blood micro-samples are often acquired with capillary tubes, and are then either centrifuged to produce plasma or analysed directly as whole blood. Direct analysis requires an

accurate blood sample volume and precise, low-temperature storage conditions, and may occasionally result in clotting within the micro-tube (although using EDTA-coated tubes avoids clotting). Preparation of plasma samples also requires an accurate volume and restrictive storage conditions, with additional handling steps to remove the red blood cells.

An alternative micro-sampling technique, dried blood spotting (DBS), removes the requirements for accurate blood sample volume and low-temperature storage. It is a widely accepted blood sampling technique for individual testing and population screening. A DBS card usually consists of four circular regions (each 10 mm in diameter), within which blood volumes of around 10 – 30 µL are spotted (Fig. 5.2). The cards are dried at room temperature for two hours before being sealed in an airtight bag with desiccant sachets and stored at room temperature until required. A punched core of 3 – 6 mm diameter from each spot, equating to a blood volume of approximately 3 – 12 µL (187), is then placed in an extraction solution prior to spectral analysis.

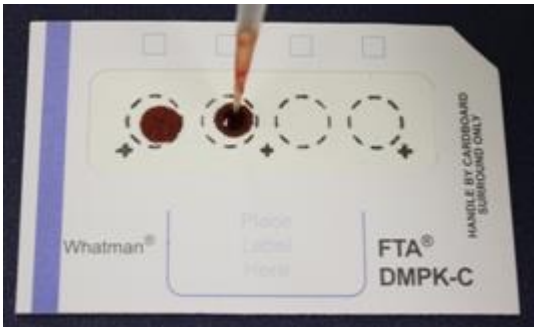

Figure 5.2: Transferring blood to DBS card (image from Whatman web site (188))

The DBS technique has been actively used since Robert Guthrie's pioneering work in the 1960s for screening new-born babies for metabolic anomalies such as phenylketonuria and congenital hypothyroidism (189). More recently, it has also been used for early detection of a range of diseases including cystic fibrosis (190) and the hepatitis C virus (191). DBS is considered a stable, inexpensive method of collecting and storing DNA for epidemiological studies (192).

Advantages of DBS over conventional blood sampling techniques include ease of collection and economical storage (samples are stored at room temperature, rather than in a freezer). As the samples remain stable at room temperature, they can be collected at remote locations and posted to a central laboratory for analysis. DBS also requires smaller collection volumes, which increases the number of potential data points per experimental animal and facilitates the reduction in animal numbers required for preclinical studies (193). Serial sampling from a small number of animals also has the advantage of reducing the influence of inter-animal variability.

5.1.3 Measuring Gd content

Inductively-coupled plasma mass spectrometry (ICP-MS) is one of a range of spectrometry techniques available to analyse blood samples. It is a highly sensitive element-detection technique, commonly used by the pharmaceutical industry for identification of inorganic impurities at levels as low as parts per trillion (194) and with many applications in a wide variety of industries including food quality assessment and environmental monitoring (195). ICP-MS has been utilised as a means of monitoring environmental Gd levels and measuring tissue Gd accumulation, resulting directly from the use of MRI contrast agents (196). It has also been adopted as the gold standard for measurement of Gd content in several in vitro studies characterising gadofosveset (for example, (68, 75)).

A schematic diagram of the ICP-MS process is shown in Fig. 5.3, and an illustration of the key components is given in Fig. 5.4. The process begins with a liquid sample, pumped into the mass spectrometer and nebulised into an aerosol by a stream of argon gas within the spray chamber. Large drops are drained by gravitational force, with only small drops (up to a diameter of 10 μm) continuing to the sample injector. Utilising pressure gradients, the aerosol is fed into a plasma torch, where argon gas is converted to a plasma discharge and heated to a maximum of 7000 K by a radiofrequency (RF) coil. As the liquid aerosol travels through different temperature zones within the plasma, it dries

and becomes a solid, and is vaporised into molecular and then atomic form. When the sample reaches the extremely hot centre of the plasma, there is sufficient energy in the plasma electrons to knock an electron from the outer orbit of the sample atoms. The resulting positively charged ions are driven into the analyser through a sample and skimmer cone, which are maintained within a vacuum, and then focused and steered by ion lenses through to a quadrupole mass separation device. This device consists of two pairs of rods, one pair with a direct current (DC) field and the other pair with an RF field. Selecting the appropriate RF–DC voltage enables the operator to tune the device to allow only ions of a specific mass-to-charge ratio to pass down the middle of the rods, with other ions falling through gaps between the rods and being ejected. The selected ions finally reach the ion detector, where they are counted and a mass spectrum is created.

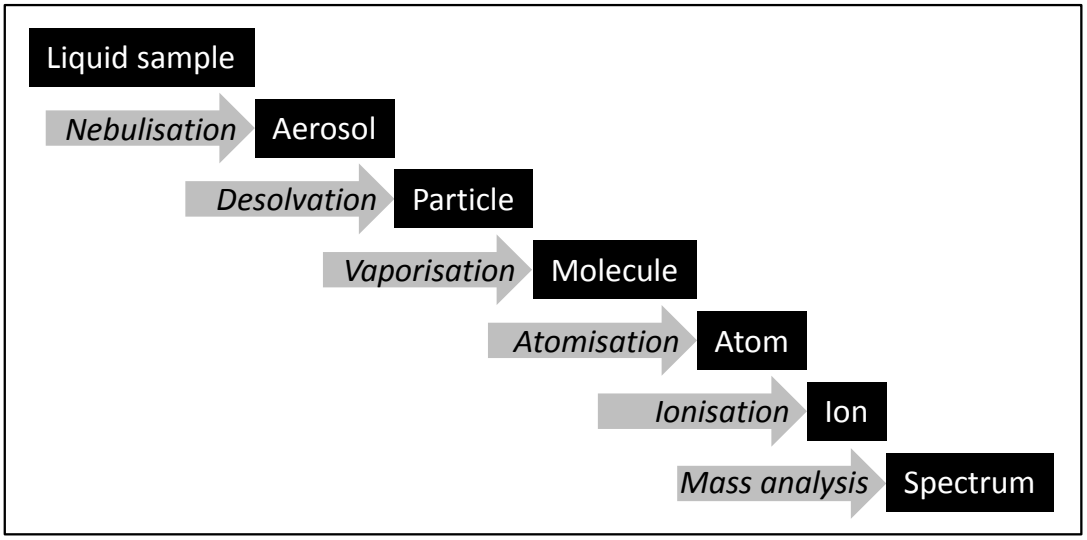

Figure 5.3: Schematic diagram showing the steps in the process of ICP-MS

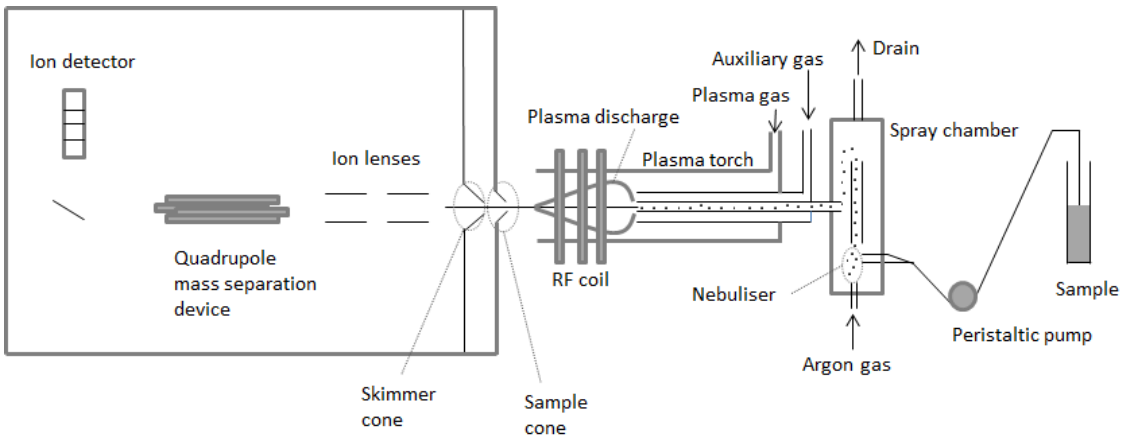

Figure 5.4: Key components in an inductively-coupled plasma mass spectrometer (not to scale); sample movement in diagram is from right to left

To prevent signal saturation and accumulation of particulate matter, it is important that samples are diluted and large molecules broken down prior to being pumped into the spectrometer. Whole blood samples containing Gd-based MRI contrast agents have previously been analysed with ICP-MS, using 20% v/v nitric acid as the digestion agent. An acid content at this level is very effective at releasing Gd, and nitric acid is noted to be the best acid medium for ICP-MS (197). Concentrations should be above the detection limit, i.e. sufficiently high to be distinguishable from system noise, but should not be so high as to saturate the ion counter. A detection limit has previously been measured for Gd at 1 ng mL^{-1} (198).

Pilot studies have been carried out to assess the validity of combining DBS with ICP-MS to screen for heavy metal environmental pollutants such as lead, mercury and cadmium in new-born babies (199). The study concluded that this was a useful screening method, and also found that samples remained stable when stored over an 8.5 month period. Another study on levels of lead in the blood was carried out using laser ablation to create particulates directly from DBS cores, followed by ICP-MS analysis (200).

A literature search (May 2013) found no previous studies using DBS to measure Gd concentration. Although a similar technique to ICP-MS, inductively-coupled plasma atomic emission spectroscopy (ICP-AES), has

previously been used to measure blood concentrations of gadofosveset in rabbits following bolus injection (78), the blood sampling volumes used would be inappropriate for smaller animals. An aforementioned study in rats (182) used ICP-MS to measure the Gd content of blood samples following injection of gadopentetate, although blood sampling volumes are not stated. To successfully measure the gadofosveset time course in a mouse model, the novel combination of micro-sampling mouse blood using DBS followed by Gd measurement using ICP-MS is suggested.

5.2 AIMS

The aim of this study was to combine the established techniques of DBS and ICP-MS to develop a method for accurate measurement of the Gd content of blood samples at a temporal rate suitable for characterising a VIF in small mammals. This would be achieved in three steps:

1. Demonstrate in a proof-of-concept study that Gd levels could be accurately measured using ICP-MS with gadofosveset-spiked mouse blood samples on DBS cards. By plotting Gd counts against known Gd concentrations, calibration curves could then be created to enable conversion of Gd counts back to Gd concentrations. Applying a linear fit to these plotted data points enables assessment of the accuracy of the calibration method.

2. The method developed in vitro could then be applied in a benchtop experiment by injecting several mice with a standard dose of gadofosveset, collecting blood samples on DBS cards at specific, interleaved time points and analysing these samples for Gd using ICP-MS. These Gd counts would be converted to Gd concentrations using the calibration curves generated from the in vitro data, and Gd concentrations could be plotted as a VIF.

3. Using the same injection protocol as the benchtop experiment, MR images of mice would be acquired at corresponding time points. The measured variation

in signal intensity within a major vessel as the injected bolus makes its first pass through the animal could then be compared with the previously acquired VIF.

There are two novel aspects to this study: firstly, the use of DBS in conjunction with ICP-MS to facilitate accurate Gd measurement in low-volume blood samples; and secondly, the application of this combined technique to determine a VIF for gadofosveset in a murine model. As gadofosveset was withdrawn from the European market before the animal studies commenced, only the in vitro method development stage could be completed. Although it would have been feasible to use an alternative Gd-based contrast agent to assess the method in vivo, the primary research purpose of this project is characterisation of gadofosveset. As gadofosveset has unique properties not found in other clinically approved agents, the option to complete the in vivo assessment with another contrast agent was rejected on ethical grounds.

5.3 METHOD

To separately validate the accuracy of Gd measurement using ICP-MS and the method for releasing Gd from DBS card, three sets of ICP-MS calibration curves were created. The first set of curves used gadofosveset in mouse plasma, directly prepared in solution form (without being transferred to DBS cards), to verify that Gd content could be accurately measured with the chosen diluent and dilution levels. The second set of curves used solutions of gadofosveset in phosphate-buffered saline (PBS), transferred to DBS cards and prepared for ICP-MS, to confirm that unbound gadofosveset would be released from the card and Gd content could be accurately measured. The third set of curves used mouse blood samples spiked with gadofosveset, transferred to DBS cards and prepared for ICP-MS, to confirm that bound gadofosveset would be released from the card and Gd content could be accurately measured at low blood volumes. This final set of curves would have

been used to convert Gd counts in ex vivo blood samples to Gd concentrations if an animal benchtop experiment had been carried out.

5.3.1 Sample preparation

Gadofosveset (Vasovist) at an initial concentration of 250 mM (244 mg mL^{-1}) was added to lyophilised mouse plasma (reconstituted with deionised water) to give a concentration of 5.0 mM. This was serially diluted to give additional concentrations of gadovosveset in mouse plasma of 2.0, 1.0, 0.5 and 0.25 mM (a range of 0.24 – 4.88 mg mL^{-1}), along with a sample of mouse plasma without gadofosveset. 10 µL of each solution was then diluted by a factor of 10^4 in nitric acid (20% v/v) to give final sample concentrations in the range 24 – 488 ng mL^{-1}.

To generate the DBS samples, gadofosveset was diluted in phosphate-buffered saline (PBS, as used in Chapter 4 experiments) to a concentration of 15 mM, followed by serial dilutions in PBS to give concentrations of 6, 3, 1.5 and 0.75 mM. 50 µL of each of these solutions was added to 100 µL mouse blood (CD-1 mouse type) to give final concentrations of 5, 2, 1, 0.5 and 0.25 mM (0.24 – 4.88 mg mL^{-1}). An equivalent set of concentrations for gadofosveset in PBS (without blood) was also created. EDTA-coated 20 µL capillary tubes (Starstedt AG, Germany) were used to draw samples from each gadofosveset–blood and gadofosveset–PBS solution and spot onto Whatman FTA DMPK-C cards (GE Healthcare). An additional card containing spots of plain mouse blood was also created. The cards were stacked horizontally in a drying rack for 2 h at room temperature (approximately 22°C, with a measured relative humidity of 36%). Each card was then sealed in an airtight bag containing two desiccant sachets and stored at room temperature until use.

To prepare the DBS samples for ICP-MS analysis, a single 3 mm diameter punched core from the centre of each spot was placed into a plastic Eppendorff tube (0.5 mL) and 200 µL nitric acid (20% v/v) added. The tubes were vortexed for 20 s, left to stand for 40 min and then centrifuged at 5000 rpm for 5 min.

200 µL of supernate was extracted to a plastic Corning tube (15 mL), 1980 µL of nitric acid (20% v/v) added and the combined solution vortexed for 5 s prior to ICP-MS. Assuming a blood volume in the core of approximately 3 µL, this overall process amounts to a dilution from the original blood concentration levels of approximately 1 in 6,800, giving final concentrations in the range 37 –732 ng mL^{-1}. Coring took place four days after samples were spotted on the DBS cards.

5.3.2 ICP-MS

ICP-MS was carried out on an Elan DRC-e spectrometer (Perkin Elmer, Waltham, MA) with quadrupole mass analyzer, peristaltic pump and pneumatic concentric nebulizer, using argon gas. Counts were determined for the four most commonly occurring isotopes of Gd (mass/charge values of 156, 157, 158 and 160), which account for around 83% of the stable element (201). A sample flush of 35 s at 24 rpm was followed by a read delay of 35 s at 20 rpm and a wash with 0.1% (v/v) nitric acid of 60 s at 30 rpm.

5.4 RESULTS

Figures 5.5, 5.6, and 5.7 show the calibration curves for gadofosveset in mouse plasma (solution form), gadofosveset in PBS (DBS core extraction) and gadofosveset in mouse blood (DBS core extraction), respectively. All three sets of plots show a high degree of linearity between gadofosveset concentration and Gd count, with R^2 values exceeding 0.998 for all plots.

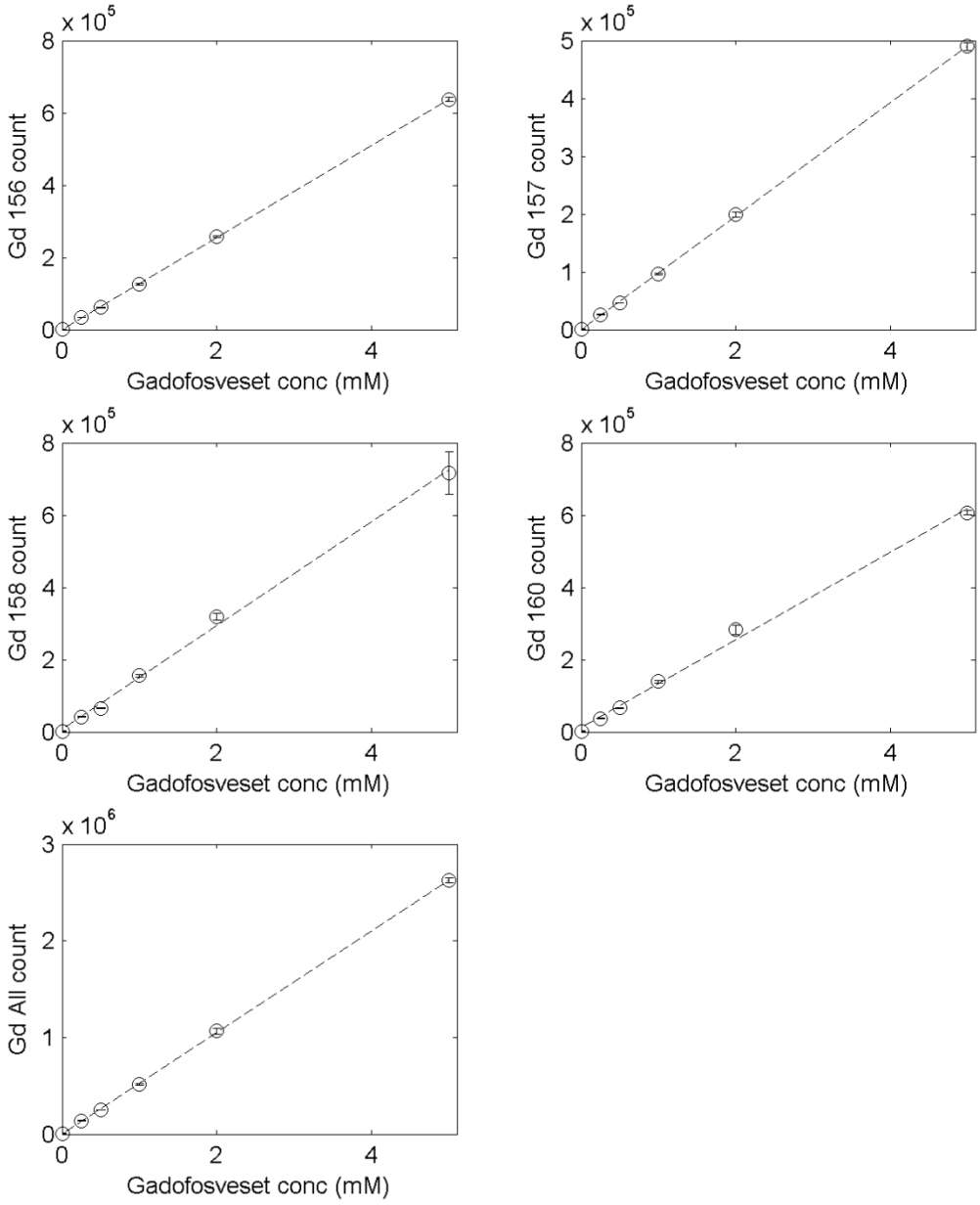

Figure 5.5: Calibration curves showing Gd counts (mass/charge values of 156, 157, 158 and 160, and the total count for all four) for a range of gadofosveset concentrations in mouse plasma, using samples taken from in vitro solutions; error bars indicate standard deviation of four measurements. R^2 values for all plots ≥ 0.999

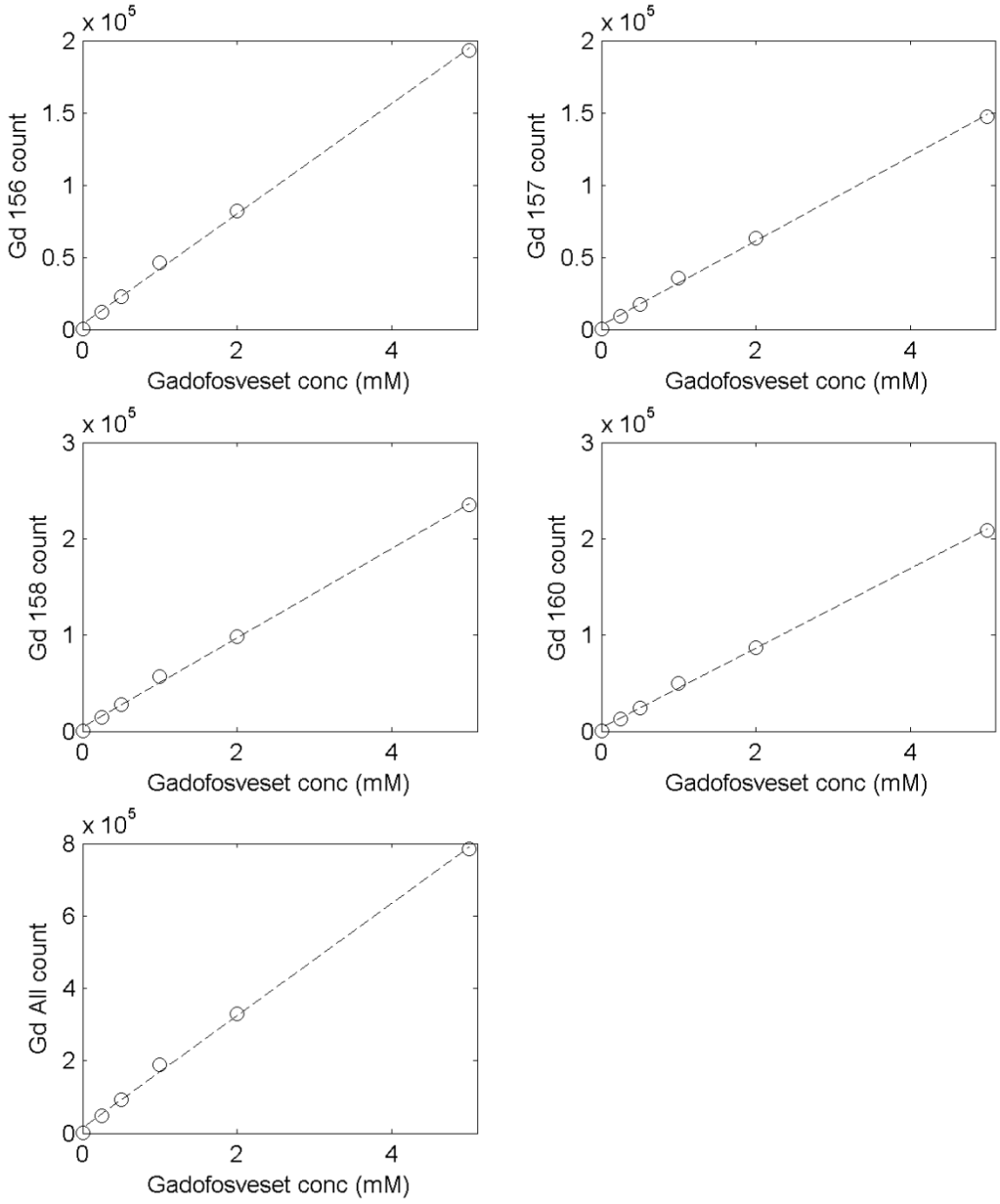

Figure 5.6: Calibration curves showing Gd counts (mass/charge values of 156, 157, 158 and 160, and the total count for all four) for a range of gadofosveset concentrations in PBS, using DBS collection method. R^2 values for all plots ≥ 0.998

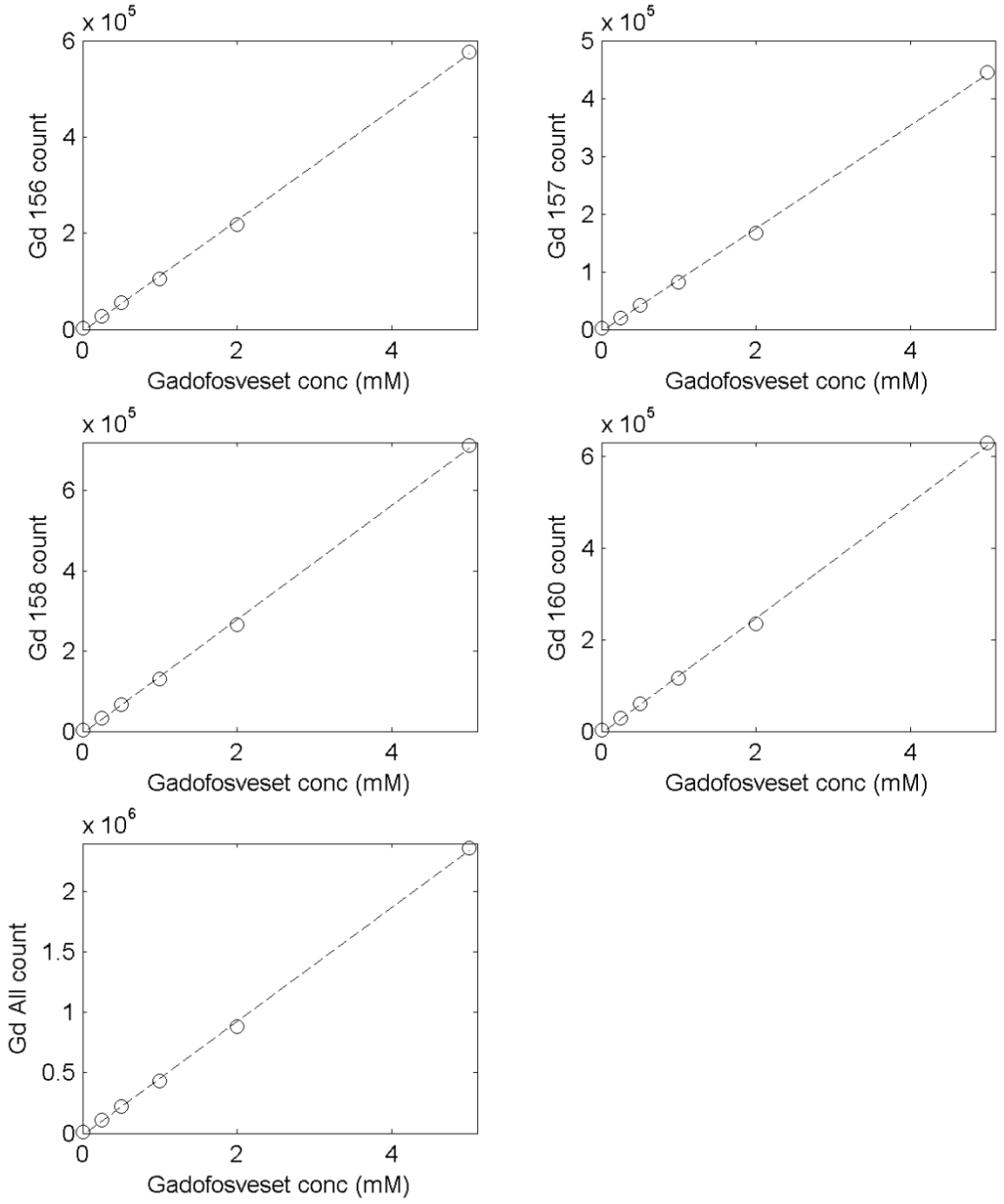

Figure 5.7: Calibration curves showing Gd counts (mass/charge values of 156, 157, 158 and 160, and the total count for all four) for a range of gadofosveset concentrations in mouse blood, using DBS collection method. R^2 values for all plots ≥ 0.999

5.5 DISCUSSION

5.5.1 Method validation

The high degree of linearity between gadofosveset concentration and Gd count for the in vitro solutions of gadofosveset in mouse plasma (Fig. 5.5), diluted by a factor of 10^4, confirms that ICP-MS is a very sensitive method for measuring Gd concentration. These results also show that the extraction solution and dilution methodology are valid preparation for ICP-MS measurement. The additional methodology for releasing samples from DBS cores and creating liquid solutions is validated initially for gadofosveset in PBS (Fig. 5.6), where no gadofosveset binding will occur, and subsequently for gadofosveset in mouse blood (Fig. 5.7), where the majority of the gadofosveset will be bound to albumin. The linearity of both sets of plots suggests that this method adequately releases Gd from the DBS core, regardless of albumin-binding state. The consistency between samples prepared in solution form and those prepared from DBS cores demonstrates that the preparation method used to generate solutions from blood samples on DBS cards was appropriate for ICP-MS analysis. Overall, the results demonstrate the viability of using blood samples acquired and stored on DBS cards in conjunction with ICP-MS to measure Gd levels. This suggests the method may be a viable, accurate means of monitoring Gd concentrations in the blood (ex vivo) following contrast agent administration.

ICP-MS has previously been used to measure Gd from MRI contrast agents in tissue and environmental samples (196). The technique was found to be highly sensitive to Gd in rat tissue, with a detection limit of approximately 6×10^{-6} µmol of Gd per g of tissue (197). Concern around the build-up of Gd in tissue has increased with the establishment of a link between Gd contrast agent administration and nephrogenic systemic fibrosis (NSF) (49); a study using ICP-MS to measure Gd in hair, fingernail and blood samples of an NSF patient previously exposed to Gd contrast agents (202) found substantially higher Gd levels than in healthy control subjects. ICP-MS has also been used

to study the elimination time course of Gd from the skin in rats in the days following administration of a range of contrast agents (203, 204). Recently, the VIF in a rat model was captured using ICP-MS by blood sampling after injection of gadopentetate, and was reproduced with an MRI sequence (182). Tissue distribution for gadopentetate has also been assessed in rats using laser ablation ICP-MS on histological samples (205). ICP-MS has been used to assess levels of Gd passing through hospital sewage systems into rivers following excretion by patients injected with Gd-based contrast agents during MRI procedures (198, 206). The potential to differentiate specific Gd chelates has been demonstrated using ICP-MS in conjunction with size-exclusion chromatography (207) and hydrophilic interaction chromatography (208). ICP-MS was used in a murine study to correlate histological tissue Gd concentration in cardiac slices with change in relaxation rate (ΔR_1) (209). A study combining MRI, ICP-MS and histology assessed the clearance rate of a macromolecular contrast agent (albumin-Gd-DTPA) in mice following avadin chase (210), although the sampling intervals were insufficient to capture the first bolus pass.

Several studies characterising gadofosveset in vitro (for example, (68, 75)) have used ICP-MS Gd measurements following solution filtration to determine the binding fraction for physiologically relevant gadofosveset concentrations across selected animal species. A study in rabbits (78) used ICP-AES to analyse acquired blood samples at multiple time points immediately following injection of gadofosveset. A total of 44 samples, each of volume 300 µL, were acquired for a single animal, amounting to a total blood sample volume of approximately 13 mL (around 8% of the total circulating blood volume of a 2.5 kg rabbit); these blood sample volumes would be unsuitable for a smaller animal.

Blood sampling using DBS cards requires smaller blood volumes and has practical advantages over other micro-sampling techniques (including ease of sample handling, room-temperature transportation and storage of samples, and the ability to store samples for several months without degradation). DBS may be considered particularly useful for collection of blood samples in small

animals, where low circulating blood volumes prohibit multiple sampling at conventional volumes. In line with the commitment to the welfare of animals used in scientific experimentation (the ‘3Rs’ approach: replacement, reduction, refinement, (211)), smaller individual blood sampling volumes facilitate the use of fewer animals. In addition, acquiring multiple samples from the same animal reduces the experimental risk of inter-animal variability.

5.5.2 Proposed in vivo validation methodology

Due to its withdrawal from the European market in 2011 (see Chapter 3, section 3.1.1), it was not possible to validate the proposed method in vivo using gadofosveset. As the primary research aim was characterisation of this contrast agent, it was not considered ethical to carry out in vivo animal experiments using another contrast agent. A suggested protocol for in vivo validation in a murine model would involve two parallel experiments, subject to necessary ethical approval and Home Office personal and project licence authorisation at a designated establishment, in accordance with the Animals (Scientific Procedures) Act 1986. In the first experiment, anaesthetised mice would be injected with gadofosveset at the clinical dose (0.03 mmol kg^{-1}), and blood would be extracted to DBS cards at specific time points following injection. Using the same injection protocol, the second experiment would involve acquiring MR images at time points corresponding with those used for blood sampling.

Assuming the animal is anaesthetised with isoflurane or an isoflurane/oxygen mix, and gadofosveset is administered using a cannula in one of the tail veins, the following blood extraction methodology is suggested. The first blood sample is taken by needle pricking the non-cannulated tail vein, placing an EDTA-coated 20 µL capillary tube on the site and allowing the blood to be drawn up using capillary action. Although injection and sampling both use veins, this should not be an issue due to the rapid rate at which blood circulates in small mammals. Subsequent blood samples are taken from the same site; if necessary, the flow of blood is stemmed between samples by applying

pressure to the sampling site. The capillary tubes are placed temporarily into labelled Eppendorf tubes until all samples are collected for the animal. Taking six blood samples per animal, the total captured blood volume per animal is no more than 120 µL (approximately 7% of the total blood volume of a 20 g mouse). The actual volume drawn into each tube by capillary action is likely to be around 10 – 12 µL (60 – 72 µL total for six samples), plus a small amount of wastage between samples. When all samples are collected for one animal, the full volume of blood from each capillary tube is transferred to a DBS card. The process is repeated for additional animals, using a range of time points, to build up a full picture of the variation of contrast agent concentration with time. Although laboratory mice are bred to give a similar physiological response, the potential influence of inter-animal variability may be assessed by choosing a combination of coincident and interleaved time points. DBS cards are allowed to dry for two hours and then stored in airtight plastic bags with desiccant sachets. The DBS core extraction method described in section 5.3 is then used to prepare each sample for ICP-MS.

A log spacing of blood sample acquisition times is suggested, to provide a greater number of data points soon after injection, where concentrations are changing more rapidly. Fig. 5.8 gives a suggested distribution of sample times, with 8 animals and 6 samples per animal. The total number of animals required and the timing of blood sample acquisitions may be confirmed following a small (n = 2) pilot study.

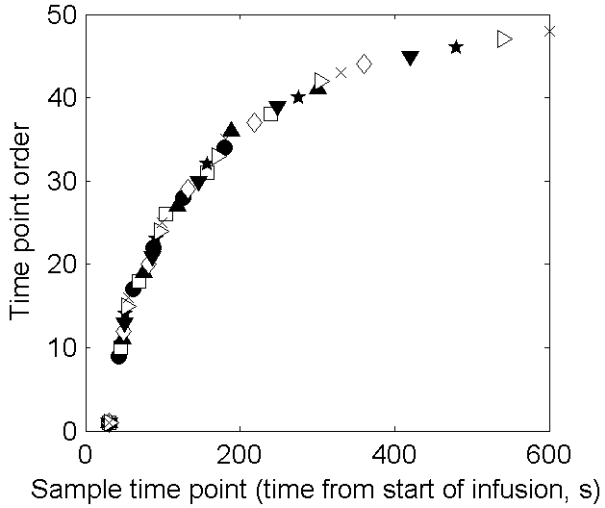

Figure 5.8: Proposed blood sampling times (6 time points for 8 animals), with the first time point immediately after a 30 s infusion; each symbol represents a different animal, with the same initial time point used for each animal

The MR imaging sequence should use cardiac and respiratory gating where possible, and images should include a plane incorporating the aorta, vena cava or ventricles, to enable accurate blood T_1 measurement (175). As deoxygenated haemoglobin is slightly paramagnetic, and the degree of deoxygenation is 1 – 2% in arteries and 30 – 40% in veins (212), differences in the vascular input function would be observed depending on whether the region of interest incorporates venous or arterial blood.

5.5.3 Potential limitations

A potential limitation of the DBS method is the ability to acquire blood samples rapidly enough to capture the first-pass peak contrast agent concentration. There is also a requirement to generate consistent blood spot cores. The volume of blood in a DBS core has been shown to vary with haematocrit levels (213), overall volume of the blood spot (187) and with the relative positioning of the core within the spot (214).

For ICP-MS, it is essential at very low Gd concentrations that measurements exceed the limit of detection, the level above which a signal may be

distinguished from background noise, and the limit of quantification, the level above which accurate measurement is possible. These levels may be determined from the standard deviation of ion counts of solutions prepared from blank cores. Although Gd concentrations in this study were well above the expected detection and quantification limits, it may be of value in a repeated experiment if Gd ion counts of blank solutions were recorded. False-positive counts are possible when oxides matching the mass-to-charge ratio of the isotope of interest are created during the ionisation process (from combinations of elements within the sample solution and input gas), or as a result of interference from other spectra. For example, isotopes of dysprosium occur naturally (although rarely) at atomic masses of 156, 158 and 160.

CHAPTER 6: OVERCOMING THE LOW RELAXIVITY OF GADOFOSVESET AT HIGH FIELD WITH SPIN LOCKING

6.1 BACKGROUND

The albumin-binding nature of gadofosveset, discussed in Chapter 3, leads to reduced extravasation and excretion rates and potentially favourable relaxation properties. Results from Chapter 4 (Table 4.2) confirm that the longitudinal relaxivity of the bound gadofosveset molecule (r_{1bound}) is significantly higher than the relaxivity of the free molecule (r_{1free}) at low fields. However, r_{1bound} decreases rapidly with field strength and the two relaxivities are comparable at 4.7 T (Chapter 4, Fig. 4.4). Where these relaxivities converge, observed relaxivity (r_{1obs}) is similar to that for a non-binding contrast agent and the high-relaxivity advantage of gadofosveset is lost. Regardless of the reduction in relaxivity, the unique kinetic properties of gadofosveset resulting from its binding to albumin are displayed at all field strengths. An alternative contrast mechanism that provides high gadofosveset relaxivity at high fields may be required to fully exploit these properties.

Spin locking (SL), first described as an imaging technique in 1985 (15) but investigated in NMR prior to this (215), involves the application of a 90° excitation pulse followed by a radio frequency (RF) pulse (phase shifted by 90° to the excitation pulse), applied for a duration of time (spin-lock time, TSL), which locks the spins in the rotating frame of reference (Fig. 6.1).

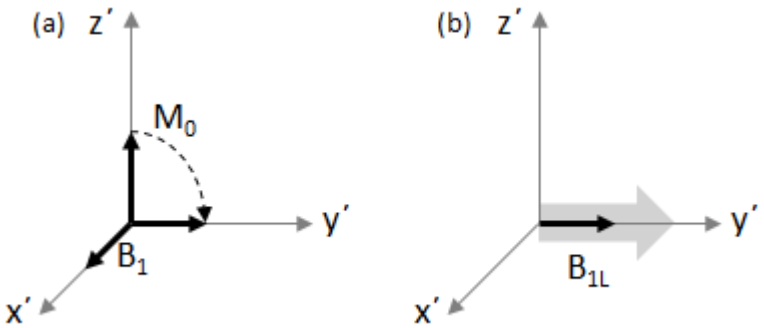

Figure 6.1: (a) Magnetisation M_0 is tilted 90° around x' axis of rotating frame of reference x'y'z' by excitatory pulse B_1; (b) spin locking pulse B_{1L} is applied along y' axis

Relaxation of the magnetisation in the presence of this SL field (B_{1L}) is characterised by the time constant $T_{1\rho}$, with free induction decay (FID) only occurring once the spin-locking pulse has been switched off (Fig. 6.2a). The SL pulse may be followed by a 90° pulse (phase shifted by 180° to the original excitation pulse) and an imaging sequence (Fig. 6.2b) (216), or a 180° pulse and readout (Fig. 6.2c) (15).

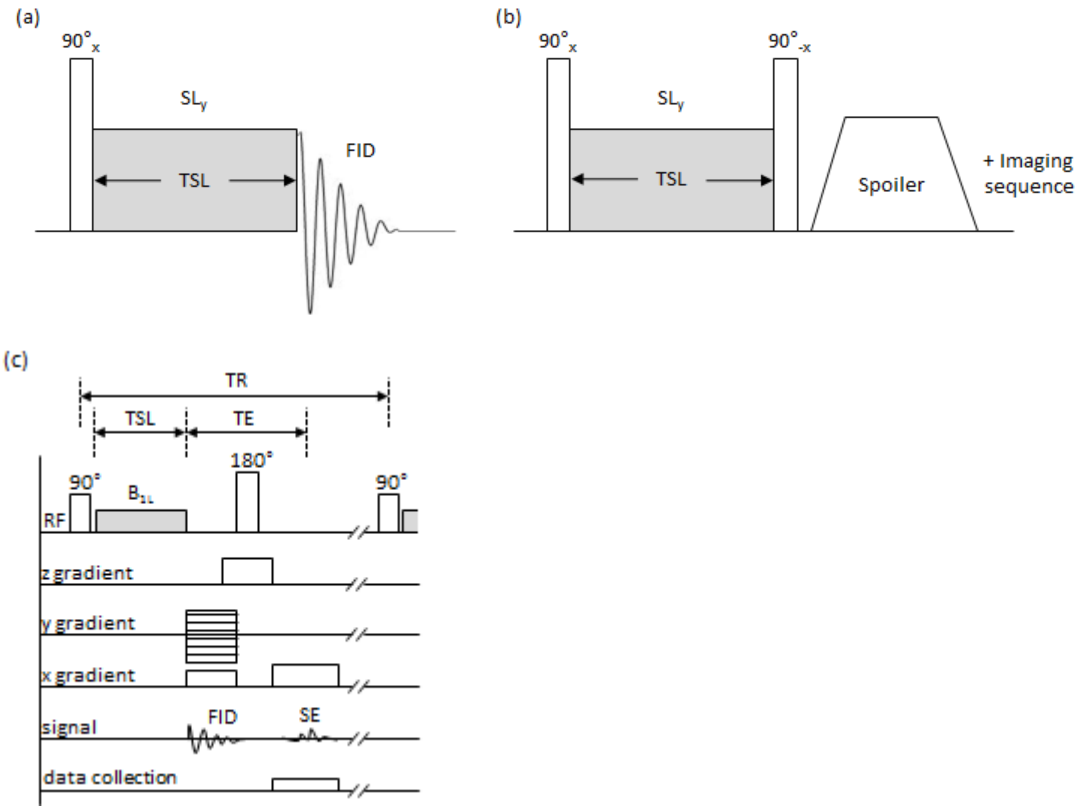

Figure 6.2: (a) Free induction decay follows the cessation of the spin-locking pulse; (b) an example of how an imaging sequence may be applied following spin locking (216); (c) a pulse sequence diagram showing spin-locking pulse followed by a selective 180° pulse and readout (15)

$T_{1\rho}$ is influenced by the strength of the SL field, which is commonly in the μT (low kHz) range, rather than the main magnetic field (B_0). As a result, the image contrast generated by SL is equivalent to image contrast obtained at low magnetic fields, with the advantage that a high signal-to-noise ratio, a characteristic of high B_0, may be maintained (217). It should be noted that the SL RF pulse may contribute significantly to patient specific absorption rate (SAR), particularly at high B_0 as SAR is proportional to the product of B_0^2, B_{1L}^2 and the ratio of TSL to TR (within a practical range for TR) (Eq. 6.1) (15).

$$SAR \propto B_0^2 . B_{1L}^2 . \frac{TSL}{TR} \qquad [6.1]$$

The interaction times associated with SL at very low field strengths give this technique an increased sensitivity to proteins and other macromolecules (218). This correlation between signal intensity and tissue protein has been utilised as a potential biomarker for response to tumour therapy, including treatment designed to reduce protein synthesis (219) and gene therapy resulting in reduced protein content due to cell death (220). The clinical potential of SL has also been highlighted in a study of injured myocardium (221) and in the assessment of brain plaque composition in early-onset Alzheimer's disease (222).

Small-molecule Gd-based contrast agents have been used in combination with SL to provide improved myocardium–blood contrast (221, 223) and in the assessment of articular cartilage (224). SL after injection of gadopentetate has also been shown to improve tumour contrast in glioma patients (218). A literature search for published studies assessing the effect of gadofosveset on $T_{1\rho}$ (July 2013) found only the paper on which this thesis chapter is based (1).

Tissue $T_{1\rho}$ values fall between T_1 and T_2, with $T_{1\rho} \rightarrow T_2$ as $B_{1L} \rightarrow 0$ (225). Conventionally $B_{1L} << B_0$, therefore $T_{1\rho}$ may be expected to be close to T_2. The transverse relaxivity of bound gadofosveset is known to remain high at all relevant field strengths (89), and T_2 values are known to be sensitive to tissue macromolecules (226). A secondary consideration in this study is whether the potential benefits of $T_{1\rho}$ contrast could also be achieved using T_2 contrast, without the complication of adding a spin-locking pulse and without the requirement to consider additional SAR factors.

6.2 AIMS AND OBJECTIVES

The primary aim of this study was to test the hypothesis that by combining the macromolecular sensitivity of SL with the albumin-binding affinity of gadofosveset a large contrast shift may be achieved at field strengths where the T_1 effects of gadofosveset are very similar to those of conventional Gd-

based agents. In addition, the influence of species' differences in binding on spin-lock relaxation was investigated, along with the influence of spin-lock field strength on image quality. A further aspect of the study was to investigate whether the potential benefits of $T_{1\rho}$ contrast could also be achieved using T_2 contrast. The following objectives were set:

1. Measure spin-lock relaxation rates ($R_{1\rho}$, $1/T_{1\rho}$) for in vitro gadofosveset solutions, in the presence and absence of serum albumin, at a B_0 value of 4.7 T and B_{1L} values of 5, 25 and 90 μT.

2. Repeat $R_{1\rho}$ measurements for solutions of the non-binding contrast agent gadopentetate dimeglumine, to act as a control and to separate the influence of the macromolecular solution from that of Gd.

3. Repeat $R_{1\rho}$ measurements for gadofosveset in mouse plasma, to identify differences between albumin species. This may be informative for translating the outcome of pre-clinical studies utilising gadofosveset with spin locking.

4. Compare gadofosveset $R_{1\rho}$ measurements with equivalent R_1 measurements presented in Chapter 4.

5. Measure R_2 for gadofosveset in the presence and absence of albumin, at low (0.47 T) and high (4.7 T) B_0, to determine whether transverse relaxation rates display a similar trend to spin-lock relaxation rates.

6.3 METHOD

6.3.1 In vitro solutions

In vitro solutions of gadofosveset in phosphate-buffered saline (PBS), with and without bovine serum albumin (BSA), were prepared as described in Chapter 4 (section 4.4.1). An equivalent set of solutions of the non-binding contrast agent gadopentetate dimeglumine (Magnevist, Bayer Healthcare Pharmaceuticals,

Germany) in BSA (4.5% w/v) was also created, along with samples of gadofosveset in mouse plasma. Prior to scanning at 4.7 T, all solutions were heated to 37°C in a water bath; this temperature was maintained during scanning with warm air flow and verified with a fibre optic temperature probe in an adjacent water tube. At 0.47 T, samples were heated to 37°C and the temperature monitored with an integral heating system.

6.3.2 Data acquisition: $R_{1\rho}$

Tubes were placed vertically in a cylindrical cradle of diameter 60 mm and inserted into a 63 mm quad coil in a horizontal bore 4.7 T magnet with Bruker console running ParaVision 5.1 software (Bruker BioSpin MRI GmbH, Ettlingen, Germany). Spin locking was achieved using a B_{1L} pulse value of 90 μT (3.8 kHz), applied for 14 durations (TSL): 0.01, 0.05, 0.1, 0.5, 1.0, 5.0, 12.5, 25.0, 50.0, 75.0, 100.0, 125.0, 150.0 and 200.0 ms. This was followed by a rapid acquisition with relaxation enhancement (RARE) readout, using a coronal (horizontal) slice of thickness 1 mm. The acquisition parameters were: TR = 2000 ms; TE = 10 ms; field of view = 60 x 60 mm; matrix size = 128 x 128 pixels; RARE factor = 2; averages = 1; centric encoding. No spoiler gradients were applied between repetitions. In addition to the B_{1L} pulse value of 90 μT, images were also acquired using spin-lock pulse strengths of 5 and 25 μT (0.2 and 1.1 kHz, respectively).

6.3.3 Data acquisition: R_1 and R_2

R_1 measurements at 0.47 T and 4.7 T were made using the instrumentation and techniques described in Chapter 4 (sections 4.4.2 and 4.4.4, respectively).

R_2 values at 4.7 T were measured using a RARE saturation recovery imaging sequence without the preparatory SL pulse. Tubes were placed horizontally in the cradle and coil described previously and a single axial (vertical) slice used. TE ranged between 11 and 66 ms; TR (BSA) = 2000 ms; TR (PBS) = 8000 ms;

field of view = 60 x 60 mm; matrix size = 256 x 256 pixels; RARE factor = 2; averages = 1; centric encoding; slice thickness = 1 mm.

R_2 measurements at 0.47 T were made on a 20 MHz Maran NMR spectrometer (Oxford Instruments, Abingdon, UK), using a standard Carr–Purcell–Meiboom–Gill (CPMG) sequence, with 1000 TE values.

6.3.4 Calculating relaxation rates

R_1 relaxation rates were calculated using the methods described in Chapter 4 (section 4.4.6). For $R_{1\rho}$ and R_2 at 4.7 T, circular regions of interest (ROI) were drawn on the images within each tube and the mean signal intensity (SI) of each ROI measured using ImageJ software (v1.42q, Rasband, W.S., ImageJ, U. S. National Institutes of Health, Bethesda, Maryland, USA, http://imagej.nih.gov/ij/, 1997-2011). SI values were adjusted for noise bias using a simple Rician correction (227), based on mean standard deviations of four background regions in each image. Fitting of $R_{1\rho}$ followed a nonlinear three-parameter fit suggested by Engelhart & Johnson (228) using MATLAB (v7.9, MathWorks, Natick, Ma) to determine the fully recovered SI (S_0) values and relaxation rates ($R_{1\rho}$), along with a parameter (*a*) to account for residual magnetisation in the y axis due to the SL pulse (Eq. 6.2). R_2 ($1/T_2$) was determined using a two-parameter nonlinear fit (Eq. 6.3).

$$SI = S_0 . e^{-TSL.R_{1\rho}} + a \qquad [6.2]$$

$$SI = S_0 . e^{-TE.R_2} \qquad [6.3]$$

Confidence intervals (CI) were calculated at the 95% level. Datasets were compared for statistical significance at α = 0.05 using a paired t-test in SPSS (v 16.0, IBM SPSS, NY).

6.4 RESULTS

Results are shown in Figs. 6.3 – 6.8, with error bars representing 95% confidence intervals. R_1 results for gadofosveset have previously been presented in a different format (Chapter 4, Fig. 4.1); in Fig. 6.3 PBS and BSA results are presented together to enable direct comparison. The overall R_1 values for solutions of gadofosveset in BSA and in PBS were significantly different at B_0 = 0.47 T (P = 0.003, Fig. 6.3a) but not different at 4.7 T (P = 0.757, Fig. 6.3b), confirming the lack of influence of albumin binding on gadofosveset longitudinal relaxivity at high field strength.

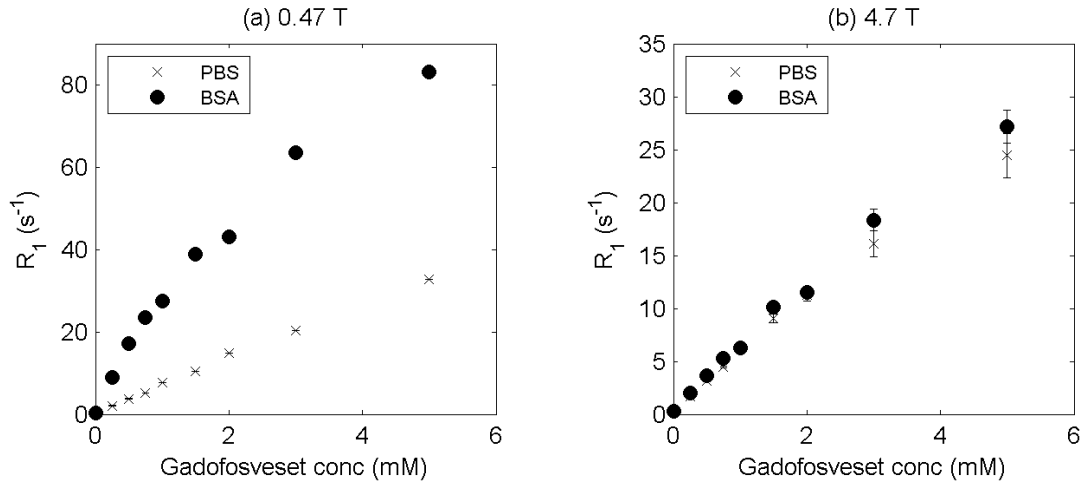

Figure 6.3: R_1 values for gadofosveset in BSA (circles) and in PBS (crosses) at (a) 0.47 T and (b) 4.7 T. Error bars in (a) are smaller than data points

The $R_{1\rho}$ relaxation rates for solutions of gadofosveset in BSA at 4.7 T were significantly higher than for gadofosveset in PBS (P = 0.001, Fig. 6.4). PBS $R_{1\rho}$ values (Fig. 6.4) were similar to R_1 values at 4.7 T (BSA and PBS solutions, Fig. 6.3b). The $R_{1\rho}$ values for solutions of gadopentetate in BSA were similar to those for solutions of gadofosveset in PBS (P = 0.380, Fig. 6.4).

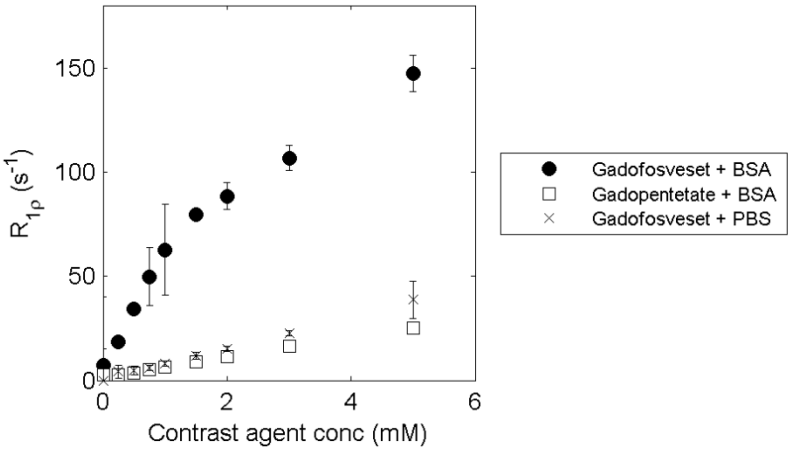

Figure 6.4: $R_{1\rho}$ values for gadofosveset in BSA (circles) and in PBS (crosses) and gadopentetate in BSA (squares) at B_0 = 4.7 T, B_{1L} = 90 μT

R_2 values for solutions of gadofosveset in BSA and in PBS at 0.47 T displayed a similar pattern to R_1 values at this field strength, with significantly higher R_2 values for the BSA solutions (P = 0.032, Fig. 6.5a). R_2 values for equivalent solutions at 4.7 T were comparable to the R_2 values at 0.47 T and the $R_{1\rho}$ values at 4.7 T, with the BSA R_2 values being significantly higher than the PBS R_2 values (P < 0.001, Fig. 6.5b).

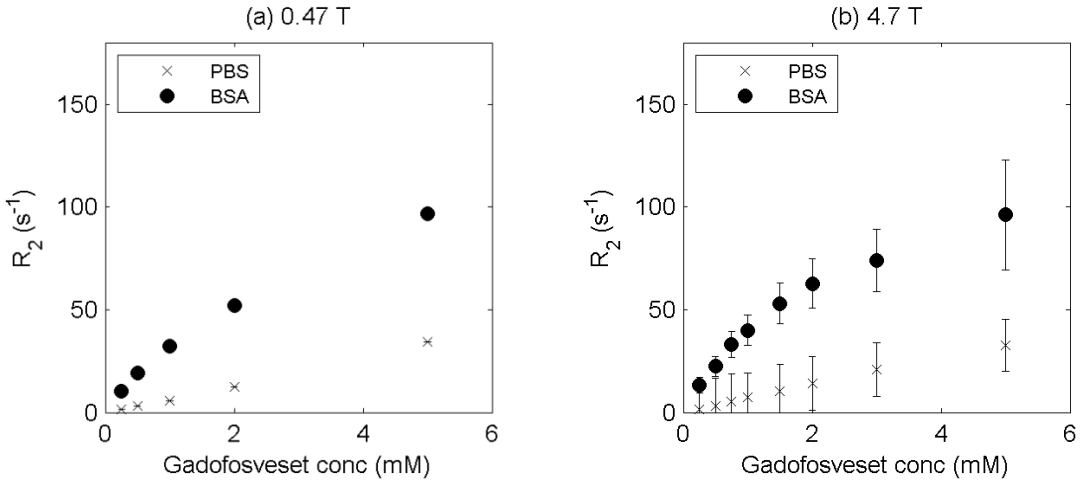

Figure 6.5: R_2 values for gadofosveset in BSA (circles) and in PBS (crosses) at (a) 0.47 T and (b) 4.7 T. Error bars in (a) are smaller than data points

Measurement of R_1, $R_{1\rho}$ and R_2 for gadofosveset in mouse plasma at B_0 = 4.7 T and B_{1L} = 90 μT (Fig. 6.6) shows that $R_{1\rho}$ and R_2 are similar and

significantly higher than R_1, complementing the findings for gadofosveset in BSA. However, when $R_{1\rho}$ values for gadofosveset in mouse plasma are directly compared with those for gadofosveset in BSA, the mouse plasma values are much lower (Fig. 6.7).

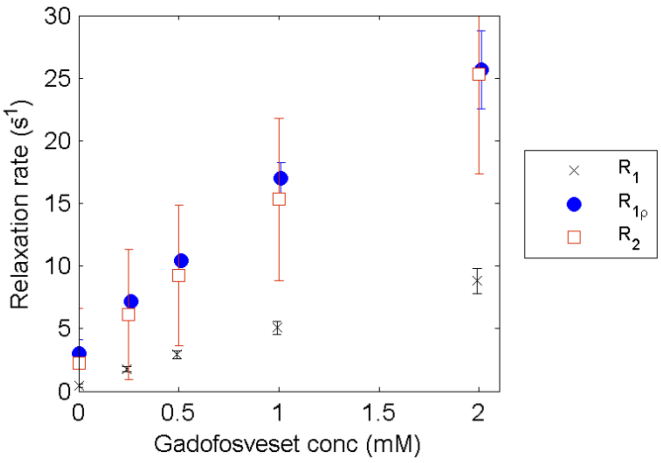

Figure 6.6: R_1 (crosses), $R_{1\rho}$ (circles) and R_2 (squares) for gadofosveset in mouse plasma at B_0 = 4.7 T, B_{1L} = 90 µT; data points presented with a slight offset in C_g to improve clarity

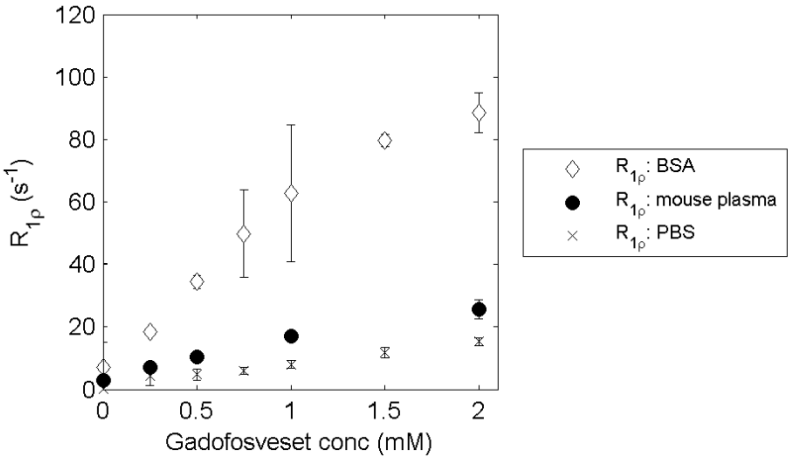

Figure 6.7: Comparison of $R_{1\rho}$ values for gadofosveset in BSA (diamonds), mouse plasma (circles) and PBS (crosses) at B_0 = 4.7 T, B_{1L} = 90 µT

A comparison of $R_{1\rho}$ measurements at three B_{1L} values (Fig. 6.8a) shows that although $R_{1\rho}$ values are generally similar at all three spin-lock field strengths,

the confidence intervals are generally much larger at lower B_{1L}. Image quality is noticeably poorer at 5 µT when sample images from each of the three spin-lock fields are visually compared (Fig. 6.8 (b – d)).

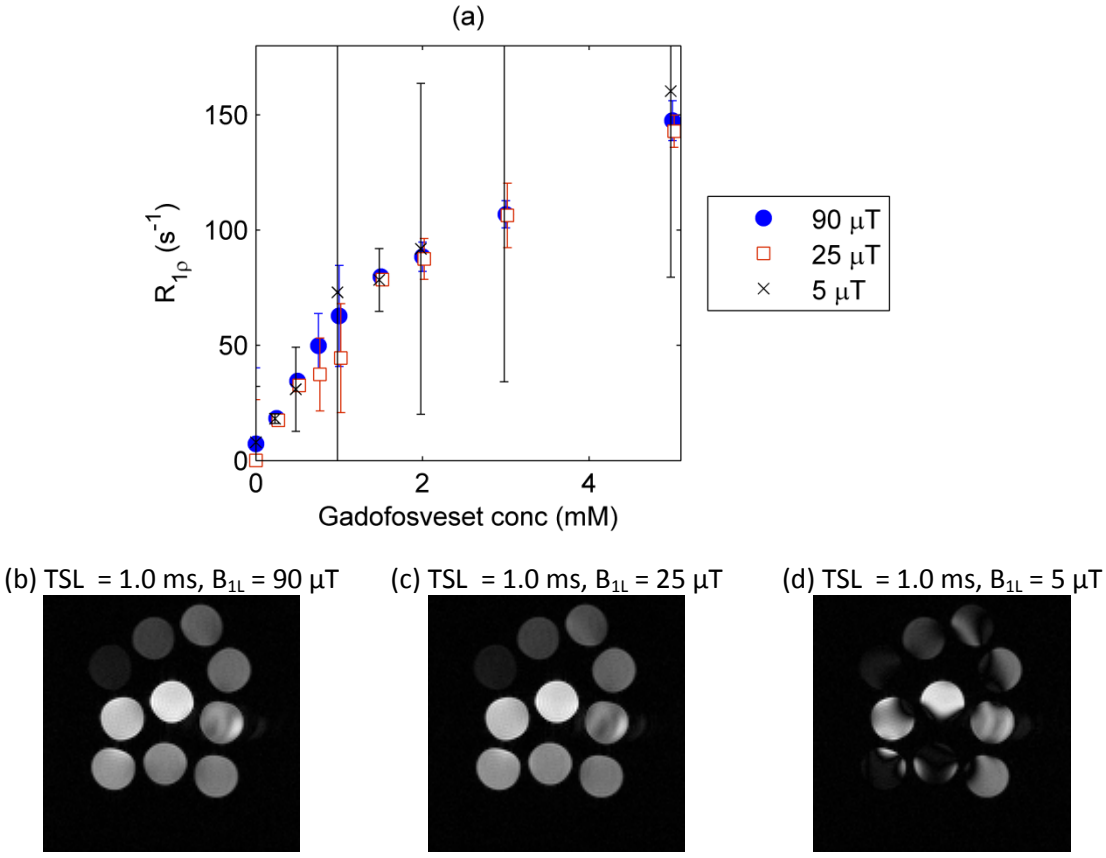

Figure 6.8: (a) Plot of calculated $R_{1\rho}$ at three B_{1L} values for gadofosveset in BSA (data points presented with a slight offset in C_g to improve clarity); sample images at TSL = 1.0 ms at (b) B_{1L} = 90 µT, (c) B_{1L} = 25 µT, and (d) B_{1L} = 5 µT

6.5 DISCUSSION

6.5.1 Spin locking

The high albumin-binding affinity of gadofosveset differentiates it from other clinically approved Gd-based contrast agents. The influence of binding on gadofosveset R_1 is clear at 0.47 T (Fig. 6.3a), but is not observed at 4.7 T (Fig. 6.3b). Most clinical scanners operate at 3.0 T or lower, where the longitudinal relaxivity of gadofosveset in the presence of albumin is still higher

than other Gd agents (91). However, as clinical field strengths continue to increase, this advantage of high relaxivity diminishes and an alternative method for exploiting gadofosveset characteristics would be of benefit. This study demonstrates the feasibility of a previously unpublished method for combining the albumin-binding properties of gadofosveset with the macromolecular sensitivity of spin locking to generate improved contrast modification at high field strengths. $R_{1\rho}$ values at 4.7 T for BSA solutions containing mostly bound gadofosveset were found to be significantly greater than $R_{1\rho}$ values for PBS solutions containing unbound gadofosveset at the same concentration (Fig. 6.4).

Because of the sensitivity of the SL technique to macromolecules, it is not clear from these findings alone the extent to which the difference in $R_{1\rho}$ is attributable to the binding of gadofosveset or the presence of serum albumin macromolecules. Comparison of $R_{1\rho}$ values for BSA and PBS solutions in the absence of contrast agent (0 mM) should give an indication of the influence of the albumin molecules on SL relaxation. However, the lengthy relaxation times of these blank solutions led to poor model fits to signal intensity data. Instead, the influence of albumin is better illustrated here by measurements using the non-binding contrast agent gadopentetate in BSA. A previous study at contrast agent concentrations ≤ 0.5 mM (91) showed longitudinal relaxivity values at 4.7 T to be higher for gadofosveset in water than for gadopentetate in plasma (5.5 versus 3.7 mM^{-1} s^{-1}, respectively). If the SL relaxivity of gadopentetate in BSA is found to be higher than that of gadofosveset in PBS, this may be attributable to the BSA solution macromolecules. The $R_{1\rho}$ values for solutions of gadopentetate in BSA and gadofosveset in PBS (Fig. 6.4), and their associated relaxivity values, were not significantly different. The similarity of $R_{1\rho}$ values for gadofosveset in PBS and gadopentetate in BSA together with the observation of relatively large $R_{1\rho}$ values for gadofosveset in BSA all suggest, firstly, that the gadolinium has a greater effect on $R_{1\rho}$ than the mere presence of the macromolecule and, secondly, that it is the binding rather than any non-specific interactions with the protein that has the largest effect on $R_{1\rho}$.

Further evidence for the influence of binding on $R_{1\rho}$ is provided by the $R_{1\rho}$ measurements of gadofosveset in mouse plasma. Gadofosveset binds at a lower fraction in mouse plasma (approximately 67% versus 91% in human plasma (75)), primarily due to a lower albumin concentration (3.3% in mice (79) compared to around 4.5% in humans (68)). A comparison of $R_{1\rho}$ for gadofosveset in mouse plasma and for gadofosveset in BSA at a concentration equivalent to that found in human serum albumin (Fig. 6.7) clearly shows that although mouse plasma $R_{1\rho}$ values are higher than those recorded in PBS, they are still significantly lower than values recorded in BSA, as would be expected from the differences in bound fraction. This mouse plasma data shows a potential problem with translating the outcome of pre-clinical studies with this technique.

Although the SL contrast alteration observed with gadofosveset is not seen to the same extent with a small Gd-based non-binding contrast agent in an equivalent macromolecular solution (Fig. 6.4), SL has previously been successfully utilised in combination with non-binding agents (218, 221, 223, 224). The outcome of this study suggests that additional contrast may be generated by exploiting the albumin-binding characteristics of an agent such as gadofosveset, although the reduced extravasation of the bound molecule may limit the extent of any increases in tissue contrast. Although it is not possible to use R_1 measurements to differentiate signal alteration from bound and free gadofosveset at high field, due to their equivalent relaxivities (see Chapter 4, Table 4.2), it may be possible to differentiate bound and free gadofosveset through spin locking as $R_{1\rho}$ is substantially altered by binding.

It should be noted that for this in vitro study it was not necessary to optimise SL imaging parameters to take into account potential tissue heating issues resulting from high SAR. For the majority of measurements a relatively high B_{1L} value of 90 μT was chosen to give improved image quality. Although $R_{1\rho}$ increases as B_{1L} decreases, images become increasingly susceptible to artefacts caused by magnetic field inhomogeneities at very low B_{1L} values (216). This finding is confirmed by the large error bars at low B_{1L} in Fig. 6.8a and the prominent image artefacts at 5 μT in Fig. 6.8d, although artefacts at a

B_{1L} of 25 μT were less obvious. A range of patient and volunteer studies have successfully applied spin locking in vivo with a B_{1L} value of 500 Hz (11.7 μT) at B_0 values of 1.5 T (216, 222, 229) and at 3.0 T (230-232). Other methods for reducing SAR, such as off-resonance spin locking (233), were not explored in this study.

6.5.2 Transverse relaxation rates

To avoid SAR-related constraints when carrying out in vivo measurements, an alternative, more practical solution may be to exploit the differences between bound and free gadofosveset transverse relaxation rates (R_2). T_2 values are regularly acquired on clinical scanners, and the effect of gadofosveset is clearly shown by R_2 values in the presence and absence of albumin at 4.7 T (Fig. 6.5b). For these in vitro solutions, both R_2 and $R_{1\rho}$ demonstrate greater relaxation for bound gadofosveset than R_1. Transverse relaxation rates for gadofosveset will be explored further in Chapter 7.

Although measurement of T_2 is more easily achieved in practice than $T_{1\rho}$, $T_{1\rho}$ is less influenced by the effect of diffusion from microscopic susceptibility gradients. As a result several studies, in particular those looking at tumour response to cytotoxic treatment, have suggested that $T_{1\rho}$ may be a more responsive early indicator of physiological change than T_2 (219, 220). It has also been suggested that improved (qualitative) tumour boundary definition may be achieved utilising $T_{1\rho}$ rather than T_2 (234). A study of brain images in healthy volunteers at 1.5 T (235) found that $T_{1\rho}$-weighted images displayed improved spatial resolution over T_2-weighted images and in vivo $T_{1\rho}$ maps had a greater dynamic range than equivalent T_2 maps, due to the tissue $T_{1\rho}$ signal only being sensitive to the spin-lock pulse frequency.

6.5.3 Limitations

The scanning parameters at 4.7 T were optimised for physiological contrast agent concentrations. As a result, model fitting was less precise for the

solutions containing the lowest and highest concentrations. The long T_1 values on the 0 mM solutions caused particular problems with model fitting and were excluded from this analysis. In addition, the PBS R_2 values at 4.7 T were based on a model fit to just three TE points, rather than the six points used for the BSA solutions, leading to greater imprecision in the calculated PBS R_2 values.

For the purpose of this study gadopentetate was assumed to be a non-binding contrast agent, although there is some evidence to suggest that the chelate displays a weak tendency for binding to albumin (41). At the comparatively low serum albumin concentration used here, however, the measured relaxation rates suggested little influence of albumin binding for gadopentetate and it may effectively be considered to be non-binding.

6.5.4 Summary

In summary, this study has shown the $R_{1\rho}$ response to gadofosveset in serum albumin at high fields to be significantly larger than to a conventional small-molecule Gd-based contrast agent. This suggests that spin locking may be a viable method for regaining the longitudinal relaxivity lost by gadofosveset at high fields, and may also provide an opportunity for additional tissue characterisation through the differentiation of bound and free gadofosveset molecules. Despite offering potential benefits, implementation of this method in a SAR-limited clinical setting would require further investigation of optimal SL parameters prior to assessment in humans. If pre-clinical evaluation of spin locking with gadofosveset is undertaken, species differences in albumin levels must also be considered.

Note: A reduced version of this chapter appeared in the October 2012 edition of *Magnetic Resonance in Medicine* (1).

CHAPTER 7: A GADOFOSVESET-BASED BIOMARKER OF TISSUE ALBUMIN CONCENTRATION

7.1 BACKGROUND

Albumin is the most abundant protein in human plasma, accounting for half of all serum proteins (69); its role within the body was discussed in Chapter 3 (section 3.1.2). Albumin is not stored, but continuously synthesized by the liver and broken down by most organs in the body. The distribution of albumin may be described by a single intravascular and two extravascular compartments, one easily mobilised and exchangeable with the intravascular compartment and the other remote (particularly in the skin, (236)). Around 33% of albumin is found in the intravascular compartment, with 49% and 18% in the exchangeable and remote extravascular compartments, respectively (71). The normal level of serum albumin in plasma is approximately 3.5 – 5.0 g per 100 ml (237), equating to a concentration of approximately 0.52 – 0.74 mM.

Albumin concentrations may be accurately measured in urine or blood samples, with altered levels caused by changes in rates of synthesis, catabolism or extravascular leakage. Low levels of albumin have been linked to critical illness (238) and may be a risk factor for myocardial infarction (239). The body's natural transcapillary exchange rate of around 5% of intravascular albumin per hour (81) may increase in damaged or angiogenic vessels. Localised increases in extravascular macromolecular content may be symptomatic of, for example, reperfused myocardial infarction (157) or tumour angiogenesis (240).

Although albumin concentrations in blood and urine are valuable indicators of albumin imbalance, they do not fully describe its biodistribution. Direct measurement of interstitial albumin concentration is not straightforward, with

varying results found using invasive techniques such as wick implantation (241), blister suction (242) or double lumen catheterization (243). It is suggested that a non-invasive biomarker (244) of localised extravascular albumin may facilitate quantitative assessment of extravascular leakage. This technique may have prognostic and/or diagnostic value in assessment of tumour angiogenesis and response to treatment, as an increase in the leakage of macromolecules from the vasculature of tumours has been demonstrated (245). Although conventional small-molecule gadolinium (Gd) contrast agents are frequently used in MRI to assess microvascular permeability, macromolecular Gd agents have shown increased sensitivity to malignancy (159) and response to anti-angiogenic treatment (246). Increased albumin leakage may also be expected in myocardial infarction (247), where the use of macromolecular agents may aid assessment of ischaemic microvascular damage (248).

The general properties of the albumin-binding MRI contrast agent gadofosveset have been discussed in Chapter 3, with longitudinal relaxivity (r_1) assessed in Chapter 4. In the presence of albumin, gadofosveset r_1 is high at low fields but decreases rapidly as field strength increases (Chapter 4, Fig. 4.4). Conversely, the transverse relaxivity of the bound molecule is expected to be high at low field and increase slightly with field strength (89). Results from Chapter 6 show that, unlike longitudinal relaxation rates (R_1, Fig. 6.3), transverse relaxation rates (R_2) are significantly higher for gadofosveset in BSA than in PBS at both 0.47 T and 4.7 T (Fig. 6.5).

The decline in the bound fraction of gadofosveset as contrast agent concentration increases above a specific value (related to the albumin concentration, and based on the assumption of a single binding site on the albumin molecule) suggests that bound fraction may be used as a biomarker for albumin concentration. Through manipulation of equations presented in earlier chapters, it is possible to calculate bound and free gadofosveset concentrations and serum albumin concentration directly from measured R_1 and R_2 values (with assumed K_a and relaxivity values). This theory holds for other albumin-binding contrast agents, such as gadoxetate and gadobenate,

although these agents have much lower binding affinities (and lower peak bound fractions). The accuracy of the albumin calculation model is dependent on accurate R_1 and R_2 measurements; for agents with low binding affinity, results may be increasingly susceptible to experimental imprecision in the measurement of R_1 and R_2.

7.2 AIMS AND OBJECTIVES

This study aims to assess the viability of utilising measured relaxation rates in solutions with and without gadofosveset to develop a biomarker of albumin concentration in vitro. The viability of this method is also assessed in vitro using gadoxetate and gadobenate, and the feasibility of applying the method in a clinical setting is tested in vivo using gadofosveset-enhanced images from a small (n = 7) volunteer study. The following objectives were set:

1. Carry out simulation studies to assess the potential influence on albumin calculation of realistic experimental imprecision in R_1 and R_2.

2. Measure R_1 and R_2 at two field strengths for in vitro solutions of gadofosveset, gadoxetate and gadobenate, along with the non-binding agent gadopentetate.

3. Calculate bound and free relaxivities based on measured relaxation rates, and use these results to determine bound fractions and albumin concentrations for each solution.

4. Use the relaxivity values derived in vitro, along with measured in vivo R_1 and R_2 values, to determine gadofosveset and albumin concentrations in left ventricular blood and myocardial tissue of healthy human volunteers at 3.0 T.

If the method is successful, it may be applied to generate a spatially located measure of tissue albumin which could be used as an alternative to current

invasive techniques. Identification of abnormal extravascular albumin distribution correlating with increased capillary leakage may have a number of applications, including early indication of disease progression or treatment response in tumour angiogenesis, or assessment of reperfused myocardial infarction.

7.3 THEORY

7.3.1 Bound fraction

Basic theory relating to albumin-binding contrast agents is covered in Chapter 3; key equations are repeated here with their original numbering. The overall contrast agent (C_g) and serum albumin (C_{sa}) concentrations equal the sum of their bound and free components (Eq. 3.3 and 3.4).

$$C_g = C_{gbound} + C_{gfree} \quad [3.3]$$

$$C_{sa} = C_{sabound} + C_{safree} \quad [3.4]$$

Assuming gadofosveset binds at a single site on the albumin molecule, $C_{gbound} = C_{sabound}$; binding affinity (K_a) is then defined by Eq. 3.6.

$$K_a = \frac{C_{gbound}}{C_{gfree}.(C_{sa} - C_{gbound})} \quad [3.6]$$

Bound fraction (f_b, C_{gbound}/C_g) decreases as C_g increases, with the highest f_b occurring when C_g (and therefore C_{gbound}) is very low. As C_{gbound} approaches 0, a first order Taylor expansion of Eq. 3.6 provides a theoretical maximum bound fraction (f_{bmax}, Eq. 7.1). A step-by-step derivation of this equation is provided in Appendix C.

$$f_{bmax} \approx \frac{C_{sa}.K_a}{(1 + C_{sa}.K_a)} \quad [7.1]$$

Assuming gadofosveset, gadoxetate and gadobenate K_a values of 11.0 mM^{-1} , 0.255 mM^{-1} and 0.226 mM^{-1}, respectively, f_{bmax} in human plasma (with an assumed C_{sa} value of 0.7 mM) at very low C_g would be 0.89 (gadofosveset), 0.15 (gadoxetate) and 0.14 (gadobenate).

Replacing C_{gfree} in Eq. 3.6 using Eq. 3.3, the quadratic may be solved to give an expression for C_{gbound} if total contrast agent concentration, albumin concentration and binding affinity are known (Eq. 7.2).

$$C_{gbound} = \frac{K_a.C_g + K_a.C_{sa} + 1 - \sqrt{\left(K_a.C_g + K_a.C_{sa} + 1\right)^2 - 4.{K_a}^2.C_g.C_{sa}}}{2.K_a} \quad [7.2]$$

Only the negative form of the quadratic solution is applicable as the positive form would give a non-zero solution for C_{gbound} at C_g = 0. Fig. 7.1a shows the variation of C_{gbound} with C_g using Eq. 7.2, with C_{sa} = 0.7 mM and K_a = 11.0, 0.255 and 0.226 mM^{-1} (for gadofosveset, gadoxetate and gadobenate, respectively). With the assumption of a 1:1 binding ratio of the contrast agent to albumin, the plot shows that C_{gbound} approaches a maximum value equivalent to C_{sa} at high C_g. The variation of bound fraction with C_g (using the same fixed parameters) is plotted in Fig. 7.1b, with f_b approaching f_{bmax} at very low C_g.

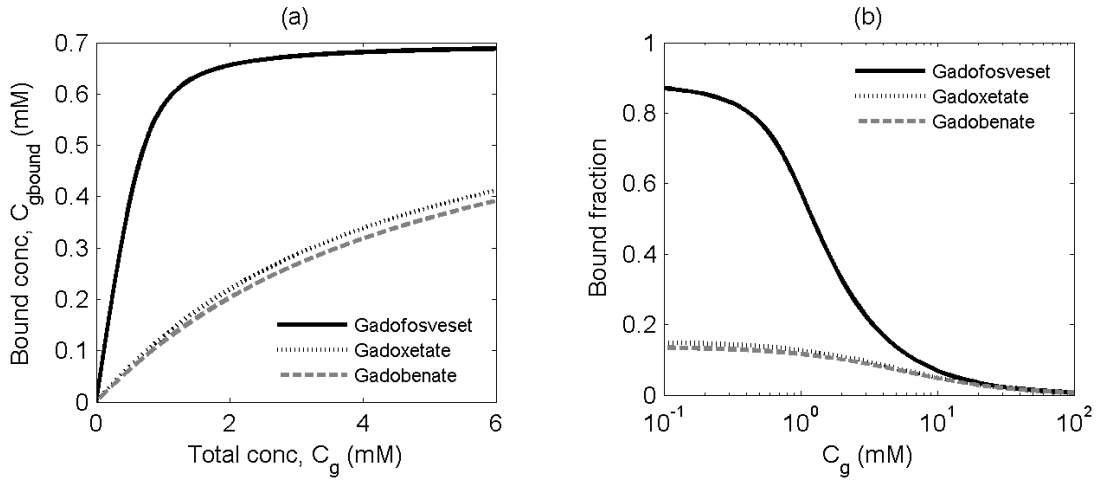

Figure 7.1: Modelled variation of (a) bound concentration and (b) bound fraction with total gadofosveset concentration, for C_{sa} = 0.7 mM and K_a = 11.0 mM^{-1} (gadofosveset), 0.255 mM^{-1} (gadoxetate) and 0.226 mM^{-1} (gadobenate); note semi log scale on (b)

7.3.2 Measuring albumin binding fraction

As represented in Chapter 4, the contrast-agent induced change in relaxation rate R_i (ΔR_i) for non-binding Gd-based contrast agents, or albumin-binding agents in the absence of albumin, is conventionally represented by a linear relationship, defined by the free relaxivity (r_{ifree}) (Eq. 4.1).

$$\Delta R_i = r_{ifree}.C_g \quad [4.1]$$

where i = 1,2.

For an albumin-binding agent composite relaxivities are observed, comprising contributions from both the bound (r_{ibound}) and free molecule, and variations of Eq. 3.8 (Chapter 3) may be used (Eq. 7.3 and 7.4).

$$\Delta R_1 = r_{1bound}.C_{gbound} + r_{1free}.C_{gfree} \quad [7.3]$$

$$\Delta R_2 = r_{2bound}.C_{gbound} + r_{2free}.C_{gfree} \quad [7.4]$$

Assuming ΔR_1 and ΔR_2 may be measured and r_{1bound}, r_{1free}, r_{2bound} and r_{2free} are known, it is possible to rearrange Eqs. 7.3 and 7.4 to give expressions for bound and free contrast agent concentrations (Eqs. 7.5 and 7.6).

$$C_{gbound} = \frac{r_{2free}.\Delta R_1 - r_{1free}.\Delta R_2}{r_{1bound}.r_{2free} - r_{2bound}.r_{1free}} \quad [7.5]$$

$$C_{gfree} = \frac{r_{1bound}.\Delta R_2 - r_{2bound}.\Delta R_1}{r_{1bound}.r_{2free} - r_{2bound}.r_{1free}} \quad [7.6]$$

Total contrast agent concentration is then defined by Eq. 7.7.

$$C_g = \frac{\Delta R_2(r_{1bound} - r_{1free}) - \Delta R_1(r_{2bound} - r_{2free})}{r_{1bound}.r_{2free} - r_{1free}.r_{2bound}} \quad [7.7]$$

Bound, free and overall contrast agent concentrations can therefore be derived from measurement of ΔR_1 and ΔR_2.

7.3.3 Measuring albumin concentration

In a second step, contrast agent concentration is related to albumin concentration by assuming a chemical equilibrium between free and bound substances. Eq. 3.6 can be rearranged for C_{sa} (Eq. 7.8).

$$C_{sa} = C_{gbound} + \frac{1}{K_a}.\frac{C_{gbound}}{C_{gfree}} \quad [7.8]$$

Inserting Eqs. 7.5 and 7.6 into Eq. 7.8 gives an expression for total albumin concentration (Eq. 7.9).

$$C_{sa} = \frac{r_{2free}.\Delta R_1 - r_{1free}.\Delta R_2}{r_{1bound}.r_{2free} - r_{2bound}.r_{1free}} + \frac{1}{K_a}.\frac{r_{2free}.\Delta R_1 - r_{1free}.\Delta R_2}{r_{1bound}.\Delta R_2 - r_{2bound}.\Delta R_1} \quad [7.9]$$

Eq. 7.9 therefore provides a method for deriving albumin concentration through measurement of ΔR_1 and ΔR_2, assuming fixed relaxivity and binding affinity values.

7.3.4 Measuring bound relaxivity

It remains to derive a method for measuring the relaxivity values from in vitro samples with known contrast agent concentrations. Free relaxivity is derived using Eq. 4.1, applied to a solution without albumin. An equation for bound relaxivity is provided in Chapter 3 (Eq. 3.10).

$$\Delta R_i = r_{ifree}.C_g + (r_{ibound} - r_{ifree}).\left\{\frac{(C_{sa}.K_a + C_g.K_a + 1) - \sqrt{\left[(C_{sa}.K_a + C_g.K_a + 1)^2 - 4.{K_a}^2.C_{sa}.C_g\right]}}{2.K_a}\right\} \quad [3.10]$$

where i = 1,2.

Eq. 3.10 has been represented in a similar form in a number of papers (for example, (37, 77, 78)). This model describes a gradual transition of binding fraction, from a maximum at low C_g, where observed relaxivity is dominated by $r_{1,2bound}$, towards a minimum at high C_g, where $r_{1,2free}$ has the greater influence. As the model assumes a single binding site, the shift in emphasis from $r_{1,2bound}$ to $r_{1,2free}$ occurs at around $C_g = C_{sa}$.

Accepting that $r_{2bound} > r_{2free}$ and $C_{gfree} > 0$, it follows from Eq. 3.3 and Eq. 7.4 that, in all cases:

$$\Delta R_2 < r_{2bound}.C_g \quad [7.10]$$

It should be noted that experimental imprecision in R_2 measurement (and R_1 measurement, as C_g is calculated using Eq. 7.7) may violate this inequality, and may lead to calculated values of $C_{sa} \leq 0$ mM. For transverse relaxivity,

r_{2bound} is much higher than r_{2free} at all B_0 values; for longitudinal relaxivity, r_{1bound} is much higher than r_{1free} at low B_0 but both are effectively equivalent at very high B_0 (89). This variation with field strength means that at low B_0 any imprecision in R_2 measurement has a much greater influence on calculated C_g (Eq. 7.7), therefore it is expected that the albumin-calculation model may not be applicable at low B_0 values.

7.4 EXPERIMENTAL METHOD

7.4.1 Simulation

The influence of experimental imprecision in the measurement of ΔR_1 and ΔR_2 on calculated C_{sa} was assessed through simulation. Estimated 3.0 T relaxivity values for gadofosveset and gadoxetate were applied to Eq. 3.10 with fixed K_a values of 11.0 mM^{-1} (gadofosveset) and 0.255 mM^{-1} (gadoxetate) to determine 'true' ΔR_1 and ΔR_2 values within the C_{sa} range 0.1 – 1.0 mM and at C_g = 0.1 and 1.0 mM. These ΔR_1 and ΔR_2 values were then independently adjusted by ± 10% and inserted into Eq. 7.9 in order to determine a calculated C_{sa}. Results from Chapter 4 suggest that 95% confidence intervals of around ± 10% are realistic for measurement of relaxation rates.

A further simulated study incorporated a randomly fluctuating variance in both ΔR_1 and ΔR_2 (rather than a fixed ± 10%), limited to a Gaussian distribution with a 5% standard deviation. C_{sa} was calculated for each random variance and the process repeated 1000 times.

7.4.2 In vitro validation

Model validation was carried out by calculating C_{sa} (using Eq. 7.9) for a range of in vitro solutions. This requires values of K_a, ΔR_1, ΔR_2, r_{2bound}, r_{2free}, r_{1bound} and r_{1free}. ΔR_1 and ΔR_2 were measured within the study, fixed K_a values of

11.0, 0.255 and 0.226 mM^{-1} for gadofosveset, gadoxetate and gadobenate, respectively, were assumed, and relaxivity values were derived from the data (as values for matching experimental conditions could not be found in the literature).

In vitro solutions of gadofosveset (Vasovist), gadopentetate (Magnevist), gadoxetate (Primovist) and gadobenate (MultiHance) were prepared in phosphate-buffered saline (PBS) and bovine serum albumin (BSA) using the method described in Chapter 4, at concentrations shown in Table 7.1. In total, 28 combinations of gadofosveset and BSA were prepared, along with 12 combinations of contrast agent and BSA for gadoxetate and gadobenate.

Table 7.1: Contrast agent–serum albumin concentration combinations used for in vitro solutions

	Albumin concentration, C_{sa}		Contrast agent concentration, C_g
Contrast agent	mM	% (w/v)	(mM)
Gadofosveset	0.0	-	0, 0.1, 0.2, 0.3, 0.4, 0.5, 0.6, 0.7, 0.8, 0.9, 1.0
	0.15	1.0%	0, 0.1, 0.2, 0.3, 0.4
	0.3	2.0%	0, 0.1, 0.2, 0.3, 0.4, 0.6, 0.8, 1.0
	0.45	3.0%	0, 0.2, 0.3, 0.4, 0.5, 0.6, 0.7, 0.9
	0.6	4.0%	0, 0.2, 0.5
	0.7	4.7%	0, 0.2, 0.4, 0.6, 0.7, 0.8, 1.0
	1.0	6.7%	0,0.6, 1.0
Gadopentetate	0.3	2.0%	0, 0.1, 0.2, 0.3, 0.4, 0.6, 0.8, 1.0
	0.45	3.0%	0, 0.2, 0.3, 0.4, 0.5, 0.6, 0.7, 0.9
	0.7	4.7%	0, 0.2, 0.4, 0.6, 0.7, 0.8, 1.0
Gadoxetate	0.0	-	0, 0.2, 0.5, 0.7, 1.0
	0.45	3.0%	0, 0.2, 0.5, 0.7, 1.0
	0.7	4.7%	0, 0.2, 0.5, 0.7, 1.0
	1.0	6.7%	0, 0.2, 0.5, 0.7, 1.0
Gadobenate	0.0	-	0, 0.2, 0.5, 0.7, 1.0
	0.45	3.0%	0, 0.2, 0.5, 0.7, 1.0
	0.7	4.7%	0, 0.2, 0.5, 0.7, 1.0
	1.0	6.7%	0, 0.2, 0.5, 0.7, 1.0

7.4.3 In vitro data acquisition: 3.0 T

Tubes were placed vertically within a head coil (SENSE-Head 8) in a 3.0 T Philips Achieva TX system at room temperature (approximately 21 °C). R_1 values were measured using a spin echo inversion recovery sequence with 10 inversion times (TI = 50, 83, 136, 225, 371, 611, 1009, 1665, 2747, 4925 ms), TR = 5000 ms, TE = 6.2 ms. R_2 values were measured using a multi-echo sequence with eight echo times (TE = 10, 20, 30, 40, 50, 60, 70, 80 ms), TR = 1000 ms. Even echoes only were used for model fitting. Additional parameters common to both R_1 and R_2 measurement: FOV = 231 x 231 mm; matrix size = 240 x 240 pixels; single coronal (horizontal) slice; slice thickness = 10 mm.

7.4.4 In vitro data acquisition: 4.7 T

Tubes were placed vertically in a cylindrical cradle of diameter 60 mm and inserted into a 63 mm quad coil in a horizontal bore 4.7 T magnet with Bruker console running ParaVision 5.1 software (Bruker BioSpin MRI GmbH, Ettlingen, Germany). Solutions were maintained at a temperature of 37 °C with warm air flow, verified with a fibre optic temperature probe in an adjacent water tube. R_1 values were measured using a RARE saturation recovery imaging sequence, with nine recovery times (57.2, 68.5, 78.5, 88.5, 103.5, 183.5, 283.5, 383.5, 983.5 ms for gadofosveset and gadopentetate; 57.2, 68.5, 78.5, 88.5, 103.5, 183.5, 483.5, 983.5, 2983.5 ms for gadoxetate and gadobenate) and a TE of 11 ms. R_2 values were measured using a multi-slice multi-echo (MSME) sequence, with 20 equally spaced TE values from 11 to 220 ms and a TR of 1000 ms. Additional parameters common to both R_1 and R_2 measurement: FOV = 60 x 60 mm; matrix size = 256 x 256 pixels; RARE factor = 2; averages = 1; centric encoding; single coronal (horizontal) slice; slice thickness = 1 mm.

7.4.5 Relaxation rates

A circular region of interest (ROI) was drawn within each tube and the mean signal intensity (SI) of each ROI measured using ImageJ software (v1.42q, Rasband, W.S., ImageJ, U. S. National Institutes of Health, Bethesda, Maryland, USA, http://imagej.nih.gov/ij/, 1997-2011). SI values at 4.7 T were adjusted for noise bias using a simple Rician correction (227), based on mean standard deviations of four background regions in each image. R_1 values at 4.7 T and R_2 values at 3.0 T and 4.7 T, along with 95% confidence intervals, were determined from two-parameter nonlinear fits to Eqs. 7.11 and 7.12, respectively, using MATLAB (v 7.9, MathWorks, Natick, MA). R_1 calculation at 3.0 T included an extra term for TR (Eq. 7.13).

$$SI = S_0.(1 - e^{-TR.R1}) \quad [7.11]$$

$$SI = S_0.e^{-TE.R2} \quad [7.12]$$

$$SI = S_0.|1 - b.e^{-TI.R1} + e^{-TR.R1}| \quad [7.13]$$

where S_0 represents the fully recovered SI value and b is a factor accounting for imprecision in the 180° inversion pulse, applied to each ROI.

Contrast agent-induced changes in relaxation rate ($\Delta R_{1,2}$) were calculated by subtracting $R_{1,2}$ values for each non-Gd C_{sa} solution ($C_g = 0$) from equivalent Gd-containing C_{sa} solutions ($C_g > 0$).

7.4.6 Calculating relaxivity and C_{sa}

Once ΔR_1 and ΔR_2 values were established, C_{sa} calculation was a three-step process. In the first step, r_{1free} and r_{2free} were calculated by applying the linear model in Eq. 4.1 to the ΔR_1 and ΔR_2 values for the contrast agent–PBS samples (C_{sa} = 0 mM), where no binding was assumed. The second step then used these free relaxivities and ΔR_1 and ΔR_2 values to calculate bound relaxivities. To prevent bias, bound relaxivities were calculated separately for

each sample by adopting a leave-one-out approach. For example, for the gadofosveset C_{sa} = 0.15 mM, C_g = 0.1 mM sample, r_{1bound} and r_{2bound} were calculated using Eq. 3.10 by applying one-parameter fits to the ΔR_1 and ΔR_2 values for all the other gadofosveset samples. In this way, a unique set of relaxivity values were calculated for each sample.

The final step in the process then used the calculated relaxivities and measured ΔR_1 and ΔR_2 values for a given sample (for example, for the C_{sa} = 0.15, C_g = 0.1 mM sample) and applied Eq. 7.9 to determine a calculated C_{sa} value for that sample. This process was repeated for each sample until an individual C_{sa} value was calculated for each sample.

In addition, an overall, observed relaxivity (r_{1obs}, r_{2obs}) was calculated for each set of C_{sa} > 0 mM samples by applying a linear fit to the contrast agent–BSA ΔR_1 and ΔR_2 values.

7.4.7 Temperature adjustment

Although measurements at 3.0 T were made at room temperature (approximately 21 °C), equivalent relaxivity values at body temperature were also required. To determine a method for adjusting 3.0 T relaxivities at 21 °C to 37 °C equivalents, temperature-related relaxivity values from published studies were reviewed and supplemented by data acquired at other B_0 values as part of this project.

Relaxivity of the free gadofosveset molecule is expected to decrease as temperature increases (37). At 3.0 T, a decrease in r_{1free} of around 25% from room to body temperature has been shown (77); calculated values at 4.7 T in Chapter 4 (Table 4.2) show a similar decrease. Measurement of gadopentetate r_2 at 1.5 T showed a decrease between room and body temperature of 35% (93); assuming the free gadofosveset molecule has similar attributes to the non-binding gadopentetate molecule, this gives an indication of the likely change in gadofosveset r_{2free} with temperature at 3.0 T.

Studies of r_{1bound} at low field demonstrate an opposite temperature dependence, increasing between room and body temperature (37). However, this relationship alters as field strength increases (75). Data collected here at a range of field strengths (Chapter 4, Table 4.2) demonstrate this variation, with r_{1bound} being 27% higher at 37 °C than at 21 °C at 0.47 T, but 12% lower and 13% lower at 37 °C at 4.7 T and 9.4 T, respectively. It was not possible to find direct indication of the likely change in r_{2bound} at 3.0 T. However, r_{2bound} (unlike r_{1bound}) increases with field strength (89), therefore it is suggested that if a similar increase in r_{2bound} with temperature to r_{1bound} is shown at low field (27% increase between 21 °C and 37 °C, Table 4.2), a larger increase may be expected at higher fields.

On the basis of these findings, the following conversions were used to adjust 3.0 T relaxivities from 21 °C to 37 °C: r_{1free} = -25%; r_{1bound} = -10%; r_{2free} = -30%; r_{2bound} = +40%.

7.4.8 In vivo feasibility assessment: 3.0 T

A total of seven healthy volunteers (five male, mean age 36 ± 10 years, mean weight 81 ± 15 kg) underwent pre- and post-contrast short-axis cardiac scans on a 3.0 T Siemens Skyra system at Northwestern Memorial Hospital, Chicago. The study was approved by the Institutional Review Board (IRB) at Northwestern University (IRB project number STU00061779, IRB Office, Northwestern University, Chicago, Illinois), with informed consent obtained from all participants. IRB approval did not include provision for taking blood samples, therefore per-volunteer measures of haematocrit and blood albumin were not available.

Images were acquired as part of a larger study mapping flow patterns in thoracic aortic aneurisms (TAA) in different progression stages. Myocardial T_1 and T_2 values with administration of an MR contrast agent were also acquired to study changes of these parameters associated with inflammatory and

connective tissue diseases that are in turn associated with the progression of TAA. A small timing bolus of 1.0 – 2.0 ml of gadofosveset (Ablavar) was used to establish arrival time and was followed by a main bolus of 6.2 – 8.8 ml, giving a total dose of 0.12 ml kg^{-1} (0.03 mmol kg^{-1}). A modified Look-Locker inversion recovery (MOLLI) sequence (249) with motion correction (250) (field of view = 270 x 360 mm, matrix size = 144 x 256 pixels, flip angle = 35°, TR = 313.45 ms, TE = 1.13 ms, bandwidth/pixel = 975 Hz) was used for T_1, with T_1 maps created inline by the system software. This version of the MOLLI sequence consisted of two inversions, with three images acquired after the first inversion (initial effective TI of 120 ms, and RR interval added to the other two acquisitions), and five images acquired after the second inversion (first effective TI of 200 ms; 200 ms + RR for subsequent acquisitions). Images were acquired with a specific trigger delay to select for end diastole. MOLLI acquisition was followed by a T_2 mapping sequence using a single-shot T_2-prepared steady-state free precession (SSFP) acquisition with three T_2-preparation echo times: 0, 24, and 55 ms (field of view = 337 x 450 mm, matrix size = 144 x192 pixels, TR = 201.88 ms, TE = 1.07 ms, flip angle = 40°, bandwidth/pixel = 930 Hz). For all sequences, 8 mm slices were acquired at cardiac short axis base, mid and apex locations. Post-contrast images were acquired at up to three time points for each volunteer, with T_2 image acquisition occurring 1 – 2 min after T_1 acquisition (Table 7.2). The mid-point between T_1 and T_2 image acquisitions was used as the post-contrast reference time.

Table 7.2: Main bolus and image acquisition times for volunteers (time from first administration of contrast agent (timing bolus), MM:SS)

Volunteer	Main bolus	Measurement					
		T_1 [1]	T_2 [1]	T_1 [2]	T_2 [2]	T_1 [3]	T_2 [3]
#1	07:08	14:31	16:47	–	–	–	–
#2	03:52	08:57	11:19	38:34	39:35	54:06	55:53
#3	02:35	07:10	08:10	29:12	30:15	–	–
#4	04:15	29:17	31:44	–	–	–	–
#5	08:24	41:43	43:25	–	–	–	–
#6	03:24	23:45	25:02	28:09	29:29	39:23	40:38
#7	03:06	05:34	07:21	18:34	20:16	27:02	28:36

ROIs were drawn within the left ventricle and within the myocardium on each pre- and post-contrast T_1 and T_2 map at the middle of the short axis view, and median and standard deviation values derived using MATLAB. Relaxation times were converted to relaxation rates and Eq. 7.7 and 7.9 used to determine gadofosveset and albumin concentrations, respectively. A K_a value of 11.0 mM^{-1} was assumed and the temperature-adjusted 3.0 T in vitro bound and free relaxivities used. For albumin calculation each ROI is considered as a single well-mixed compartment, which is a valid assumption for the left ventricle, where gadofosveset is entirely intravascular, but is a simplification of conditions in the myocardium, where ΔR_1 and ΔR_2 are influenced by gadofosveset in vascular and extravascular spaces.

7.5 RESULTS

7.5.1 Simulation

Simulated data are shown in Fig. 7.2 and 7.3. The influence on calculated C_{sa} of a ± 10% variance in ΔR_1 or ΔR_2 is illustrated by a plot of percentage difference between calculated and actual C_{sa} for gadofosveset and gadoxetate, at contrast agent concentrations of 0.1 mM and 1.0 mM (Fig. 7.2). A boxplot of percentage error in calculated C_{sa} is shown at a gadofosveset concentration of 0.5 mM, with a Gaussian distribution on ΔR_1 and ΔR_2 variability (Fig. 7.3).

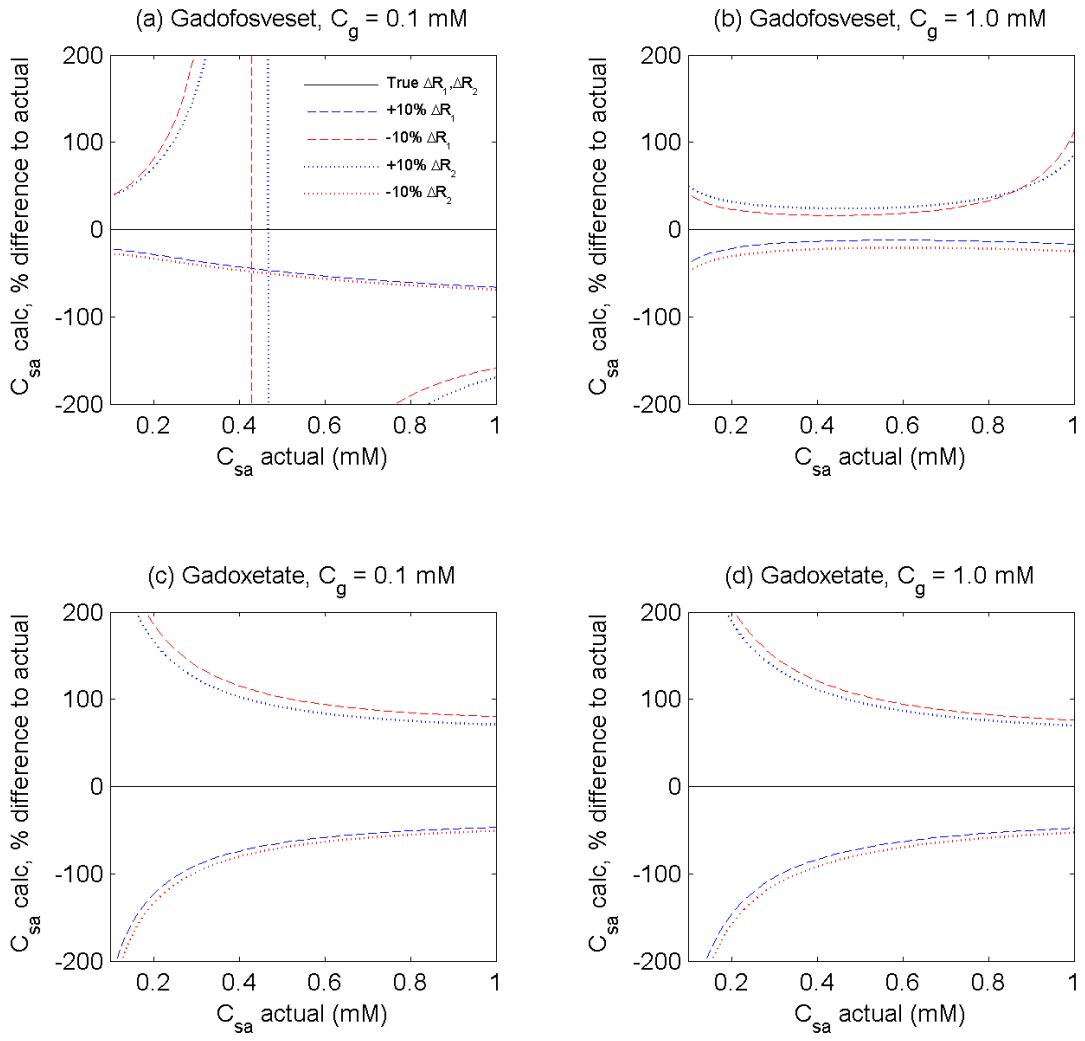

Figure 7.2: Simulated effect of error in measured relaxation rate (± 10%) on calculated C_{sa} at C_g = 0.1 mM (left) and 1.0 mM (right) for gadofosveset (top) and gadoxetate (bottom) using representative relaxivity values

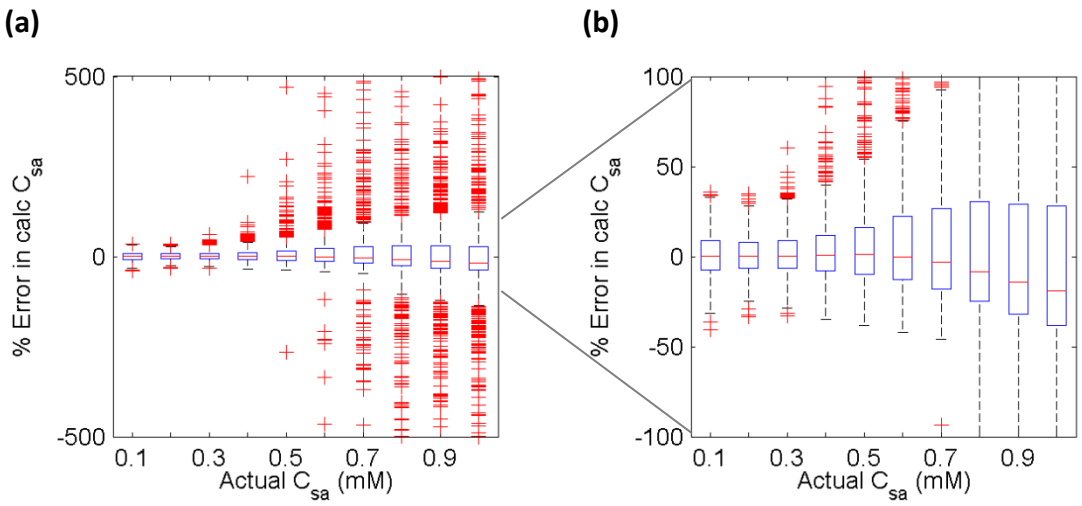

Figure 7.3: (a) Simulated spread of error in calculated C_{sa} for gadofosveset when applying a 5% standard deviation on $\Delta R_{1,2}$ variability using a Gaussian distribution (1000 repetitions; C_g = 0.5 mM, K_a = 11.0 mM^{-1}, representative relaxivity values). Red lines represent median value, box limits are 25th and 75th percentiles, whiskers cover 99.3% of data points and red '+' signs are outliers beyond this range; (b) as (a), with reduced vertical scale to highlight detail

7.5.2 In vitro data at 3.0 T and 4.7 T

Mean individual gadofosveset, gadoxetate and gadobenate relaxivity values measured at 3.0 T and 4.7 T for the range of C_{sa} – C_g combinations are given in Table 7.3; standard deviations in brackets indicate the variance in calculated relaxivity. Calculated 3.0 T relaxivity values were acquired at approximately 21 °C and the values adjusted to 37 °C using the method described in section 7.4.7.

Table 7.3: Calculated relaxivity values and standard deviations (mM^{-1} s^{-1})

	3.0 T, 21 °C				3.0 T, adjusted to 37 °C			4.7 T, 37 °C		
	Gadofosveset	Gadoxetate	Gadobenate	Temperature adjustment *	Gadofosveset	Gadoxetate	Gadobenate	Gadofosveset	Gadoxetate	Gadobenate
r_{1bound}	12.2 (0.3)	11.6 (0.6)	13.9 (1.5)	-10%	11.0	10.4	12.5	6.5 (0.0)	5.5 (1.4)	8.6 (4.6)
r_{1free}	8.1 (0.3)	7.4 (0.2)	5.7 (0.1)	-25%	6.0	5.6	4.3	4.5 (0.1)	5.2 (0.3)	3.6 (0.1)
r_{2bound}	43.8 (1.0)	28.4 (2.1)	32.9 (2.8)	+40%	61.3	39.7	46.1	60 (1.4)	45.8 (2.4)	54.4 (5.4)
r_{2free}	9.7 (0.2)	8.7 (0.2)	7.6 (1.1)	-30%	6.8	6.1	5.3	10.7 (1.7)	6.4 (0.1)	4.4 (0.4)

* Temperature adjustment for 3.0 T data as described in methods (section 7.4.7)

Figs. 7.4 and 7.5 show gadofosveset, gadoxetate and gadobenate model fits (Eq. 3.10) plotted against actual ΔR_1 and ΔR_2 data points for three (gadofosveset) or two (gadoxetate and gadobenate) C_{sa} values at 3.0 T (Fig. 7.4) and 4.7 T (Fig. 7.5), using the mean individual relaxivities in Table 7.3, along with a linear fit to the gadopentetate data.

The bound relaxivity values in Table 7.3 were based on a range of C_{sa} values. Observed relaxivity values (r_{1obs} and r_{2obs}) were not included in this table as it was expected there may be an underlying relationship between observed relaxivity and C_{sa}. Fig. 7.6 shows the variation in observed relaxivity with C_{sa} at 3.0 T and 4.7 T, based on a linear fit to ΔR_1 and ΔR_2 data points for the BSA solutions.

Fig. 7.7 shows calculated bound fractions derived from ΔR_1 and ΔR_2 measurements (Eqs. 7.5 and 7.7) for gadofosveset, gadoxetate and gadobenate, at all albumin concentrations and at 3.0 T and 4.7 T, along with theoretical bound fractions for each albumin concentration (Eq. 7.2).

In Fig. 7.8 calculated C_{sa} values (using Eq. 7.9) are compared to actual values for each solution using individually derived relaxivity values at 3.0 T and 4.7 T. Two data points for gadofosveset at 4.7 T, one point for gadobenate at 3.0 T and two points for gadobenate at 4.7 T are missing from these plots as they

were outside the range shown (calculated C_{sa} more than double actual C_{sa}). Four gadofosveset data points at 4.7 T violated the inequality described in Eq. 7.10 and gave negative values of calculated C_{sa}, and were therefore also excluded. For gadofosveset, the model-derived C_{sa} values correlate with actual C_{sa} at a statistically significant level at both field strengths (Pearson correlation coefficients of 0.95 and 0.88 for 3.0 T and 4.7 T, respectively). If the two points not shown in Fig 7.8b for gadofosveset are excluded from the calculation, the Pearson correlation at 4.7 T increases to 0.95. For gadoxetate, a significant correlation between actual and calculated C_{sa} is seen at 4.7 T, but not at 3.0 T (Pearson correlations of 0.89 and 0.33, respectively). For gadobenate, no correlation was seen between actual and calculated C_{sa} at either field (-0.13 at 3.0 T and -0.03 at 4.7 T); even excluding the two data points not shown in Fig. 7.8f, the correlation is still not significant (0.37).

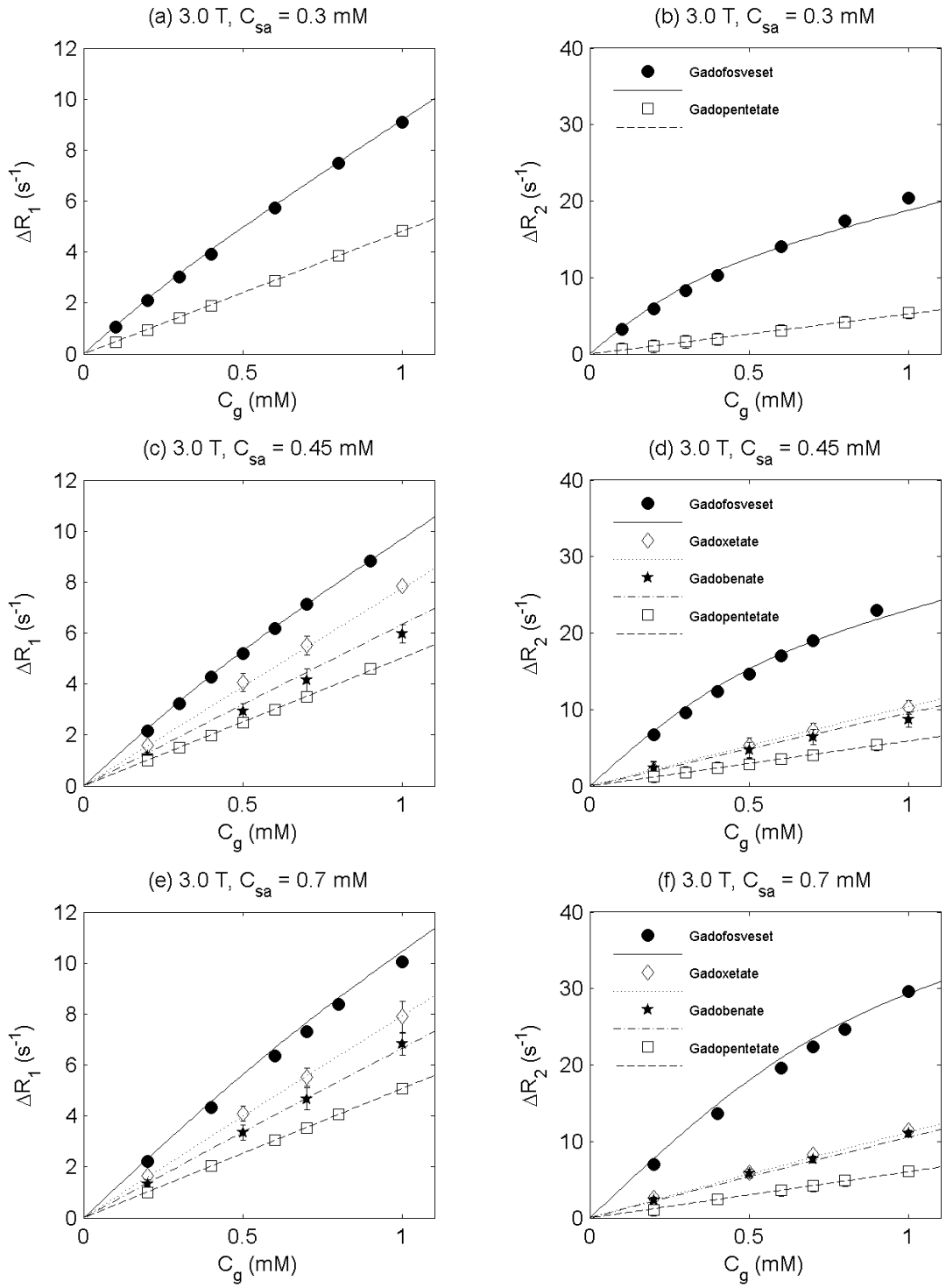

Figure 7.4: ΔR_1 (left column) and ΔR_2 (right column) values at 3.0 T (at room temperature) for gadofosveset (circles) and gadopentetate (squares) at C_{sa} = 0.3, 0.45 and 0.7 mM, and gadoxetate (diamonds) and gadobenate (stars) at C_{sa} = 0.45 and 0.7 mM; error bars indicate 95% confidence intervals. Gadofosveset, gadoxetate and gadobenate model fits (Eq. 3.10, solid, dotted and dot-dash lines, respectively) are represented using mean relaxivity values (Table 7.3); a linear fit is applied to gadopentetate data (Eq. 4.1, dashed line)

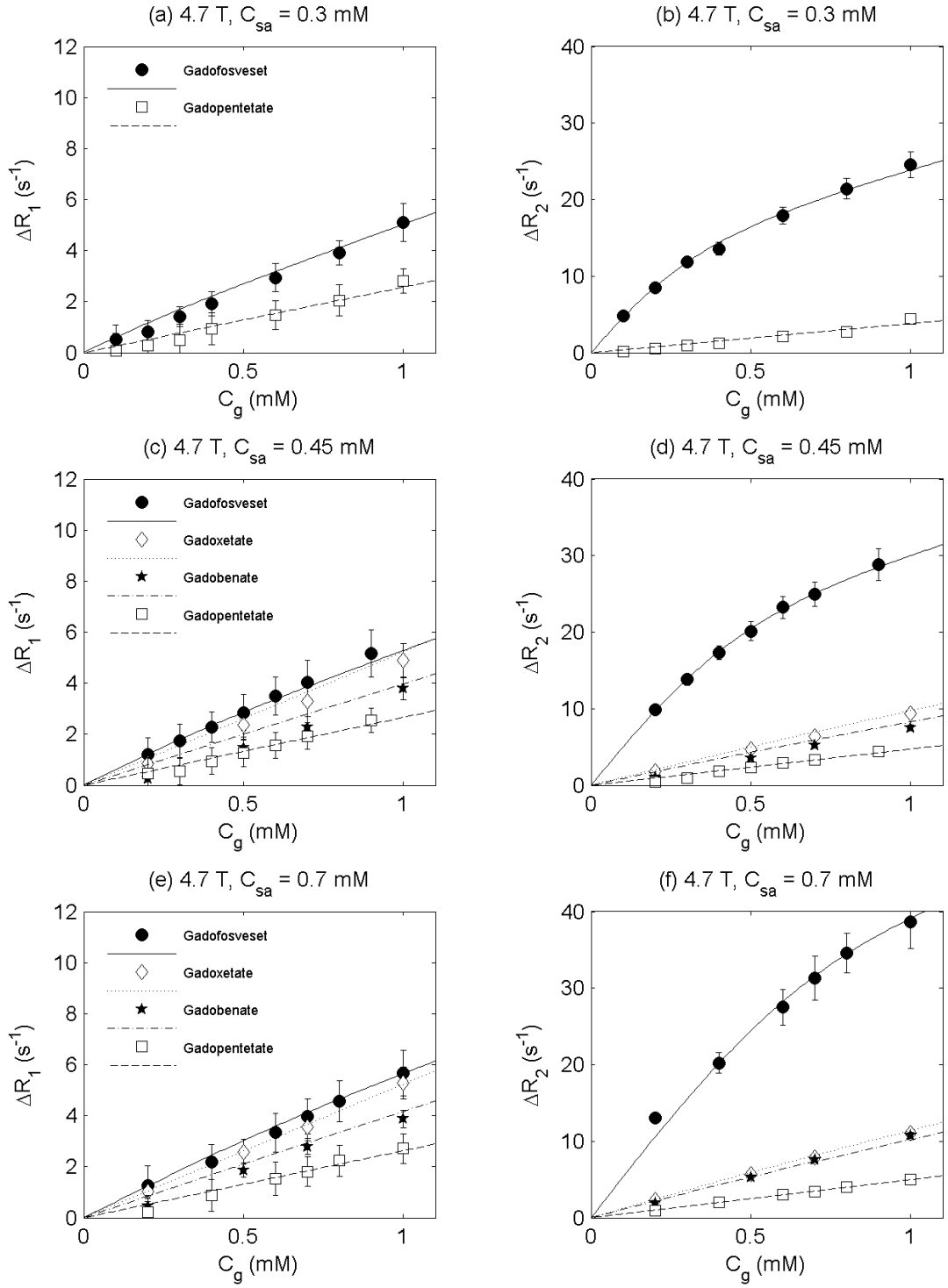

Figure 7.5: ΔR_1 (left column) and ΔR_2 (right column) values at 4.7 T (at body temperature) for gadofosveset (circles) and gadopentetate (squares) at C_{sa} = 0.3, 0.45 and 0.7 mM, and gadoxetate (diamonds) and gadobenate (stars) at C_{sa} = 0.45 and 0.7 mM; error bars indicate 95% confidence intervals. Gadofosveset, gadoxetate and gadobenate model fits (Eq. 3.10, solid, dotted and dot-dash lines, respectively) are represented using mean relaxivity values (Table 7.3); a linear fit is applied to gadopentetate data (Eq. 4.1, dashed line)

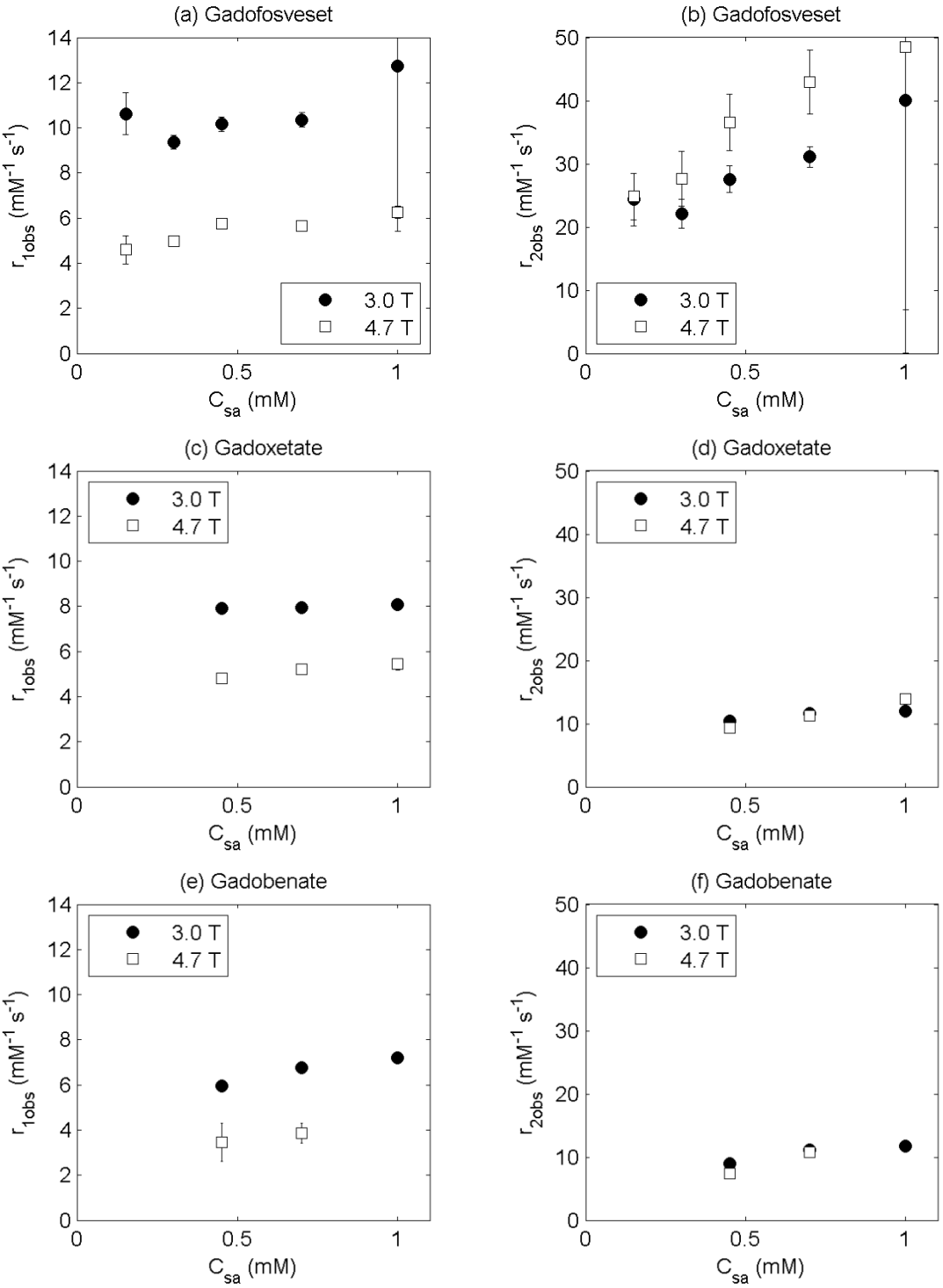

Figure 7.6: Variation of observed relaxivity (r_{1obs}, left column; r_{2obs}, right column) with C_{sa} at 3.0 T (circles) and 4.7 T (squares), based on linear fit to BSA ΔR_1 and ΔR_2 values

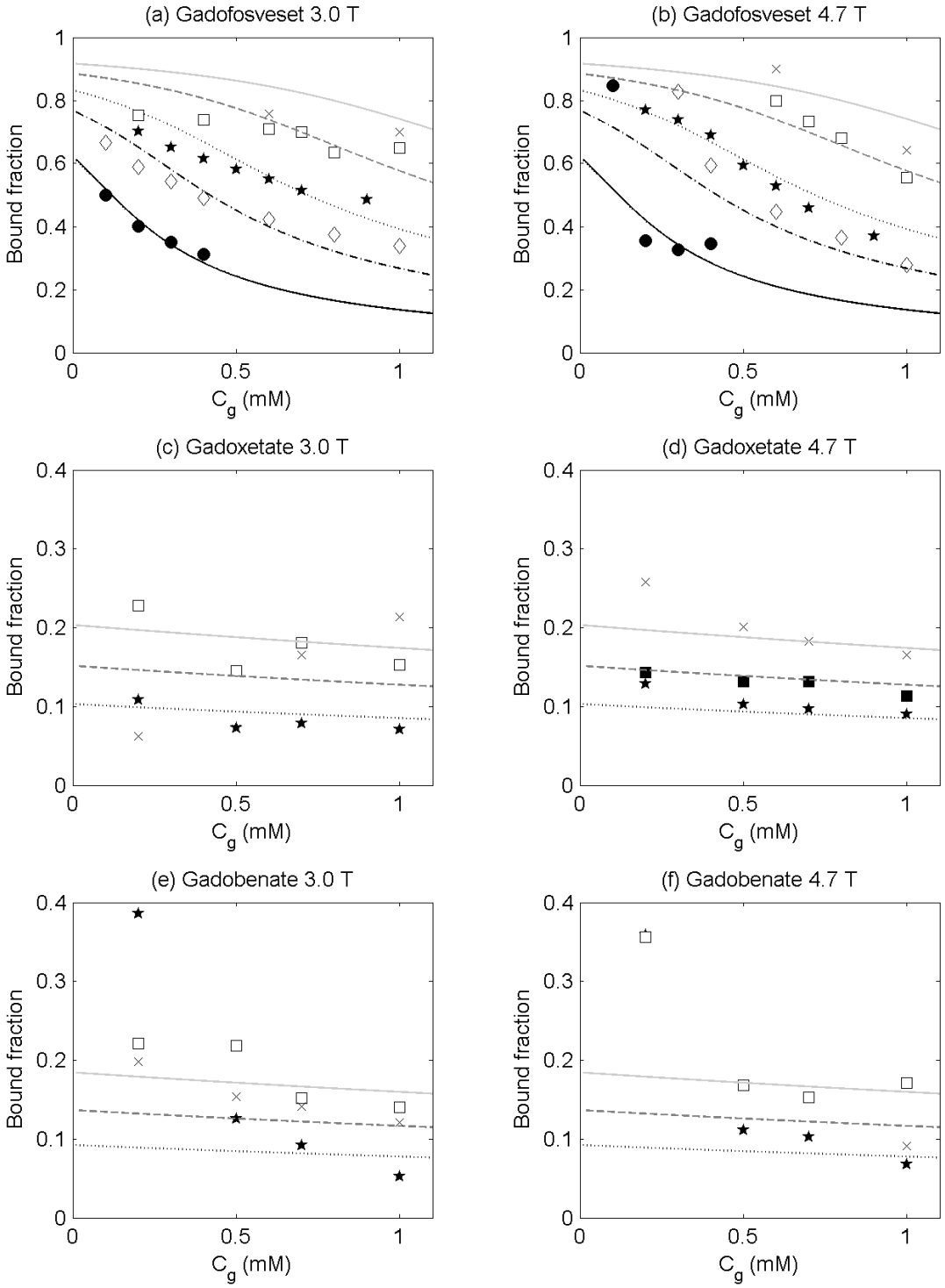

Figure 7.7: Calculated bound fraction (C_{gbound}/C_g) based on measured data using Eq. 7.5 and 7.7 at C_{sa} = 0.15 (circles), 0.3 (diamonds), 0.45 (stars), 0.7 (squares) and 1.0 mM (crosses); lines represent theoretical bound fraction using Eq. 7.2 and literature binding affinity values quoted previously at C_{sa} = 0.15 (black solid line), 0.3 (dot-dash line), 0.45 (dotted line), 0.7 (dashed line) and 1.0 mM (grey solid line)

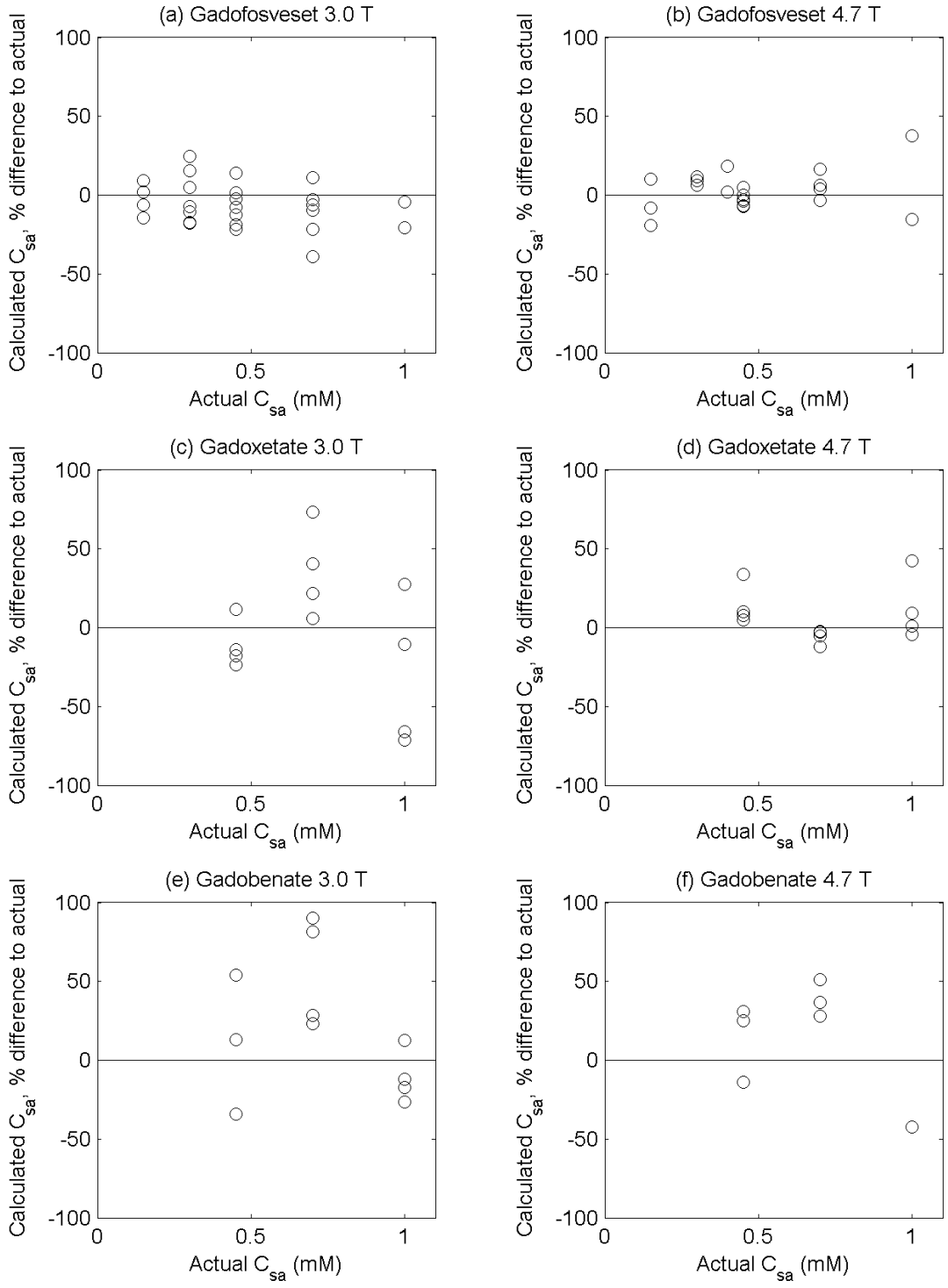

Figure 7.8: Spread of calculated C_{sa} values (represented as a percentage difference to actual C_{sa}) using Eq. 7.9; two data points in (b) are beyond plot scale (calculated C_{sa} = 0.55 mM, actual C_{sa} = 0.15 mM; calculated C_{sa} = 0.63 mM, actual C_{sa} = 0.3 mM); one data point in (e) is beyond plot scale (calculated C_{sa} = 2.82 mM, actual C_{sa} = 0.45 mM); two data points in (f) are beyond plot scale (calculated C_{sa} = 2.41 mM, actual C_{sa} = 0.45 mM; calculated C_{sa} = 2.53 mM, actual C_{sa} = 0.7 mM)

7.5.3 Volunteer data at 3.0 T

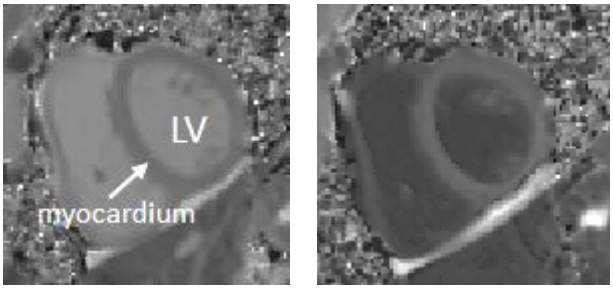

Figure 7.9: Example of (a) pre-contrast and (b) post-contrast T_1 maps (T_1 values calculated separately for each pixel and assigned a greyscale value) for a single volunteer, with left ventricle (LV) surrounded by myocardium in centre of image

Examples of pre- and post-contrast T_1 maps for one volunteer are shown in Fig. 7.9. Pre-contrast T_1 values in the left ventricle and myocardium were in the range 1493 – 1818 ms and 1099 – 1124 ms, respectively. Pre-contrast T_2 values in the left ventricle and myocardium were in the range 117 – 158 ms and 43 – 47 ms, respectively.

Calculated gadofosveset and albumin concentrations in the left ventricle and myocardium are shown in Fig. 7.10, with data for all seven volunteers plotted against time from first bolus administration. The models for calculating gadofosveset (Eq. 7.7) and albumin (Eq. 7.9) concentrations used the temperature-adjusted 3.0 T relaxivity values shown in Table 7.3.

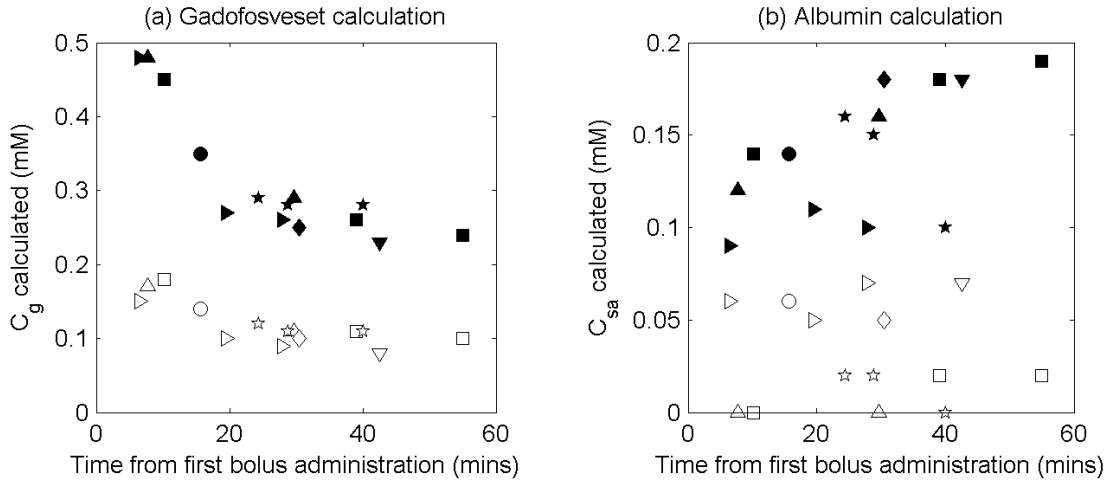

Figure 7.10: Calculated (a) gadofosveset and (b) albumin concentrations in left ventricle (filled symbols) and myocardium (open symbols) in healthy volunteers at 3.0 T. Each symbol shape represents a different volunteer; values are plotted against time from first administration of contrast agent (to mid-point between T_1 and T_2 image acquisition times)

7.6 DISCUSSION

Increased capillary leakage is symptomatic of a range of pathologies and healthy processes, resulting in rapid wash-in and wash-out of small molecule contrast agents and an increased transfer of macromolecules, including intravascular albumin, to the interstitial space. In vivo measurement of extravascular albumin content is not straightforward, although a range of invasive techniques are currently available. This study has explored the possibility of utilising albumin-binding Gd-based contrast agents to generate a novel and location-specific non-invasive method for measuring levels of albumin at moderate to high magnetic field strengths. The albumin-calculation model was assessed in vitro with agents binding in low and high fraction, and in vivo with the high-binding agent gadofosveset. Pre- and post-contrast R_1 and R_2 measurements are regularly carried out in MRI; the models presented here combine these changes in relaxation rate with calculated relaxivity values and a literature binding affinity value to produce a basic measure of tissue albumin concentration.

7.6.1 Simulation

At low gadofosveset C_g (Fig. 7.2a), a +10% inaccuracy in ΔR_1 or a -10% inaccuracy in ΔR_2 leads to an underestimation of C_{sa}; a -10% inaccuracy in ΔR_1 or a +10% inaccuracy in ΔR_2 causes the model to behave erratically. This is due to the denominator in the right-hand term of Eq. 7.9 ($r_{1bound}.\Delta R_2 - r_{2bound}.\Delta R_1$) approaching zero at a certain combination of shifted relaxation rates. Results from Chapter 4 suggest that an imprecision in ΔR_1 or ΔR_2 of 10% is not unfeasible, therefore it is important that relaxation rates are measured as accurately as possible, particularly where low gadofosveset concentrations are expected. At high gadofosveset C_g (Fig. 7.2b), the model performs much more consistently at intermediate C_{sa} values (0.2 – 0.8 mM): a +10% inaccuracy in ΔR_1 or a -10% inaccuracy in ΔR_2 leads to a slight underestimation of C_{sa}; a -10% inaccuracy in ΔR_1 or a +10% inaccuracy in ΔR_2 leads to a slight overestimation of C_{sa}. However, the model becomes increasingly inaccurate at very high or very low C_{sa} values.

For gadoxetate, an underestimation of C_{sa} results from a +10% inaccuracy in ΔR_1 or a -10% inaccuracy in ΔR_2; an overestimation of C_{sa} is caused by a -10% inaccuracy in ΔR_1 or a +10% inaccuracy in ΔR_2. The pattern is very similar at both C_g = 0.1 mM (Fig. 7.2c) and C_g = 1.0 mM (Fig. 7.2d), and shows that calculated C_{sa} values using gadoxetate are more susceptible to inaccuracies in ΔR_1 and ΔR_2 at higher C_g values than gadofosveset. These simulations were not carried out for gadobenate, but the patterns would be expected to be very similar to those of gadoxetate.

Although these simulations at the extreme limits of the expected range of imprecision in ΔR_1 and ΔR_2 are useful to assess model robustness, a more realistic simulation would incorporate a Gaussian distribution within this range of imprecision. Applying such a distribution to a randomly varying error in ΔR_1 or ΔR_2 for gadofosveset at a concentration of 0.5 mM (Fig. 7.3), it can be seen that the majority of calculated C_{sa} values have an error much less than 50%.

Although the median value is accurate at lower C_{sa} values, the model begins to underestimate C_{sa} at high C_{sa} values.

7.6.2 In vitro model validation

Gadofosveset relaxivity

Calculated r_1 and r_2 relaxivity values at both 3.0 T and 4.7 T are in general agreement with previously published values (91). Using mean calculated relaxivity values, the model represents a good fit to gadofosveset ΔR_1 and ΔR_2 data points at all C_{sa} values (Figs. 7.4 and 7.5), suggesting that the assumption of a single binding site on the albumin molecule is adequate at these concentrations. The primary binding site is known to provide the greatest contribution to relaxivity (68), and it is unlikely that C_g levels would be sufficiently high in vivo during the post-bolus phase to necessitate inclusion of additional binding sites in this model (78). Although a literature K_a value of 11.0 mM^{-1} was assumed for these calculations, a plot of K_a at half and double this value was previously shown to make very little difference to a model fit of similar data (Chapter 4, Fig. 4.7). It should be noted that in vitro data at 3.0 T were acquired at room temperature (21 °C). An increase from room to body temperature reduces the relaxivity of the free gadofosveset molecule slightly; the relationship between the relaxivity of the bound gadofosveset molecule and temperature is additionally influenced by field strength, and will differ for r_{1bound} and r_{2bound}. An attempt was made to adjust room temperature 3.0 T relaxivities to their body temperature equivalents (Table 7.3), and the resulting values are similar to those published elsewhere (91). r_{2obs} shows a clear increase with increasing albumin concentrations at both field strengths (Fig. 7.6b), but this relationship is less clear for r_{1obs} (Fig. 7.6a).

The longitudinal relaxivity values presented here for gadofosveset differ slightly from those calculated in Chapter 4. r_{1free} estimates are 7% and 12% lower at 3.0 T and 4.7 T, respectively, in this chapter than estimated in Chapter 4. However, r_{1free} values in Chapter 4 were based on 8 gadofosveset

concentrations in the range 0.25 – 5.0 mM (with four C_g values ≤ 1.0 mM); the r_{1free} values in this chapter were based on 10 C_g values in the range 0.1 – 1.0 mM. It is possible that some nonlinearity at very high C_g was introduced in the Chapter 4 data that may have skewed the results slightly. r_{1bound} values are 2% higher and 12% lower at 3.0 T and 4.7 T, respectively, in this chapter than in Chapter 4. The r_{1bound} values in Chapter 4 were calculated based on solutions of gadofosveset at concentrations up to 0.75 mM at a single fixed serum albumin concentration (C_{sa} = 0.67 mM), whereas the r_{1bound} values in this chapter are based on a range of C_g concentrations up to 1 mM at five C_{sa} values between 0.15 mM and 1.0 mM. It is possible that the larger number of data points used for model fitting in this chapter (28 points, compared to just 8 in Chapter 4), along with a greater range of albumin concentrations, make the calculated values in this chapter more precise.

Gadoxetate and gadobenate relaxivity

Free relaxivity values for gadoxetate and gadobenate at 3.0 T and 4.7 T are similar to those published elsewhere (91). It is difficult to find published relaxivity values for the bound molecule at these field strengths, so the calculated values could not be directly verified. However, observed relaxivities at C_{sa} = 0.7 mM (Fig. 7.6c to 7.6f), based on a linear fit to ΔR_1 and ΔR_2 values at all C_g values, are comparable with those published elsewhere (91).

r_{1free} values for gadoxetate and gadobenate are identical in this chapter to those values given in Chapter 4, as the same solution combinations were used. At 3.0 T, there was very little difference between r_{1bound} values in Chapter 4 and those given in this chapter. However, at 4.7 T, r_{1bound} values were 20% (gadoxetate) and 54% (gadobenate) higher in this chapter than in Chapter 4. Although these differences may appear large, they are not statistically significant as the 95% confidence intervals overlap. The relatively large confidence intervals suggest it is more difficult to accurately determine bound relaxivity values for these agents than for gadofosveset.

As may be expected by their relative binding affinities, ΔR_1 and ΔR_2 values plotted in Fig. 7.4 and 7.5 are higher for gadoxetate and gadobenate than those for gadopentetate but lower than those for gadofosveset. As with gadofosveset, ΔR_1 values decrease with field strength; however, unlike gadofosveset, where ΔR_2 values increase between 3.0 T and 4.7 T, the ΔR_2 values for both gadoxetate and gadobenate change very little with field strength.

Bound fraction calculations

Calculated bound fractions for gadofosveset are in good general agreement with theoretical expected values at 3.0 T (Fig. 7.7a). At 4.7 T (Fig. 7.7b), a consistent pattern still generally holds, although the value at C_{sa} = 0.15 mM, C_g = 0.1 mM is higher than expected. For gadoxetate at 3.0 T (Fig. 7.7c), calculated bound fractions at C_{sa} = 1.0 mM do not behave as expected (increasing, instead of decreasing, with C_g), but bound fractions at other C_{sa} values are closer to their theoretical equivalents. For gadoxetate at 4.7 T (Fig. 7.7d), the bound fraction at C_g = 0.2 mM, C_{sa} = 1.0 mM is higher than expected, but all other values are close to their expected values. For gadobenate at both fields (Fig. 7.7e and 7.7f), the bound fractions at the lowest C_g appear to be too high. This pattern of high calculated bound fraction at low C_g may be the result of the relative uncertainty in measured R_{i0} (relaxation rates at C_g = 0 mM) having a greater influence on the ΔR_i values at low C_g.

A study which derived bound fractions from relaxation rate measurements in rabbits (78) found bound fractions at 300 s post-bolus of 0.77 and 0.18 for gadofosveset and gadobenate, respectively (at C_g values of approximately 0.4 mM). Assuming a plasma albumin concentration of 3.9% (approximately 0.6 mM) in rabbits (79), the points plotted in Fig. 7.7 which are closest to these C_g and C_{sa} values correlate reasonably well.

Albumin calculations

If negative calculated C_{sa} values resulting from measurement imprecision are excluded, a comparison of the remaining calculated and actual C_{sa} values for gadofosveset (Fig. 7.8a and 7.6b) shows a correlation at a statistically significant level at both field strengths. Two further data points at 4.7 T were beyond the chosen scale in Fig. 7.8b, possibly as a result of imprecision in ΔR_1 and ΔR_2 measurement; if these points are also excluded, the correlation at 4.7 T is strengthened.

For gadoxetate, a significant correlation between actual and calculated C_{sa} is seen at 4.7 T (Fig. 7.8d), but not at 3.0 T (Fig. 7.8c). For gadobenate, no correlation was seen between actual and calculated C_{sa} at either field (Fig. 7.8e and 7.8f); the correlation improves if the two data points not shown in Fig. 7.8f are excluded, but not to a statistically significant level.

These results highlight the potential difficulty in applying the albumin-calculation model to agents such as gadoxetate or gadobenate, which bind to albumin at a relatively low fraction. Although the overall performance of gadofosveset in calculating C_{sa} is better, there are still data points where the model is inaccurate or fails altogether (producing negative C_{sa} estimates). Simulated errors in calculated C_{sa} (Figs. 7.2 and 7.3) suggest the model is susceptible to imprecision in measured relaxation rates.

Although all three albumin-binding contrast agents were assessed at the same contrast agent concentrations, gadobenate is used at a higher standard clinical dose (0.1 mmol kg^{-1}) compared to gadofosveset (0.03 mmol kg^{-1}) or gadoxetate (0.025 mmol kg^{-1}) (Table 2.1 in Chapter 2). This higher gadobenate dose gives in vivo concentrations 3 – 4 times those of gadofosveset or gadoxetate, but as can be seen from Fig 7.1b bound fraction would only be slightly lower at these higher concentrations. As the albumin-calculation model was assessed here across a range of albumin and contrast agent concentrations, the results are still expected to be relevant.

The albumin calculation model presented here is expected to work well for gadofosveset at higher B_0 values (3.0 T and above), where there is a large difference between r_{2bound} and r_{2free} but a small difference between r_{1bound} and r_{1free}. At low fields, r_{1bound} is close to r_{2bound} and the difference between ΔR_1 and ΔR_2 is small. In this case, the precision of the model input parameters would be insufficient to overcome the sensitivity of the model to the variability in those parameters. At very high B_0, r_{1bound} and r_{1free} values for gadofosveset may be considered equivalent and the model may be simplified to incorporate a linear relationship between ΔR_1 and C_g. The C_g calculation described in Eq. 7.7 may then be represented as $C_g = \Delta R_1 / r_1$.

An underlying correlation between relaxivity and protein content has been shown in previous studies for Gd-based contrast agents not conventionally described as albumin binding (41, 251). In vitro gadopentetate ΔR_2 data points are well represented here by a linear fit (Figs. 7.4 and 7.5), suggesting no observable influence of weak binding on contrast agent relaxivity at the albumin levels used in this study. Without separate bound and free transverse relaxivities, gadopentetate provides no means of estimating C_{sa} through application of the model presented here. The high binding affinity of gadofosveset makes it a much more sensitive biomarker of albumin.

7.6.3 In vivo feasibility

Gadofosveset-enhanced cardiovascular imaging is an area of active research (99, 100, 102, 106, 252), and likely to remain so in North America where the agent is available under the trade name Ablavar. One potential clinical application of the technique for calculating albumin concentration relates to myocardial infarction, therefore a feasibility assessment utilising human cardiac images was considered relevant. Cardiac imaging has the advantage of enabling direct comparison of calculated albumin values from blood in the left ventricle and from highly perfused myocardial tissue. However, before the

model can be assessed, motion correction and other technical challenges must be overcome.

Pre-contrast T_1 and T_2 values obtained here correlate well with literature values in blood (253, 254) and in the myocardium (253, 255, 256). Combining data from seven volunteers with images acquired at a range of time points gave remarkably consistent values of the two model input variables ΔR_1 and ΔR_2, and supported calculation of appropriate C_g values in both the left ventricle and the myocardium (Fig. 7.10a). As expected, gadofosveset concentration peaks at the earliest time points post-bolus and decreases towards an equilibrium value, although this was not a dynamic acquisition therefore the temporal resolution is such that the bolus peak is not fully described. In the left ventricle, a maximum value of 0.48 mM is calculated at the earliest time points (6 – 8 min post-bolus), with a later calculated C_g of 0.24 mM (at 55 min post-bolus). Lower peak and equilibrium gadofosveset concentrations are observed in the myocardium (0.18 mM and 0.1 mM, respectively).

At a dose of 0.03 mmol kg^{-1}, the average blood concentration of gadofosveset for an 81 kg adult with a total blood volume of 6.4 L would be 0.4 mM; allowing for some extravasation and excretion, the gadofosveset values calculated here in the left ventricle appear reasonable. For a small molecule agent such as gadopentetate, approximately 50% may diffuse to the extravascular space from the blood on the first pass through the capillary bed (257). Although, as a ‘blood pool’ agent, gadofosveset may be expected to remain predominantly within the intravascular space, at high concentrations (immediately after bolus injection, for example) the bound fraction will be low and the extravasation rate may be similar to that of a conventional agent (258). A study in rabbits showed that 61% of injected gadofosveset was still in the blood at 1 minute post-injection (78). Certainly, a reduction in C_g between the left ventricle and myocardium is expected, as noted in the relative values here.

Unlike gadofosveset, albumin concentration is expected to remain consistent within an individual for the image acquisition duration. Although there is some within-subject variability (Fig. 7.10b), this variability may be representative of an

imprecision in the data acquisition and does not correlate with time post-bolus. The mean calculated albumin concentration in the left ventricle of the seven volunteers was 0.14 mM (range 0.10 – 0.18 mM); in the myocardium the mean calculated C_{sa} was 0.03 mM (range 0.00 – 0.07 mM).

A reference measure of albumin concentration was not available for comparison. Serum albumin levels in plasma (C_{sa_plasma}) are expected to be approximately 3.5 – 5.0 g dl^{-1} (0.52 – 0.74 mM) (237). Assuming a haematocrit (Hct) of 0.42, this equates to albumin levels in whole blood of 0.30 – 0.43 mM (where blood concentration = $C_{sa\_plasma}.(1 – Hct)$). Previous studies quote interstitial fluid albumin concentrations ($C_{sa\_interstitial}$) of 0.2 – 0.4 mM (83, 241, 242). However, the myocardium ROI contains intravascular, extravascular extracellular and intracellular spaces. Neglecting the intracellular space, as gadofosveset cannot directly access it, and assuming an extracellular volume fraction (EVF) of 0.25 (259), a myocardial blood volume (MBV) of 8% (260) and a haematocrit in capillaries (Hct_{cap}) of 0.25, tissue albumin (C_{sa_tissue}, measurable using gadofosveset) may be expected to be in the range 0.07 – 0.11 mM (where $C_{sa\_tissue} = MBV.(C_{sa\_plasma}.(1 – Hct_{cap})) + C_{sa\_interstitial}.(EVF – MBV)$). This range of expected values assumes that all blood vessels in the myocardium are capillaries; in reality, a proportion would be larger than capillaries and would therefore have a higher Hct, leading to a slightly lower range of expected C_{sa_tissue} values.

Calculated C_{sa} values were lower than might be expected in healthy volunteers. This underestimation may be partly attributable to the relative timings of the T_1 and T_2 measurements used as the basis for calculating C_{sa}. Images used for T_1 and T_2 measurement were taken at different time points post-bolus, with the images for T_2 measurement acquired 1 – 2 minutes after the images for T_1 measurement (Table 7.2). This time difference is unlikely to be an issue at the later time points (within the equilibrium phase). However, at earlier time points, where the concentration of gadofosveset is initially high and then drops rapidly, ΔR_1 values at the T_1 time point are higher than they would be at the equivalent T_2 time point. The model is sensitive to the ratio of ΔR_2 to ΔR_1; if ΔR_1 is artificially high in relation to ΔR_2, the resulting calculated C_{sa} will be lower. This

may account for an element of model underestimation in vivo, particularly at the earlier time points. Also, the gadofosveset dose was administered in the form of a small timing bolus followed 2 – 8 minutes later by the main bolus. Again, this is unlikely to have an effect at equilibrium, but could influence calculations at the earliest time points.

Another consideration is whether the relaxivities used in C_{sa} calculation, derived in vitro, were directly applicable in vivo. These relaxivities were based on values determined at room temperature and converted to body temperature; it is possible that the temperature conversion factor was slightly inaccurate. In addition, bovine serum albumin was used in vitro; although bovine serum albumin is structurally similar to human serum albumin, and BSA is often used as a surrogate for HSA in laboratory studies (for example, (261)), the molecules may display slightly different binding properties (165). There is also some evidence to suggest that relaxivities derived in vitro for a non-binding Gd agent may be higher than equivalent measurements in vivo (262), which may have implications for the free relaxivity measurements used in this study.

It should also be noted that the bound gadofosveset fraction will be at its maximum in the left ventricle at equilibrium, where $C_{sa} > C_g$. The model is less sensitive in this scenario, as confirmed by the observed underestimation of C_{sa} at higher albumin concentrations in vitro at 3.0 T (Fig. 7.8a). This feature is also noted in the median C_{sa} values from the simulated data (Fig. 7.3b). Although calculations in the left ventricle were carried out in this study, the method may not be appropriate or necessary here as albumin levels in blood can be readily measured from blood samples. The primary utility of the method may be in providing measurement of albumin concentration in tissue, where C_g is lower and C_{sa} is conventionally difficult to acquire.

A previous study using the contrast agent gadobenate (152) suggested that renal protein leakage could be identified by analysing tubular flow differences following injection of two contrast agents, one binding and one non-binding. Attempts have also been made to map protein levels by utilising the distinct field dependency of the bound and free gadofosveset molecule (termed delta

relaxation enhanced MR, DREMR) (263, 264), although this approach requires the use of additional hardware to modulate B_0. The advantage of the method described in this study over either of these approaches is that it only requires a single contrast agent injection and may be readily derived from routinely acquired R_1 and R_2 measurements using conventional equipment.

It should be noted that a single MRI voxel on the cardiac T_1 maps represents a volume of tissue 1.9 x 1.4 x 8.0 mm, and on the T_2 maps represents a volume of 2.3 x 2.3 x 8.0 mm. Each myocardial voxel will contain a combination of interstitial, intravascular and intracellular space, therefore it is difficult to use this method to isolate and measure interstitial albumin. In reality, the measurement of albumin will relate to tissue levels, and the interstitial proportion will depend on the density of vessels and cells within this voxel.

7.6.4 Summary

In summary, the albumin calculation model presented here demonstrates the feasibility of determining in vitro serum albumin concentration using pre- and post-gadofosveset measurements of R_1 and R_2 at high B_0 values. The method was successfully validated using in vitro samples at 3.0 T and 4.7 T. Extending the methodology to other albumin-binding agents, gadoxetate and gadobenate, was less successful, due to the low binding fraction of these agents. It was not possible to implement the method using the non-binding agent gadopentetate.

Feasibility assessment in a small number of human volunteers was performed using gadofosveset, and consistent ΔR_1, ΔR_2 and C_g values were determined. Underestimation of C_{sa} may be the result of several contributing factors, including the timing of the image acquisitions and translation of in vitro relaxivities. Due to the withdrawal of gadofosveset from the European market, it was not possible to complete additional in vivo experiments. However, further in vivo assessment is suggested, to include: simultaneous T_1 and T_2 measurement; additionally acquiring images between the timing bolus and the

main bolus; and blood sampling to establish Hct and reference blood albumin levels.

This novel approach may enable non-invasive assessment of extravascular leakage of albumin, utilising parameters acquired during routine imaging, in regions where implementation of invasive techniques for measurement of interstitial albumin is conventionally challenging. A range of potential clinical applications are envisaged, including assessment of myocardial infarction, tumour angiogenesis and response to treatment.

CHAPTER 8: SUMMARY AND CONCLUSIONS

8.1 SUMMARY

The albumin-binding affinity of gadofosveset makes this molecule unique amongst the gadolinium-based clinically approved MRI contrast agents. Binding prolongs its intravascular retention and increases the relaxivity of the agent, primarily through reduction of the rotational correlation time. However, the fraction of gadofosveset that binds varies with concentration and the relaxivities of the bound and free molecules display differential responses to variations in field strength and temperature.

Although originally intended as an assessment of the in vivo use of gadofosveset for dynamic contrast-enhanced MRI studies, the lack of availability of gadofosveset due to its withdrawal from the European market (shortly after the project commenced) limited the extent to which in vivo studies could be carried out. As a result, the aims of the project were adjusted to incorporate further in vitro characterisation of gadofosveset and other albumin-binding agents, along with the development of a technique that would enable accurate measurement of a vascular input function which may be of value in future tracer kinetic studies.

The first aim of this study, therefore, was to address gaps in the current gadofosveset literature, by determining the relaxivity of the bound and free molecule across a range of field strengths, and at two temperatures. In addition, the study addressed the issue of binding sites, by comparing models incorporating one, two and three bound molecules at a fixed albumin concentration, and assessed the general influence of binding by measuring relaxation rates and bound fractions at a range of contrast agent and serum albumin concentrations, and for gadofosveset in mouse plasma.

The second aim of the study was to assess several novel techniques for exploiting the albumin-binding nature of gadofosveset. This included developing a method for combining blood sampling and spectroscopic techniques, which may enable accurate gadofosveset concentration measurement in small mammals immediately following bolus injection. These measurements may be converted to a vascular input function for use in tracer kinetic modelling. In addition, the possibility of combining the albumin-binding properties of gadofosveset with the macromolecule-sensitive imaging technique of spin locking was explored, along with the feasibility of using gadofosveset as a biomarker for tissue albumin.

A third aim of the study was to extend these in vitro experiments to two other albumin-binding agents, gadoxetate and gadobenate. The lower binding affinity of these agents gave an opportunity to compare the properties of high- and low-binding agents, and determine the extent to which novel techniques suggested for gadofosveset may also be appropriate for gadoxetate and gadobenate.

8.1.1 Experimental results: Relaxivity

Bound, free and observed longitudinal relaxivity values were calculated for gadofosveset at field strengths ranging from 0.47 T to 9.4 T at room and body temperature. The general relationship between gadofosveset relaxivity and field strength has been shown in previous studies and was confirmed with these results:

- The longitudinal relaxivity of the free molecule is low at low field and reduces slightly with field strength.
- The longitudinal relaxivity of the bound molecule is high at low field but reduces rapidly with field strength, and is equivalent to the relaxivity of the free molecule at high field.
- The transverse relaxivity of the bound molecule increases with field strength, but the transverse relaxivity of the free molecule decrease slightly.

Calculated bound and free relaxivities for gadoxetate and gadobenate are similar to gadofosveset (a direct result of the similarity of their core structures, as predicted by basic contrast agent theory) and display a similar variation with field strength. Differences in observed longitudinal relaxivity are due to the significantly higher albumin binding affinity for gadofosveset than for gadoxetate or gadobenate.

Variations in relaxivity with temperature may have implications for translation of in vitro results. Measurements at room and body temperature suggest that, within this general temperature range:

- Bound longitudinal relaxivity increases with temperature at low field but has little variation with temperature at high field.
- Bound transverse relaxivity increases with temperature at all fields.
- Free (longitudinal and transverse) relaxivity decreases as temperature increases.

Novel findings:

- Separate relaxivities of the bound and free molecule at 3.0 T and above have not previously been published for gadofosveset, gadoxetate or gadobenate.
- The variation of bound relaxivity with temperature has not previously been shown at high field.

8.1.2 Experimental results: Bound fraction

Binding has been shown to significantly alter observed longitudinal relaxivity at low field (where bound relaxivity is much higher than free relaxivity) but has little influence on observed relaxivity at high field (where bound and free longitudinal relaxivities are effectively equivalent). A comparison of measured gadofosveset relaxation rates at low field showed significantly higher relaxation rates in serum albumin (at a concentration of 0.67 mM) than in mouse plasma. This is a direct reflection of the difference in albumin concentration between the

two solutions. At high field, relaxation rates for serum albumin were similar to those for mouse plasma, due to the similarity of bound and free relaxivities. This may have implications for using the results of pre-clinical studies in small mammals carried out at high field to predict the outcome of human clinical studies at lower fields.

Calculated bound fractions based on measured relaxation rates are close to the values predicted by theory, with bound fraction being highest at lowest contrast agent concentration and increasing with albumin concentration.

Novel findings:

- To the author's knowledge, a comparison of relaxation rates for gadofosveset in serum albumin and mouse plasma has not previously been carried out at high field.
- The method for calculating bound fraction from measured longitudinal and transverse relaxation rates has not previously been reported.

8.1.3 Experimental results: Binding sites

At low field, model-derived relaxation rates were lower than measured values at high gadofosveset concentration. To compensate for this potential underestimation it may be necessary to account for the influence of additional binding sites at low field, particularly at higher gadofosveset concentrations. A proposed method for including a second and/or third binding site, according to gadofosveset concentration, improved the model fit to measured relaxation rates at 0.47 T, but had little influence at higher fields. Inclusion of an additional binding site makes very little difference to the model fits for gadoxetate or gadobenate, due to the lower bound fraction for these agents. Although gadobenate has a higher approved clinical dose, it is unlikely that concentrations will be high enough to warrant consideration of additional binding sites.

Novel findings:

- The method for including additional binding sites is a novel variation of an existing model.
- To the author's knowledge, a relaxation rate model incorporating two binding sites has not previously been applied to gadoxetate or gadobenate measurements.

8.1.4 Experimental results: Gadolinium measurement

A method was developed to accurately determine gadolinium levels in micro-samples of blood spotted onto card, using inductively-coupled plasma mass spectrometry. This technique requires a very small quantity of blood (approximately 10 – 12 μL) per sample, making it ideal for use in small mammals, and its accuracy was demonstrated for mouse blood samples spiked with gadofosveset. The proposed method has the potential to capture the first pass of a bolus of contrast agent in a small mammal.

Novel findings:

- The combination of acquiring blood samples using dried blood spotting and analysing the gadolinium content using ICP-MS is novel, although previous studies have used ICP-MS to measure gadolinium directly from blood samples.

8.1.5 Experimental results: Spin locking

Applying spin locking to gadofosveset samples at a high magnetic field produces significantly higher relaxation rates compared with longitudinal relaxation rates at the same field. The difference between spin-lock relaxation rates in the presence and absence of albumin is comparable with the difference observed for transverse relaxation rates in the presence and absence of albumin.

Novel findings:

- The experimental results presented here are novel and form the basis of the first published paper combining spin locking with gadofosveset.

8.1.6 Experimental results: Albumin biomarker

A suggested model for calculating albumin concentration, based on longitudinal and transverse relaxation rate measurements, demonstrated a significant correlation between calculated and actual values at 3.0 T and 4.7 T for gadofosveset, although supplementary simulations suggest the model may be vulnerable to imprecision in relaxation rate measurement at low gadofosveset concentrations. Extending this model to gadoxetate and gadobenate, a significant correlation between calculated and actual albumin concentration was found for gadoxetate at 4.7 T, but not at 3.0 T; no correlation was seen for gadobenate at either field. It is suggested that the low bound fraction for these two agents increases the sensitivity to imprecision in the relaxation rate measurements. Although albumin calculations were lower than expected when the model was applied to in vivo gadofosveset data from healthy volunteers, actual albumin concentrations were not available for comparison.

Novel findings:

- The described method for calculating albumin concentration from measured gadofosveset relaxation rates, and its potential application as a biomarker for albumin, has not previously been published.

8.2 STUDY LIMITATIONS

The primary limitation of this study, resulting from the withdrawal of gadofosveset from the European market soon after the project commenced, was the lack of in vivo data. Although in vitro samples were created at physiologically applicable concentrations, it was not possible to validate the

method for blood sampling (described in Chapter 5) or to assess the feasibility of applying spin locking (Chapter 6) in vivo. Through collaboration with a research team at Northwestern University, Chicago, some human volunteer images were acquired, enabling in vivo assessment of the albumin calculation model described in Chapter 7. Although calculated gadofosveset concentrations were within the expected range and it was possible to calculate albumin concentrations, comparison of these calculated values against a reference standard was not possible as blood samples were not taken at the time of imaging.

A second limitation was that 3.0 T in vitro data were acquired at room temperature only, due to the lack of an available heating mechanism for the clinical scanners. A method for converting room temperature relaxivities to body temperature was provided (Chapter 7), but this was based partly on extrapolation of relaxivities at other field strengths. In general, room and body temperatures did not match exactly across all field strengths, although this variation is unlikely to have a large influence on the measured results.

A third limitation was that in vitro samples were created using bovine serum albumin (BSA) rather than human serum albumin (HSA). Unlike in animal plasma, where albumin concentration may vary considerably by species, in vitro samples were created at fixed albumin concentrations, therefore any potential difference between results presented here and those acquired using HSA would be solely attributable to differences in binding characteristics. BSA is often used in laboratory experiments as a surrogate for HSA, and the two molecules are structurally very similar.

8.3 AREAS FOR FURTHER INVESTIGATION

As mentioned within the study limitations, the lack of availability of gadofosveset in Europe has limited the extent to which in vivo experiments could be carried out. A natural extension of the work presented here would be

to carry out these in vivo experiments in a location (such as North America) where gadofosveset is readily available. In Chapter 5 (section 5.5.2) a suggested methodology for in vivo validation of the blood sampling technique is provided, for use in small mammals following injection of gadofosveset. If in vivo validation were carried out, a vascular input function could be created and assessed against signal intensity measurements acquired using a dynamic MRI sequence. A representative vascular input function is essential in tracer kinetic modelling for determining accurate physiological parameters.

An extension of this work may involve improved use of the kinetic characteristics of the bound albumin molecule. General pharmacokinetic models do not currently accommodate the separate contributions of the bound and free gadofosveset molecule, resulting in potentially inaccurate calculated physiological parameters. Adapting existing kinetic models to improve perfusion and permeability quantification may facilitate the use of gadofosveset in the assessment of tumour angiogenesis and the diagnosis, staging and treatment response monitoring of a range of tumour types, for example. In this respect, bound and free relaxivity values calculated in this study at field strengths of 3.0 T and above may be of particular value.

The in vivo data used in the albumin calculation model (Chapter 7) may have benefited from alterations in the T_1 and T_2 acquisition times. Collection of blood samples for measurement of blood albumin concentration would be useful to enable a direct comparison with calculated blood albumin concentrations. In addition, the sensitivity of the model could be assessed by repeating the study in other tissue, where albumin levels may be expected to be low or high. Applying the model to regions where images are not influenced by cardiac or respiratory motion may also be of benefit for model assessment.

Differences in gadofosveset binding between HSA and BSA could be assessed by repeating in vitro experiments using HSA.

8.4 CONCLUSIONS AND FINAL REMARKS

This study has contributed to the existing knowledge base for gadofosveset by assessing the relaxivity response to changes in contrast agent and albumin concentration at both low and high field. In addition, novel techniques and potential clinical applications have been suggested and their validity assessed in vitro. The lower binding affinities of gadoxetate and gadobenate limit the extent to which these techniques may be of value for these agents. Although longitudinal relaxivity is increased by binding to albumin at low fields, it is unlikely that separate bound and free relaxivities need to be considered for gadoxetate or gadobenate at higher fields.

Without additional in vivo studies to support the positive gadofosveset results seen in vitro it is difficult to estimate the clinical value of implementing such techniques. However, it is suggested that the unique characteristics of gadofosveset warrant further in vivo investigation.

List of References

1. RICHARDSON, O.C., M.L.J. SCOTT, S.F. TANNER, J.C. WATERTON and D.L. BUCKLEY. Overcoming the low relaxivity of gadofosveset at high field with spin locking. *Magnetic Resonance in Medicine*, 2012, **68**(4), pp.1234-1238.
2. *NHS Reference Costs 2010-2011* [online]. 2011. [Accessed 23/04/13]. Available from: http://data.gov.uk/dataset/nhs-reference-costs-2010-11.
3. HANSON, L.G. Is quantum mechanics necessary for understanding magnetic resonance? *Concepts in Magnetic Resonance Part A*, 2008, **32A**(5), pp.329-340.
4. LEVITT, M.H. *Spin Dynamics: Basics of Nuclear Magnetic Resonance.* Chichester: John Wiley & Sons, 2001.
5. MERZBACHER, E. *Quantum mechanics.* 3rd ed. Chichester: Wiley, 1998.
6. PURCELL, E.M., H.C. TORREY and R.V. POUND. Resonance absorption by nuclear magnetic moments in a solid. *Physical Review*, 1946, **69**(1-2), pp.37-38.
7. BLOCH, F. Nuclear induction. *Physical Review*, 1946, **70**(7-8), pp.460-474.
8. LAUTERBUR, P.C. Image formation by induced local interactions: Examples employing nuclear magnetic resonance. *Nature*, 1973, **242**(5394), pp.190-191.
9. MANSFIELD, P. and A.A. MAUDSLEY. Medical imaging by NMR. *British Journal of Radiology*, 1977, **50**(591), pp.188-194.
10. HASHEMI, R.H., W.G. BRADLEY and C.J. LISANTI. *MRI: the basics.* 3rd ed. Philadelphia: Lippincott Williams & Wilkins, 2010.
11. MCROBBIE, D.W., E.A. MOORE, M.J. GRAVES and M.R. PRINCE. *MRI from picture to proton.* 2nd ed. Cambridge: Cambridge University Press, 2007.
12. AI, T., J.N. MORELLI, X. HU, D. HAO, F.L. GOERNER, B. AGER and V.M. RUNGE. A historical overview of magnetic resonance imaging, focusing on technological innovations. *Investigative Radiology*, 2012, **47**(12), pp.725-741.
13. WOLFF, S.D. and R.S. BALABAN. Magnetization transfer contrast (MTC) and tissue water proton relaxation in vivo. *Magnetic Resonance in Medicine*, 1989, **10**(1), pp.135-44.
14. WARD, K.M., A.H. ALETRAS and R.S. BALABAN. A new class of contrast agents for MRI based on proton chemical exchange dependent saturation transfer (CEST). *Journal of Magnetic Resonance*, 2000, **143**(1), pp.79-87.
15. SEPPONEN, R.E., J.A. POHJONEN, J.T. SIPPONEN and J.I. TANTTU. A method for T1-rho imaging. *Journal of Computer Assisted Tomography*, 1985, **9**(6), pp.1007-1011.
16. KWONG, K.K., J.W. BELLIVEAU, D.A. CHESLER, I.E. GOLDBERG, R.M. WEISSKOFF, B.P. PONCELET, D.N. KENNEDY, B.E. HOPPEL, M.S. COHEN, R. TURNER, H.-M. CHENG, T.J. BRADY and B.R. ROSEN. Dynamic magnetic resonance imaging of human brain activity during primary sensory stimulation. *Proceedings of the National*

Academy of Sciences of the United States of America, 1992, **89**(12), pp.5675-9.

17. DETRE, J.A. and D.C. ALSOP. Perfusion magnetic resonance imaging with continuous arterial spin labeling: methods and clinical applications in the central nervous system. *European Journal of Radiology*, 1999, **30**(2), pp.115-24.
18. HARTUNG, M.P., T.M. GRIST and C.J. FRANCOIS. Magnetic resonance angiography: Current status and future directions. *Journal of Cardiovascular Magnetic Resonance*, 2011, **13**(1).
19. SOURBRON, S., M. INGRISCH, A. SIEFERT, M. REISER and K. HERRMANN. Quantification of cerebral blood flow, cerebral blood volume, and blood-brain-barrier leakage with DCE-MRI. *Magnetic Resonance in Medicine*, 2009, **62**(1), pp.205-217.
20. DONALDSON, S.B., D.L. BUCKLEY, J.P. O'CONNOR, S.E. DAVIDSON, B.M. CARRINGTON, A.P. JONES and C.M.L. WEST. Enhancing fraction measured using dynamic contrast-enhanced MRI predicts disease-free survival in patients with carcinoma of the cervix. *British Journal of Cancer*, 2010, **102**(1), pp.23-26.
21. TOFTS, P.S., M. CUTAJAR, I.A. MENDICHOVSZKY, A.M. PETERS and I. GORDON. Precise measurement of renal filtration and vascular parameters using a two-compartment model for dynamic contrast-enhanced MRI of the kidney gives realistic normal values. *European Radiology*, 2012, **22**(6), pp.1320-1330.
22. LOW, R.N. Contrast agents for MR imaging of the liver. *Journal of Magnetic Resonance Imaging*, 1997, **7**(1), pp.56-67.
23. PADHANI, A.R., C.J. GAPINSKI, D.A. MACVICAR, G.J. PARKER, J. SUCKLING, P.B. REVELL, M.O. LEACH, D.P. DEARNALEY and J.E. HUSBAND. Dynamic contrast enhanced MRI of prostate cancer: correlation with morphology and tumour stage, histological grade and PSA. *Clinical Radiology*, 2000, **55**(2), pp.99-109.
24. AREF, M., A.R. CHAUDHARI, K.L. BAILEY, S. AREF and E.C. WIENER. Comparison of tumor histology to dynamic contrast enhanced magnetic resonance imaging-based physiological estimates. *Magnetic Resonance Imaging*, 2008, **26**(9), pp.1279-1293.
25. EVELHOCH, J.L. Key factors in the acquisition of contrast kinetic data for oncology. *Journal of Magnetic Resonance Imaging*, 1999, **10**(3), pp.254-259.
26. SOURBRON, S.P. and D.L. BUCKLEY. Tracer kinetic modelling in MRI: estimating perfusion and capillary permeability. *Physics in Medicine and Biology*, 2011, **57**(2), pp.R1-R33.
27. LEACH, M., B. MORGAN, P. TOFTS, D. BUCKLEY, W. HUANG, M. HORSFIELD, T. CHENEVERT, D. COLLINS, A. JACKSON, D. LOMAS, B. WHITCHER, L. CLARKE, R. PLUMMER, I. JUDSON, R. JONES, R. ALONZI, T. BRUNNER, D. KOH, P. MURPHY, J. WATERTON, G. PARKER, M. GRAVES, T. SCHEENEN, T. REDPATH, M. ORTON, G. KARCZMAR, H. HUISMAN, J. BARENTSZ, A. PADHANI and O.B.O.T.E.C.M.C.I.N.S. COMMITTEE. Imaging vascular function for early stage clinical trials using dynamic contrast-enhanced magnetic resonance imaging. *European Radiology*, 2012, **22**(7), pp.1451-1464.

28. BIGLANDS, J.D., A. RADJENOVIC and J.P. RIDGWAY. Cardiovascular magnetic resonance physics for clinicians: Part II. *Journal of Cardiovascular Magnetic Resonance*, 2012, **14**(1), pp.66-66.
29. WEISSLEDER, R., A. BOGDANOV, JR., C.H. TUNG and H.J. WEINMANN. Size optimization of synthetic graft copolymers for in vivo angiogenesis imaging. *Bioconjugate Chemistry*, 2001, **12**(2), pp.213-219.
30. TURETSCHEK, K., A. PREDA, V. NOVIKOV, R.C. BRASCH, H.J. WEINMANN, P. WUNDERBALDINGER and T.P.L. ROBERTS. Tumor microvascular changes in antiangiogenic treatment: Assessment by magnetic resonance contrast media of different molecular weights. *Journal of Magnetic Resonance Imaging*, 2004, **20**(1), pp.138-144.
31. BARRETT, T., M. BRECHBIEL, M. BERNARDO and P.L. CHOYKE. MRI of tumor angiogenesis. *Journal of Magnetic Resonance Imaging*, 2007, **26**(2), pp.235-249.
32. TÓTH, E., L. HELM and A.E. MERBACH. Relaxivity of gadolinium(III) complexes: Theory and mechanism. *In:* A.E. MERBACH and E. TÓTH, eds. *The chemistry of contrast agents in medical magnetic resonance imaging*. Chichester: John Wiley & Sons, 2001, pp.45-121.
33. KOENIG, S.H. From the relaxivity of Gd (DTPA) 2- to everything else. *Magnetic Resonance in Medicine*, 1991, **22**(2), pp.183-190.
34. CARAVAN, P., J.J. ELLISON, T.J. MCMURRY and R.B. LAUFFER. Gadolinium(III) chelates as MRI contrast agents: Structure, dynamics, and applications. *Chemical Reviews*, 1999, **99**(9), pp.2293-2352.
35. MANSSON, S. and A. BJORNERUD. Physical principles of medical imaging by nuclear magnetic resonance. *In:* A.E. MERBACH and E. TÓTH, eds. *The chemistry of contrast agents in medical magnetic resonance imaging*. Chichester: John Wiley & Sons, 2001, pp.1-44.
36. VILLARAZA, A.J.L., A. BUMB and M.W. BRECHBIEL. Macromolecules, dendrimers, and nanomaterials in magnetic resonance imaging: the interplay between size, function, and pharmacokinetics. *Chemical Reviews*, 2010, **110**(5), pp.2921-59.
37. AIME, S., M. CHIAUSSA, G. DIGILIO, E. GIANOLIO and E. TERRENO. Contrast agents for magnetic resonance angiographic applications: ^{1}H and ^{17}O NMR relaxometric investigations on two gadolinium(III) DTPA-like chelates endowed with high binding affinity to human serum albumin. *Journal of Biological Inorganic Chemistry*, 1999, **4**(6), pp.766-774.
38. HEILMANN, M., F. KIESSLING, M. ELDERLIN and L.R. SCHAD. Determination of pharmacokinetic parameters in DCE MRI: consequence of nonlinearity between contrast agent concentration and signal intensity. *Investigative Radiology*, 2006, **41**(6), pp.536-543.
39. ROBERTS, H.C., M. SAEED, T.P.L. ROBERTS, A. MUHLER, D.M. SHAMES, J.S. MANN, M. STISKAL, F. DEMSAR and R.C. BRASCH. Comparison of albumin-(Gd-DTPA)30 and Gd-DTPA-24-cascade-polymer for measurements of normal and abnormal microvascular permeability. *Journal of Magnetic Resonance Imaging*, 1997, **7**(2), pp.331-338.
40. BUCKLEY, D.L., L.E. KERSHAW and G.J. STANISZ. Cellular-interstitial water exchange and its effect on the determination of contrast agent concentration in vivo: Dynamic contrast-enhanced MRI of human

internal obturator muscle. *Magnetic Resonance in Medicine*, 2008, **60**(5), pp.1011-1019.

41. WANG, Y., M. SPILLER and P. CARAVAN. Evidence for weak protein binding of commercial extracellular gadolinium contrast agents. *Magnetic Resonance in Medicine*, 2010, **63**(3), pp.609-616.
42. YOUNG, I.R., G.J. CLARKE and D.R. BAILES. Enhancement of relaxation rate with paramagnetic contrast agents in NMR imaging. *CT: Journal of Computed Tomography*, 1981, **5**(6), pp.543-547.
43. RUNGE, V.M., T. AI, D. HAO and X. HU. The developmental history of the gadolinium chelates as intravenous contrast media for magnetic resonance. *Investigative Radiology*, 2011, **46**(12), pp.807-816.
44. IDÉE, J.-M., M. PORT, C. ROBIC, C. MEDINA, M. SABATOU and C. COROT. Role of thermodynamic and kinetic parameters in gadolinium chelate stability. *Journal of Magnetic Resonance Imaging*, 2009, **30**(6), pp.1249-1258.
45. WEINMANN, H.J., R.C. BRASCH, W.R. PRESS and G.E. WESBEY. Characteristics of gadolinium-DTPA complex: a potential NMR contrast agent. *American Journal of Roentgenology*, 1984, **142**(3), pp.619-624.
46. AIME, S. and P. CARAVAN. Biodistribution of gadolinium-based contrast agents, including gadolinium deposition. *Journal of Magnetic Resonance Imaging*, 2009, **30**(6), pp.1259-1267.
47. RUNGE, V.M. Safety of approved MR contrast media for intravenous injection. *Journal of Magnetic Resonance Imaging*, 2000, **12**(2), pp.205-13.
48. SHELLOCK, F.G. and E. KANAL. Safety of magnetic resonance imaging contrast agents. *Journal of Magnetic Resonance Imaging*, 1999, **10**(3), pp.477-484.
49. GROBNER, T. Gadolinium – a specific trigger for the development of nephrogenic fibrosing dermopathy and nephrogenic systemic fibrosis? *Nephrology Dialysis Transplantation*, 2006, **21**(4), pp.1104-1108.
50. HIGH, W.A., R.A. AYERS, J. CHANDLER, G. ZITO and S.E. COWPER. Gadolinium is detectable within the tissue of patients with nephrogenic systemic fibrosis. *Journal of the American Academy of Dermatology*, 2007, **56**(1), pp.21-26.
51. THOMSEN, H.S., S.K. MORCOS, T. ALMÉN, M.-F. BELLIN, M. BERTOLOTTO, G. BONGARTZ, O. CLEMENT, P. LEANDER, G. HEINZ-PEER, P. REIMER, F. STACUL, A. VAN DER MOLEN and J.A. WEBB. Nephrogenic systemic fibrosis and gadolinium-based contrast media: updated ESUR Contrast Medium Safety Committee guidelines. *European Radiology*, 2013, **23**(2), pp.307-318.
52. OGAN, M.D., U. SCHMIEDL, M.E. MOSELEY, W. GRODD, H. PAAJANEN and R.C. BRASCH. Albumin labeled with Gd-DTPA. An intravascular contrast-enhancing agent for magnetic resonance blood pool imaging: Preparation and characterization. *Investigative Radiology*, 1987, **22**(8), pp.665-671.
53. MOHS, A.M. and Z.R. LU. Gadolinium(III)-based blood-pool contrast agents for magnetic resonance imaging: status and clinical potential. *Expert Opinion on Drug Delivery*, 2007, **4**(2), pp.149-164.
54. CYRAN, C.C., Y. FU, H.-J. RAATSCHEN, V. ROGUT, B. CHAOPATHOMKUL, D.M. SHAMES, M.F. WENDLAND, B.M. YEH and R.C. BRASCH. New macromolecular polymeric MRI contrast agents for

application in the differentiation of cancer from benign soft tissues. *Journal of Magnetic Resonance Imaging*, 2008, **27**(3), pp.581-589.

55. YE, Z., X. WU, M. TAN, J. JESBERGER, M. GRISWORLD and Z.-R. LU. Synthesis and evaluation of a polydisulfide with Gd–DOTA monoamide side chains as a biodegradable macromolecular contrast agent for MR blood pool imaging. *Contrast Media & Molecular Imaging*, 2013, **8**(3), pp.220-228.
56. GERALDES, C.F.G.C. and S. LAURENT. Classification and basic properties of contrast agents for magnetic resonance imaging. *Contrast Media & Molecular Imaging*, 2009, **4**(1), pp.1-23.
57. JOSEPHSON, L., J. BIGLER and D. WHITE. The magnetic properties of some materials affecting MR images. *Magnetic Resonance in Medicine*, 1991, **22**(2), pp.204-208.
58. NOREK, M. and J.A. PETERS. MRI contrast agents based on dysprosium or holmium. *Progress in Nuclear Magnetic Resonance Spectroscopy*, 2011, **59**(1), pp.64-82.
59. BULTE, J.W.M. and D.L. KRAITCHMAN. Iron oxide MR contrast agents for molecular and cellular imaging. *NMR in Biomedicine*, 2004, **17**(7), pp.484-99.
60. WEISSLEDER, R., D.D. STARK, B.L. ENGELSTAD, B.R. BACON, C.C. COMPTON, D.L. WHITE, P. JACOBS and J. LEWIS. Superparamagnetic iron oxide: Pharmacokinetics and toxicity. *American Journal of Roentgenology*, 1989, **152**(1), pp.167-173.
61. LIN, Y.-J. and A.P. KORETSKY. Manganese ion enhances T1-weighted MRI during brain activation: An approach to direct imaging of brain function. *Magnetic Resonance in Medicine*, 1997, **38**(3), pp.378-388.
62. FASANO, M., S. CURRY, E. TERRENO, M. GALLIANO, G. FANALI, P. NARCISO, S. NOTARI and P. ASCENZI. The extraordinary ligand binding properties of human serum albumin. *IUBMB Life*, 2005, **57**(12), pp.787-796.
63. LAUFFER, R.B., D.J. PARMELEE, S.U. DUNHAM, H.S. OUELLET, R.P. DOLAN, S. WITTE, T.J. MCMURRY and R.C. WALOVITCH. MS-325: Albumin-targeted contrast agent for MR angiography. *Radiology*, 1998, **207**(2), pp.529-538.
64. LAUFFER, R.B., D.J. PARMELEE, H.S. OUELLET, R.P. DOLAN, H. SAJIKI, D.M. SCOTT, P.J. BERNARD, E.M. BUCHANAN, K.Y. ONG, Z. TYEKLÁR, K.S. MIDELFORT, T.J. MCMURRY and R.C. WALOVITCH. MS-325: a small-molecule vascular imaging agent for magnetic resonance imaging. *Academic Radiology*, 1996, **3 Suppl 2**, pp.S356-8.
65. NUNN, A.D. The cost of developing imaging agents for routine clinical use. *Investigative Radiology*, 2006, **41 (3)**, pp.206-212.
66. RAPP, J.H., S.D. WOLFF, S.F. QUINN, J.A. SOTO, S.C. MERANZE, S. MULUK, J. BLEBEA, S.P. JOHNSON, N.M. ROFSKY, A. DUERINCKX, G.S. FOSTER, K.C. KENT, G. MONETA, M.R. MIDDLEBROOK, V.R. NARRA, B.D. TOOMBS, J. POLLAK, E.K. YUCEL, K. SHAMSI and R.M. WEISSKOFF. Aortoiliac occlusive disease in patients with known or suspected peripheral vascular disease: Safety and efficacy of gadofosveset-enhanced MR angiography - Multicenter comparative phase III study. *Radiology*, 2005, **236**(1), pp.71-78.
67. GOYEN, M., M. EDELMAN, P. PERREAULT, E. O'RIORDAN, H. BERTONI, J. TAYLOR, D. SIRAGUSA, M. SHARAFUDDIN, E.R.

MOHLER, R. BREGER, E.K. YUCEL, K. SHAMSI and R.M. WEISSKOFF. MR angiography of aortoiliac occlusive disease: A phase III study of the safety and effectiveness of the blood-pool contrast agent MS-325. *Radiology*, 2005, **236**, pp.825-833.

68. CARAVAN, P., N.J. CLOUTIER, M.T. GREENFIELD, S.A. MCDERMID, S.U. DUNHAM, J.W.M. BULTE, J.C. AMEDIO JR, R.J. LOOBY, R.M. SUPKOWSKI, W.D. HORROCKS JR, T.J. MCMURRY and R.B. LAUFFER. The interaction of MS-325 with human serum albumin and its effect on proton relaxation rates. *Journal of the American Chemical Society*, 2002, **124**(12), pp.3152-3162.
69. DOWEIKO, J.P. and D.J. NOMPLEGGI. Role of albumin in human physiology and pathophysiology. *Journal of Parenteral and Enteral Nutrition*, 1991, **15 (2)**, pp.207-211.
70. BHATTACHARYA, A.A., T. GRÜNE and S. CURRY. Crystallographic analysis reveals common modes of binding of medium and long-chain fatty acids to human serum albumin. *Journal of Molecular Biology*, 2000, **303**(5), pp.721-32.
71. NICHOLSON, J.P., M.R. WOLMARANS and G.R. PARK. The role of albumin in critical illness. *British Journal of Anaesthesia*, 2000, **85**(4), pp.599-610.
72. KRATOCHWIL, N.A., W. HUBER, F. MÜLLER, M. KANSY and P.R. GERBER. Predicting plasma protein binding of drugs: a new approach. *Biochemical Pharmacology*, 2002, **64**(9), pp.1355-1374.
73. HE, X.M. and D.C. CARTER. Atomic structure and chemistry of human serum albumin. *Nature*, 1992, **358**(6383), pp.209-215.
74. SUGIO, S., A. KASHIMA, S. MOCHIZUKI, M. NODA and K. KOBAYASHI. Crystal structure of human serum albumin at 2.5 A resolution. *Protein Engineering*, 1999, **12**(6), pp.439-446.
75. ELDREDGE, H.B., M. SPILLER, J.M. CHASSE, M.T. GREENWOOD and P. CARAVAN. Species dependence on plasma protein binding and relaxivity of the gadolinium-based MRI contrast agent MS-325. *Investigative Radiology*, 2006, **41**(3), pp.229-243.
76. AIME, S., M. FASANO, E. TERRENO and M. BOTTA. Protein-bound metal chelates. *In:* A.E. MERBACH and E. TÓTH, eds. *The chemistry of contrast agents in medical magnetic resonance imaging*. Chichester: John Wiley & Sons, 2001, pp.193-242.
77. MULLER, R.N., B. RADUCHEL, S. LAURENT, J. PLATZEK, C. PIERART, P. MARESKI and L. VANDER ELST. Physicochemical characterization of MS-325, a new gadolinium complex, by multinuclear relaxometry. *European Journal of Inorganic Chemistry*, 1999, **1999**(11), pp.1949-1955.
78. PORT, M., C. COROT, X. VIOLAS, P. ROBERT, I. RAYNAL and G. GAGNEUR. How to compare the efficiency of albumin-bound and nonalbumin-bound contrast agents in vivo. *Investigative Radiology*, 2005, **40**(9), pp.565-573.
79. DAVIES, B. and T. MORRIS. Physiological parameters in laboratory animals and humans. *Pharmaceutical Research*, 1993, **10**(7), pp.1093-1095.
80. TARBELL, J.M. Shear stress and the endothelial transport barrier. *Cardiovascular research*, 2010, **87**(2), pp.320-30.

81. BALLMER, P.E. Causes and mechanisms of hypoalbuminaemia. *Clinical Nutrition*, 2001, **20**(3), pp.271-3.
82. CANCEL, L.M., A. FITTING and J.M. TARBELL. In vitro study of LDL transport under pressurized (convective) conditions. *American Journal of Physiology - Heart and Circulatory Physiology*, 2007, **293**(1), pp.H126-H132.
83. FOGH-ANDERSEN, N., B.M. ALTURA, B.T. ALTURA and O. SIGGAARDANDERSEN. Composition of interstitial fluid. *Clinical Chemistry*, 1995, **41**(10), pp.1522-1525.
84. ESSIG, M., M. ROHRER, F. GIESEL, J. TUTTENBERG, M.-A. WEBER, H. MICHAELY, L. GERIGK and M. VOTH. Human brain tumor imaging with a protein-binding MR contrast agent: Initial experience. *European Radiology*, 2010, **20**(1), pp.218-226.
85. FOURNIER, L.S. and R.C. BRASCH. The role of blood pool contrast media in the study of tumor pathophysiology. *In:* A. JACKSON, D.L. BUCKLEY and G.J.M. PARKER, eds. *Dynamic contrast-enhanced magnetic resonance imaging in oncology*. Berlin: Springer-Verlag, 2005, pp.39-52.
86. BELLIN, M.-F. and A.J. VAN DER MOLEN. Extracellular gadolinium-based contrast media: An overview. *European Journal of Radiology*, 2008, **66**(2), pp.160-167.
87. PARMELEE, D.J., R.C. WALOVITCH, H.S. OUELLET and R.B. LAUFFER. Preclinical evaluation of the pharmacokinetics, biodistribution, and elimination of MS-325, a blood pool agent for magnetic resonance imaging. *Investigative Radiology*, 1997, **32**(12), pp.741-747.
88. BARRETT, T., H. KOBAYASHI, M. BRECHBIEL and P.L. CHOYKE. Macromolecular MRI contrast agents for imaging tumor angiogenesis. *European Journal of Radiology*, 2006, **60**(3), pp.353-366.
89. CARAVAN, P., C.T. FARRAR, L. FRULLANO and R. UPPAL. Influence of molecular parameters and increasing magnetic field strength on relaxivity of gadolinium- and manganese-based T_1 contrast agents. *Contrast Media & Molecular Imaging*, 2009, **4**(2), pp.89-100.
90. BLOCKLEY, N.P., L. JIANG, A.G. GARDENER, C.N. LUDMAN, S.T. FRANCIS and P.A. GOWLAND. Field strength dependence of R_1 and R_2^* relaxivities of human whole blood to ProHance, Vasovist, and Deoxyhemoglobin. *Magnetic Resonance in Medicine*, 2008, **60**(6), pp.1313-1320.
91. ROHRER, M., H. BAUER, J. MINTOROVITCH, M. REQUARDT and H.-J. WEINMANN. Comparison of magnetic properties of MRI contrast media solutions at different magnetic field strengths. *Investigative Radiology*, 2005, **40**(11), pp.715-724.
92. CARAVAN, P. Protein-targeted gadolinium-based magnetic resonance imaging (MRI) contrast agents: Design and mechanism of action. *Accounts of Chemical Research*, 2009, **42**(7), pp.851-862.
93. REICHENBACH, J.R., T. HACKLANDER, T. HARTH, M. HOFER, M. RASSEK and U. MODDER. 1H T1 and T2 measurements of the MR imaging contrast agents Gd-DTPA and Gd-DTPA BMA at 1.5T. *European Radiology*, 1997, **7**(2), pp.264-274.
94. NISSEN, J.C., U.I. ATTENBERGER, C. FINK, O. DIETRICH, M. ROHRER, S.O. SCHOENBERG and H.J. MICHAELY. Thoracic and

abdominal MRA with gadofosveset: Influence of injection rate on vessel signal and image quality. *European Radiology*, 2009, **19**(8), pp.1932-1938.

95. SHAMSI, K., E.K. YUCEL and P. CHAMBERLIN. A summary of safety of gadofosveset (MS-325) at 0.03 mmol/kg body weight dose: Phase II and phase III clinical trials data. *Investigative Radiology*, 2006, **41**(11), pp.822-830.
96. *Questions and answers on the review of gadolinium-containing contrast agents* [online]. 2010. [Accessed 06/06/13]. Available from: http://www.ema.europa.eu/docs/en_GB/document_library/Referrals_document/gadolinium_31/WC500015635.pdf.
97. MCGREGOR, R., J. VYMAZAL, M. MARTINEZ-LOPEZ, J. NEUWIRTH, P. SALGADO, J.P. BEREGI, A. PEDUTO, E. DE LA PENA-ALMAGUER, G.J. SLATER, K. SHAMSI and E.C. PARSONS JR. A multi-center, comparative, phase 3 study to determine the efficacy of gadofosveset-enhanced magnetic resonance angiography for evaluation of renal artery disease. *European Journal of Radiology*, 2008, **65**(2), pp.316-325.
98. KELLE, S., T. THOUET, T. TANGCHAROEN, K. NASSENSTEIN, A. CHIRIBIRI, I. PAETSCH, B. SCHNACKENBURG, J. BARKHAUSEN, E. FLECK and E. NAGEL. Whole-heart coronary magnetic resonance angiography with MS-325 (Gadofosveset). *Medical Science Monitor*, 2007, **13**(11), pp.CR469-CR474.
99. MAKOWSKI, M.R., A.J. WIETHOFF, S. URIBE, V. PARISH, R.M. BOTNAR, A. BELL, C. KIESEWETTER, P. BEERBAUM, C.H.P. JANSEN, R. RAZAVI, T. SCHAEFFTER and G.F. GREIL. Congenital heart disease: Cardiovascular MR imaging by using an intravascular blood pool contrast agent. *Radiology*, 2011, **260**(3), pp.680-688.
100. WAGNER, M., R. ROSLER, A. LEMBCKE, C. BUTLER, M. DEWEY, M. LAULE, A. HUPPERTZ, C. SCHWENKE, C. WARMUTH, M. RIEF, B. HAMM and M. TAUPITZ. Whole-heart coronary magnetic resonance angiography at 1.5 tesla: Does a blood-pool contrast agent improve diagnostic accuracy? *Investigative Radiology*, 2011, **46**(3), pp.152-159.
101. JEROSCH-HEROLD, M., X. HU, N.S. MURTHY, C. RICKERS and A.E. STILLMAN. Magnetic resonance imaging of myocardial contrast enhancement with MS-325 and its relation to myocardial blood flow and the perfusion reserve. *Journal of Magnetic Resonance Imaging*, 2003, **18 (5)**, pp.544-554.
102. RITTER, C.O., A. WILKE, T. WICHMANN, M. BEER, D. HAHN and H. KÖSTLER. Comparison of intravascular and extracellular contrast media for absolute quantification of myocardial rest-perfusion using high-resolution MRI. *Journal of Magnetic Resonance Imaging*, 2011, **33**(5), pp.1047-1051.
103. PRASAD, P.V., J. CANNILLO, D.R. CHAVEZ, E.S. PINCHASIN, R.P. DOLAN, R. WALOVITCH and R.R. EDELMAN. First-pass renal perfusion imaging using MS-325, an albumin-targeted MRI contrast agent. *Investigative Radiology*, 1999, **34**(9), pp.566-566.
104. LÜDEMANN, L., B. NAFZ, F. EISNER, C. GROSZLIGE-SIESTRUP, M. MEISSLER, N. KAUFELS, H. REHBEIN, P.B. PERSSON, H.J. MICHAELY, P. LENGSFELD, M. VOTH and M. GUTBERLET. Absolute quantification of regional renal blood flow in swine by dynamic contrast-

enhanced magnetic resonance imaging using a blood pool contrast agent. *Investigative Radiology*, 2009, **44**(3), pp.125-134.

105. KRAUSE, M.H.J., K.K. KWONG, J. XIONG, E.S. GRAGOUDAS and L.H.Y. YOUNG. MRI of blood volume with MS 325 in experimental choroidal melanoma. *Magnetic Resonance Imaging*, 2003, **21**(7), pp.725-732.
106. PEDERSEN, S.F., S.A. THRYSOE, W.P. PAASKE, T. THIM, E. FALK, S. RINGGAARD and W.Y. KIM. CMR Assessment of endothelial damage and angiogenesis in porcine coronary arteries using gadofosveset. *Journal of Cardiovascular Magnetic Resonance*, 2011, **13**, p.10.
107. LEPORQ, B., J. DUMORTIER, F. PILLEUL and O. BEUF. 3D-liver perfusion MRI with the MS-325 blood pool agent: A noninvasive protocol to asses liver fibrosis. *Journal of Magnetic Resonance Imaging*, 2012, **35**(6), pp.1380-1387.
108. PHINIKARIDOU, A., M.E. ANDIA, A. PROTTI, A. INDERMUCHLE, A. SHAH, A. SMITH, A. WARLEY and R.M. BOTNAR. Noninvasive magnetic resonance imaging evaluation of endothelial permeability in murine atherosclerosis using an albumin-binding contrast agent. *Circulation*, 2012, **126**(6), pp.707-719.
109. FARACE, P., G. CONTI, F. MERIGO, S. TAMBALO, P. MARZOLA, A. SBARBATI, C. QUARTA, D. D'AMBROSIO, S. CHONDROGIANNIS, C. NANNI and D. RUBELLO. Potential role of combined FDG PET/CT & contrast enhancement MRI in a rectal carcinoma model with nodal metastases characterized by a poor FDG-avidity. *European Journal of Radiology*, 2012, **81**(4), pp.658-662.
110. SESHADRI, M., N.T. SACADURA and T. COULTHARD. Monitoring antivascular therapy in head and neck cancer xenografts using contrast-enhanced MR and US imaging. *Angiogenesis*, 2011, **14**(4), pp.491-501.
111. SCHREINEMACHER, M.H., W.H. BACKES, J.M. SLENTER, S. XANTHOULEA, B. DELVOUX, L. VAN WINDEN, R.G. BEETS-TAN, J.L.H. EVERS, G.A.J. DUNSELMAN and A. ROMANO. Towards endometriosis diagnosis by gadofosveset-trisodium enhanced magnetic resonance imaging. *PLoS ONE*, 2012, **7**(3), p.e33241.
112. MILOT, L., M. HAIDER, L. FOSTER, C. MCGREGOR and C. LAW. Gadofosveset trisodium in the investigation of focal liver lesions in noncirrhotic liver: Early experience. *Journal of Magnetic Resonance Imaging*, 2012, **36**(3), pp.738-742.
113. ADZAMLI, K., D.A. YABLONSKIY, M.R. CHICOINE, E.K. WON, K.P. GALEN, M.C. ZAHNER, T.A. WOOLSEY and J.J.H. ACKERMAN. Albumin-binding MR blood pool agents as MRI contrast agents in an intracranial mouse glioma model. *Magnetic Resonance in Medicine*, 2003, **49**(3), pp.586-590.
114. PUIG, J., G. BLASCO, M. ESSIG, J. DAUNIS-I-ESTADELLA, G. LAGUILLO, A. QUILES, S. REMOLLO, K. BERGMANN, C. JOLY, L. BERNADO, J. SÁNCHEZ-GONZÁLEZ and S. PEDRAZA. Albumin-binding MR blood pool contrast agent improves diagnostic performance in human brain tumour: comparison of two contrast agents for glioblastoma. *European Radiology*, 2012, pp.1-9.
115. HERBORN, C.U., T.C. LAUENSTEIN, F.M. VOGT, R.B. LAUFFER, J.F. DEBATIN and S.G. RUEHM. Interstitial MR lymphography with MS-325:

Characterization of normal and tumor-invaded lymph nodes in a rabbit model. *American Journal of Roentgenology*, 2002, **179**(6), pp.1567-1572.

116. LAMBREGTS, D.M.J., G.L. BEETS, M. MAAS, A.G.H. KESSELS, F.C.H. BAKERS, V.C. CAPPENDIJK, S.M.E. ENGELEN, M.J. LAHAYE, A.P. DE BRUINE, G. LAMMERING, T. LEINER, J.L. VERWOERD, J.E. WILDBERGER and R.G.H. BEETS-TAN. Accuracy of gadofosveset-enhanced MRI for nodal staging and restaging in rectal cancer. *Annals of Surgery*, 2011, **253**(3), pp.539-545.
117. SCHIPPER, R.-J., M.L. SMIDT, L.M. VAN ROOZENDAAL, C.J.G. CASTRO, B. DE VRIES, E.M. HEUTS, K.B.M.I. KEYMEULEN, J.E. WILDBERGER, M.B.I. LOBBES and R.G.H. BEETS-TAN. Noninvasive nodal staging in patients with breast cancer using gadofosveset-enhanced magnetic resonance imaging: A feasibility study. *Investigative Radiology*, 2013, **48**(3), pp.134-139.
118. LOBBES, M.B.I., R. MISERUS, S. HEENEMAN, V.L. PASSOS, P.H.A. MUTSAERS, N. DEBERNARDI, B. MISSELWITZ, M. POST, M. DAEMEN, J.M.A. VAN ENGELSHOVEN, T. LEINER and M.E. KOOI. Atherosclerosis: Contrast-enhanced MR imaging of vessel wall in rabbit model - comparison of gadofosveset and gadopentetate dimeglumine. *Radiology*, 2009, **250**(3), pp.682-691.
119. LOBBES, M.B.I., S. HEENEMAN, V.L. PASSOS, R. WELTEN, R.M. KWEE, R.J. VAN DER GEEST, A.J. WIETHOFF, P. CARAVAN, B. MISSELWITZ, M. DAEMEN, J.M.A. VAN ENGELSHOVEN, T. LEINER and M.E. KOOI. Gadofosveset-enhanced magnetic resonance imaging of human carotid atherosclerotic plaques: A proof-of-concept study. *Investigative Radiology*, 2010, **45**(5), pp.275-281.
120. NIEDERMAYER, S., S. SOURBRON, M. PROMPONA, C. CYRAN, M. REISER and A. HUBER. Dose response of the intravascular contrast agent gadofosveset trisodium in MR perfusion imaging of the myocardium using a quantitative evaluation. *The International Journal of Cardiovascular Imaging*, 2013, pp.1-10.
121. THOUET, T., B. SCHNACKENBURG, T. KOKOCINSKI, E. FLECK, E. NAGEL and S. KELLE. Visualization of chronic myocardial infarction using the intravascular contrast agent MS-325 (gadofosveset) in patients. *Scientific World Journal*, 2012, pp.1-6.
122. TURETSCHEK, K., E. FLOYD, T. HELBICH, T.P.L. ROBERTS, D.M. SHAMES, M.F. WENDLAND, W.O. CARTER and R.C. BRASCH. MRI assessment of microvascular characteristics in experimental breast tumors using a new blood pool contrast agent (MS-325) with correlations to histopathology. *Journal of Magnetic Resonance Imaging*, 2001, **14**(3), pp.237-242.
123. KIESSLING, F., B. MORGENSTERN and C. ZHANG. Contrast agents and applications to assess tumor angiogenesis In Vivo by magnetic resonance imaging. *Current Medicinal Chemistry*, 2007, **14 (1)**, pp.77-91.
124. VAN MONTFOORT, J.E., B. STIEGER, D.K.F. MEIJER, H.J. WEINMANN, P.J. MEIER and K.E. FATTINGER. Hepatic uptake of the magnetic resonance imaging contrast agent gadoxetate by the organic anion transporting polypeptide Oatp1. *Journal of Pharmacology and Experimental Therapeutics*, 1999, **290**(1), pp.153-157.

125. GSCHWEND, S., W. EBERT, M. SCHULTZE-MOSGAU and J. BREUER. Pharmacokinetics and imaging properties of Gd-EOB-DTPA in patients with hepatic and renal impairment. *Investigative Radiology*, 2011, **46**(9), pp.556-66.
126. HENROTTE, V., L. VANDER ELST, S. LAURENT and R.N. MULLER. Comprehensive investigation of the non-covalent binding of MRI contrast agents with human serum albumin. *Journal of Biological Inorganic Chemistry*, 2007, **12**(6), pp.929-937.
127. VANDER ELST, L., F. MATON, S. LAURENT, F. SEGHI, F. CHAPELLE and R.N. MULLER. A multinuclear MR study of Gd-EOB-DTPA: comprehensive preclinical characterization of an organ specific MRI contrast agent. *Magnetic Resonance in Medicine*, 1997, **38**(4), pp.604-14.
128. WEINMANN, H.J., G. SCHUHMANN-GIAMPIERI, H. SCHMITT-WILLICH, H. VOGLER, T. FRENZEL and H. GRIES. A new lipophilic gadolinium chelate as a tissue-specific contrast medium for MRI. *Magnetic Resonance in Medicine*, 1991, **22**(2), pp.233-7; discussion 242.
129. FEUERLEIN, S., R.T. GUPTA, D.T. BOLL and E.M. MERKLE. Hepatocellular MR contrast agents: Enhancement characteristics of liver parenchyma and portal vein after administration of gadoxetic acid in comparison to gadobenate dimeglumine. *European Journal of Radiology*, 2012, **81**(9), pp.2037-2041.
130. PINTASKE, J., P. MARTIROSIAN, H. GRAF, G. ERB, K.-P. LODEMANN, C.D. CLAUSSEN and F. SCHICK. Relaxivity of gadopentetate dimeglumine (Magnevist), gadobutrol (Gadovist), and gadobenate dimeglumine (MultiHance) in human blood plasma at 0.2, 1.5, and 3 Tesla. *Investigative Radiology*, 2006, **41**(3), pp.213-221.
131. CARAVAN, P., A.V. ASTASHKIN and A.M. RAITSIMRING. The gadolinium(III)-water hydrogen distance in MRI contrast agents. *Inorganic Chemistry*, 2003, **42**(13), pp.3972-3974.
132. GIESEL, F.L., H. VON TENGG-KOBLIGK, I.D. WILKINSON, P. SIEGLER, C.W. VON DER LIETH, M. FRANK, K.P. LODEMANN and M. ESSIG. Influence of human serum albumin on longitudinal and transverse relaxation rates (r1 and r2) of magnetic resonance contrast agents. *Investigative Radiology*, 2006, **41**(3), pp.222-228.
133. KIRCHIN, M.A., G.P. PIROVANO and A. SPINAZZI. Gadobenate dimeglumine (Gd-BOPTA): an overview. *Investigative Radiology*, 1998, **33**(11), pp.1-9.
134. NILSSON, H., L. BLOMQVIST, L. DOUGLAS, A. NORDELL and E. JONAS. Assessment of liver function in primary biliary cirrhosis using Gd-EOB-DTPA-enhanced liver MRI. *HPB : the official journal of the International Hepato Pancreato Biliary Association*, 2010, **12**(8), pp.567-576.
135. SAITO, K., J. LEDSAM, S. SOURBRON, J. OTAKA, Y. ARAKI, S. AKATA and K. TOKUUYE. Assessing liver function using dynamic Gd-EOB-DTPA-enhanced MRI with a standard 5-phase imaging protocol. *Journal of Magnetic Resonance Imaging*, 2013, **37**(5), pp.1109-1114.
136. HUPPERTZ, A., T. BALZER, A. BLAKEBOROUGH, J. BREUER, A. GIOVAGNONI, G. HEINZ-PEER, M. LANIADO, R.M. MANFREDI, D.G. MATHIEU, D. MUELLER, P. REIMER, P.J. ROBINSON, M.

STROTZER, M. TAUPITZ and T.J. VOGL. Improved detection of focal liver lesions at MR imaging: multicenter comparison of gadoxetic acid-enhanced MR images with intraoperative findings. *Radiology*, 2004, **230**(1), pp.266-75.

137. GUPTA, R.T., D. MARIN, D.T. BOLL, D.B. HUSARIK, D.E. DAVIS, S. FEUERLEIN and E.M. MERKLE. Hepatic hemangiomas: Difference in enhancement pattern on 3T MR imaging with gadobenate dimeglumine versus gadoxetate disodium. *European Journal of Radiology*, 2012, **81**(10), pp.2457-2462.
138. KORKUSUZ, H., L.L. KNAU, W. KROMEN, V. BIHRER, D. KEESE, A. PIIPER and T.J. VOGL. Different signal intensity at Gd-EOB-DTPA compared with Gd-DTPA-enhanced MRI in hepatocellular carcinoma transgenic mouse model in delayed phase hepatobiliary imaging. *Journal of Magnetic Resonance Imaging*, 2012, **35**(6), pp.1397-1402.
139. SOURBRON, S., W.H. SOMMER, M.F. REISER and C.J. ZECH. Combined quantification of liver perfusion and function with dynamic gadoxetic acid-enhanced MR imaging. *Radiology*, 2012, **263**(3), pp.874-883.
140. KNOPP, M.V., H. VON TENGG-KOBLIGK, F. FLOEMER and S.O. SCHOENBERG. Contrast agents for MRA: Future directions. *Journal of Magnetic Resonance Imaging*, 1999, **10**(3), pp.314-316.
141. SCHNEIDER, G., M. PASOWICZ, J. VYMAZAL, Z. SEIDL, M. ASCHAUER, M. KONOPKA, D. BILECEN, R. IEZZI and C. BALLARATI. Gadobenate dimeglumine and gadofosveset trisodium for MR angiography of the renal arteries: Multicenter intraindividual crossover comparison. *American Journal of Roentgenology*, 2010, **195**(2), pp.476-85.
142. IEZZI, R., G. SOULEZ, S. THURNHER, G. SCHNEIDER, M.A. KIRCHIN, N. SHEN, G. PIROVANO and A. SPINAZZI. Contrast-enhanced MRA of the renal and aorto-iliac-femoral arteries: Comparison of gadobenate dimeglumine and gadofosveset trisodium. *European Journal of Radiology*, 2011, **77**(2), pp.358-368.
143. LUZZANI, F., P. CIPOLLA, M.L. PELAPRAT, F. ROBERT, C. GOTTI, P. TIRONE and C. DE HAEN. Brain penetration and neurological effects of gadobenate dimeglumine in the rat. *Acta Radiologica*, 1997, **38**(2), pp.268-272.
144. WENDLAND, M.F., M. SAEED, K. LAUERMA, N. DERUGIN, J. MINTOROVITCH, F.M. CAVAGNA and C.B. HIGGINS. Alterations in T1 of normal and reperfused infarcted myocardium after Gd-BOPTA versus GD-DTPA on inversion recovery EPI. *Magnetic Resonance in Medicine*, 1997, **37 (3)**, pp.448-456.
145. CAVAGNA, F.M., F. MAGGIONI, P.M. CASTELLI, M. DAPRA, L.G. IMPERATORI, V. LORUSSO and B.G. JENKINS. Gadolinium chelates with weak binding to serum proteins: A new class of high-efficiency, general purpose contrast agents for magnetic resonance imaging. *Investigative Radiology*, 1997, **32**(12), pp.780-796.
146. KNOPP, M.V., V.M. RUNGE, M. ESSIG, M. HARTMAN, O. JANSEN, M.A. KIRCHIN, A. MOELLER, A.H. SEEBERG and K.P. LODEMANN. Primary and secondary brain tumors at MR imaging: Bicentric intraindividual crossover comparison of gadobenate dimeglumine and gadopentetate dimeglumine. *Radiology*, 2004, **230**(1), pp.55-55.

147. RUMBOLDT, Z., H.A. ROWLEY, F. STEINBERG, J.A. MALDJIAN, J. RUSCALLEDA, L. GUSTAFSSON and S. BASTIANELLO. Multicenter, double-blind, randomized, intra- individual crossover comparison of gadobenate dimeglumine and gadopentetate dimeglumine in MRI of brain tumors at 3 tesla. *Journal of Magnetic Resonance Imaging*, 2009, **29**(4), pp.760-767.
148. PEDICONI, F., C. CATALANO, S. PADULA, A. ROSELLI, V. DOMINELLI, S. CAGIOLI, M.A. KIRCHIN, G. PIROVANO and R. PASSARIELLO. Contrast-enhanced MR mammography: Improved lesion detection and differentiation with gadobenate dimeglumine. *American Journal of Roentgenology*, 2008, **191**(5), pp.1339-1346.
149. HUPPERTZ, A., T. FRANIEL, M. WAGNER, O. PÜTTCHER, J. WAGNER, M. RIEF, C. SCHWENKE, B. HAMM and J. STRASSBURG. Whole-body MRI with assessment of hepatic and extraabdominal enhancement after administration of gadoxetic acid for staging of rectal carcinoma. *Acta Radiologica*, 2010, **51**(8), pp.842-50.
150. DYM, R.J., V. CHERNYAK and A.M. ROZENBLIT. MR imaging of renal collecting system with gadoxetate disodium: Feasibility for MR urography. *Journal of Magnetic Resonance Imaging*, 2013. doi: 10.1002/jmri.24059.
151. SOURBRON, S.P., H.J. MICHAELY, M.F. REISER and S.O. SCHOENBERG. MRI-measurement of perfusion and glomerular filtration in the human kidney with a separable compartment model. *Investigative Radiology*, 2008, **43**(1), pp.40-48.
152. NOTOHAMIPRODJO, M., M. PEDERSEN, C. GLASER, A.D. HELCK, K.-P. LODEMANN, B. JESPERSEN, M. FISCHEREDER, M.F. REISER and S.P. SOURBRON. Comparison of Gd-DTPA and Gd-BOPTA for studying renal perfusion and filtration. *Journal of Magnetic Resonance Imaging*, 2011, **34**(3), pp.595-607.
153. CAVAGNA, F.M., V. LORUSSO, P.L. ANELLI, F. MAGGIONI and C. DE HAAN. Preclinical profile and clinical potential of gadocoletic acid trisodium salt (B22956/1), a new intravascular contrast medium for MRI. *Academic Radiology*, 2002, **9**(2, Supplement), pp.S491-S494.
154. DE HAEN, C., P.L. ANELLI, V. LORUSSO, A. MORISETTI, F. MAGGIONI, J. ZHENG, F. UGGERI and F.M. CAVAGNA. Gadocoletic acid trisodium salt (b22956/1): a new blood pool magnetic resonance contrast agent with application in coronary angiography. *Investigative Radiology*, 2006, **41**(3), pp.279-291.
155. PREDA, A., V. NOVIKOV, M. MOGLICH, K. TURETSCHEK, D.M. SHAMES, R.C. BRASCH, F.M. CAVAGNA and T.P.L. ROBERTS. MRI monitoring of Avastin antiangiogenesis therapy using B22956/1, a new blood pool contrast agent, in an experimental model of human cancer. *Journal of Magnetic Resonance Imaging*, 2004, **20**(5), pp.865-873.
156. MARZOLA, P., S. RAMPONI, E. NICOLATO, E. LOVATI, M. SANDRI, L. CALDERAN, C. CRESCIMANNO, F. MERIGO, A. SBARBATI, A. GROTTI, S. VULTAGGIO, F. CAVAGNA, V. LORUSSO and F. OSCULATI. Effect of tamoxifen in an experimental model of breast tumor studied by dynamic contrast-enhanced magnetic resonance imaging and different contrast agents. *Investigative Radiology*, 2005, **40**(7), pp.421-429.

157. SAEED, M., C.F. VAN DIJKE, J.S. MANN, M.F. WENDLAND, W. ROSENAU, C.B. HIGGINS and R.C. BRASCH. Histologic confirmation of microvascular hyperpermeability to macromolecular MR contrast medium in reperfused myocardial infarction. *Journal of Magnetic Resonance Imaging*, 1998, **8**(3), pp.561-567.
158. BRASCH, R.C., H. DALDRUP, D. SHAMES, M. WENDLAND, Y. OKUHATA and W. ROSENAU. Macromolecular contrast media—enhanced MRI estimates of microvascular permeability correlate with histopathologic tumor grade. *Academic Radiology*, 1998, **5**(SUPPL1), pp.S2-S5.
159. DALDRUP, H., D.M. SHAMES, M. WENDLAND, Y. OKUHATA, T.M. LINK, W. ROSENAU, Y. LU and R.C. BRASCH. Correlation of dynamic contrast-enhanced MR imaging with histologic tumor grade: Comparison of macromolecular and small-molecular contrast media. *American Journal of Roentgenology*, 1998, **171**(4), pp.941-949.
160. SENNINO, B., H.-J. RAATSCHEN, M.F. WENDLAND, Y. FU, W.-K. YOU, D.M. SHAMES, D.M. MCDONALD and R.C. BRASCH. Correlative dynamic contrast MRI and microscopic assessments of tumor vascularity in RIP-Tag2 transgenic mice. *Magnetic Resonance in Medicine*, 2009, **62**(3), pp.616-625.
161. CYRAN, C.C., B. SENNINO, Y. FU, V. ROGUT, D.M. SHAMES, B. CHAOPATHOMKUL, M.F. WENDLAND, D.M. MCDONALD, R.C. BRASCH and H.-J. RAATSCHEN. Permeability to macromolecular contrast media quantified by dynamic MRI correlates with tumor tissue assays of vascular endothelial growth factor (VEGF). *European Journal of Radiology*, 2012, **81**(5), pp.891-896.
162. CARAVAN, P., G. PARIGI, J.M. CHASSE, N.J. CLOUTIER, J.J. ELLISON, R.B. LAUFFER, C. LUCHINAT, S.A. MCDERMID, M. SPILLER and T.J. MCMURRY. Albumin binding, relaxivity, and water exchange kinetics of the diastereoisomers of MS-325, a gadolinium(III)-based magnetic resonance angiography contrast agent. *Inorganic Chemistry*, 2007, **46**(16), pp.6632-6639.
163. LAURENT, S., L.V. ELST and R.N. MULLER. Comparative study of the physicochemical properties of six clinical low molecular weight gadolinium contrast agents. *Contrast Media & Molecular Imaging*, 2006, **1**(3), pp.128-137.
164. COROT, C., X. VIOLAS, P. ROBERT, G. GAGNEUR and M. PORT. Comparison of different types of blood pool agents (P792, MS325, USPIO) in a rabbit MR angiography-like protocol. *Investigative Radiology*, 2003, **38**(6), pp.311-319.
165. BUJACZ, A. Structures of bovine, equine and leporine serum albumin. *Acta crystallographica. Section D, Biological crystallography*, 2012, **68**(Pt 10), pp.1278-89.
166. LARSSON, H.B.W., T. FRITZHANSEN, E. ROSTRUP, L. SONDERGAARD, P. RING and O. HENRIKSEN. Myocardial perfusion modeling using MRI. *Magnetic Resonance in Medicine*, 1996, **35**(5), pp.716-726.
167. HATABU, H., E. TADAMURA, D.L. LEVIN, Q. CHEN, W. LI, D. KIM, P.V. PRASAD and R.R. EDELMAN. Quantitative assessment of pulmonary perfusion with dynamic contrast-enhanced MRI. *Magnetic Resonance in Medicine*, 1999, **42**(6), pp.1033-1038.

168. O'CONNOR, J.P., A. JACKSON, M.C. ASSELIN, D.L. BUCKLEY, G.J. PARKER and G.C. JAYSON. Quantitative imaging biomarkers in the clinical development of targeted therapeutics: current and future perspectives. *The Lancet Oncology*, 2008, **9**(8), pp.766-776.
169. TOFTS, P.S. Modeling tracer kinetics in dynamic Gd-DTPA MR imaging. *Journal of Magnetic Resonance Imaging*, 1997, **7**(1), pp.91-101.
170. BUCKLEY, D.L. Uncertainty in the analysis of tracer kinetics using dynamic contrast-enhanced T_1-weighted MRI. *Magnetic Resonance in Medicine*, 2002, **47**(3), pp.601-606.
171. SOURBRON, S.P. and D.L. BUCKLEY. On the scope and interpretation of the Tofts models for DCE-MRI. *Magnetic Resonance in Medicine*, 2011, **66**(3), pp.735-745.
172. MCGRATH, D.M., D.P. BRADLEY, J.L. TESSIER, T. LACEY, C.J. TAYLOR and G.J.M. PARKER. Comparison of model-based arterial input functions for dynamic contrast-enhanced MRI in tumor bearing rats. *Magnetic Resonance in Medicine*, 2009, **61**(5), pp.1173-1184.
173. SU, M.Y., J.C. JAO and O. NALCIOGLU. Measurement of vascular volume fraction and blood-tissue permeability constants with a pharmacokinetic model: Studies in rat muscle tumors with dynamic Gd-DTPA enhanced MRI. *Magnetic Resonance in Medicine*, 1994, **32**(6), pp.714-724.
174. CHENG, H.-L.M. Investigation and optimization of parameter accuracy in dynamic contrast-enhanced MRI. *Journal of Magnetic Resonance Imaging*, 2008, **28**(3), pp.736-743.
175. CHECKLEY, D., J.J.L. TESSIER, S.R. WEDGE, M. DUKES, J. KENDREW, B. CURRY, B. MIDDLETON and J.C. WATERTON. Dynamic contrast-enhanced MRI of vascular changes induced by the VEGF-signalling inhibitor ZD4190 in human tumour xenografts. *Magnetic Resonance Imaging*, 2003, **21**(5), pp.475-482.
176. PICKUP, S., R. ZHOU and J. GLICKSON. MRI estimation of the arterial input function in mice. *Academic Radiology*, 2003, **10**(9), pp.963-8.
177. PRADEL, C., N. SIAUVE, G. BRUNETEAU, O. CLEMENT, C. DE BAZELAIRE, F. FROUIN, S.R. WEDGE, J.L. TESSIER, P.H. ROBERT, G. FRIJA and C.A. CUENOD. Reduced capillary perfusion and permeability in human tumour xenografts treated with the VEGF signalling inhibitor ZD4190: An in vivo assessment using dynamic MR imaging and macromolecular contrast media. *Magnetic Resonance Imaging*, 2003, **21**(8), pp.845-851.
178. PARKER, G.J., C. ROBERTS, A. MACDONALD, G.A. BUONACCORSI, S. CHEUNG, D.L. BUCKLEY, A. JACKSON, Y. WATSON, K. DAVIES and G.C. JAYSON. Experimentally-derived functional form for a population-averaged high-temporal-resolution arterial input function for dynamic contrast-enhanced MRI. *Magnetic Resonance in Medicine*, 2006, **56**(5), pp.993-1000.
179. LOVELESS, M.E., J. HALLIDAY, C. LIESS, L. XU, R.D. DORTCH, J. WHISENANT, J.C. WATERTON, J.C. GORE and T.E. YANKEELOV. A quantitative comparison of the influence of individual versus population-derived vascular input functions on dynamic contrast enhanced-MRI in small animals. *Magnetic Resonance in Medicine*, 2012, **67**(1), pp.226-236.

180. STEINGOETTER, A., J. SVENSSON, Y. KOSANKE, R.M. BOTNAR, M. SCHWAIGER, E. RUMMENY and R. BRAREN. Reference region-based pharmacokinetic modeling in quantitative dynamic contract-enhanced MRI allows robust treatment monitoring in a rat liver tumor model despite cardiovascular changes. *Magnetic Resonance in Medicine*, 2011, **65**(1), pp.229-38.
181. FRITZ-HANSEN, T., E. ROSTRUP, H.B.W. LARSSON, L. SONDERGAARD, P. RING and O. HENRIKSEN. Measurement of the arterial concentration of Gd-DTPA using MRI: A step toward quantitative perfusion imaging. *Magnetic Resonance in Medicine*, 1996, **36**(2), pp.225-231.
182. POULIN, E., R. LEBEL, E. CROTEAU, M. BLANCHETTE, L. TREMBLAY, R. LECOMTE, M. BENTOURKIA and M. LEPAGE. Conversion of arterial input functions for dual pharmacokinetic modeling using Gd-DTPA/MRI and 18F-FDG/PET. *Magnetic Resonance in Medicine*, 2013, **69**(3), pp.781-792.
183. DIEHL, K.H., R. HULL, D. MORTON, R. PFISTER, Y. RABEMAMPIANINA, D. SMITH, J.M. VIDAL and C. VAN DE VORSTENBOSCH. A good practice guide to the administration of substances and removal of blood, including routes and volumes. *Journal of Applied Toxicology*, 2001, **21**(1), pp.15-23.
184. PARASURAMAN, S., R. RAVEENDRAN and R. KESAVAN. Blood sample collection in small laboratory animals. *Journal of pharmacology & pharmacotherapeutics*, 2010, **1**(2), pp.87-93.
185. MORTON, D.B., D. ABBOT, R. BARCLAY, B.S. CLOSE, R. EWBANK, D. GASK, M. HEATH, S. MATTIC, T. POOLE, J. SEAMER, J. SOUTHEE, A. THOMPSON, B. TRUSSELL, C. WEST and M. JENNINGS. Removal of blood from laboratory mammals and birds. *Laboratory Animals*, 1993, **27**(1), pp.1-22.
186. MUSTEATA, F.M. Recent progress in in-vivo sampling and analysis. *TrAC - Trends in Analytical Chemistry*, 2013, **45**, pp.154-168.
187. MEI, J.V., J.R. ALEXANDER, B.W. ADAM and W.H. HANNON. Use of filter paper for the collection and analysis of human whole blood specimens. *Journal of Nutrition*, 2001, **131**(5), pp.1631S-1636S.
188. *Image of DBS card* [online]. [Accessed 12/07/13]. Available from: http://www.whatman.com/DMPK.aspx.
189. GUTHRIE, R. and A. SUSI. A simple phenylalanine method for detecting phenylketonuria in large populations of newborn infants. *Pediatrics*, 1963, **32**, pp.338-343.
190. POLLITT, R.J. New technologies extend the scope of newborn blood-spot screening, but old problems remain unresolved. *Acta Pædiatrica*, 2010, **99**(12), pp.1766-1772.
191. BRANDÃO, C.P.U., B.L.C. MARQUES, V.A. MARQUES, C.A. VILLELA-NOGUEIRA, K.M.R. DO Ó, M.T. DE PAULA, L.L. LEWIS-XIMENEZ, E. LAMPE, J.A. SÁ FERREIRA and L.M. VILLAR. Simultaneous detection of hepatitis c virus antigen and antibodies in dried blood spots. *Journal of Clinical Virology*, 2013, **57**(2), pp.98-102.
192. STEINBERG, K., J. BECK, D. NICKERSON, M. GARCIA-CLOSAS, M. GALLAGHER, M. CAGGANA, Y. REID, M. COSENTINO, J. JI, D. JOHNSON, R.B. HAYES, M. EARLEY, F. LOREY, H. HANNON, M.J.

KHOURY and E. SAMPSON. DNA banking for epidemiologic studies: A review of current practices. *Epidemiology*, 2002, **13**(3), pp.246-254.

193. MAJORS, R.E. New directions in whole blood analysis: Dried blood spot analysis and beyond. *LCGC North America*, 2011, **29**(1), pp.14-27.
194. RAO, R.N. and M. TALLURI. An overview of recent applications of inductively coupled plasma-mass spectrometry (ICP-MS) in determination of inorganic impurities in drugs and pharmaceuticals. *Journal of Pharmaceutical and Biomedical Analysis*, 2007, **43**(1), pp.1-13.
195. AMMANN, A.A. Inductively coupled plasma mass spectrometry (ICP MS): a versatile tool. *Journal of Mass Spectrometry*, 2007, **42**(4), pp.419-427.
196. TELGMANN, L., M. SPERLING and U. KARST. Determination of gadolinium-based MRI contrast agents in biological and environmental samples: A review. *Analytica Chimica Acta*, 2013, **764**, pp.1-16.
197. SKELLY FRAME, E.M. and E.E. UZGIRIS. Gadolinium determination in tissue samples by inductively coupled plasma mass spectrometry and inductively coupled plasma atomic emission spectrometry in evaluation of the action of magnetic resonance imaging contrast agents. *Analyst*, 1998, **123**(4), pp.675-679.
198. KUMMERER, K. and E. HELMERS. Hospital effluents as a source of gadolinium in the aquatic environment. *Environmental Science and Technology*, 2000, **34**(4), pp.573-577.
199. CHAUDHURI, S.N., S.J.M. BUTALA, R.W. BALL and C.T. BRANIFF. Pilot study for utilization of dried blood spots for screening of lead, mercury and cadmium in newborns. *Journal of Exposure Science and Environmental Epidemiology*, 2009, **19**(3), pp.298-316.
200. HSIEH, H.-F., W.-S. CHANG, Y.-K. HSIEH and C.-F. WANG. Using dried-droplet laser ablation inductively coupled plasma mass spectrometry to quantify multiple elements in whole blood. *Analytica Chimica Acta*, 2011, **699**(1), pp.6-10.
201. THOMAS, R. Spectroscopy tutorial - A beginner's guide to ICP-MS. Part I. *Spectroscopy*, 2001, **16**(4), pp.38-42.
202. SAUSSEREAU, E., C. LACROIX, A. CATTANEO, L. MAHIEU and J.P. GOULLE. Hair and fingernail gadolinium ICP-MS contents in an overdose case associated with nephrogenic systemic fibrosis. *Forensic Science International*, 2008, **176**(1), pp.54-57.
203. PIETSCH, H., P. LENGSFELD, G. JOST, T. FRENZEL, J. HUTTER and M.A. SIEBER. Long-term retention of gadolinium in the skin of rodents following the administration of gadolinium-based contrast agents. *European Radiology*, 2009, **19**(6), pp.1417-1424.
204. FRETELLIER, N.M.S., J.-M.P. IDEE, A.P. DENCAUSSE, O.P. KARROUM, S.P. GUERRET, N.M.S. POVEDA, G.B.S. JESTIN, C.P. FACTOR, I.P. RAYNAL, P.M.S. ZAMIA, M.P. PORT and C.P. COROT. Comparative in vivo dissociation of gadolinium chelates in renally impaired rats: A relaxometry study. *Investigative Radiology*, 2011, **46**(5), pp.292-300.
205. PUGH, J.A.T., A.G. COX, C.W. MCLEOD, J. BUNCH, M.J. WRITER, S.L. HART, A. BIENEMANN, E. WHITE and J. BELL. Elemental imaging of MRI contrast agents: Benchmarking of LA-ICP-MS to MRI. *Analytical and Bioanalytical Chemistry*, 2012, **403**(6), pp.1641-1649.

206. RAJU, C.S.K., A. COSSMER, H. SCHARF, U. PANNE and D. LUCK. Speciation of gadolinium based MRI contrast agents in environmental water samples using hydrophilic interaction chromatography hyphenated with inductively coupled plasma mass spectrometry. *Journal of Analytical Atomic Spectrometry*, 2010, **25**(1), pp.55-61.
207. LORETI, V. and J. BETTMER. Determination of the MRI contrast agent Gd-DTPA by SEC-ICP-MS. *Analytical and Bioanalytical Chemistry*, 2004, **379**(7-8), pp.1050-1054.
208. KUNNEMEYER, J., L. TERBORG, B. MEERMANN, C. BRAUCKMANN, I. MOLLER, A. SCHEFFER and U. KARST. Speciation analysis of gadolinium chelates in hospital effluents and wastewater treatment plant sewage by a novel HILIC/ICP-MS method. *Environmental Science and Technology*, 2009, **43**(8), pp.2884-2890.
209. COOLEN, B.F., T. GEELEN, L.E.M. PAULIS, K. NICOLAY and G.J. STRIJKERS. Regional contrast agent quantification in a mouse model of myocardial infarction using 3D cardiac T1 mapping. *Journal of Cardiovascular Magnetic Resonance*, 2011, **13**(1).
210. DAFNI, H., A. GILEAD, N. NEVO, R. EILAM, A. HARMELIN and M. NEEMAN. Modulation of the pharmacokinetics of macromolecular contrast material by avidin chase: MRI, optical, and inductively coupled plasma mass spectrometry tracking of triply labeled albumin. *Magnetic Resonance in Medicine*, 2003, **50**(5), pp.904-914.
211. RUSSELL, W.M.S. The three Rs: Past, present and future. *Animal Welfare*, 2005, **14**(4), pp.279-286.
212. SILVENNOINEN, M.J., M.I. KETTUNEN and R.A. KAUPPINEN. Effects of hematocrit and oxygen saturation level on blood spin-lattice relaxation. *Magnetic Resonance in Medicine*, 2003, **49**(3), pp.568-571.
213. O'BROIN, S. INFLUENCE OF HEMATOCRIT ON QUANTITATIVE-ANALYSIS OF BLOOD SPOTS ON FILTER-PAPER. *Clinical Chemistry*, 1993, **39**(6), pp.1354-1355.
214. EL-HAJJAR, D.F., K.H. SWANSON, J.D. LANDMARK and D.F. STICKLE. Validation of use of annular once-punched filter paper bloodspot samples for repeat lead testing. *Clinica Chimica Acta*, 2007, **377**(1-2), pp.179-184.
215. REDFIELD, A.G. Nuclear magnetic resonance saturation and rotary saturation in solids. *Physical Review*, 1955, **98**(6), pp.1787-1809.
216. MARTIROSIAN, P., E. ROMMEL, F. SCHICK and M. DEIMLING. Control of susceptibility-related image contrast by spin-lock techniques. *Magnetic Resonance Imaging*, 2008, **26**(10), pp.1381-1387.
217. SANTYR, G.E., R.M. HENKELMAN and M.J. BRONSKILL. Spin locking for magnetic-resonance imaging with application to human-breast. *Magnetic Resonance in Medicine*, 1989, **12**(1), pp.25-37.
218. ARONEN, H.J., U. ABO RAMADAN, T.K. PELTONEN, A.T. MARKKOLA, J.I. TANTTU, J. JÄÄSKELÄINEN, A.-M. HÄKKINEN and R. SEPPONEN. 3D spin-lock imaging of human gliomas. *Magnetic Resonance Imaging*, 1999, **17**(7), pp.1001-1010.
219. DUVVURI, U., H. POPTANI, M. FELDMAN, L. NADAL-DESBARATS, M.S. GEE, W.M.F. LEE, R. REDDY, J.S. LEIGH and J.D. GLICKSON. Quantitative T-1 rho magnetic resonance imaging of RIF-1 tumors in vivo: Detection of early response to cyclophosphamide therapy. *Cancer Research*, 2001, **61**(21), pp.7747-7753.

220. KETTUNEN, M.I., A. SIERRA, M.J. NARVAINEN, P.K. VALONEN, S. YLA-HERTTUALA, R.A. KAUPPINEN and O.H.J. GROHN. Low spin-lock field T1 relaxation in the rotating frame as a sensitive MR imaging marker for gene therapy treatment response in rat glioma. *Radiology*, 2007, **243**(3), pp.796-803.
221. MUTHUPILLAI, R., S.D. FLAMM, J.M. WILSON, R.I. PETTIGREW and W.T. DIXON. Acute myocardial infarction: Tissue characterization with T1(rho)-weighted MR imaging - Initial experience. *Radiology*, 2004, **232**(2), pp.606-610.
222. BORTHAKUR, A., M. SOCHOR, C. DAVATZIKOS, J.Q. TROJANOWSKI and C.M. CLARK. T1(rho) MRI of Alzheimer's disease. *Neuroimage*, 2008, **41**(4), pp.1199-1205.
223. DIXON, W.T., J.N. OSHINSKI, J.D. TRUDEAU, B.C. ARNOLD and R.I. PETTIGREW. Myocardial suppression in vivo by spin locking with composite pulses. *Magnetic Resonance in Medicine*, 1996, **36**(1), pp.90-94.
224. TAYLOR, C., J. CARBALLIDO-GAMIO, S. MAJUMDAR and X.J. LI. Comparison of quantitative imaging of cartilage for osteoarthritis: T2, T1 rho, dGEMRIC and contrast-enhanced computed tomography. *Magnetic Resonance Imaging*, 2009, **27**(6), pp.779-784.
225. COBB, J.G., J. XIE and J.C. GORE. Contributions of chemical exchange to T(1ρ) dispersion in a tissue model. *Magnetic Resonance in Medicine*, 2011, **66**(6), pp.1563-1571.
226. ROMMEL, E. and R. KIMMICH. T1-rho dispersion imaging and volume-selective T1-rho dispersion weighted NMR-spectroscopy. *Magnetic Resonance in Medicine*, 1989, **12**(3), pp.390-399.
227. HENKELMAN, R.M. Measurement of signal intensities in the presence of noise in MR images. *Medical Physics*, 1985, **12**(2), pp.232-233.
228. ENGELHARDT, R.T. and G.A. JOHNSON. T1 rho relaxation and its application to MR histology. *Magnetic Resonance in Medicine*, 1996, **35**(5), pp.781-786.
229. WHEATON, A.J., A. BORTHAKUR, J.B. KNEELAND, R.R. REGATTE, S.V.S. AKELLA and R. REDDY. In vivo quantification of T-1 rho using a multislice spin-lock pulse sequence. *Magnetic Resonance in Medicine*, 2004, **52**(6), pp.1453-1458.
230. COBB, J.G., J.H. KAN and J.C. GORE. T1ρ mapping of pediatric epiphyseal and articular cartilage in the knee. *Journal of Magnetic Resonance Imaging*, 2013. doi: 10.1002/jmri.23963.
231. TAKAYAMA, Y., M. HATAKENAKA, H. TSUSHIMA, K. OKAZAKI, T. YOSHIURA, M. YONEZAWA, K. NISHIKAWA, Y. IWAMOTO and H. HONDA. T1ρ is superior to T2 mapping for the evaluation of articular cartilage denaturalization with osteoarthritis: Radiological–pathological correlation after total knee arthroplasty. *European Journal of Radiology*, 2013, **82**(4), pp.e192-8.
232. WANG, Y.-X., F. ZHAO, J. GRIFFITH, G. MOK, J. LEUNG, A. AHUJA and J. YUAN. T1rho and T2 relaxation times for lumbar disc degeneration: an in vivo comparative study at 3.0-Tesla MRI. *European Radiology*, 2012, pp.1-7.
233. SANTYR, G.E., E.J. FAIRBANKS, F. KELCZ and J.A. SORENSON. Off-resonance spin locking for MR-imaging. *Magnetic Resonance in Medicine*, 1994, **32**(1), pp.43-51.

234. POPTANI, H., U. DUVVURI, C.G. MILLER, A. MANCUSO, S. CHARAGUNDLA, N.W. FRASER, J.D. GLICKSON, J.S. LEIGH and R. REDDY. T1(rho) imaging of murine brain tumors at 4 T. *Academic Radiology*, 2001, **8**(1), pp.42-47.
235. BORTHAKUR, A., A.J. WHEATON, A.J. GOUGOUTAS, S.V. AKELLA, R.R. REGATTE, S.R. CHARAGUNDLA and R. REDDY. In vivo measurement of T1rho dispersion in the human brain at 1.5 tesla. *Journal of Magnetic Resonance Imaging*, 2004, **19**(4), pp.403-409.
236. MARGARSON, M.P. and N. SONI. Serum albumin: touchstone or totem? *Anaesthesia*, 1998, **53**(8), pp.789-803.
237. ROTHSCHILD, M., M. ORATZ and S. SCHREIBER. Albumin synthesis. *New England Journal of Medicine*, 1972, **286**(14), pp.748-757.
238. BRADLEY, J., K. CUNNINGHAM and V. JACKSON. Serum protein levels in critically ill surgical patients. *Intensive care*, 1981, **7**(6), pp.291-295.
239. DJOUSSE, L., K.J. ROTHMAN, L.A. CUPPLES, D. LEVY and R.C. ELLISON. Serum albumin and risk of myocardial infarction and all-cause mortality in the Framingham offspring study. *Circulation*, 2002, **106**(23), pp.2919-2924.
240. SEITZ, R.J. and W. WECHSLER. Immunohistochemical demonstration of serum proteins in human cerebral gliomas. *Acta Neuropathologica*, 1987, **73**(2), pp.145-152.
241. POULSEN, H.L. Subcutaneous interstitial fluid albumin concentration in long-term diabetes-mellitus. *Scandinavian Journal of Clinical & Laboratory Investigation*, 1973, **32**(2), pp.167-173.
242. HAAVERSTAD, R., I. ROMSLO and S. LARSEN. Protein concentration of subcutaneous interstitial fluid in the human leg. *Journal of Vascular Research*, 1996, **16**(3), pp.111-117.
243. ELLMERER, M., L. SCHAUPP, G.A. BRUNNER, G. SENDLHOFER, A. WUTTE, P. WACH and T.R. PIEBER. Measurement of interstitial albumin in human skeletal muscle and adipose tissue by open-flow microperfusion. *American Journal of Physiology, Endocrinology and Metabolism*, 2000, **278**, pp.E352-6.
244. WATERTON, J.C. Translational magnetic resonance imaging and spectroscopy: Opportunities and challenges. *In:* L. GARRIDO and N. BECKMANN, eds. *New applications of NMR in drug discovery and development*. RSC press, 2013.
245. HEUSER, L.S. and F.N. MILLER. Differential macromolecular leakage from the vasculature of tumors. *Cancer*, 1986, **57**(3), pp.461-4.
246. ROBERTS, T.P.L., K. TURETSCHEK, A. PREDA, V. NOVIKOV, M. MOEGLICH, D.M. SHAMES, R.C. BRASCH and H.J. WEINMANN. Tumor microvascular changes to anti-angiogenic treatment assessed by MR contrast media of different molecular weights. *Academic Radiology*, 2002, **9**(SUPPL. 2), pp.S511-S513.
247. DAUBER, I.M., K.M. VANBENTHUYSEN, I.F. MCMURTRY, G.S. WHEELER, E.J. LESNEFSKY, L.D. HORWITZ and J.V. WEIL. Functional coronary microvascular injury evident as increased permeability due to brief ischemia and reperfusion. *Circulation Research*, 1990, **66**(4), pp.986-998.
248. SCHWITTER, J., M. SAEED, M.F. WENDLAND, N. DERUGIN, E. CANET, R.C. BRASCH and C.B. HIGGINS. Influence of severity of

myocardial injury on distribution of macromolecules: Extravascular versus intravascular gadolinium-based magnetic resonance contrast agents. *Journal of the American College of Cardiology*, 1997, **30**(4), pp.1086-1094.

249. MESSROGHLI, D.R., A. RADJENOVIC, S. KOZERKE, D.M. HIGGINS, M.U. SIVANANTHAN and J.P. RIDGWAY. Modified Look-Locker inversion recovery (MOLLI) for high-resolution T1 mapping of the heart. *Magnetic Resonance in Medicine*, 2004, **52**(1), pp.141-6.
250. XUE, H., S. SHAH, A. GREISER, C. GUETTER, A. LITTMANN, M.-P. JOLLY, A.E. ARAI, S. ZUEHLSDORFF, J. GUEHRING and P. KELLMAN. Motion correction for myocardial T1 mapping using image registration with synthetic image estimation. *Magnetic Resonance in Medicine*, 2012, **67**(6), pp.1644-1655.
251. BAGHER-EBADIAN, H., R. PAUDYAL, T.N. NAGARAJA, R.L. CROXEN, J.D. FENSTERMACHER and J.R. EWING. MRI estimation of gadolinium and albumin effects on water proton. *Neuroimage*, 2011, **54**(SUPPL. 1), pp.S176-S179.
252. BIRIS, O., B. BENEFIELD, K.R. HARRIS and D.C. LEE. A steady-state method for computation of myocardial blood volume with the intravascular contrast agent Ablavar. *Journal of Cardiovascular Magnetic Resonance*, 2012, **14**(Suppl 1), p.P49.
253. NOESKE, R., F. SEIFERT, K.H. RHEIN and H. RINNEBERG. Human cardiac imaging at 3 T using phased array coils. *Magnetic Resonance in Medicine*, 2000, **44**(6), pp.978-82.
254. ZHAO, J., C. CLINGMAN, M. NARVAINEN, R. KAUPPINEN and P. VAN ZIJL. Oxygenation and hematocrit dependence of transverse relaxation rates of blood at 3T. *Magnetic Resonance in Medicine*, 2007, **58**(3), pp.592-597.
255. ZAMAN, A., D.M. HIGGINS, M. KOUWENHOVEN, A. KIDAMBI, J.P. GREENWOOD and S. PLEIN. Robust myocardial T2 and T2* mapping at 3T. *Journal of Cardiovascular Magnetic Resonance*, 2012, **14**(Suppl 1), p.P306.
256. STANISZ, G.J., E.E. ODROBINA, J. PUN, M. ESCARAVAGE, S.J. GRAHAM, M.J. BRONSKILL and R.M. HENKELMAN. T1, T2 relaxation and magnetization transfer in tissue at 3T. *Magnetic Resonance in Medicine*, 2005, **54**(3), pp.507-12.
257. BRASCH, R.C. Rationale and applications for macromolecular Gd-based contrast agents. *Magnetic Resonance in Medicine*, 1991, **22**(2), pp.282-287.
258. BANE, O., D.C. LEE, B. BENEFIELD, M. MARKL, J. CARR and T.J. CARROLL. A pilot study of leakage and compartmentalization of the contrast agent Ablavar. *Journal of Cardiovascular Magnetic Resonance*, 2013, **15**(Suppl 1), pp.E7-E7.
259. KELLMAN, P., J.R. WILSON, H. XUE, W.P. BANDETTINI, S.M. SHANBHAG, K.M. DRUEY, M. UGANDER and A.E. ARAI. Extracellular volume fraction mapping in the myocardium, part 2: Initial clinical experience. *Journal of Cardiovascular Magnetic Resonance*, 2012, **14**(1), p.64.
260. BROADBENT, D.A., J.D. BIGLANDS, A. LARGHAT, S.P. SOURBRON, A. RADJENOVIC, J.P. GREENWOOD, S. PLEIN and D.L. BUCKLEY. Myocardial blood flow at rest and stress measured with dynamic

contrast-enhanced MRI: Comparison of a distributed parameter model with a Fermi function model. *Magnetic Resonance in Medicine*, 2013. doi: 10.1002/mrm.24611.

261. SINIBALDI, R., M.G. ORTORE, F. SPINOZZI, S. DE SOUZA FUNARI, J. TEIXEIRA and P. MARIANI. SANS/SAXS study of the BSA solvation properties in aqueous urea solutions via a global fit approach. *European Biophysics Journal*, 2008, **37**(5), pp.673-681.
262. PICKUP, S., A.K. WOOD and H.L. KUNDEL. Gadodiamide T1 relaxivity in brain tissue in vivo is lower than in saline. *Magnetic Resonance in Medicine*, 2005, **53**(1), pp.35-40.
263. ALFORD, J.K., B.K. RUTT, T.J. SCHOLL, W.B. HANDLER and B.A. CHRONIK. Delta relaxation enhanced MR: Improving activation-specificity of molecular probes through R1 dispersion imaging. *Magnetic Resonance in Medicine*, 2009, **61**(4), pp.796-802.
264. ALFORD, J.K., A.G. SORENSEN, T. BENNER, A.B. CHRONIK, B.W. HANDLER, J.T. SCHOLL, G. MADAN and P. CARAVAN. Direct protein imaging of inflammation in the human hand. *In: Proceedings of the International Society for Magnetic Resonance in Medicine*, 2011.

Bibliography

RICHARDSON, O. C., M. L. J. SCOTT, S. F. TANNER, J. C. WATERTON and D. L. BUCKLEY. 2012. Overcoming the low relaxivity of gadofosveset at high field with spin locking. Magnetic Resonance in Medicine, 68(4), pp.1234-1238.

List of Abbreviations

ASL	Arterial spin labelling
B_0	Main magnetic field strength
B_1	Applied RF pulse strength
B_{1L}	Spin-lock pulse strength
BOLD	Blood oxygenation level dependent contrast
BSA	Bovine serum albumin
CEST	Chemical exchange saturation transfer
C_g; C_{gbound}; C_{gfree}	Contrast agent concentration: total; bound; free
CI	Confidence intervals
C_{sa}; $C_{sabound}$; C_{safree}	Serum albumin concentration: total; bound; free
DBS	Dried blood spotting
DC	Direct current
DCE-MRI	Dynamic contrast-enhanced magnetic resonance imaging
DD	Dipole–dipole
DREMR	Delta relaxation enhanced magnetic resonance
EDTA	Ethylenediaminetetraacetic acid
EES	Extravascular extracellular space
EVF	Extracellular volume fraction
FID	Free induction decay
FOV	Field of view
Gd	Gadolinium
GE	Gradient echo
Hct	Haematocrit

HSA	Human serum albumin
ICP-AES	Inductively-coupled plasma atomic emission spectroscopy
ICP-MS	Inductively-coupled plasma mass spectroscopy
IR	Inversion recovery
IS	Inner sphere
K_a	Binding affinity
LV	Left ventricle
MBV	Myocardial blood volume
MOLLI	Modified Look-Locker inversion recovery
MRI	Magnetic resonance imaging
NSF	Nephrogenic systemic fibrosis
OS	Outer sphere
PRE	Proton relaxation enhancement
r	Electron spin–proton spin distance
R_1; R_{10}; R_{1obs}	Longitudinal relaxation rate (generally); in the absence of contrast agent; observed
r_1; r_{1bound}; r_{1free}; r_{1obs}	Longitudinal relaxivity (generally); of the bound molecule; of the free molecule; observed
$R_{1\rho}$	Spin-lock relaxation rate
R_2; R_{20}; R_{2obs}	Transverse relaxation rate (generally); in the absence of contrast agent; observed
r_2; r_{2bound}; r_{2free}; r_{2obs}	Transverse relaxivity (generally); of the bound molecule; of the free molecule; observed
RARE	Rapid acquisition with relaxation enhancement
RF	Radiofrequency
R_{iDD}	Dipole–dipole relaxation rate (longitudinal (i=1), transverse (i = 2))

R_{ie}	Electron spin relaxation rate (longitudinal (i=1), transverse (i = 2))
R_{iIS}	Inner sphere relaxation rate (longitudinal (i=1), transverse (i = 2))
R_{im}	Relaxation rate of the bound water molecule (longitudinal (i=1), transverse (i = 2))
R_{iOS}	Outer sphere relaxation rate (longitudinal (i=1), transverse (i = 2))
R_{iSC}	Scalar relaxation rate (longitudinal (i=1), transverse (i = 2))
ROI	Region of interest
rpm	Revolutions per minute
SAR	Specific absorption rate
SC	Scalar
SD	Standard deviation
SE	Spin echo
SI	Signal intensity
SL	Spin locking
SNR	Signal-to-noise ratio
SPIO	Superparamagnetic iron oxide particles
SSFP	Steady state free precession
T_1	Longitudinal relaxation time
$T_{1\rho}$	Spin-lock relaxation time
T_2	Transverse relaxation time
T_2^*	Transverse relaxation time, accounting for field inhomogeneity
TAA	Thoracic aortic aneurism
TE	Echo time
TI	Inversion time
TR	Repetition time

TSL	Spin-lock time
USPIO	Ultrasmall superparamagnetic iron oxide particles
VIF	Vascular input function
ZFS	Zero-field-splitting
ΔR_1	Change in longitudinal relaxation rate induced by contrast agent
ΔR_2	Change in transverse relaxation rate induced by contrast agent
τ_{ci}	Dipole–dipole correlation time
τ_D	Diffusional correlation time
τ_{ei}	Scalar correlation time
τ_M	Correlation time of coordinated water molecule
τ_R	Rotational correlation time

Appendix A: Contrast agent equations

A.1 Inner sphere relaxation

Longitudinal and transverse inner sphere relaxation rates (R_{1IS} and R_{2IS}, respectively) may be determined using Eq. A.1 and A.2 (34). The parameter q represents the number of bound water nuclei per Gd ion (also known as the hydration number); for most Gd-based agents, q = 1.

$$R_{1IS} = \left(\frac{qP_m}{R_{1m}^{-1} + \tau_m}\right) \quad [A.1]$$

$$R_{2IS} = qP_m \frac{1}{\tau_m}\left[\frac{R_{2m}(\tau_m^{-1} + R_{2m}) + \Delta\omega_m^2}{(\tau_m^{-1} + R_{2m})^2 + \Delta\omega_m^2}\right] \quad [A.2]$$

where P_m is the mole fraction of the bound water nuclei, τ_m is the lifetime of a water molecule in the inner sphere of the complex (this is the reciprocal of the solvent exchange rate, k_{ex}), R_{1m} and R_{2m} are proton relaxation rates in the bound water, and $\Delta\omega_m$ is the chemical shift difference between the bound water and the bulk water.

Dipole–dipole (DD) and scalar (SC) components of the bound water relaxation rates (Eq. 2.11) may be calculated using the Solomen–Bloembergen–Morgan equations (Eq. A.3 – A.6) (34).

$$R_{1DD} = \frac{2}{15}\frac{\gamma_I^2 g^2 \mu_B^2 S(S+1)}{r^6}\left[\frac{3\tau_{c1}}{(1+\omega_I^2\tau_{c1}^2)} + \frac{7\tau_{c2}}{(1+\omega_S^2\tau_{c2}^2)}\right] \quad [A.3]$$

$$R_{1SC} = \frac{2}{3}S(S+1)\left(\frac{A}{\hbar}\right)^2\left[\frac{\tau_{e2}}{(1+\omega_S^2\tau_{e2}^2)}\right] \quad [A.4]$$

$$R_{2DD} = \frac{1}{15}\frac{\gamma_I^2 g^2 \mu_B^2 S(S+1)}{r^6}\left[\frac{3\tau_{c1}}{(1+\omega_I^2\tau_{c1}^2)} + \frac{13\tau_{c2}}{(1+\omega_s^2\tau_{c2}^2)} + 4\tau_{c1}\right] \quad [A.5]$$

$$R_{2SC} = \frac{1}{3}S(S+1)\left(\frac{A}{\hbar}\right)^2\left[\frac{\tau_{e2}}{(1+\omega_s^2\tau_{e2}^2} + \tau_{e1}\right] \quad [A.6]$$

where γ_I is the nuclear gyromagnetic ratio, g is the electron g-factor, μ_B is the Bohr magneton, r is the electron spin–proton distance, ω_I and ω_S are the nuclear and electron Larmor frequencies, respectively (and $\omega = \gamma B$), and $A/\hbar$ is the scalar coupling constant between the electron at the paramagnetic centre and the proton of the coordinated water molecule. τ_c and τ_e represent the dipole–dipole and scalar correlation times, respectively.

The electronic relaxation rates in Eq. 2.12 and 2.13 also vary with the magnetic field; for Gd^{3+} complexes they are usually interpreted in terms of a zero-field-splitting (ZFS) interaction (Eq. A.7 – A.9) (35).

$$R_{1e} = 2B\left[\frac{1}{1+\omega_s^2\tau_v^2} + \frac{4}{1+4\omega_s^2\tau_v^2}\right] \quad [A.7]$$

$$R_{2e} = B\left[\frac{5}{1+\omega_s^2\tau_v^2} + \frac{2}{1+4\omega_s^2\tau_v^2} + 3\right] \quad [A.8]$$

where:

$$B = \frac{\Delta^2}{50}[4S(S+1) - 3]\tau_v \quad [A.9]$$

Δ^2 is the mean-square ZFS energy and τ_v is the correlation time for the modulation of the ZFS interaction.

A.2 Outer sphere relaxation

Second and outer sphere are usually combined into a single relaxation rate, R_{iOS} (Eq. A.10 – A.14) (34).

$$R_{1OS} = C[3j(\omega_I) + 7j(\omega_s)] \quad [A.10]$$

$$R_{2OS} = C[2 + 1.5j(\omega_I) + 6.5j(\omega_s)] \quad [A.11]$$

$$C = \left(\frac{32\pi}{405}\right)\gamma_I^2\gamma_s^2\hbar^2 S(S+1)\frac{N_A M}{1000aD} \quad [A.12]$$

$$j(\omega) = Re\left(\frac{1+\frac{z}{4}}{1+z+\frac{4z^2}{9}+\frac{z^3}{9}}\right) \quad [A.13]$$

$$z = \sqrt{i\omega\tau_D + \frac{\tau_D}{R_{1e}^{-1}}} \quad [A.14]$$

where k = 1,2, N_A is Avagadro's constant (6.02 x 10^{23}), M is the concentration of the complex, a is the distance of closest approach of the water molecule and the complex (spins I and S), D is the sum of the diffusion constants of water and the complex, τ_D is diffusional correlation time ($\tau_D = a^2/D$). Spectral densities j(ω) are Fourier transforms of the time correlation functions.

Appendix B: Supplemental experimental results

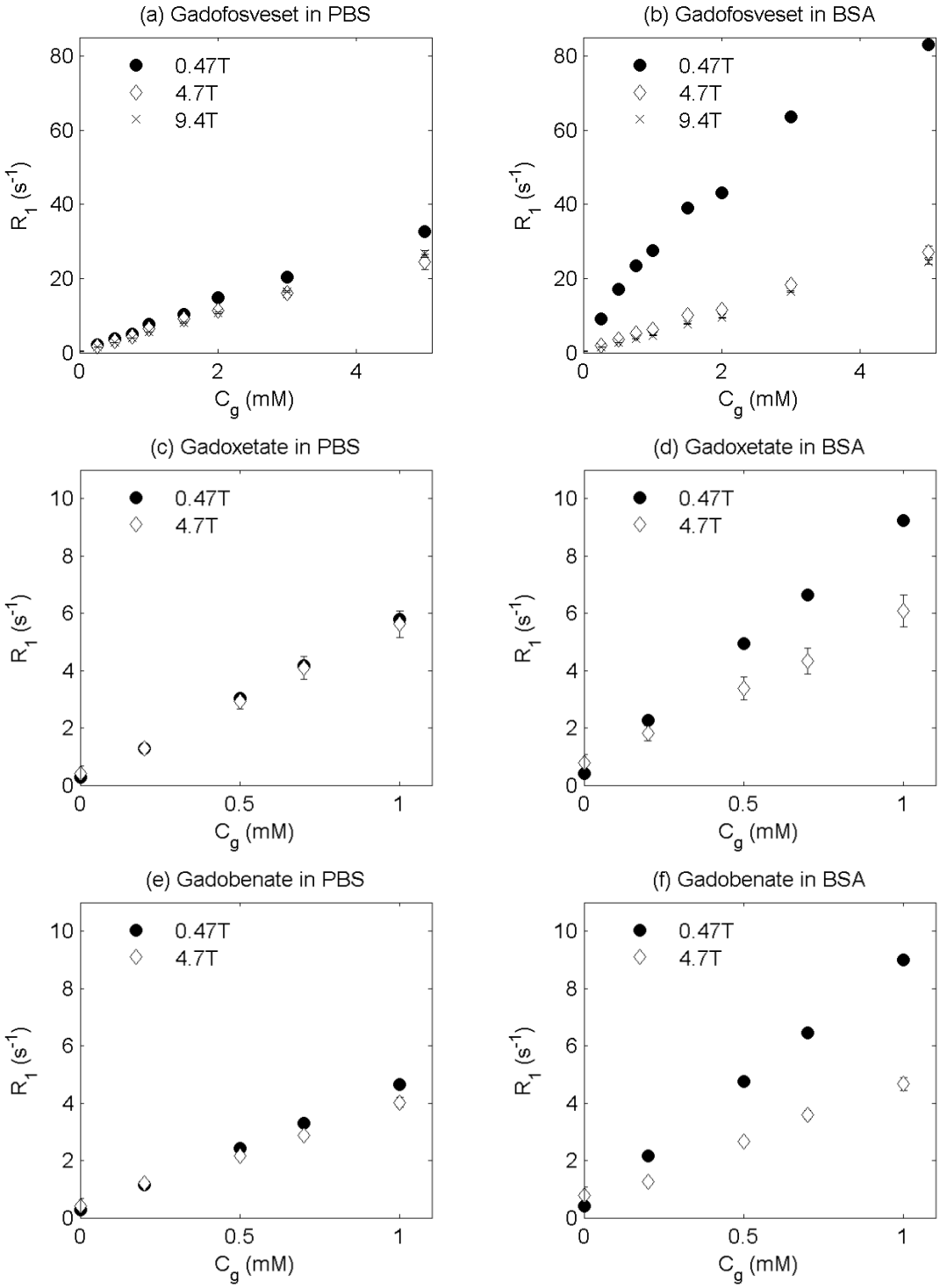

Figure B.1: Measured relaxation rates (R_1) for gadofosveset, gadoxetate and gadobenate in PBS (left column) and BSA (right column) at body temperature (approximately 37 °C) at 0.47 T and 4.7 T (all agents), and at 9.4 T (gadofosveset only); error bars represent 95% CI (omitted where smaller than data point)

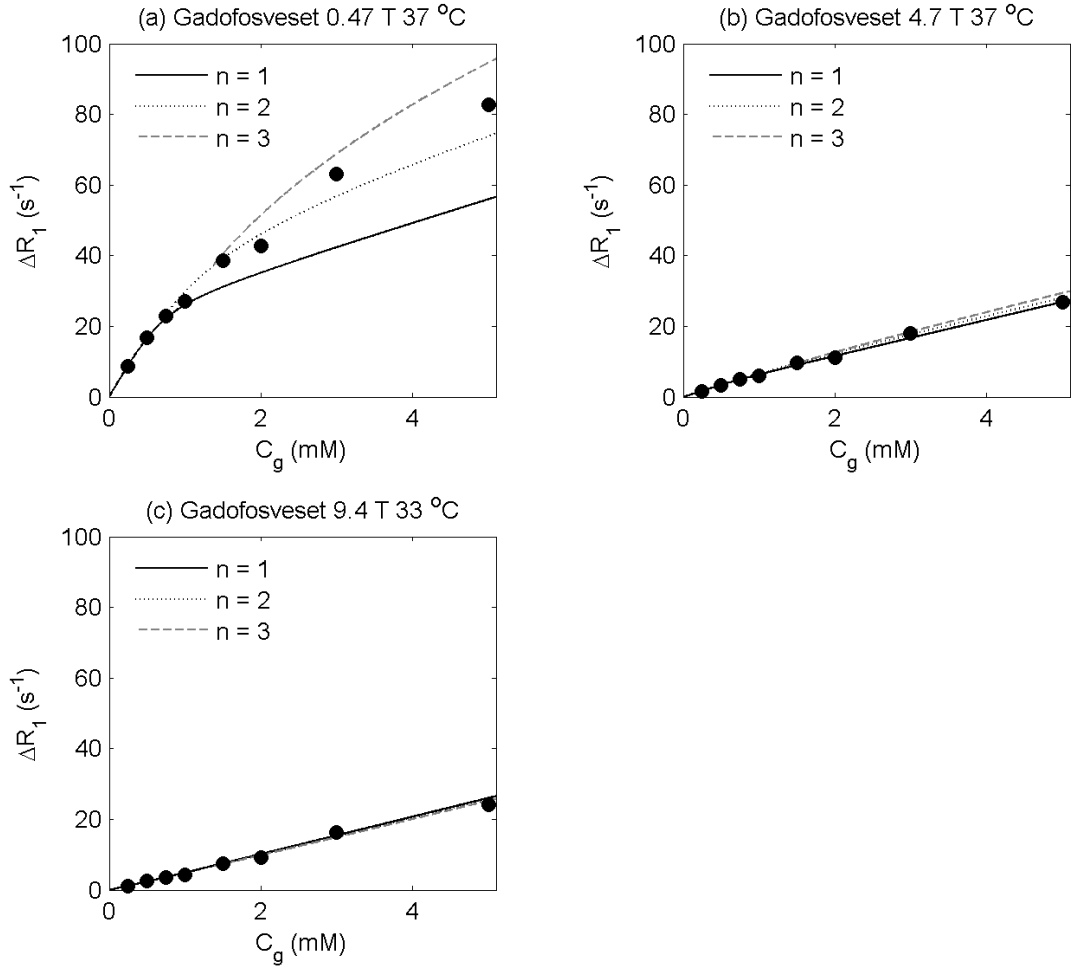

Figure B.2: Modelling n = 1 – 3 binding sites at all field strengths at body temperature, using Eq. 4.3a–c. Circles represent measured gadofosveset data points; solid line is original model (single binding site, Eq. 4.3a, K_{a1} = 11.0 mM^{-1}); dotted line also includes a second binding site (Eq. 4.3b, K_{a2} = 0.86 mM^{-1}); dashed line also includes a third binding site (Eq. 4.3c, K_{a3} = 0.26 mM^{-1}); the same relaxivity values (from Table 4.2) were used at all three binding sites

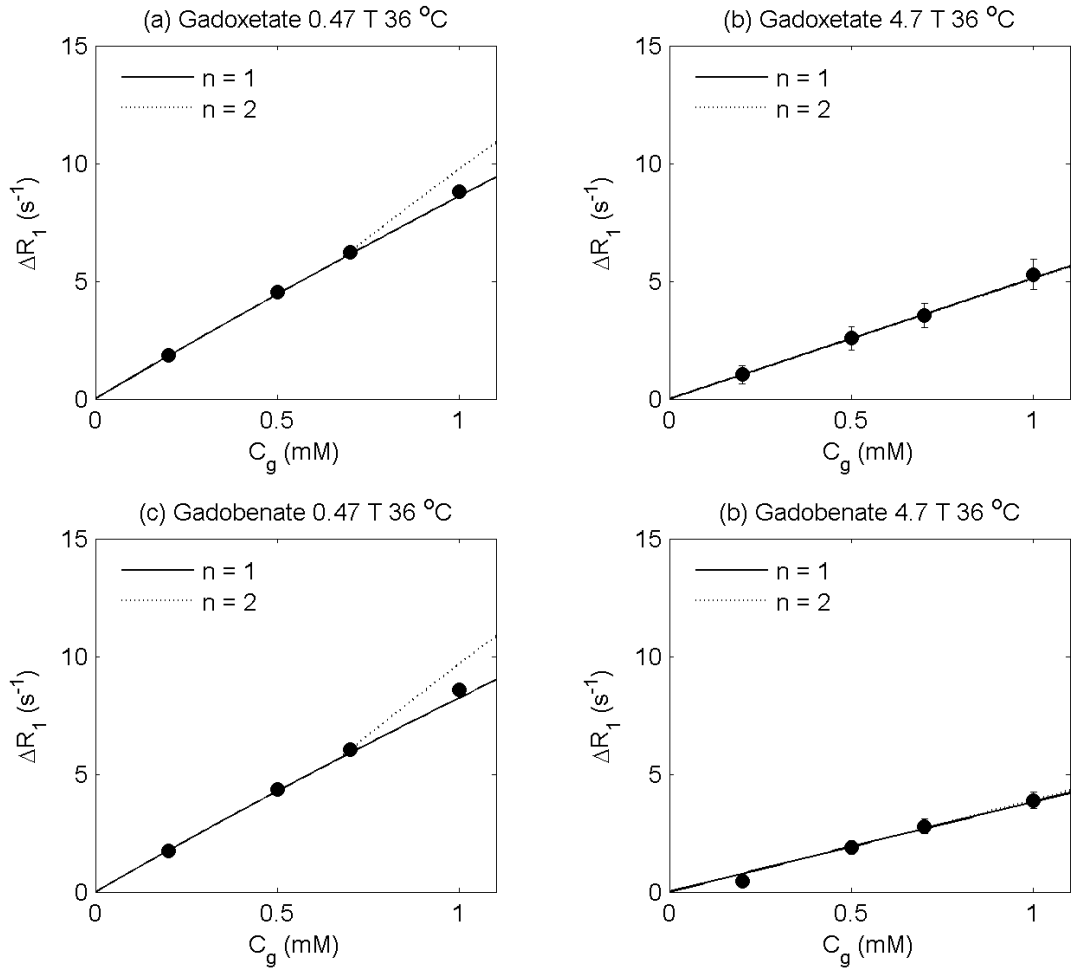

Figure B.3: Modelling n = 1 – 2 binding sites for gadoxetate and gadobenate at body temperature and at 0.47 T and 4.7 T, using Eq. 4.3a–b. Circles represent measured data points; solid line is original model (single binding site, Eq. 4.3a, K_{a1} = 0.255 mM^{-1} (gadoxetate) and 0.226 mM^{-1} (gadobenate)); dotted line also includes a second binding site (Eq. 4.3b, $K_{a2} = K_{a1}$, as no literature binding affinity values could be found for a second site); the same relaxivity values (from Table 4.2) were used at both binding sites

Appendix C: Derivation of maximum bound fraction

The steps to determine the bound fraction (f_b) as contrast agent concentration approaches zero, from Eq. 3.3 and 3.6, are shown below.

$$C_g = C_{gbound} + C_{gfree} \quad [3.3]$$

$$K_a = \frac{C_{gbound}}{C_{gfree}.(C_{sa} - C_{gbound})} \quad [3.6]$$

Replacing C_{gfree} in Eq. 3.6 using Eq. 3.3:

$$K_a = \frac{C_{gbound}}{(C_g - C_{gbound}).(C_{sa} - C_{gbound})} \quad [C.1]$$

Multiplying out the denominator and moving terms across the equals sign:

$$K_a.C_g.C_{sa} - K_a.C_g.C_{gbound} - K_a.C_{gbound}.C_{sa} + K_a.C_{gbound}^2 = C_{gbound} \quad [C.2]$$

Grouping the C_g and C_{gbound} terms:

$$C_g.\left(K_a.C_{sa} - K_a.C_{gbound}\right) = C_{gbound}.(1 - K_a.C_{gbound} + K_a.C_{sa}) \quad [C.3]$$

f_b is C_{gbound}/C_g, therefore dividing Eq. C.3 by C_g gives:

$$\left(K_a.C_{sa} - K_a.C_{gbound}\right) = f_b.(1 - K_a.C_{gbound} + K_a.C_{sa}) \quad [C.4]$$

Rearranging Eq. C.4 gives:

$$f_b = \frac{(K_a.C_{sa} - K_a.C_{gbound})}{(1 - K_a.C_{gbound} + K_a.C_{sa})} \quad [C.5]$$

The bound fraction as C_{gbound} approaches 0, equivalent to the maximum bound fraction (f_{bmax}), is then given by:

$$f_{bmax} \approx \frac{C_{sa}.K_a}{(1 + C_{sa}.K_a)} \qquad [7.1]$$